X-ray studies of magnetic and structural transitions in iridates

Christian Donnerer

Department of Physics and Astronomy
University College London

A thesis presented for the degree of Doctor of Philosophy

August 2017

First supervisor: Des McMorrow
Second supervisor: Andrew Wills

I, Christian Donnerer confirm that the work presented in this thesis is my own. Where information has been derived from other sources, I confirm that this has been indicated in the thesis.

Abstract

In this thesis, I describe x-ray experiments that first detect the symmetry breaking at magnetic and structural transitions in iridium based transition metal oxides, and then characterise the ensuing state.

The magnetic transition in pyrochlore iridates $R_2\text{Ir}_2\text{O}_7$, where $R = \text{Sm}$, Nd and Tb, was studied with resonant x-ray scattering at the Ir L_3 edge. In all samples, $\mathbf{k} = \mathbf{0}$ magnetic order was discovered below 120 K (Sm), 5 K (Nd) and 78 K (Tb), respectively. It is demonstrated how resonant x-ray scattering can determine the size of the magnetic moment, yielding approximately $0.3\,\mu_B$ (Sm) and $0.06\,\mu_B$ (Tb). The magnetic dynamics of Sm and Nd pyrochlores could be well described by excitations from an all-in all-out magnetic structure within a minimal nearest-neighbour Hamiltonian of Heisenberg exchange (27 meV) and Dzyaloshinskii-Moriya interactions (5 meV). This provides a consistent description of the magnetic order and excitations, and suggests that a topological Weyl semimetal could be realised in pyrochlore iridates.

A structural transition from tetragonal to monoclinic symmetry was discovered in the perovskite iridate $\text{Sr}_3\text{Ir}_2\text{O}_7$ at 54 GPa using x-ray diffraction. The high-pressure phase adopts an altered stacking sequence of perovskite layers, and may coupled to the emergence of a metallic state. X-ray absorption spectroscopy was used to characterise the resulting electronic state at high pressure. Compared to the spin-orbit induced insulating state at ambient conditions, the influence of spin-orbit coupling in the high-pressure, metallic phase appears diminished.

Acknowledgments

I would like to thank my supervisor D. McMorrow for the courage of taking on a PhD student who was (and still is) somewhat confused by the notion of magnetism. His constant guidance on all aspects of the life scientific was invaluable. I am particularly grateful for his convincing me to continue studying pyrochlore iridates, after two years of fruitless endeavours. The persistence was eventually rewarded with a series of successful experiments, which now form a major part of this thesis.

I consider myself lucky to have had a steady supply of iridate samples that were synthesised by E. Hunter, R. Perry, D. Prabhakaran and A. Boothroyd.

I am especially thankful to S. Boseggia and M. Moretti, for many useful discussions on x-rays and iridates, which have lead to a joint effort in calculating resonant x-ray scattering cross-sections of iridates.

I am deeply indebted to M. Rahn. His tireless dedication to the pyrochlore iridate project, particularly regarding sample characterisation and preparation, were of great importance in making it a success.

The beamtime experiments described in this thesis would not have been possible without the excellent support from A. Efimenko, M. Moretti, M. Krisch, D. Casa, G. Nisbet, S. Collins, M. Hanfland, S. Francoual, J. Strempfer, J. Jacobs and S. Pascarelli.

I am grateful to have had the company of M. Rahn, L. Veiga, M. Moretti, D. Pincini, J. Vale, Z. Feng, E. Hunter and H. Rønnow during these experiments.

My thanks to C. Howard and A. Wills, who took on the task of examining my upgrade report and provided helpful feedback.

A special thanks to P. Zubko and G. Ghiringhelli who examined this thesis and lead an insightful discussion during the viva. I believe the resulting corrections have strengthened the final version of this document.

I would also like to thank my parents and my brother for their unconditional support, often in the form of food.

Finally, I recognise that this PhD would not have been possible without the financial support I received from the Engineering and Physical Research Council.

Contents

List of Figures **15**

List of Tables **23**

1 Introduction **25**

1.1 Iridates . . . 26

1.1.1 Spin-orbit coupling in iridates . . . 27

1.1.2 $J_{\text{eff}} = 1/2$ magnetism . . . 30

1.2 The pyrochlore iridates . . . 31

1.2.1 Structure and bulk properties . . . 31

1.2.2 Novel topological phases . . . 34

1.2.3 Magnetism . . . 37

1.3 The perovskite iridates . . . 41

1.3.1 High-pressure properties . . . 42

1.4 Probing iridates with x-rays . . . 43

1.5 Overview of thesis . . . 45

1.6 Co-Authorship . . . 46

1.7 Open-access data . . . 47

2 Experimental method **49**

2.1 Resonant x-ray scattering . . . 50

2.1.1 REXS: beamline P09 . . . 53

2.1.2 RIXS: beamline ID20 . . . 54

2.2 High-pressure x-ray techniques . . . 55

2.2.1 The Diamond Anvil Cell . . . 55

2.2.2 HP-XRD: beamline ID09a . . . 56

2.2.3 HP-XAS: beamline ID24 . . . 57

3 RXS at the Ir $L_{2,3}$ edge **59**

3.1 Single-ion model for Ir^{4+} iridates . . . 60

3.2 Cross-section computation . . . 64

3.3 Atomic scattering tensors . . . 65

3.3.1 REXS . . . 66

3.3.2 RIXS . . . 69

3.4 Structure factor for pyrochlore iridates . . . 72

3.5 Conclusion . . . 77

4 REXS of R_2Ir$_2$O$_7$ (R = Sm, Nd, Tb) 79
4.1 Sm$_2$Ir$_2$O$_7$ 80
4.1.1 Bulk properties 80
4.1.2 XRMS 81
4.1.3 XRMS at high magnetic fields 86
4.2 Nd$_2$Ir$_2$O$_7$ 94
4.2.1 Bulk properties 94
4.2.2 XRMS 95
4.3 Tb$_2$Ir$_2$O$_7$ 97
4.3.1 Bulk properties 97
4.3.2 XRMS 98
4.4 Conclusion 101

5 RIXS of R_2Ir$_2$O$_7$ (R = Sm, Nd, Tb) 103
5.1 Preliminaries 104
5.2 Magnetic excitations of R_2Ir$_2$O$_7$ (R = Sm, Nd, Tb) 106
5.2.1 Sm$_2$Ir$_2$O$_7$ 106
5.2.2 Nd$_2$Ir$_2$O$_7$ 111
5.2.3 Tb$_2$Ir$_2$O$_7$ 115
5.3 *dd* excitations of R_2Ir$_2$O$_7$ (R = Sm, Nd, Tb) 118
5.4 Conclusion 121

6 Structural and electronic properties of Sr$_3$Ir$_2$O$_7$ at high pressure 125
6.1 Introduction 126
6.2 High-pressure x-ray diffraction 128
6.2.1 Experimental method 128
6.2.2 Results and discussion 128
6.3 High-pressure x-ray absorption spectroscopy 132
6.3.1 Experimental method 133
6.3.2 Results and discussion 133
6.4 Conclusion 141

7 Conclusion 145
7.1 RXS of pyrochlore iridates 145
7.2 Sr$_3$Ir$_2$O$_7$ at high pressure 147
7.3 Future perspectives 147

A Details on Ir RXS cross-section computations 167
A.1 Trigonal and tetragonal frames 167
A.2 $p - d$ matrix elements 167
A.3 Atomic scattering tensors 170
A.3.1 Tetragonal reference frame 170
A.3.2 Trigonal reference frame 172

B REXS on the pyrochlore lattice **175**
B.1 XRMS of $\mathbf{k} = \mathbf{0}$ magnetic order 175
B.2 Anisotropic tensor susceptibility (ATS) 179
B.3 REXS cross sections 181

C RIXS momentum resolution effects **183**
C.1 RIXS momentum resolution 183
C.2 Effect of momentum resolution on magnetic excitations 185

List of Figures

1.1 Ir^{4+} energy levels in single ion and multi ion pictures. 28
1.2 Density profile of angular part of $J_{\mathrm{eff}} = 1/2$ wavefunction (left), which arises from a combination of t_{2g} orbitals with different orbital and spin contributions (right). 29
1.3 Structure of pyrochlore iridates $R_2\mathrm{Ir}_2\mathrm{O}_7$. (Top left) Full crystal structure. The R atoms are shown in grey, Ir atoms in bronze and O atoms in red. For clarity, the oxygen octahedral environments are drawn without trigonal distortions. (Top right) Ir sublattice only, showing the corner-shared tetrahedra. The structures were plotted with Vesta [33]. (Bottom) Atomic coordinates for pyrochlore iridates $R_2\mathrm{Ir}_2\mathrm{O}_7$, space group $Fd\bar{3}m$ (No. 227), origin choice 2. R is a rare-earth or lanthanide element. . . 32
1.4 Bulk properties of pyrochlore iridates $R_2\mathrm{Ir}_2\mathrm{O}_7$. (a) Resistivity and (b) magnetisation, taken from Ref. [34]. (Bottom) Proposed phase diagram of pyrochlore iridates $R_2\mathrm{Ir}_2\mathrm{O}_7$, taken from Ref. [1]. Non-magnetic rare-earth ions are coloured in pink (Lu, Y and Eu). 33
1.5 Low-energy band structure of a Weyl semimetal, showing two linearly dispersing Weyl nodes of opposite chirality. Red (blue) cones indicate filled (empty) states. 35
1.6 Phase diagram of pyrochlore iridates within a minimal tight-binding model, showing insulating antiferromagnetic (I-AF), Weyl semimetal (WSM), semi-metal (SM) phases (among others). Taken from Ref. [1]. 36
1.7 The tetrahedral network formed by Ir sites in the pyrochlore lattice. 37
1.8 All-in all-out magnetic structure on the pyrochlore lattice. . . . 39
1.9 Evolution of structural and electronic properties of Ruddlesden Popper series of perovskite iridates $\mathrm{Sr}_{n+1}\mathrm{Ir}_n\mathrm{O}_{3n+1}$ for members $n = 1, 2, \infty$. For clarity, the crystal structures were drawn without the octahedral rotations and tilts that are present in the real materials. 41

2.1 Illustration of the two-step RXS process. In the first step, an incoming x-ray promotes a core electron to the valence band. In the second step, another electron decays from the valence band to fill the core hole. The final state can either be identical to the initial state (REXS) or in some excited configuration (RIXS). 51
2.2 Overview of excitations that can be measured by RIXS, taken from Ref. [112]. 52
2.3 Schematic setup of the REXS beamline P09 at PETRA III. . . . 53
2.4 Schematic setup the of RIXS beamline ID20, ESRF. The blue and red lines indicate high and low energy x-ray beams scattered from the sample, respectively. 54
2.5 Operating principle of Diamond Anvil Cell. 55
2.6 Schematic setup of high-pressure XRD beamline ID09a. 56
2.7 Schematic setup of energy dispersive XAS setup on beamline ID24. The red and blue lines indicate low and high energy cutoffs of the polychromatic beam, respectively. 57

3.1 (a) Tetragonal and (b) trigonal octahedral reference frames. . . 61
3.2 Energy level diagram for Ir^{4+} ($5d^5$) in a cubic crystal field (CF) $10Dq$, with spin-orbit coupling (SOC) and non-cubic crystal-fields (CFs) applied perturbatively. 63
3.3 Polarisation resolved single-ion RIXS intensity of crystal-field transitions within t_{2g} manifold at the L_3 edge (left) and L_2 edge (right) as a function of trigonal distortion Δ at constant $\zeta = 450$ meV. Each panel corresponds to specific incoming and outgoing polarisations vectors, as indicated in the figure. 71
3.4 The four inequivalent Ir sites in the pyrochlore unit cell. The coordinates of the local bases follow the convention of Ref. [155]. 73

4.1 Temperature dependence of field-cooled (FC, red line) and zero-field-cooled (ZFC, blue line) magnetisation of multiple $Sm_2Ir_2O_7$ single crystals in a magnetic field of 0.1 T. Data courtesy of D. Prabhakaran. 81
4.2 Scattering geometry for REXS of $Sm_2Ir_2O_7$. 81
4.3 REXS data showing $\mathbf{k} = \mathbf{0}$ magnetic order in $Sm_2Ir_2O_7$. (a) Energy dependence of the (10 0 0) reflection in $\sigma\sigma'$ (red squares, ATS resonance) and $\sigma\pi'$ (blue circles, magnetic resonance) polarisation channels, plotted with Ir L_3 absorption spectrum recorded in total fluorescence yield mode (black line). The data were corrected for self-absorption. (b) Temperature dependence of the (14 0 0) magnetic reflection in $\sigma\pi'$ polarisation, revealing $T_N \sim 108$ K. 82
4.4 Temperature dependence of magnetic (14 0 0) reflection showing substantial beam heating of the sample. The black, filled data points are taken without attenuation, and the blue, open data points are taken with 20% beam intensity. 83

4.5 Symmetry-allowed $\mathbf{k} = \mathbf{0}$ magnetic structures of Ir site of the pyrochlore lattice, as described in Ref. [160]. 84

4.6 Analysis of REXS cross-sections of $Sm_2Ir_2O_7$. (a) Azimuthal dependence of integrated intensity of the (14 0 0) reflection in $\sigma\pi'$ polarisation. The solid line is the calculated ATS and magnetic scattering $\boldsymbol{\psi}_{1,2,3}$, dotted lines are calculated magnetic contributions of basis vectors $\boldsymbol{\psi}_i$. (b) Energy dependence of the (14 0 0) reflection in $\sigma\pi'$ polarisation at azimuthal angles $\phi = 0°$ and $\phi = 45°$ (bottom). The corresponding difference signal is proportional to the resonance at $\phi = 0°$ in the nonmagnetic $\sigma\sigma'$ polarisation channel (top). (c) Integrated intensity of space group forbidden ($h00$) reflections, plotted with calculated intensities of basis vectors $\boldsymbol{\psi}_i$. 85

4.7 Schematic of experimental setup for high-field REXS of $Sm_2Ir_2O_7$. $\mathbf{B}$ shows the direction of the magnetic field, χ is the rotation of the phase-plate ensemble and η the rotation of the linear polarimeter. Rotating χ corresponds to changing the angle of incoming linear polarisation; rotating η selects the component of outgoing linear polarisation that will reach the detector. . . . 87

4.8 Measured Poincaré-Stokes parameters P_1 (blue circles) and P_2 (red circles) of the direct beam at the Ir L_3 edge (11.215 keV), as a function of phase plate rotation χ. P'_{lin} (magenta) is the deduced degree of linear polarisation. The solid lines are calculated Poincaré-Stokes parameters of an ideal setup. 90

4.9 Measured (circles) and calculated (solid lines) Poincaré-Stokes parameters P'_1 (blue) and P'_2 (red) after scattering from the (10 0 0) reflection of $Sm_2Ir_2O_7$ at (a) T = 150 K and (b) T = 5 K, as a function of phase plate rotation χ. P'_{lin} (magenta) is the deduced degree of linear polarisation. 91

4.10 Measured (circles) and calculated (solid lines) temperature difference in Poincaré-Stokes parameters, $\Delta P'_1$ (blue) and $\Delta P'_2$ (red), of the (10 0 0) reflection of $Sm_2Ir_2O_7$ at B = 0 T as a function of phase-plate angle χ. This signal is a direct signature of the magnetic structure, and can be well described by AIAO order. 92

4.11 Measured (circles) and calculated (solid lines) Poincaré-Stokes parameters P'_1 (blue) and P'_2 (red) of the (10 0 0) reflection of $Sm_2Ir_2O_7$ at T = 5 K and B = 12 T as a function of phase plate angle χ. P'_{lin} (magenta) is the deduced degree of linear polarisation. 93

4.12 Temperature dependence of resistivity (left) and magnetisation (right) of $Nd_2Ir_2O_7$ single-crystal. Data courtesy of M. Rahn and D. Prabhakaran. 94

4.13 Temperature dependence of integrated intensity of (14 0 0) reflection of $Nd_2Ir_2O_7$ at the Ir L_3 edge with incident π polarisation. The incident beam was attenuated by a factor of ~ 28 using 700 μm of Al foil. 96
4.14 (Left) Resistivity of $Tb_2Ir_2O_7$ single-crystal as a function of temperature. (Right) Temperature dependence of magnetisation of multiple $Tb_2Ir_2O_7$ single-crystals. Data courtesy of M. Rahn and D. Prabhakaran. 97
4.15 REXS data of $Tb_2Ir_2O_7$. (a) Temperature dependence of (14 0 0) reflection in the $\sigma\pi'$ polarisation (blue circles), at an incident energy of 11.215 keV. The solid black line is a power law fit to the data, yielding $T_N = 71$ K. (b) Reciprocal lattice scan along the h direction of (14 0 0) reflection (blue circles) and Lorentzian fit to the data (black solid line). (c, d) Energy dependence of (14 0 0) reflection in $\sigma\pi'$, $\sigma\sigma'$ polarisation at 5 K (blue circles) and 90 K (red squares). The data were corrected for self-absorption. The black solid line is the total fluorescence yield (TFY). 99
4.16 Azimuthal scan of (14 0 0) reflection of $Tb_2Ir_{2-x}O_7$ in $\sigma\pi'$ polarisation at 5 K (blue circles) and 100 K (red squares), at an incident energy of 11.215 keV. The solid lines are calculated intensities for ATS scattering and magnetic scattering from AIAO order (blue), and ATS scattering only (red). 101

5.1 Incident energy dependence of RIXS energy loss features of $Sm_2Ir_2O_7$ at $\mathbf{Q} = (7.5\ 7.5\ 7.5)$ at 20 K. The dotted and solid lines indicate incident energies where transitions predominantly to $5d(t_{2g})$ and $5d(e_g)$ levels occur, respectively. The observed energy loss features correspond to excitations within the t_{2g} manifold (intra t_{2g}), crystal field excitation to the e_g manifold (t_{2g} to e_g) and charge transfer (CT) excitations. 105
5.2 (a-c) Constant wave vector RIXS energy scans along high-symmetry directions of $Sm_2Ir_2O_7$ at 20 K. (d) Temperature dependence of magnetic excitations at $\mathbf{Q} = (7.4\ 7.4\ 7.4)$. (e) Momentum subtraction of RIXS energy scans, the energy scan at the zone boundary L was subtracted from energy scans towards the Γ point (elastic line subtracted). (f) Temperature subtraction of RIXS energy scans, the energy scans at 160 K were subtracted from energy scans at 20 K along the $\Gamma - L$ line (elastic line not subtracted). 107
5.3 (a-b) Representative fitted RIXS energy scans of $Sm_2Ir_2O_7$. (c) Fitted energy dispersion of feature B as a function of momentum transfer (black dots) plotted with calculated magnon dispersion of AIAO order (blue dotted lines). (d) Fitted intensity dispersion of feature B (black dots) plotted with calculated total dynamical structure factor $\sum_{a=x,y,z} S^{aa}(\mathbf{q}, \omega)$ of AIAO order (blue dotted lines). 109

5.4 Constant wavevector RIXS energy scans of $Nd_2Ir_2O_7$. (a) Dispersion of low-lying excitations in the magnetically ordered state along (h00) reciprocal lattice direction. (b) Temperature dependence of selected $\mathbf{Q}$ points, below (black lines) and above (red lines) the ordering temperature. (c) Momentum subtraction of RIXS energy scans at 2.5 K, the zone boundary scan (13 0 0) was subtracted from all other scans. (d) Temperature subtraction of RIXS energy, the data at 5 K were subtracted from the data at 2.5 K. . . . 112
5.5 Representative fitted energy scans of $Nd_2Ir_2O_7$ at 2.5 K. 113
5.6 Fitted energy (a) and intensity dispersion (b) of feature B, plotted over calculated single-magnon dynamical structure factor $[S^{yy}(\mathbf{q},\omega)+S^{zz}(\mathbf{q},\omega)]$ of AIAO magnetic order within linear spin-wave theory, using J = 28(2) meV and D = 4.8(5) meV. 113
5.7 RIXS constant wavevector energy scans of $Tb_2Ir_2O_7$. (a) Low-energy excitations along (88L) direction towards the antiferromagnetic zone centre at (886). The black solid line is the measured energy resolution. (b) Temperature dependence of excitations above (red solid line) and below (black solid line) the magnetic ordering temperature. (c) Momentum subtraction, the zone boundary data at (887) were subtracted from (88L) scans. (d) Temperature subtraction, data points at 100 K were subtracted from data at 6 K. 116
5.8 Fitted RIXS energy scan of $Tb_2Ir_2O_7$ at $\mathbf{Q}$ = (8 8 6.2) at 6 K. . 117
5.9 (a) RIXS data of $Sm_2Ir_2O_7$ and $Nd_2Ir_2O_7$ showing dd excitations within t_{2g} manifold. The vertical lines indicate the position of the maxima, as determined by fitting Lorentzian functions to the data. (b) Calculated excitation energies $f \rightarrow g, h$ doublets, Δ is the strength of trigonal distortions, the spin-orbit coupling ζ was set to 450 meV. The grey area shows a typical value of Δ for pyrochlore iridates. 118
5.10 RIXS experimental geometry for $Nd_2Ir_2O_7$. 120
5.11 RIXS constant wavevector energy scans of $Nd_2Ir_2O_7$ along (hkk), showing t_{2g} crystal-field excitations E_1, E_2 (circles) plotted with calculated RXS intensities (solid lines). For the latter, a phenomenological Lorentzian broadening was introduced. 120

6.1 Integrated XRD spectra of $Sr_3Ir_2O_7$ at high pressure at ambient temperature. (a) $Sr_3Ir_2O_7$ in its monoclinic phase (space group $C2$) at 61 GPa; (d) the corresponding structure. (b) Tetragonal phase of $Sr_3Ir_2O_7$ (space group $I4/mmm$) at 17 GPa; (c) the corresponding structure. In (a) and (b) the red circles are background-subtracted data points, the black solid line presents the Rietveld refinement, blue tick marks are the calculated Bragg reflections, and the residuals of the refinement are shown by the black line beneath. Reflections from SrB_4O_7:Sm^{2+} are marked by an asterisk. The inset in (a) shows the pressure evolution of small-angle reflections. In (c) and (d) the iridium atoms are shown in bronze, the oxygen atoms in red and the strontium atoms in purple. The structures in (c) and (d) were visualised via VESTA [33]. 129

6.2 Equation of state of $Sr_3Ir_2O_7$. (a) and (b) Lattice parameters as a function of pressure at room temperature. The inset in (a) shows the normalised lattice constants as a function of pressure at 20 K. (c) Equation of state of $Sr_3Ir_2O_7$ at room temperature. The solid line is a Vinet-type fit to the observed equation of state of $Sr_3Ir_2O_7$. The inset in (c) shows the c/a ratio as a function of pressure at room temperature. In all panels, the black circles and red squares correspond to low and high pressure phases of $Sr_3Ir_2O_7$, respectively, and the dotted line indicates the transition pressure of 53 GPa. Data points of the high-pressure phase falling below the dotted line were taken during decompression. . 131

6.3 High-pressure XAS data of $Sr_3Ir_2O_7$. (a, b) Pressure evolution of XAS at the Ir L_3, L_2 absorption edges. (c) Representative fitted XAS at 25 GPa at the Ir L_3 and L_2 absorption edges of $Sr_3Ir_2O_7$. The red circles are the normalised data points, the black solid line is a fit of arctangent and a Lorentzian functions, as described in the text. 133

6.4 Fitted high-pressure XAS data of $Sr_3Ir_2O_7$. (a, b) White line integrated intensities at the Ir L_3, L_2 edge. (c, d) White line energy position (absorption maximum) of the Ir L_3, L_2 edge. (e) Ground state SOC expectation value $\langle \mathbf{L} \cdot \mathbf{S} \rangle$, deduced from the branching ratio of integrated intensities of white lines, I_{L_3}/I_{L_2}. The solid line is the calculated $\langle \mathbf{L} \cdot \mathbf{S} \rangle$ of the $\zeta - 10Dq$ model, using $\zeta = 0.45$ eV and $10Dq$ values from Ref. [100]. In all panels, the vertical dotted line denotes the structural phase transition at 53 GPa. 135

6.5 Spin-orbit induced hybridisation of t_{2g} and e_g levels within $\zeta - 10Dq$ model. (a) $5d$ energy levels as a function of $\zeta/10Dq$. The energy differences e_1 and e_2 are defined in the text. (b) Projection of $5d$ wavefunctions onto t_{2g} (blue, solid line) and e_g (red, dashed line) basis states at $\zeta/10Dq = 0.5$. (c) $\langle \mathbf{L} \cdot \mathbf{S} \rangle$ contributions of individual $5d$ levels as a function of $\zeta/10Dq$. In panels (a) and (c) the vertical dotted line denotes a characteristic value of $\zeta/10Dq = 0.15$ for Ir^{4+} iridates at ambient pressure. 137

B.1 Symmetry-allowed $\mathbf{k} = \mathbf{0}$ magnetic structures of $16c$ or $16d$ site of the pyrochlore lattice, as described in Ref. [160]. 176

C.1 RIXS momentum resolution due to finite analyser crystal area. . 183
C.2 RIXS momentum resolution in real and reciprocal space for $Nd_2Ir_2O_7$ at $\mathbf{Q} = (14\ 0\ 0)$, using a circular analyser mask of $r_{an} = 30$ mm. 185
C.3 Integrated momentum resolution along specific reciprocal space directions at $\mathbf{Q} = (14\ 0\ 0)$. 185
C.4 Effect of momentum resolution on the magnetic excitations in $Nd_2Ir_2O_7$. The black solid lines are the expected dispersion of magnetic excitations using a reciprocal space grid of $\sim$ 1e3 points centred on the nominal $\mathbf{Q}$ value. The red line is a convolution of the momentum sampled data with the energy resolution, and corresponds to what would be measured in a RIXS experiment. 186
C.5 Effect of momentum resolution on the single-magnon dispersion of AIAO order, using J=27 meV, D = 5 meV. The data points indicate the maxima of the single-magnon excitation, after taking into account momentum and energy resolution. 187

List of Tables

1.1 Survey of experimental investigations into the magnetic order of pyrochlore iridates $R_2\mathrm{Ir}_2\mathrm{O}_7$. Here, AIAO = all-in all-out, μSR = muon spin rotation, NPD = neutron powder diffraction and RXS = resonant x-ray scattering. The * refers to experiments presented in this thesis. 40

3.1 Strength of non-cubic crystal field Δ in magnetically ordered Ir^{4+} iridates. 68

5.1 Summary of t_{2g} crystal-field excitations of pyrochlore iridates. The values for E_1 and E_2 and their respective errorbars were determined by fitting Lorentzian functions to the data. Energy scales of spin-orbit coupling ζ and trigonal distortion Δ were estimated within the single-ion model. 119

A.1 Definitions of t_{2g} orbitals in tetragonal and trigonal basis functions. 167

B.1 ATS-allowed, forbidden reflections for dipolar transitions involving the 16d or 16c site of $Fd\bar{3}m$. The structure factors are defined in the crystallographic reference frame. 181

Chapter 1

Introduction

Contents

1.1 Iridates 26

1.1.1 Spin-orbit coupling in iridates 27

1.1.2 $J_{\mathrm{eff}} = 1/2$ magnetism 30

1.2 The pyrochlore iridates 31

1.2.1 Structure and bulk properties 31

1.2.2 Novel topological phases 34

1.2.3 Magnetism 37

1.3 The perovskite iridates 41

1.3.1 High-pressure properties 42

1.4 Probing iridates with x-rays 43

1.5 Overview of thesis 45

1.6 Co-Authorship 46

1.7 Open-access data 47

In this chapter, we provide the general motivation for studying iridium oxides, by giving an overview of the many novel phenomena that may be observed in these materials. We show how the electronic ground state of iridates is dominated by the strong spin-orbit coupling of the Ir ion, and discuss implications for unconventional electronic and magnetic properties. We then review the families of pyrochlore and perovskite iridates, the materials investigated in this thesis. We highlight open research questions concerning magnetic (pyrochlore) and structural (perovskite) aspects in these iridates, and how we address them using x-ray scattering techniques. The chapter closes with an overview of the thesis.

1.1 Iridates

In the past decade, interest in iridium-based transition metal oxides (or iridates) has surged. This can be traced to the recent discovery that the strong atomic spin-orbit coupling inherent to the $5d$ Ir ion, which competes on the same magnitude as electronic correlations and crystal-fields, can result in a rich variety of unusual electronic and magnetic states [1, 2]. First among these was the discovery of a "spin-orbit induced" Mott insulating state in the perovskite iridate Sr_2IrO_4 [3, 4], which shows similarities to the Mott insulators found in $3d$ transition metal oxides (TMOs). This was surprising, since electronic correlations in $5d$ TMOs were thought to be too weak to form Mott-like insulating states. Since then, Sr_2IrO_4 was shown to share many key characteristics of Mott insulating cuprates, which raises hopes of discovering another family of high-temperature superconductors in iridates. Nevertheless, the microscopic physics governing a spin-orbit Mott insulator is very different to a regular Mott insulator. For example, in the former, the spin-orbit coupling entangles spin and orbital components of the ground state wavefunction, which enables to tune the magnetic interactions through the lattice geometry, and allows to stabilise exotic magnetic states, such as quantum spin liquids [5]. Furthermore, the spin-orbit coupling strongly affects the electronic band structure of iridates, and many unprecedented topological phases have been predicted, such as the Weyl semimetal, the axion insulator and the topological Mott insulator [2, 6–10]. It is remarkable that a single family of materials manages to unite such a diversity of research areas of solid state physics, including superconductivity, strongly correlated electrons, quantum magnetism and topology.

1.1.1 Spin-orbit coupling in iridates

The key motivation for studying iridates, and more generally $5d$ TMOs, is the physics emerging from the interplay of strong spin-orbit coupling (SOC) and electronic correlations (U). In general, for transition metal ions, as one descends the periodic table, electronic correlations become weaker. This can be understood from the increased radial extent of electronic orbitals with increasing principal quantum number, which tends to reduce the Coulomb repulsion U. Hence the strongly correlated $3d$ TMOs tend to form Mott insulators, where the electronic charge is localised by Coulomb repulsions (in contrast to band insulators, where an energy gap arises solely from free electrons in a periodic lattice potential). For $5d$ TMOs, the Coulomb repulsions U are expected to be comparatively moderate, such that the electronic behaviour should generally be more itinerant and tend towards metallic ground states.

The atomic spin-orbit coupling ζ can oppose this trend. Microscopically, the spin-orbit coupling arises from the nuclear charge Z. In the reference frame of valence electrons, the nuclear charge appears as a current loop, generating a magnetic field that interacts with the electron spin as $\zeta \mathbf{L} \cdot \mathbf{S}$. In a semi-classical derivation, one can derive $\zeta \propto Z^4$ [11], but other treatments find a proportionality of $\zeta \propto Z^2$ [12]. Ultimately, the value of ζ has to be empirically determined, typical values for $3d$ ions are $\zeta \sim 20$ meV, whereas in $5d$ elements $\zeta \sim 500$ meV [13]. Thus it becomes clear that for heavy transition metal ions, ζ becomes important in forming the electronic ground state.

In order to understand how SOC can act cooperatively with U to create a Mott-like insulating state, we consider the specific example of iridates. We confine the discussion to Ir^{4+} ($5d^5$) in a cubic environment of oxygen ligands, relevant to the pyrochlore and perovskite iridates studied in this thesis.

Starting from the free Ir^{4+} ion, the strongest energy scale is typically the cubic crystal field splitting $10Dq$, which lifts the degeneracy of the ten $5d$ orbitals into six-fold t_{2g} and four-fold e_g levels. The large radial extent of the $5d$ wavefunctions leads to significant overlap with oxygen ligands, resulting in a strong splitting of $10Dq \sim 3$ eV [14]. A d^5 configuration can then fill the crystal levels in either high spin ($t_{2g}^3 e_g^2$; $S = \frac{5}{2}$) or low spin (t_{2g}^5; $S = \frac{1}{2}$) configurations. The relative strengths of Hund's coupling J_H and $10Dq$ determine which state will be realised, their respective energies are $E(t_{2g}^3 e_g^2) = 2 \times 10Dq - 10J_H$ and $E(t_{2g}^5) = -4J_H$. Hence the low spin configuration becomes favourable if $10Dq > 3J_H$. Assuming typical energy scales of $10Dq \sim 3$ eV and $J_H \sim 0.5$ eV

[14], iridates tend to adopt a low spin state, where all five d electrons occupy t_{2g} levels.

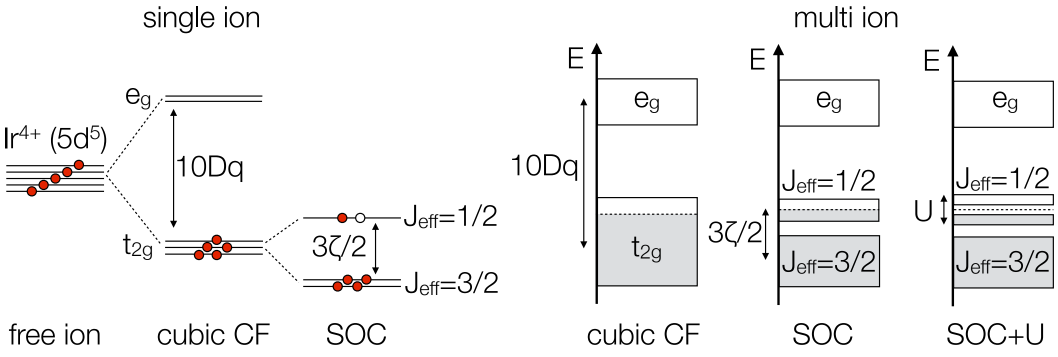

Figure 1.1: Ir^{4+} energy levels in single ion and multi ion pictures.

We then consider the effect of the spin-orbit coupling ζ on the isolated t_{2g} manifold. This implies that the spin-orbit coupling is treated as a perturbation on the cubic crystal field ($\zeta \ll 10Dq$). By evaluating the expectation values of the angular momentum operator, one can show that $\mathbf{L}(t_{2g}) = -\mathbf{L}(p)$ [14]. The t_{2g} states can thus be mapped onto an effective angular momentum one multiplet [$l_{\text{eff}}(t_{2g}) = -1$], in which case the spin-orbit coupling operator becomes $-\zeta\mathbf{L}\cdot\mathbf{S}$. Switching on the spin-orbit coupling then removes the orbital degeneracy by splitting the t_{2g} manifold into a $J_{\text{eff}} = 1/2$ doublet and a $J_{\text{eff}} = 3/2$ quartet. The use of effective angular momentum here reverses the order of multiplets (i.e. reverses Hund's second rule), hence the $J_{\text{eff}} = 1/2$ doublet lies higher in energy than the $J_{\text{eff}} = 3/2$ quartet. Recalling that there are five $5d$ electrons, we completely fill the $J_{\text{eff}} = 3/2$ quartet and leave the $J_{\text{eff}} = 1/2$ doublet half occupied. The electronic ground state of Ir^{4+} iridates can therefore be approximated by a single hole in the $J_{\text{eff}} = 1/2$ state.

In order to understand the consequences of the $J_{\text{eff}} = 1/2$ state on electronic and magnetic phenomena, we first analyse its orbital character. The spin-orbit coupling operator can be expanded as $\zeta\mathbf{L}\cdot\mathbf{S} = \zeta[\frac{1}{2}(L^+S^- + L^-S^+) + L^zS^z]$. The presence of $L^\pm S^\mp$ terms immediately shows that its eigenstates will comprise of wavefunctions with differing spin and orbital angular momenta. Specifically, the $J_{\text{eff}} = 1/2$ doublet in a basis of t_{2g} orbitals, labelled by $|L_z, S_z\rangle$, can be written as:

$$|J_{\text{eff}} = 1/2, \uparrow\rangle = \sqrt{\frac{1}{3}}\,|0, \uparrow\rangle - \sqrt{\frac{2}{3}}\,|{+1}, \downarrow\rangle$$
$$|J_{\text{eff}} = 1/2, \downarrow\rangle = \sqrt{\frac{1}{3}}\,|0, \downarrow\rangle - \sqrt{\frac{2}{3}}\,|{-1}, \uparrow\rangle$$

While this $J_{\text{eff}} = 1/2$ electronic state has been known to exist in iridates since the 1960s [14], it only recently rose to prominence, following pioneering work by Kim *et al.* [3, 4] who proposed that a “spin-orbit induced” Mott insulator is realised in the perovskite iridate Sr_2IrO_4.

This novel phase can be intuitively understood from the combination of orbitals involved in the $J_{\text{eff}} = 1/2$ state, which leads to a peculiar cubic probability density of the angular part of the wavefunction, see Fig. 1.2. Compared to t_{2g} orbitals without spin-orbit coupling, the spatial extent of the $J_{\text{eff}} = 1/2$ state is strongly reduced (as the angular wavefunctions are all normalised, any anisotropy in orbital shape will result in a larger spatial extent). In a crystalline environment, this reduces the overlap with neighbouring orbitals and hence the hopping amplitudes, leading to a narrowed electronic bandwidth and a more localised behaviour (see Fig. 1.1). The narrow $J_{\text{eff}} = 1/2$ bandwidth then allows for the comparatively modest U of $5d$ electrons to open an electronic gap, resulting in a spin-orbit Mott insulator [3, 4]. Thus we find that SOC and U can act cooperatively in iridates to create a spin-orbit induced Mott insulator.

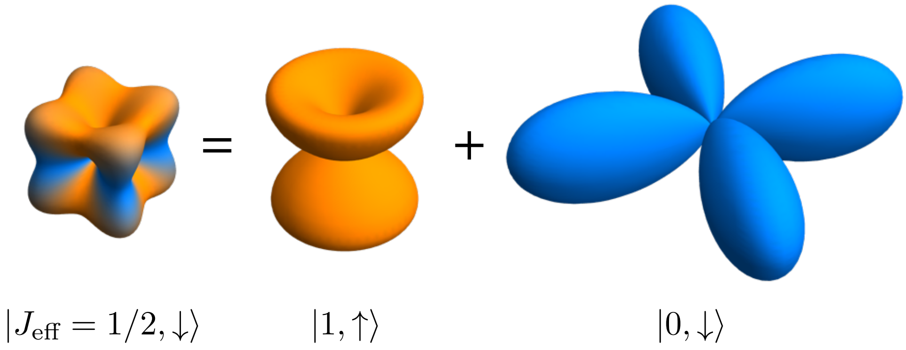

Figure 1.2: Density profile of angular part of $J_{\text{eff}} = 1/2$ wavefunction (left), which arises from a combination of t_{2g} orbitals with different orbital and spin contributions (right).

1.1.2 $J_{\mathrm{eff}} = 1/2$ magnetism

The proposal of a $J_{\mathrm{eff}} = 1/2$ spin-orbit Mott insulator has prompted many investigations to examine the implications for magnetic and electronic properties [1, 2, 5–10, 15]. Although the $J_{\mathrm{eff}} = 1/2$ wavefunction has an orbital component, the magnetic moment remains isotropic, with a g-factor of $g = -2$, opposite to a real $S = 1/2$ of $g = 2$. This implies that any magnetic anisotropy is expected to arise from exchange, as opposed to single-ion, terms.

The anisotropic exchange originates from the orbital component of the $J_{\mathrm{eff}} = 1/2$ wavefunction, which is sensitive to the crystal environment, as opposed to the spin component, which does not couple to crystal fields. One of the most influential studies is the strong coupling limit described by Jackeli and Khaliullin [5], where the two canonical examples of the 180 and 90 degree Ir-O-Ir bond were derived. In the former, the magnetic exchange is predominantly of antiferromagnetic Heisenberg character, whereas in the latter the oxygen-mediated exchange interactions cancel, suppressing the Heisenberg exchange. When considering excited states generated by Hund's coupling, a highly anisotropic, bond-directional exchange is found. On a honeycomb lattice, this bond directional exchange could stabilise an exactly soluble quantum spin liquid (QSL) state, known as the Kitaev model [16].

A close physical realisation of the 180 degree Ir-O-Ir bond occurs in the perovskite iridate Sr_2IrO_4, where experiments have indeed found that the exchange interactions are predominantly of isotropic Heisenberg character [3, 4, 17]. This, among other structural and electronic similarities [18–21], creates strong links to the parent compounds of high-temperature cuprate superconductors, in particular La_2CuO_4, and raises hopes that Sr_2IrO_4 will superconduct when doped [15, 22–24]. However, while essentially the same effective low-energy Hamiltonian can be used for both Sr_2IrO_4 and La_2CuO_4, the underlying physics differs decidedly. This is particularly evident when doping: In Sr_2IrO_4 doped holes first populate $5d$ states, as opposed to oxygen $2p$ levels in cuprates [25]. At the time of writing, no superconductivity has been found in doped Sr_2IrO_4.

A physical realisation of the 90 degree Ir-O-Ir bond are the honeycomb iridates $(Na/Li)_2IrO_3$ and $RuCl_3$[1]. Again, strong evidence has been found that Kitaev exchange is substantial in these materials, although all samples show magnetic order at low temperature, with sometimes highly complex magnetic structures [26–30]. Theoretical studies suggest that a Kitaev state only exists in a very small parameter space [2], which might be difficult to reach in real materials. A true Kitaev state at low temperature would be of great interest, as the low energy excitations emerging from this state are yet undiscovered Majorana fermions [16]. Beyond this fundamental interest, a Kitaev QSL could also offer quantum computing stable from decoherence [16]. Already, neutron scattering investigations above the magnetic ordering temperature of $RuCl_3$ have shown signatures of Majorana excitations emerging from a Kitaev QSL [31], and further studies using magnetic fields, doping and high-pressure are very actively pursued.

---

[1] $RuCl_3$ is proposed to be a $4d^5$ realisation of the $J_{\mathrm{eff}} = 1/2$ state.

We now introduce the two families of iridate materials studied in this thesis, the pyrochlore and perovskite iridates.

1.2 The pyrochlore iridates

In addition to magnetic phenomena, strong spin-orbit coupling can induce novel electronic states. This is most well-known from topological insulators, where SOC stabilises topologically protected surface states [32]. So far, the study of non-trivial band topology has largely been confined to weakly correlated materials. Iridates offer the possibility of studying topological phenomena in the correlated electron regime, which could result in entirely new phases, such as the topological Mott insulator [6]. In this context, most attention has been received by the pyrochlore iridates R_2IrO_7 (R is a rare-earth element), where various interacting topological phases have been proposed, most prominently the Weyl semimetal [1].

Extensive review articles on pyrochlore iridates have been written, a pedagogical introduction can be found in Ref. [1], and a more recent summary in Ref. [10]. Here, we limit ourselves to a brief summary of key results and predictions, focussing on magnetic properties, which will be investigated in this thesis.

1.2.1 Structure and bulk properties

The pyrochlore iridates are a family of materials of stoichiometry $R_2Ir_2O_7$, where R is a rare-earth (or lanthanide) element. They adopt the pyrochlore crystal structure, space group $Fd\bar{3}m$ (No. 227), where rare-earth and iridium sites form interpenetrating corner-shared tetrahedral sublattices, while the oxygen sites form a trigonally distorted cubic environment for Ir. The crystal structure and atomic coordinates are shown in Fig. 1.3.

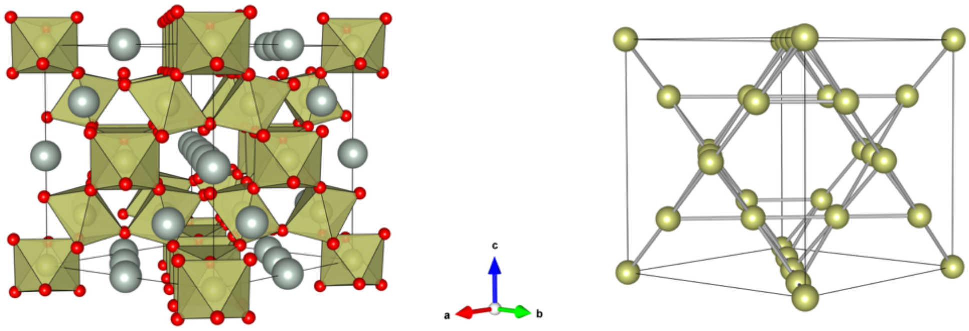

Label	Element	Site	Symmetry	x	y	z	Occupation
R	R	16d	$.\bar{3}m$	1/2	1/2	1/2	1
Ir	Ir	16c	$.\bar{3}m$	0	0	0	1
O1	O	8b	$\bar{4}3m$	3/8	3/8	3/8	1
O2	O	48f	$2.mm$	x	1/8	1/8	1

Figure 1.3: Structure of pyrochlore iridates $R_2\mathrm{Ir}_2\mathrm{O}_7$. (Top left) Full crystal structure. The R atoms are shown in grey, Ir atoms in bronze and O atoms in red. For clarity, the oxygen octahedral environments are drawn without trigonal distortions. (Top right) Ir sublattice only, showing the corner-shared tetrahedra. The structures were plotted with Vesta [33]. (Bottom) Atomic coordinates for pyrochlore iridates $R_2\mathrm{Ir}_2\mathrm{O}_7$, space group $Fd\bar{3}m$ (No. 227), origin choice 2. R is a rare-earth or lanthanide element.

A stoichiometric pyrochlore has only two free crystallographic parameters: The lattice constant a (typically around 1 nm), and the x coordinate of oxygen at the 48f Wyckoff position. This x coordinate determines the amount of trigonal distortion of the cubic crystal field. In ideal cubic symmetry, it becomes $x_c = 5/16 = 0.3125$. For all pyrochlore iridates $x > x_c$, such that the oxygen octahedra are trigonally compressed [1].

A wide range of rare-earth and lanthanide elements have been found to form pyrochlore iridates, including R = Y, Lu, Yb, Ho, Dy, Tb, Gd, Eu, Sm, Nd, Pr. Nominally, the rare-earth oxidation state is R^{3+}, leaving Ir^{4+} and O^{2-}. One consequence of different R elements is to modify the crystal structure. With decreasing atomic number Z from Dy to Pr, the ionic radius increases (lanthanide contraction), which is reflected in the lattice constants from $a \sim 10.0 - 10.4$ Å. Additionally, the radius of the R site can affect the x coordinate of 48f oxygen, which determines the Ir-O-Ir bond angle ($\sim 130°$) and the amount of (structural) trigonal distortion.

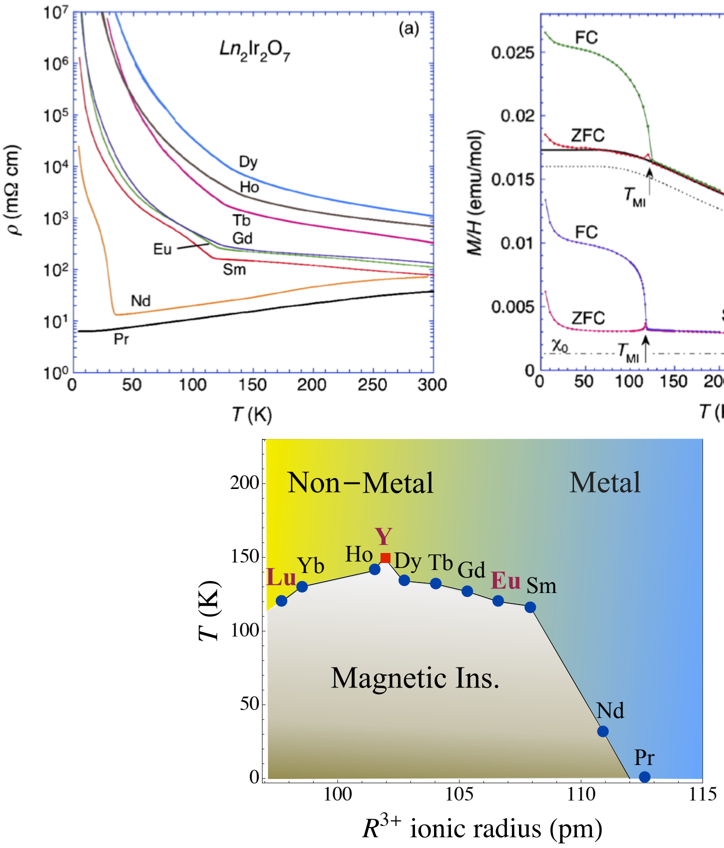

Figure 1.4: Bulk properties of pyrochlore iridates $R_2Ir_2O_7$. (a) Resistivity and (b) magnetisation, taken from Ref. [34]. (Bottom) Proposed phase diagram of pyrochlore iridates $R_2Ir_2O_7$, taken from Ref. [1]. Non-magnetic rare-earth ions are coloured in pink (Lu, Y and Eu).

The pyrochlore iridates have first gained interest with the discovery of an insulator-to-metal transition (IMT), accompanied by magnetic ordering, occurring as a function of rare-earth ion [35]. While early resistivity measurements disagreed as to where the IMT boundary lies, the data and phase diagram proposed by Matsuhira *et al.* [34, 36] has now become accepted and could be independently reproduced [37] (see Fig. 1.4). It places the $T = 0$ K boundary between Nd (antiferromagnetic insulator) and Pr (paramagnetic metal) pyrochlore iridates. Additionally, insulating pyrochlore iridates close to this boundary, such as Nd, Eu and Sm, show thermal insulator-metal transitions. At the thermal IMTs, field-cooled and zero-field-cooled magnetisations bifurcate, which was attributed to antiferromagnetic ordering of the Ir ions. The smaller rare-earth pyrochlore iridates, such as Gd, Tb, Ho and Dy, remain insulating at all temperatures. They also show antiferromagnetic transitions with ordering temperatures between 100 - 150 K, accompanied by anomalies in the resistivity.

1.2.2 Novel topological phases

In general, the realisation of non-trivial band topology requires that Coulomb repulsions are not strong enough to fully localise electrons. As the IMT in pyrochlore iridates suggests that these materials exhibit weak-to-intermediate correlations, in the presence of strong spin-orbit coupling, the electronic band structure has received substantial attention. It was proposed that pyrochlore iridates could realise topological Mott insulators, axion insulators and Weyl semimetals (WSMs) [1, 6, 8]. The latter prediction has received great interest, as its low energy emergent quasiparticles resemble massless Weyl fermions, which have not yet been observed as elementary particles.

The Weyl semimetal

Comprehensive reviews on topological semimetals can be found in Refs. [38–40]. As opposed to topological insulators, WSMs do not have a bulk energy gap. Instead, at certain points in the Brillouin zone, linear, non-degenerate valence and conduction band touch, resulting in a point-like Fermi surface. Close to the Fermi level, the low-energy Hamiltonian of WSM resembles the Weyl equation, which is a simplified version of the Dirac equation, for massless fermions with definite chirality [41]:

$$H^{\pm}_{\mathrm{Weyl}} = \pm v_f \mathbf{p} \cdot \boldsymbol{\sigma}$$

where v_f is the Femi velocity, $\mathbf{p}$ the momentum and $\boldsymbol{\sigma}$ the Pauli matrices. The resulting band structure consists of a pair of band touchings at $k_{\pm}$, such that $p = \hbar(k - k_{\pm})$, and the energy dispersion at each node is $E = v_f p$ (see Fig. 1.5). The nodes have a chirality of ±1 associated with them, such that the net chirality in the crystal cancels, in accordance with the fermion doubling theorem [42].

$H^{\pm}_{\mathrm{Weyl}}$ can be solved by two component spinors, as opposed to the four component spinors solution of the Dirac equation. It follows that in a WSM only two states must meet at the Fermi level, such that the touching conduction and valence bands must be non-degenerate. In order to achieve this accidental two-fold degeneracy in a crystal, either time-reversal or inversion symmetry must be broken [43].

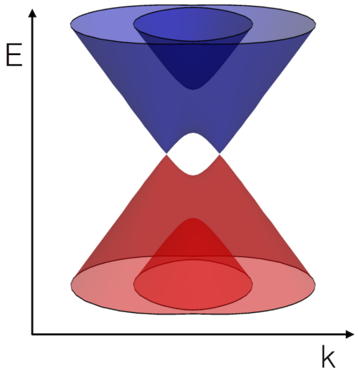

Figure 1.5: Low-energy band structure of a Weyl semimetal, showing two linearly dispersing Weyl nodes of opposite chirality. Red (blue) cones indicate filled (empty) states.

There are are number of unusual consequences associated with Weyl nodes. First, the band touching at the Weyl points is “topologically protected”, meaning that perturbations to the Hamiltonian cannot open an energy gap, but instead move the Weyl nodes in the Brillouin zone. Only when the two Weyl points of opposite chirality merge (“annihilate”), an energy gap can be opened.

In terms of physical phenomena that can be empirically detected, perhaps the most striking signature of a WSM are Fermi arc surface states [8]. On the surface of a Weyl semimetal, open arcs should be found at the Fermi energy, which terminate at the projection of corresponding bulk Weyl nodes. The appearance of these arcs stems from the opposite chirality of the Weyl points, thus their observation provides direct evidence of the presence of bulk Weyl nodes. These unusual surface states can be detected by angle-resolved photoemission spectroscopy (ARPES). Additionally, a WSM should exhibit exotic bulk properties, as a consequence of the chiral anomaly inherent to a single Weyl point, which could be observed in magneto-transport and Hall effect measurements [38, 40].

As stated above, the realisation of a WSM hinges on strict symmetry requirements: Either inversion or time-reversal symmetry must be broken to ensure non-degenerate bands. The former can be achieved in materials that adopt a non centrosymmetric crystal structure, and this type of WSM was recently discovered in a family of arsenides and phosphides, TaAs, TaP, NbP, NbAs [44–48], using ARPES. Time-reversal symmetry can be broken by the presence of magnetic order, however this type of magnetic WSM has not yet been discovered.

Magnetic WSM in pyrochlore iridates

In pyrochlore iridates, a magnetic WSM state was first predicted by Wan *et al.* [8] using density function theory (DFT) calculations within the Local Density Approximation (LDA) + U scheme. This result has since been broadly reproduced by phenomenological Hubbard models [9, 49, 50]. All studies agree that two requirements must be met to achieve a WSM state: First, the Ir magnetic moments should order in an all-in all-out (AIAO) structure, where the moments point all towards or away from the centre of tetrahedra formed by the Ir ions. Second, the electronic correlations U must not be too strong, as in that case a topologically trivial Mott insulating state results.

Figure 1.6 shows the phase diagram of a minimal nearest-neighbour Hamiltonian [50]

$$H = \sum_{ij} c_i^\dagger (t_1 + it_2 \mathbf{d}_{ij} \cdot \boldsymbol{\sigma}) c_j + H_U$$

where t_1, t_2 are real hopping parameters (which do not directly map onto microscopic models), the real vector $\mathbf{d}_{ij}$ is perpendicular to the bond i, j (in analogy to the Dzyaloshinskii-Moriya vectors, see also section 1.1), $\boldsymbol{\sigma}$ the Pauli matrices and H_U a mean-field Hubbard term.

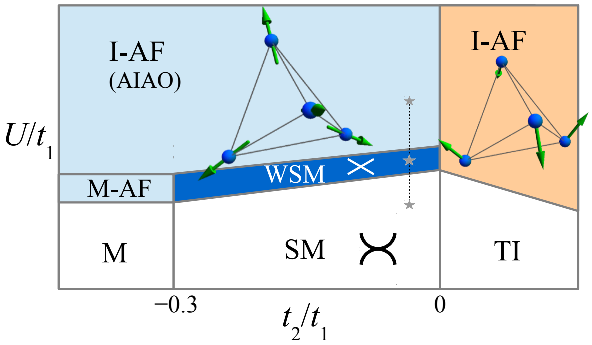

Figure 1.6: Phase diagram of pyrochlore iridates within a minimal tight-binding model, showing insulating antiferromagnetic (I-AF), Weyl semimetal (WSM), semi-metal (SM) phases (among others). Taken from Ref. [1].

In this model, for large U, within a certain range of t_2/t_1, the ground state is an AIAO magnetic insulator, as predicted by DFT. Starting from an AIAO magnetic insulator, reducing U should eventually yield a metallic state, which has to pass through an intermediate magnetic WSM phase. This tuning of U could occur across metal-insulator boundary of pyrochlore iridates as a function of rare-earth ion, pressure or temperature [50]. However, most recent dynamical mean-field theory studies have cast doubt on this mean-field picture, and instead suggest that pyrochlore iridates are strongly correlated even in the metallic state, such that the band structure remains topologically trivial in the magnetically ordered state [51, 52].

Nevertheless, the prediction of a magnetic WSM state places a strong impetus on experiments to determine the magnetic structure of pyrochlore iridates. If the Ir site orders in an AIAO fashion, a WSM could in principle be realised, although tuning of the groundstate, for example by doping, pressure or magnetic fields, might be necessary.

1.2.3 Magnetism

Pyrochlore oxides provide a fascinating platform to explore magnetism. A rich variety of magnetic phases have been proposed to emerge on the pyrochlore lattice, including spin-ice [53], spin-glass [54] and spin-liquid phases [55, 56], fragmented magnetic moments [57, 58], topological magnon states [59] and magnon Weyl points [60].

Geometric frustration

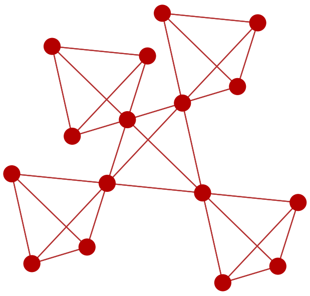

Figure 1.7: The tetrahedral network formed by Ir sites in the pyrochlore lattice.

If we place Ising spins on a 2d triangular lattice and let them interact antiferromagnetically, we find competing forces which cannot be simultaneously satisfied, as not all the spin can be antiparallel. This is the classic example of geometric frustration. A similar situation occurs on the 3d pyrochlore lattice of antiferromagnetic Heisenberg spins, where geometric frustration prevents magnetic order and a QSL may instead occur [55, 61]. Microscopically, this effective antiferromagnetic Heisenberg exchange can be thought to arise from the superexchange interaction, which favours an antiparallel alignment of the spins when virtual electron hopping between the sites is considered (which is forbidden for parallel spins by the Pauli principle) [13, 62]. However, in real pyrochlores the magnetic moments do not only interact via Heisenberg exchange, but exhibit additional anisotropic couplings, which can stabilise long-range magnetic order. When taking into account the spin-orbit coupling ζ, Moriya has shown that the superexchange interaction between two magnetic ions i and j becomes anisotropic [63]. Within perturbation theory, the two-site magnetic exchange interaction can be expanded in powers of ζ

$$J\mathbf{S}_i \cdot \mathbf{S}_j + \mathbf{D}_{ij} \cdot (\mathbf{S}_i \times \mathbf{S}_j) + \mathbf{S}_i \cdot \Gamma \cdot \mathbf{S}_j + \ldots$$

where the first term is the isotropic exchange (Heisenberg), the second term antisymmetric exchange (Dzyaloshinskii-Moriya interaction) and the third term a generic exchange anisotropy, where Γ is a symmetric tensor.

We here only consider the effect of the Dzyaloshinskii-Moriya (DM) interaction, which is expected to be the dominant exchange anisotropy. This interaction can only be present if the two-site bond does not posses inversion symmetry [63]. This is always the case on the pyrochlore lattice, where the Ir-O-Ir angle is around 130 degrees. The space group symmetry of the pyrochlore lattice then constrains the vectors $\mathbf{D}_{ij}$ to lie in (110) planes of the unitcell. The sign of $\mathbf{D}_{ij}$ however remains undetermined, and leaves two configurations, referred to as “direct” and “indirect” DM interactions [64].

The effect of including DM interactions on the pyrochlore lattice was studied by classical Monte Carlo simulations in Ref. [64]. It was found that both direct and indirect DM configurations stabilise long-range magnetic order, even when the magnitude of the DM interaction is small compared to the Heisenberg exchange. The ensuing magnetic structures differ for the two configurations of the DM vector. For a direct DM interaction, a unique magnetic ground state was found, where the spins either point all towards or away from the centre of the tetrahedra (along the local z axis), known as the all-in all-out magnetic structure (Fig. 1.8). Conversely, for the indirect DM interaction, a degenerate manifold of groundstates was found, where the magnetic moments lie in local xy planes, perpendicular to the moment directions of all-in all-out order. For both cases, since it is the DM interaction that removes the geometrical frustration, the ordering temperature scales with the magnitude of $\mathbf{D}_{ij}$ [64].

As discussed in the previous section, the AIAO magnetic structure was

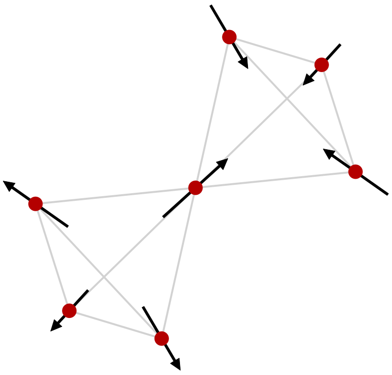

Figure 1.8: All-in all-out magnetic structure on the pyrochlore lattice.

identified as a requirement to achieve a magnetic WSM state in pyrochlore iridates [1, 8, 9, 51, 52, 65]. The microscopic magnetic properties of pyrochlore iridates have been investigated by a variety of techniques, including muon spin rotation (μSR) [66–69], neutron powder diffraction (NPD) [70–72] and single-crystal resonant x-ray scattering (RXS) [73, 74].

All investigations agree that the bifurcation of FC-ZFC magnetisations occurring at around 100 K (35 K for Nd) is associated with the onset of long-range antiferromagnetic order on the Ir site. Evidence that the microscopic magnetic structure is AIAO has been found in many pyrochlore iridates, a summary of measurements with x-rays, neutrons and muons is provided in Table 1.1. Perhaps the most convincing study is a powder neutron diffraction experiment on $Nd_2Ir_2O_7$, where an all-in all-out magnetic order of the Ir site was directly observed, with a moment size of 0.3 μ_B [72].

While some investigations appear conflicting in the literature, discrepancies can usually be resolved by taking into account subtle differences in sample stoichiometry. A common issue appears to be an excess of rare-earth ions that populate Ir sites, resulting in a $R_{2+x}Ir_{2-x}O_7$ stoichiometry (colloquially often referred to as "stuffing"). It was found that $x \sim 0.01$ - 0.02 is sufficient to drastically reduce the Neel temperature [78], and pyrochlore iridates with $x \sim 0.05$ or higher cease to show long-range magnetic order of the Ir site [74].

Most recently, the magnetic properties of the rare-earth site of pyrochlore iridates have attracted interest. As the magnetic moments can be substantially larger on the rare-earth site, neutron diffraction studies could detect all-in all-out magnetic order on $R =$ Nd [70, 72], Tb [71] and Ho [75]. It was found that these R ions order at temperatures much larger than the exchange interaction

R	R site magnetic order	Ir site magnetic order
Lu	Nonmagnetic	Unknown
Yb	Unknown	AIAO (μSR [68])
Ho	(fragmented?) AIAO (NPD [75, 76])	AIAO (NPD [75])
Y	Nonmagnetic	AIAO (μSR [68], NPD [77])
Dy	Unknown	Unknown
Tb	AIAO (NPD [71])	AIAO (NPD [71], RXS*)
Gd	Unknown	Unknown
Eu	Nonmagnetic	AIAO (μSR [66], RXS [73, 74])
Sm	Unknown	AIAO (RXS*)
Nd	AIAO (NPD [70, 72])	AIAO (NPD [72], RXS*)
Pr	Unknown	Disordered

Table 1.1: Survey of experimental investigations into the magnetic order of pyrochlore iridates $R_2Ir_2O_7$. Here, AIAO = all-in all-out, μSR = muon spin rotation, NPD = neutron powder diffraction and RXS = resonant x-ray scattering. The * refers to experiments presented in this thesis.

between rare-earths, which was proposed to be due to the Ir site inducing a magnetic moment on the rare-earth site. Furthermore, for Ho and Dy, this can lead to an interesting competition between an effective ferromagnetic Ising exchange between rare-earths and the "molecular field" of the Ir site, which might lead to a fragmented magnetic moment of the rare-earth ion [75], where long-range AIAO order and short-range spin-ice correlation coexist [57].

In this thesis, we study the magnetic transition in the pyrochlore iridates $R_2Ir_2O_7$, where R = Sm, Nd and Tb, with elastic and inelastic resonant x-ray scattering at the Ir L_3 edge. In all samples, long-range, $\mathbf{k} = \mathbf{0}$ magnetic order was discovered, consistent with an all-in all-out antiferromagnetic structure, below 120 K (Sm), 5 K (Nd) and 78 K (Tb), respectively. By comparing our data with cross-section calculations, we estimated an ordered moment size of $0.3\,\mu_B$ (Sm) and $0.06\,\mu_B$ (Tb). For $Tb_2Ir_2O_7$, the suppressed transition temperature and small moment size indicates off-stoichiometry, possibly due to an excess of Tb ions populating Ir sites. Furthermore, we studied the magnetic dynamics of these pyrochlore iridates. For Sm and Nd, magnetic excitations can be well described by a minimal nearest-neighbour Hamiltonian of Heisenberg exchange (27 meV) and Dzyaloshinskii-Moriya interactions (5 meV), providing a consistent description of the magnetic order and excitations. For Tb, magnetic excitations could only be identified close the antiferromagnetic zone centre, which indicates a departure from a strong-coupling, linear spin-wave theory description of magnetic excitations. This suggests a more weakly correlated state in $Tb_2Ir_2O_7$, which might be of interest in the context of the proposed Weyl semimetal phase.

1.3 The perovskite iridates

Recent review articles with a focus on perovskite iridates can be found in Refs. [2, 79]. We will here only provide a brief summary, aiming to make the case for high-pressure investigations. A more thorough review of the high-pressure properties of $Sr_3Ir_2O_7$ will be given in chapter 6.

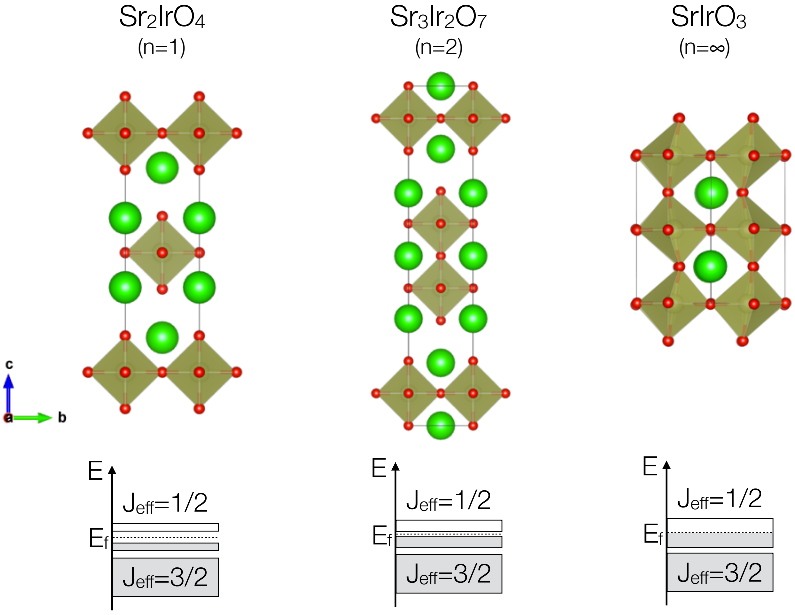

Figure 1.9: Evolution of structural and electronic properties of Ruddlesden Popper series of perovskite iridates $Sr_{n+1}Ir_nO_{3n+1}$ for members $n = 1, 2, \infty$. For clarity, the crystal structures were drawn without the octahedral rotations and tilts that are present in the real materials.

The Ruddlesden-Popper (RP) series of perovskite iridates are a family of materials with stoichiometry $Sr_{n+1}Ir_nO_{3n+1}$, where n is the number of Ir-O layers, separated by Sr-O layers. Figure 1.9 shows the crystal structure of members $n = 1, 2, \infty$ of this series.

Most interest was undoubtedly received by the single layer Sr_2IrO_4 ($n = 1$), following the discovery of a $J_{\text{eff}} = 1/2$ spin-orbit Mott insulating state [3–5]. Optical conductivity suggests an insulating gap of $\sim$ 300 meV in Sr_2IrO_4 at room temperature [80]. Additionally, the $J_{\text{eff}} = 1/2$ magnetic moments order below 240 K in a canted antiferromagnetic structure with moments lying in the basal plane [4, 81–83]. Numerous structural, electronic and magnetic properties of Sr_2IrO_4 appear strikingly similar to La_2CuO_4, a parent compound of high-temperature cuprate superconductors [18–21, 84]. In this context, perhaps most important was the discovery that the magnetic excitations of the two compounds can be described by very similar Hamiltonians [17, 85], which has lead to predictions that Sr_2IrO_4 might superconduct when doped [15, 22–24].

Adding another Ir-O layer results in the $n = 2$ structure of $Sr_3Ir_2O_7$. While the $J_{\text{eff}} = 1/2$ spin-orbit Mott insulating state is retained in $Sr_3Ir_2O_7$, the band gap is reduced to $\sim$ 100 meV at room temperature [86–93]. Increasing the dimensionality from single layer to bilayer also results in a spin-flop transition to a collinear antiferromagnetic structure, where the moments lie along the c axis, below 280 K [91, 92]. This has profound consequences on the magnetic excitation spectrum, which becomes strongly gapped, suggesting substantial anisotropic interactions, in stark contrast to the nearly isotropic Heisenberg spectrum of Sr_2IrO_4 [94, 95].

A further increase in Ir-O layers eventually yields the $n = \infty$ member of the series, $SrIrO_3$, which is a correlated metal [96]. It can hence be postulated that an insulator-metal transition occurs at some point beyond $n > 2$. Qualitatively, this transition was proposed to occur due to a bandwidth broadening when increasing the number of nearest Ir neighbours by adding Ir-O layers n, which eventually exceeds the Coulomb repulsions [80]. However, the microscopic picture is likely more complex, and even the nature of insulating states in Sr_2IrO_4 and $Sr_3Ir_2O_7$ has been under some debate. Many studies have argued that itineracy effects are significant in these materials, and that the above picture of a $J_{\text{eff}} = 1/2$ spin-orbit Mott insulator is insufficient, as the insulating state exhibits both Slater and Mott characteristics [93, 97–99].

1.3.1 High-pressure properties

The nature of the insulator-metal transition in RP iridates is of fundamental interest, as its mechanism could be very different from the Mott-Hubbard picture invoked for $3d$ transition metal oxides [1]. Unfortunately, tuning the number Ir-O layers only provides a very uncontrolled, discrete way of crossing the IMT boundary. In this context, the application of high-pressure is of interest, as it allow to continuously tune the electronic ground state in a chemically clean manner.

High-pressure resistivity studies of Sr_2IrO_4 and $Sr_3Ir_2O_7$ have shown that an insulating gap remains to at least 40 GPa [100] and 59.5 GPa [101], respectively. Another investigation reported that the insulating state is robust up to 55 GPa (Sr_2IrO_4) and 104 GPa ($Sr_3Ir_2O_7$) [102]. Given the size of the electronic gap, this persistence of the insulating state is surprising. It was suggested that pressure decreases the Ir-O-Ir bond angle, which may alleviate the bandwidth broadening from the shorter bond distances [100, 103].

Most recent high-pressure transport measurments of $Sr_3Ir_2O_7$ have observed a transition to a "confined metal" state at 59.5 GPa, which is characterised by conductance in the *ab* plane and an insulating behaviour along the *c* axis, akin to the strange metal phase in overdoped cuprates [100]. However, this metallic state is still poorly understood, largely due to the scarcity of experimental techniques available at these extreme conditions. In particular, the pressure evolution of the crystal and electronic structure across the IMT remains to be addressed. It is also not known if a similar metallic state could be observed in Sr_2IrO_4.

Here, we study the pressure evolution of the structure of $Sr_3Ir_2O_7$ with powder x-ray diffraction. We discover a first-order structural transition from tetragonal to monoclinic symmetry at 54 GPa, in close proximity to the transition to the confined metallic state at 59.5 GPa. Structural refinement suggests that the high pressure phase of $Sr_3Ir_2O_7$ adopts an altered stacking sequence of perovskite bilayers, which presents a novel modification of the Ruddlesden-Popper structure. The electronic properties at high pressure were investigated with x-ray absorption spectroscopy. We find that the evolution of the electronic state is dominated by the cubic crystal field at low pressures. In the high-pressure metallic phase, the influence of spin-orbit coupling on the electronic state is diminished, indicating a departure from a $J_{\text{eff}} = 1/2$ picture.

1.4 Probing iridates with x-rays

In this thesis, we investigate phase transitions in iridates that involve some breaking of symmetry: Time-reversal symmetry in the case of the magnetic transition in pyrochlore iridates, and translational symmetry in the high-pressure structural transition in perovskite iridates. In both cases, we will use x-ray techniques to first detect the presence or absence of that symmetry, and then to characterise the ensuing state.

In addition to examining these phase transitions, much of the work presented here aims at obtaining a better understanding of what insights specific x-ray techniques can provide in iridates. This is either because the technique itself is fairly new (resonant x-ray scattering) or because its application is unconventional (high-pressure x-ray absorption spectroscopy). To this end, we will make use of simple single-ion models that provide an intuitive understanding of the physics involved.

Why use x-ray techniques to study iridates? — Historically, the field of iridates is intimately entwined with x-ray scattering experiments. Many key studies that created interest in iridates involved resonant x-ray scattering (RXS). RXS is an element specific technique that can directly probe the order and excitations associated with the Ir ion. This was most impressively demonstrated in the perovskite iridates Sr_2IrO_4 and $Sr_3Ir_2O_7$, where not only the magnetic and electronic ground state was established, but also the dispersion of magnetic excitations throughout the entire Brillouin zone could be measured [4, 17, 81, 82, 91, 92, 94, 95, 104, 105]. The latter has only recently become feasible due to advances in instrumentation, which enabled RXS to resolve low energy excitations in iridates [17, 106]. This series of breakthrough experiments has demonstrated that RXS can be a highly effective tool for characterising the microscopic physics in iridates.

A more practical argument for using x-rays is a matter of chemistry: Single crystal iridates are currently mainly synthesised by flux-growth (as the involved elements melt incongruously), with resulting samples sizes typically in the few hundred μm range. This poses no problem to x-rays, but it rules out more traditional single-crystal neutron scattering methods that require large samples. This is further aggravated by Ir magnetic moments being usually below 1 μ_B, and a strong neutron absorption of Ir. While some progress can be made with neutrons by using powder samples, for example for determining magnetic structures, inelastic neutron scattering remains very challenging [107]. Furthermore, it is often crucial to obtain the excitation spectrum of a single crystal to establish the low-energy Hamiltonian. RXS can be used to study very small samples [the limit is roughly given by the beamsize at the sample position ($\sim 10 \times 20$ μm^2) and the x-ray penetration depth (~ 20 μm for iridates at Ir L_3)], with small magnetic moments, due to the strong resonance at the Ir L_3 edge.

X-rays are also uniquely well suited to study materials under extreme conditions. High-pressure sample environments, such as the Diamond Anvil Cell, severely constrain the array of suitable experimental techniques, and even basic bulk measurements, such as resistivity or magnetic susceptibility, become very challenging. In many cases, x-ray techniques can be fairly easily extended into the high-pressure regime. This especially applies to iridates, as the Ir L edges lie in the hard x-ray regime, where the addition of a high-pressure sample environment only attenuates the x-ray beam insignificantly, and resonant x-ray techniques remain feasible.

How are x-ray techniques used in this thesis? — A large part of the work presented here concerns resonant x-ray scattering (RXS). As RXS in iridates is still a fairly new technique, the interpretation of the acquired data is often not entirely clear. In order to make progress towards a better understanding of RXS experiments, we will provide a comprehensive account of RXS cross-sections at the Ir L edge in chapter 3. We will formulate the RXS cross-section relevant for determining the Ir magnetic structure, highlighting the importance of non-cubic crystal fields, which have so far been neglected in the literature. Furthermore, we show for the first time how the absolute size of the magnetic moment can be estimated by RXS, a quantity which could hitherto only be determined with neutron scattering.

We use RXS in the elastic channel (REXS) to detect the symmetry breaking associated with magnetic order on the Ir site of the pyrochlore iridates $R_2\mathrm{Ir}_2\mathrm{O}_7$ (R = Sm, Nd, Tb) in chapter 4. We then characterise the magnetically ordered state by studying the magnetic excitations with RXS in the inelastic channel (RIXS) in chapter 5.

We use x-ray diffraction (XRD) to detect the symmetry breaking occurring at the high-pressure structural transition of $\mathrm{Sr}_3\mathrm{Ir}_2\mathrm{O}_7$ in chapter 6. We then investigate the high-pressure electronic state using x-ray absorption spectroscopy (XAS).

Technical details on the theory and practice of these experimental methods are presented in chapter 2.

1.5 Overview of thesis

Chapter 2 describes experimental techniques used in this thesis. A pedagogical review of RXS and its implementation at beamlines is given. The diamond anvil cell high-pressure sample environment is introduced. High-pressure XRD and XAS beamlines are detailed.

In chapter 3, Ir $L_{2,3}$ edge RXS cross-sections are computed within a single-ion model. Atomic scattering tensors for elastic and inelastic transitions within the t_{2g} levels for an arbitrary moment direction in the presence of trigonal and tetragonal distortions are derived. The generic cross-section for resonant magnetic x-ray scattering at the Ir $L_{2,3}$ edges is given. The pyrochlore iridates are used as an example for obtaining structure factors from atomic scattering tensors. We show how the magnetic moment size can be estimated with REXS.

Chapter 4 describes REXS experiments on pyrochlore iridates, aimed at determining the magnetic structure of $Sm_2Ir_2O_7$, $Nd_2Ir_2O_7$ and $Tb_2Ir_2O_7$. In all samples, the magnetic scattering is consistent with AIAO magnetic order. Under the assumption of an AIAO structure, the absolute magnetic moment size was estimated for $Sm_2Ir_2O_7$ and $Tb_2Ir_2O_7$.

In chapter 5, the same three pyrochlore iridates are investigated with RIXS. In $Sm_2Ir_2O_7$ and $Nd_2Ir_2O_7$, temperature-dependent, dispersive, low-energy excitations were observed, consistent with single-magnon excitations from AIAO order. The effective spin Hamiltonian was estimated. In $Tb_2Ir_2O_7$, magnetic excitations could not be clearly identified. For all samples, crystal-field excitations within t_{2g} manifold show that the compressive trigonal field is as strong as the atomic spin-orbit coupling.

Finally, chapter 6 describes high-pressure x-ray experiments on the perovskite iridate $Sr_3Ir_2O_7$. The evolution of the crystal structure was studied by powder XRD. A first-order structural transition was discovered. The electronic state at high-pressure was characterised by XAS, which, up to the structural transition, is mainly determined by a constant spin-orbit coupling and a pressure-dependent cubic crystal field. In the high-pressure phase, the influence of spin-orbit coupling on the electronic state appears diminished.

The thesis ends in a conclusion, summarising the key results obtained. Possible directions for future research are discussed.

1.6 Co-Authorship

Although the bulk of the work presented here, in terms of data acquisition, analysis and interpretation, was performed by myself, the nature of beamtime experiments implies a collaborative effort.

The resonant x-ray cross-sections for iridates were calculated in collaboration with M. Moretti and S. Boseggia.

The REXS experiments of $R_2Ir_2O_7$ (R = Sm, Tb) were performed by myself, M. Rahn and J. Vale at beamline P09 (PETRA III) with local contact J. Strempfer, and at beamline I16 (Diamond Light Source) with local contact G. Nisbet. The RIXS experiments of $R_2Ir_2O_7$ (R = Sm, Nd, Tb) were performed by myself, M. Rahn, L. Veiga and D. Pincini at beamline ID20 (ESRF) with local contacts A. Efimenko, M. Krisch and M. Moretti, and at beamline ID27 (APS) with local contact D. Casa. $R_2Ir_2O_7$ (R = Sm, Nd, Tb) samples were grown by D. Prabhakaran and A. Boothroyd.

For $Sr_3Ir_2O_7$, the high-pressure XRD experiment was performed by myself, Z. Feng, J. Vale, E. Hunter and H. Rønnow on beamline ID09 (ESRF) with local contact M. Hanfland. The HP-XAS experiment was performed by myself and M. Moretti at beamline ID24 (ESRF) with local contact S. Pascarelli. The $Sr_3Ir_2O_7$ samples were grown by E. Hunter and R. Perry.

1.7 Open-access data

In reliance with guidelines[2] issued by the Engineering and Physical Research Council (EPSRC), all data presented in this thesis will be available online for the next 10 years. This includes input data to reproduce the figures in this thesis, as well as raw data, fully documented by meta-data, wherever this was reasonably possible.

In order to maximise usefulness of the raw data, it is typically not provided directly as it is collected ("off the detector"), but is somewhat processed. This processing involves standard procedures for the respective measurement. For example, for powder x-ray diffraction data from area detectors, instead of 2d image files, the raw data are provided as integrated 1d spectra.

The complete dataset can be obtained from Ref. [108].

---

[2] https://www.epsrc.ac.uk/about/access/roaccess/ - accessed August 2017

Chapter 2

Experimental method

Contents

2.1 Resonant x-ray scattering 50

2.1.1 REXS: beamline P09 53

2.1.2 RIXS: beamline ID20 54

2.2 High-pressure x-ray techniques 55

2.2.1 The Diamond Anvil Cell 55

2.2.2 HP-XRD: beamline ID09a 56

2.2.3 HP-XAS: beamline ID24 57

In this chapter, the x-ray techniques used in this thesis are introduced. A general introduction to resonant x-ray scattering and its implementation at synchrotron light sources is provided. The diamond anvil cell high-pressure sample environment is described. The experimental setup at high-pressure x-ray diffraction and x-ray absorption beamlines is outlined.

The x-ray techniques described here all require synchrotron radiation as the source of x-ray light, as the x-ray beam needs to be continuously tunable in energy, offer extremely narrow energy bandwidths, μm focussing and a high photon flux. In general, synchrotron radiation refers to the emission of electromagnetic radiation from accelerated, charged particles [109]. At synchrotron radiation facilities, electron bunches circulate in a storage ring. In order to follow a circular path, the electrons need to be continuously accelerated by bending magnets, such that they emit Bremsstrahlung. While the bending magnets are still used as x-ray sources at synchrotrons, a more effective way to produce electromagnetic radiation is through undulators [110]. These consist of arrays of alternating dipole magnets, which are inserted into straight sections of the storage ring. The array of magnets forces the electron bunch to follow periodic oscillations. The amplitudes of the emitted radiation can then become coherent and constructively interfere, to give a high photon flux in a narrow energy range (with harmonics).

2.1 Resonant x-ray scattering

Resonant x-ray scattering (RXS) is powerful technique to investigate magnetic, charge and orbital order and excitations [111–113]. RXS is a photon-in, photon-out x-ray scattering technique that combines elements of spectroscopy and diffraction, by allowing to transfer both energy and momentum to the sample. By tuning the energy to a resonance of an absorbing ion, an element-specific sensitivity to various type of electronic order (magnetic, orbital, charge) and the ability to create excitations thereof can be achieved.

Figure 2.1 shows the two-step process involved in RXS. In the first step, by tuning to an absorption edge, an electron from the core levels is promoted to the valence band. This intermediate state with a hole in the core levels is highly unstable. In the second step, the core hole is filled by an electron from the valence band. The final state could then be identical to the initial state, in which case the outgoing x-ray is scattered elastically (Resonant Elastic X-ray Scattering - REXS) or the system could be left in an excited state, and the outgoing beam scatters inelastically (Resonant Inelastic X-ray Scattering - RIXS). Strictly speaking, this process is referred to as "direct" RXS, to distinguish with "indirect" RXS, where the core electron is promoted far above the valence band [112]. Only the former will be considered in this thesis.

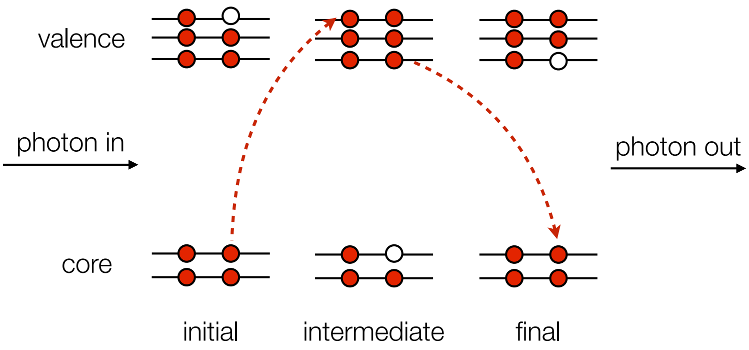

Figure 2.1: Illustration of the two-step RXS process. In the first step, an incoming x-ray promotes a core electron to the valence band. In the second step, another electron decays from the valence band to fill the core hole. The final state can either be identical to the initial state (REXS) or in some excited configuration (RIXS).

REXS can couple to magnetic, charge and orbital electronic orders. As opposed to neutron scattering or non-resonant x-ray scattering, REXS does not directly "see" e.g. magnetic dipolar order, but instead *measures an electronic transition*, which becomes modified in the presence of various types of order. It is this fundamental difference that leads to a strongly enhanced cross-section and the ability to detect various types of "hidden" orders, such as magnetic quadrupolar [114] and orbital order [115]. However, this can also complicate the data interpretation, as the REXS cross-section is determined by the electronic structure of the absorbing ion, and can hence become material dependent.

Figure 2.2 shows an overview of various excitations, such as phonons, magnons and crystal field excitations, which can be measured by RIXS [112]. Again, as opposed to inelastic neutron scattering, where the neutron directly interacts with the magnetic moment to create single magnon excitations, *RIXS measures electronic transitions* that can couple to single-magnon excitations. The nature of the electronic transition, i.e. the chosen absorption edge of the material, determines which excitations can be observed.

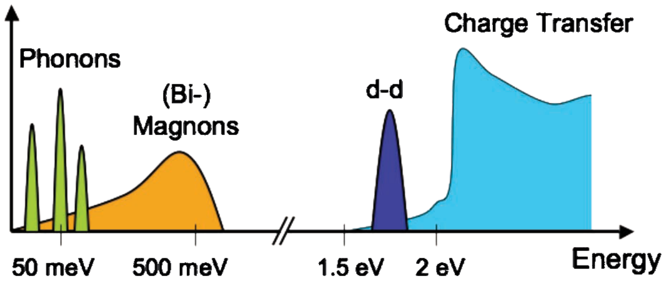

Figure 2.2: Overview of excitations that can be measured by RIXS, taken from Ref. [112].

As an example, consider magnetic excitations. At the L edges of transition metals, RIXS measures transitions from p core levels to partially-filled d states. In the intermediate state, a core hole with strong spin-orbit coupling resides in the p levels, such that the p levels split into $j = 1/2$ (L_2 edge) and $j = 3/2$ (L_3 edge) states. In this case, spin and orbital angular momenta need not be conserved. Since a photon has angular momentum of $L = 1$, it can transfer $L_z = 0, 1, 2$ to the sample in the scattering process. This implies that both single magnon ($\Delta S_z = 1$) and two magnon ($\Delta S_z = 2$) excitations can be created with RIXS at the L edge [116]. This contrasts with RIXS at the K edge, where transitions between $s \leftrightarrow p$ levels are measured. In this case, the s core-hole has no orbital angular momentum. This implies $\Delta S_z = 0$, such that magnetic excitations must involve two spin flips.[1] RIXS at the K edge thus can only couple to two magnon, and not single magnon excitations. While two magnon excitations can also be measured by optical Raman scattering, RIXS has the advantage of being able to probe the full momentum dispersion [118]. In addition to these selection rules, the cross-sections for specific RIXS excitations, e.g. single-magnons, is intimately tied to the electronic and magnetic structure of the absorbing ion [116, 119].

There are also practical considerations for the choice of absorption edge, such as the available energy resolution, the strength of the elastic scattering and the amount of accessible reciprocal space. At the Ir L_3 edge, these are all very favourable, in particular the energy resolution of 25 meV at an incoming energy of 11.215 keV was a remarkable technical achievement [94, 106] that has made it feasible to measure single-magnon excitations in many iridates [17, 94, 95, 120, 121]. A more detailed discussion of RXS at the Ir L edges will be given in chapter 3, where cross-sections for REXS and RIXS will be derived in a single-ion model.

---

[1] These selection rules may be modified when significant spin-orbit coupling is present in the d states [117].

2.1.1 REXS: beamline P09

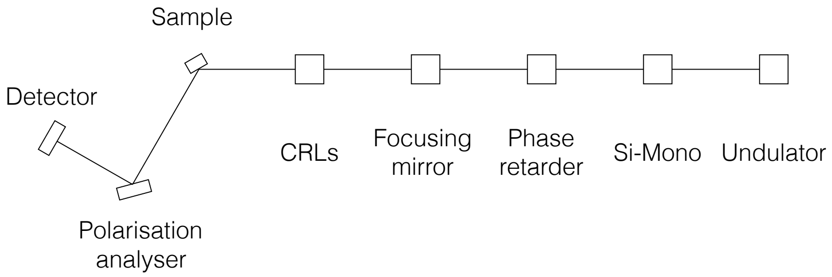

Figure 2.3: Schematic setup of the REXS beamline P09 at PETRA III.

A detailed description of beamline P09 can be found in Ref. [122]. Beamline P09 uses the storage ring of the third generation synchrotron PETRA III in Hamburg, Germany. At 2m long undulator is used to generate photons with linear polarisation parallel to the horizontal synchrotron plane. The beam is then monochromated with a Si (111) double-crystal, to a bandwidth of ~ 1 eV at the Ir L_3 edge. Afterwards, mirrors and compound refractive lenses focus the beam on the sample position to the required spot size. A six circle diffractometer allows operation in horizontal and vertical scattering geometries. An analyser crystal can be used as a linear polarimeter. This is achieved by choosing a material that has a Bragg reflection at $2\theta \approx 90°$ at the operating energy, such that only polarisation perpendicular to the scattering plane of the analyser will be diffracted and arrive at the detector (as the polarisation dependence of Thomson scattering is $|\boldsymbol{\epsilon}' \cdot \boldsymbol{\epsilon}|^2$ [111]). Thus, by rotating the analyser crystal, the linear component of the scattered beam can be deduced. For the Ir L_3 edge, the (333) reflection of Au offers $2\theta \approx 90°$ at 11.215 keV.

2.1.2 RIXS: beamline ID20

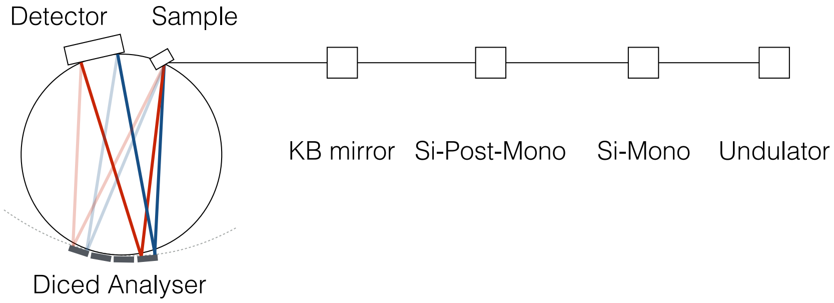

Figure 2.4: Schematic setup the of RIXS beamline ID20, ESRF. The blue and red lines indicate high and low energy x-ray beams scattered from the sample, respectively.

A detailed description of the high-resolution Ir L_3 edge setup of beamline ID20, ESRF, can be found in Ref. [106]. Beamline ID20 uses the storage ring of the European Synchrotron Radiation Facility (ESRF) in Grenoble, Italy. Figure 2.4 shows a schematic setup of the beamline. Beamline ID20 uses three undulators to generate a high flux of linearly polarised photons. The beam is monochromated with a Si (111) double-crystal. A secondary channel-cut Si (844) monochromator is operated in back-scattering geometry, the combined ensemble achieves an incident energy bandwidth of 15 meV at the Ir L_3 edge (11.215 keV). The beam is then focused to 10×20 microns (vertical $\times$ horizontal) at the sample positions with a toroidal focussing mirror and Kirkpatrick-Baez (KB) mirrors. The radiation scattered from the sample is then further diffracted by a spherical, diced Si (844) analyser crystal [123] onto a 2d Medipix2 detector (55×55 μm^2 pixel size) [124]. The sample, analyser and detector operate in a Rowland circle geometry [125]. Depending on the energy of the radiation scattered from the sample, the Bragg condition of the analyser crystal will be satisfied at different angles. Thus the position of the beam arriving at the 2d detector allows to deduce the energy of the beam scattered from the sample (indicated by blue and red lines in Fig. 2.4, corresponding to high and low energy limits, respectively). At the Ir L_3 edge, each mm on the detector corresponds to approximately 210 meV. The overall energy resolution is predominantly limited by the incident energy resolution, the finite size of the beam at the sample position and the pixel size of the detector. In practice, an energy resolution of 25 meV (FWHM) can be routinely achieved at the Ir L_3 edge. The momentum resolution is mainly determined by the angular acceptance of the spherical analyser, and can thus be controlled by masking parts of the analyser.

2.2 High-pressure x-ray techniques

2.2.1 The Diamond Anvil Cell

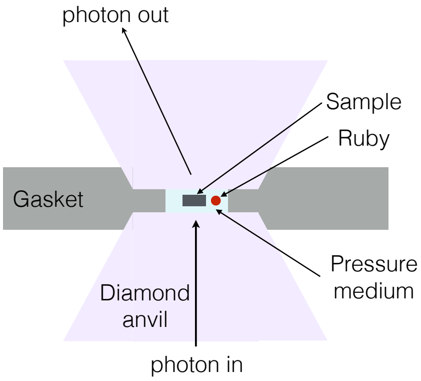

Figure 2.5: Operating principle of Diamond Anvil Cell.

A variety of methods exist to generate high-pressure (HP) sample environments. However, the ability to achieve static pressures in the Mbar range is exclusive to Diamond Anvil Cells (DACs). A pedagogical review can be found in Ref. [126]. In its simplest form, a DAC consists of two opposing diamond anvils that generate pressure on a sample (Fig. 2.5). In order to achieve hydrostatic pressure conditions, the sample is usually surrounded by a pressure transmitting medium (typically a noble gas, such as He or Ne, provides best hydrostaticity while being non-reactive), and enclosed by a metallic gasket (typically Re or steel). As the tips of the diamond anvils ("culets"), are polished to small areas between 300-10 μm in diameter, very high pressures, up to several Mbars, can be generated.

Diamonds are uniquely well-suited as anvils in pressure cells. Their bulk modulus and hardness allows to reach the highest possible static pressures. Additionally, transparency to visible light enables easy sample preparation, as well as the ability to use a variety of optical probes, such as Raman scattering. The optical transparency also allows to use Ruby fluorescence to monitor the pressure in the sample chamber [127]. Ruby is chromium doped aluminium oxide, the energy levels of excited chromium states are well calibrated against pressure, and hence provide a robust and simple way to monitor the pressure in the sample chamber.

Most importantly, the low atomic number of carbon implies a high transparency to x-rays. The most established technique is HP x-ray diffraction (XRD), where energies of around 30 keV imply that x-ray absorption by diamonds can be neglected. At the Ir L_3 edge, at around 11 keV, passing through 3 mm of diamond still only attenuates the transmitted beam by a factor of three, such that HP x-ray absorption and HP resonant x-ray scattering can be performed in iridates. The former is a well-established technique, the instrumental development is largely driven by a strong interest from earth sciences to study materials at high-pressure. The latter is still a somewhat exotic technique, and many instrumental challenges arise when extending resonant x-ray scattering into the high-pressure regime. Nevertheless, dedicated setups are being (or have been) implemented at beamlines, including ID05 and ID27 at the APS, ID20 at the ESRF, P09 at PETRA 3 and I16 at the Diamond Light Source.

2.2.2 HP-XRD: beamline ID09a

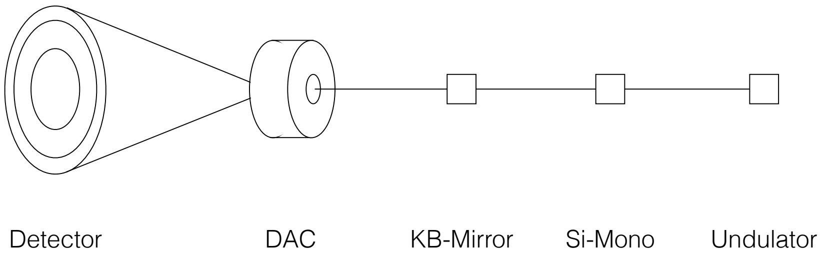

Figure 2.6: Schematic setup of high-pressure XRD beamline ID09a.

The beamline formerly known as ID09a at the ESRF was dedicated to HP-XRD measurements. Figure 2.6 show a schematic of the experimental setup. The beam emanating from the undulator is monochromated with a Si (111) crystal to an energy of around 30 keV. The beam is then focussed with Kirkpatrick-Baez (KB) mirrors to a few μm on the sample contained in the DAC. Most investigations are conducted with powder samples, in which case the diffracted peaks from randomly orientated crystallites merge into Debye-Scherrer cones. To achieve a good powder average (most real samples suffer from preferred orientation, which can be problematic for structural refinement), the DAC is rocked over a few degrees during the exposure. For iridates, the high atomic number implies that exposure times of 1s are sufficient on id09. An area detector collects the scattered radiation.

2.2.3 HP-XAS: beamline ID24

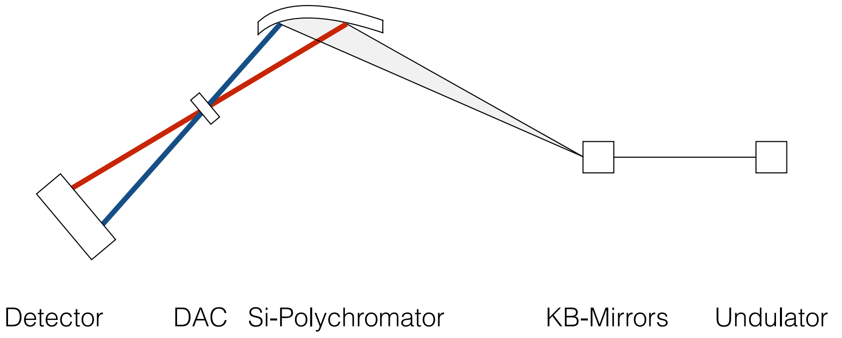

Figure 2.7: Schematic setup of energy dispersive XAS setup on beamline ID24. The red and blue lines indicate low and high energy cutoffs of the polychromatic beam, respectively.

Beamline ID24 at the ESRF provides an energy dispersive high-pressure x-ray absorption spectroscopy (XAS) setup. A detailed description of the beamline can be found in Ref. [128]. Energy dispersive XAS implies that a broad range of energies is simultaneously incident on the sample. This allows for rapid data acquisition, enabling time-resolved experiments, as well as extreme pressure and temperature conditions. Figure 2.7 shows the setup on beamline ID24. To obtain a broad energy bandwidth, the three undulators of ID24 are “tapered”, i.e. their gaps, and therefore emitted spectral ranges, differ, which provides a broad energy range. After focussing with KB mirrors, the beam is diffracted from a “polychromator”, which is an elliptically bent Si crystal. The bending of the crystal results in the Bragg condition varying throughout the crystal, such that the different energies of the beam will be diffracted on different spots (shown by red and blue lines in Fig. 2.7). This provides an angle-dispersed, polychromatic beam, which can be focussed to a few μm onto the sample in the DAC. The transmitted, outgoing beam then disperses again and is collected by a 2d detector. The position on the detector can thus be converted to incident beam energy, by using a known calibration standard. At the Ir L edges, XAS spectra can collected within 100 ms of exposure.

Chapter 3

RXS at the Ir $L_{2,3}$ edge

Contents

3.1 Single-ion model for Ir^{4+} iridates 60
3.2 Cross-section computation 64
3.3 Atomic scattering tensors 65
3.3.1 REXS 66
3.3.2 RIXS 69
3.4 Structure factor for pyrochlore iridates 72
3.5 Conclusion 77

In this chapter, we derive resonant x-ray scattering (RXS) cross-sections for iridates at the Ir $L_{2,3}$ edges within a single-ion model. We compute atomic scattering tensors for all possible transitions within the t_{2g} manifold, in the presence of trigonal and tetragonal distortions, for an arbitrary magnetic moment direction. This makes the RXS cross-sections applicable to a wide range of iridates and yields novel insights on which we focus the discussion: First, we show explicitly how the amplitude of resonant magnetic x-ray scattering depends on the non-cubic crystal field, which can be of importance for accurately determining magnetic structures. Second, by formulating atomic scattering tensors for spin-flip transitions, relevant to single-magnon excitations, and for t_{2g} crystal-field excitations, the dependence on photon polarisation, the moment direction and non-cubic crystal fields is elucidated. Third, using the example of pyrochlore iridates, we demonstrate for the first time how the size of the magnetic moment can be estimated by REXS, which has so far remained elusive to x-rays and could only be determined by neutron scattering.

It should be noted that similar single-ion Ir L edge RXS calculations were previously reported in Refs. [25, 129–132]. While these also demonstrated how the cross-sections depend on the moment direction, they are limited to the case of tetragonal distortions and mainly concern elastic and spin-flip transitions. The calculations presented here provide a more general framework, which enabled to discover the insights mentioned above, as well as making them applicable to a variety of iridates.

3.1 Single-ion model for Ir^{4+} iridates

The hierarchy of energy-scales of Ir^{4+} ($5d^5$) in a cubic environment allows to use an effective one-particle approach of one hole in the t_{2g} manifold. This rests on the assumptions that the cubic crystal-field (CF) splitting $10Dq$ dominates over Hund's coupling J_H ($10Dq > 3J_H$), and that the spin-orbit coupling (SOC) ζ and non-cubic CFs Δ can be treated perturbatively ($\zeta, \Delta \ll 10Dq$). Considering typical energy scales for iridates, the former is usually justified ($10Dq \sim 3$ eV [131], $J_H \sim 0.5$ eV [13, 14]), but the latter must be considered an approximation ($\zeta \sim 0.5$ eV, $\Delta \sim 0.1 - 1$ eV [5, 121, 130, 133–137]). Whether this approximation provides a good description of empirical phenomena depends on the experimental situation. For example, when SOC is treated on an equal footing with the cubic CF, $t_{2g} - e_g$ hybridisation occurs, which mixes $J_{\text{eff}} = 3/2$ and e_g quartets, but leaves the $J_{\text{eff}} = 1/2$ doublet unaffected [138]. Thus, experiments that probe excited e_g or $J_{\text{eff}} = 3/2$ states, such as the e_g levels populated in x-ray absorption spectroscopy, will be very sensitive to this effect. However, if mainly the behaviour of the $J_{\text{eff}} = 1/2$ doublet is involved, such as for magnetic excitations measured by RIXS, neglecting $t_{2g} - e_g$ hybridisation is justified. Here, we will confine the discussion to RXS transitions within the t_{2g} manifold and hence neglect $t_{2g} - e_g$ hybridisation.

The single-ion Hamiltonian for Ir^{4+} in a $5d$ t_{2g} basis can be written as [5, 14, 121, 130, 133, 135, 136]:

$$\mathcal{H} = \zeta \mathbf{L} \cdot \mathbf{S} - \Delta L_z^2$$

where ζ is the atomic spin-orbit coupling and Δ a non-cubic crystal field. The non-cubic CF term ΔL_z^2 can represent either tetragonal or trigonal distortions of the cubic field, depending on the choice of reference frame and quantisation axis (see Fig. 3.1). If we let the z axis coincide with the four-fold rotation axis of the oxygen octahedron, ΔL_z^2 becomes a tetragonal field. Alternatively, we can let the z axis lie parallel to the three-fold rotation axis of the octahedron, in which case ΔL_z^2 becomes a trigonal field. The corresponding sets of t_{2g} basis states for both cases, $\{|0\rangle, |\bar{1}\rangle, |1\rangle\}$, are defined in Appendix A.1. Here, within a point-charge model, a positive (negative) Δ corresponds to an elongation (compression) of the non-cubic field. However, the non-cubic distortion should rather be thought of as an effective field that contains contributions beyond the IrO$_6$ complex [136]. As such, the sign of Δ may not directly correspond to the structural distortion of the octahedron [133].

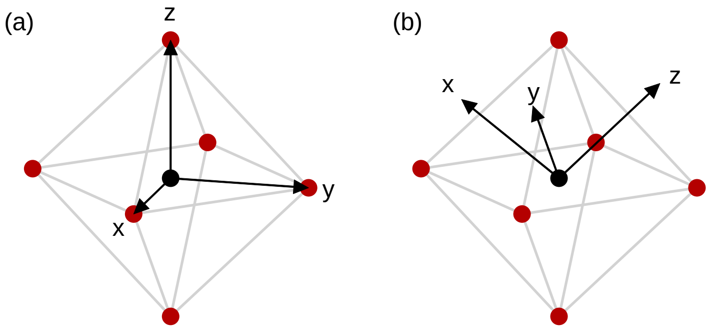

Figure 3.1: (a) Tetragonal and (b) trigonal octahedral reference frames.

This formalism has an important consequence for the formulation of RXS cross-sections: It implies that the atomic scattering tensors will be defined in different local reference frames, and care must be taken when deriving the structure factor for real experimental geometries (see Appendix A.1 for transformations between trigonal and tetragonal reference frames).

In the limit of $\zeta \gg \Delta$, the eigenstates of $\mathcal{H}$ are the $|J_{\text{eff}} = 1/2\rangle$ doublet and the $|J_{\text{eff}} = 3/2\rangle$ quartet, where we have used an effective angular momentum of $l_{\text{eff}}(t_{2g}) = -1$. The single hole occupies the $|J_{\text{eff}} = 1/2\rangle$ state. When non-cubic crystal fields become significant, the eigenstates of $\mathcal{H}$ are three non-degenerate Kramers doublets, which we label as $|f\rangle, |g\rangle$ and $|h\rangle$, where the hole occupies the $|f\rangle$ doublet. They take the form:

$$\begin{aligned}
|f,\downarrow\rangle &= \tfrac{+C_f|0,\downarrow\rangle+\sqrt{2}|\bar{1},\uparrow\rangle}{\sqrt{2+C_f^2}} & |g,\downarrow\rangle &= \tfrac{-C_g|0,\downarrow\rangle+\sqrt{2}|\bar{1},\uparrow\rangle}{\sqrt{2+C_g^2}} & |h,\downarrow\rangle &= |\bar{1},\downarrow\rangle \\
|f,\uparrow\rangle &= \tfrac{-C_f|0,\uparrow\rangle+\sqrt{2}|1,\downarrow\rangle}{\sqrt{2+C_f^2}} & |g,\uparrow\rangle &= \tfrac{+C_g|0,\uparrow\rangle+\sqrt{2}|1,\downarrow\rangle}{\sqrt{2+C_g^2}} & |h,\uparrow\rangle &= |1,\uparrow\rangle
\end{aligned}$$

with energies

$$\begin{aligned}
E_f &= \frac{\zeta}{4}\left(\delta + 1 + \sqrt{9 + \delta(\delta - 2)}\right) \\
E_g &= \frac{\zeta}{4}\left(\delta + 1 - \sqrt{9 + \delta(\delta - 2)}\right) \\
E_h &= -\frac{\zeta}{2}
\end{aligned}$$

where $2C_f = \delta - 1 + \sqrt{9 + \delta(\delta - 2)}$, $2C_g = 1 - \delta + \sqrt{9 + \delta(\delta - 2)}$ and $\delta = 2\Delta/\zeta$. Tetragonal and trigonal t_{2g} basis states $\{|0\rangle, |\bar{1}\rangle, |1\rangle\}$ are defined in Appendix A.1.

In the limit of $\Delta = 0$, we find $C_f = 1$ and $C_g = 2$, and we recover the $|J_{\text{eff}} = 1/2\rangle$ doublet and $|J_{\text{eff}} = 3/2\rangle$ quartet. In the opposite limit of $\zeta = 0$, $\delta \to \infty$, we find $C_f \to \infty$ and $C_g = 0$, and we recover $\{|0\rangle, |\bar{1}\rangle, |1\rangle\}$ t_{2g} basis states.

Associated with the f doublet, we find expectation values

$$\begin{aligned}
\langle L_z\rangle &= \frac{2}{2 + C_f^2}\,\mu_B \\
\langle S_z\rangle &= \frac{2 - C_f^2}{4 + 2C_f^2}\,\mu_B \\
\langle M_z\rangle = \langle L_z\rangle + 2\langle S_z\rangle &= \frac{4 - C_f^2}{2 + C_f^2}\,\mu_B
\end{aligned}$$

And a g-tensor of

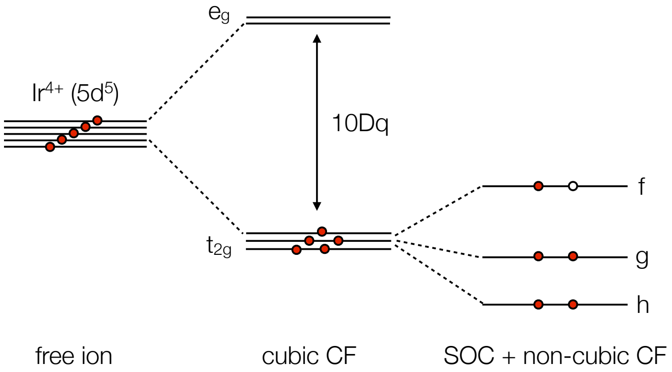

Figure 3.2: Energy level diagram for Ir^{4+} ($5d^5$) in a cubic crystal field (CF) $10Dq$, with spin-orbit coupling (SOC) and non-cubic crystal-fields (CFs) applied perturbatively.

$$\mathbf{g} = \frac{1}{2+C_f^2}\begin{pmatrix} -2C_f(2+C_f) & 0 & 0 \\ 0 & -2C_f(2+C_f) & 0 \\ 0 & 0 & -2(C_f^2-4) \end{pmatrix}$$

As expected, in the cubic limit of $C_f = 1$ we find $\langle L_z \rangle = 2/3\,\mu_B$, $\langle S_z \rangle = 1/6\,\mu_B$, $\langle M_z \rangle = 1\,\mu_B$ and $\mathbf{g} = g = -2$. More generally, even in the presence of non-cubic fields ($C_f \neq 1$) the ground state remains a half-occupied Kramers doublet, which is well separated from the first excited state by $\sim \zeta \gg k_B T$. It should hence form the Hilbert space of a spin-1/2 degree of freedom, and can be identified as an effective "spin-1/2" system [14, 139] (also referred to as "pseudospin"). The actual degrees of freedom can be inferred from the g-tensor. It is important to emphasise that the effective spins usually do not obey $SU(2)$ symmetry [139].

As pointed out in Refs. [119, 131], the direction of the (effective) spin can modify the wavefunction, and subsequently alter the RXS cross-sections. The above expression for the $|f\rangle$ doublet strictly only applies for a pseudospin along the local quantisation axis. We can generalise $|f\rangle$ to an arbitrary direction $\hat{\mathbf{m}} = (\sin\theta_s \cos\phi_s,\, \sin\theta_s \sin\phi_s,\, \cos\theta_s)$, using the Pauli matrices. The $|f\rangle$ doublet can then be written as:

$$\begin{aligned} |f,+\rangle &= e^{-i\phi_s}\cos\frac{\theta_s}{2}\,|f,\uparrow\rangle + \sin\frac{\theta_s}{2}\,|f,\downarrow\rangle \\ |f,-\rangle &= -e^{-i\phi_s}\sin\frac{\theta_s}{2}\,|f,\uparrow\rangle + \cos\frac{\theta_s}{2}\,|f,\downarrow\rangle \end{aligned}$$

where the angles θ_s, ϕ_s are defined in either the trigonal or tetragonal reference frame.

We emphasise that $\hat{\mathbf{m}}$, as defined by angles θ_s, ϕ_s, here refers to the direction of the effective spin-1/2 of the f doublet. In general, this pseudospin direction $\hat{\mathbf{m}}$ is not parallel to the real magnetic moment $\boldsymbol{\mu}$, defined as:

$$\boldsymbol{\mu} = \mu_B \frac{\mathbf{g} \cdot \hat{\mathbf{m}}}{2}$$

We can define γ as the angle between $\hat{\mathbf{m}}$ and $\boldsymbol{\mu}$

$$\arccos\gamma = \frac{(2+C_f)[(C_f-1)\cos 2\theta_s - 1]}{\sqrt{(2+C_f)^2[2+C_f(C_f-2)-2(C_f-1)\cos 2\theta_s]}}$$

Thus we find that in a non-cubic crystal field ($C_f \neq 1$), when $2\theta_s \neq n\pi$, with $n = 0, 1, \ldots$, the effective spin and magnetic moment directions are not parallel. This was recently pointed out in Ref. [140]. In general, one is interested in obtaining the pseudospin direction to determine the low-energy effective Hamiltonian. We here construct the RXS cross-section with reference to the pseudospin direction, which can be different to the magnetic moment direction $\boldsymbol{\mu}$, as is for example measured by neutron scattering. Although we emphasise that in many cases the magnetic moment lies along a high-symmetry direction with $2\theta_s = n\pi$, such that pseudospin and magnetic moment directions become equivalent.

3.2 Cross-section computation

Having computed the wavefunctions describing the low-energy electronic structure of iridates, we can proceed to calculate the RXS cross-sections. Resonant x-ray scattering is a two-step process [112]: By tuning the x-ray energy to the Ir $L_{2,3}$-edge resonance, we first promote an electron from a $2p$ core level to the $5d$ valence band. In the second step, the core hole is filled by a valence electron, under emission of an outgoing x-ray. At the L_3 edge, the RXS process can be succinctly written as: $2p^4_{3/2}5d(t^5_{2g}) \rightarrow 2p^3_{3/2}5d(t^6_{2g}) \rightarrow 2p^4_{3/2}5d(t^{5*}_{2g})$. Here, the * indicates that the system could be left in either an excited state (resonant inelastic x-ray scattering) or could be identical to the initial state (resonant elastic x-ray scattering). To describe this two-step process, we require Fermi's golden rule to second order. On resonance, the second order term dominates over the first order term and we obtain the Kramers-Heisenberg formula for the scattering amplitude [112, 141]:

$$A = \sum_n \frac{\langle \varphi_f | \mathcal{D}^\dagger_{\boldsymbol{\epsilon}'} | n \rangle \langle n | \mathcal{D}_{\boldsymbol{\epsilon}} | \varphi_i \rangle}{E_i + \hbar\omega_{\mathbf{k}} - E_n + i\Gamma_n} \tag{3.1}$$

where φ_i and φ_f are the initial and final states, n the intermediate states, $\mathcal{D}_{\boldsymbol{\epsilon}^{(\prime)}}$ the absorption (emission) operators, $E_{i,n}$ energies of initial, intermediate states, Γ_n the lifetime broadening of the intermediate state and $\hbar\omega_{\mathbf{k}}$ the incoming photon energy. This formalism requires the use of the hole picture, where a hole in an initial state φ_i travels to some intermediate state n, and finally ends up in φ_f. As we are interested in the Ir $L_{2,3}$ edges, we will use the dipole approximation for the operators $\mathcal{D}_{\boldsymbol{\epsilon}^{(\prime)}}$. On resonance, $\hbar\omega_{\mathbf{k}} \approx E_i - E_n$, and for a given edge ($E_n = E$) we set $\Gamma_n = \Gamma$. The single-ion scattering amplitude for arbitrary incoming (outgoing) polarisations vectors $\boldsymbol{\epsilon}^{(\prime)}$ thus simplifies to

$$A \propto \boldsymbol{\epsilon}'^{\alpha} \mathcal{A}^{\alpha\beta} \boldsymbol{\epsilon}^{\beta}$$

where we define the 3×3 atomic scattering tensor $\mathcal{A}^{\alpha\beta}$ as

$$\mathcal{A}^{\alpha\beta} = \sum_n \langle \varphi_f | \mathbf{r}_\alpha | n \rangle \langle n | \mathbf{r}_\beta | \varphi_i \rangle$$

and $\alpha, \beta = x, y, z$. In order to compute $\mathcal{A}^{\alpha\beta}$, we substitute the single-ion model wavefunctions of section 3.1 for initial and final states φ_i and φ_f, and the spin-orbit split $2p_{1/2}$ ($j = 1/2$) and $2p_{3/2}$ ($j = 3/2$) core levels as intermediate states n at L_2 and L_3 edges, respectively (see Appendix A.2 for explicit definitions of $2p$ levels). Note that while the $5d$ wavefunctions are defined in two different reference frames, the spherical symmetry of the $2p$ intermediate states (j is a good quantum number) implies that they are invariant under transformation from tetragonal to trigonal frames.

3.3 Atomic scattering tensors

Complete expressions of the atomic scattering tensors for all transitions within t_{2g} levels can be found in Appendix A.3. We here confine the discussion to elastic and spin-flip transitions, and explicitly show their dependence on the photon polarisation, moment direction, absorption edge and non-cubic distortions. This leads to the key result that the cross-section for resonant magnetic x-ray scattering depends on the non-cubic crystal field. A brief overview of t_{2g} crystal-field excitations is provided.

3.3.1 REXS

We first discuss the case of resonant elastic x-ray scattering (REXS), where initial and final states are identical, $\varphi_i = \varphi_f = f, -$. For tetragonal distortions of the cubic CF, we obtain the elastic (el) atomic scattering tensors

$$\mathcal{A}_{\text{el}}^{L_2,\text{tet}} = \frac{(C_f - 1)^2}{C_f^2 + 2} \begin{pmatrix} 1 & -i\cos\theta_s & 0 \\ i\cos\theta_s & 1 & 0 \\ 0 & 0 & 0 \end{pmatrix} \tag{3.2}$$

and

$$\mathcal{A}_{\text{el}}^{L_3,\text{tet}} = \frac{1}{C_f^2 + 2} \begin{pmatrix} 2[C_f^2 + C_f + 1] & i[C_f(C_f - 2) - 2]\cos\theta_s & -3iC_f \sin\theta_s \sin\phi_s \\ -i[C_f(C_f - 2) - 2]\cos\theta_s & 2[C_f^2 + C_f + 1] & 3iC_f \sin\theta_s \cos\phi_s \\ 3iC_f \sin\theta_s \sin\phi_s & -3iC_f \sin\theta_s \cos\phi_s & 6 \end{pmatrix} \tag{3.3}$$

at the L_2 and L_3 edge, respectively. For trigonal distortions we find

$$\mathcal{A}_{\text{el}}^{L_2,\text{tri}} = \frac{(C_f - 1)^2}{3(C_f^2 + 2)} \begin{pmatrix} 1 & -i\cos\theta_s & -2i\sin\theta_s\sin\phi_s \\ i\cos\theta_s & 1 & 2i\cos\phi_s\sin\theta_s \\ 2i\sin\theta_s\sin\phi_s & -2i\cos\phi_s\sin\theta_s & 4 \end{pmatrix} \tag{3.4}$$

and

$$\mathcal{A}_{\text{el}}^{L_3,\text{tri}} = \frac{1}{3(C_f^2 + 2)} \begin{pmatrix} 2[C_f^2 + C_f + 7] & -i[(C_f - 2)C_f + 10]\cos\theta_s & -i[2C_f^2 + 5C_f + 2]\sin\theta_s\sin\phi_s \\ i[(C_f - 2)C_f + 10]\cos\theta_s & 2[C_f^2 + C_f + 7] & i[2C_f^2 + 5C_f + 2]\cos\phi_s\sin\theta_s \\ i[2C_f^2 + 5C_f + 2]\sin\theta_s\sin\phi_s & -i[2C_f^2 + 5C_f + 2]\cos\phi_s\sin\theta_s & 2(2C_f + 1)^2 \end{pmatrix} \tag{3.5}$$

At the L_2 edge, we obtain the well-known result that all elements of $\mathcal{A}_{\text{el}}^{L_2}$ are proportional to $(C_f - 1)^2$ and therefore vanish in the ideal cubic crystal field limit, where $\Delta = 0$ and $C_f = 1$ [4]. In this case, the $J_{\text{eff}} = 1/2$ state is fully realised, and no intensity is expected for resonant elastic x-ray scattering of magnetic, charge or orbital order.

It is interesting to consider terms pertinent to x-ray resonant magnetic scattering (XRMS). We identify these as the off-diagonal, imaginary terms in the scattering tensors. For the case of tetragonal distortions at the L_2 edge with $\theta_s = \pi/2$, as is the case for Sr_2IrO_4 [4], these terms vanish and no XRMS intensity is expected, even if the ideal cubic limit of $\Delta/\zeta \to 0$ is realised. This was pointed out in Refs. [25, 131, 142]. The absence of XRMS intensity at the L_2 edge can therefore not in general be used to assign a $J_{\mathrm{eff}} = 1/2$ state. However, other REXS processes, involving diagonal matrix elements, could still assess the character of the wavefunction, regardless of the magnetic moment direction, as was suggested in Refs. [25, 135, 143].

At the L_3 edge, all elements of $\mathcal{A}_{\mathrm{el}}^{L_3}$ remain non-zero for any C_f, for trigonal and tetragonal distortions, implying that XRMS is fully allowed and can be used to determine magnetic structures.

XRMS

As XRMS is frequently used to determine magnetic structures in iridates [4, 26, 27, 29, 30, 73, 81, 82, 91, 92, 105, 135, 144–147], an accurate description of the cross-sections is needed. Most XRMS data are interpreted using the cross-section derived by Hannon *et al.* [148], which is strictly only accurate when the absorbing ion resides in spherical symmetry. This is usually not the case in iridates, where the local symmetry is at least reduced to a cubic environment. It is hence somewhat surprising that XRMS cross-sections within the spherical approximation could accurately determine magnetic structures, as was evidenced by comparison with neutron scattering [83, 149]. For dipole transitions, the XRMS scattering amplitude in spherical symmetry for first-order magnetic satellites was derived by Hannon *et al.* [148] as

$$\mathcal{A}_m^{\mathrm{spherical}} = -i(\boldsymbol{\epsilon}' \times \boldsymbol{\epsilon}) \cdot \hat{\mathbf{m}} \tag{3.6}$$

where $\boldsymbol{\epsilon}^{(\prime)}$ are incoming (outgoing) polarisations and $\hat{\mathbf{m}}$ the direction of the magnetic moment. From the above scattering tensors, at the Ir L_3 edge, we deduce the XRMS amplitudes

$$\begin{aligned} \mathcal{A}_m^{\mathrm{tet}} &= -i[3C_f](\boldsymbol{\epsilon}' \times \boldsymbol{\epsilon}) \cdot \hat{\mathbf{m}}_{xy} & +i[C_f(C_f-2)-2](\boldsymbol{\epsilon}' \times \boldsymbol{\epsilon}) \cdot \hat{\mathbf{m}}_z \\ \mathcal{A}_m^{\mathrm{tri}} &= -i[2C_f^2+5C_f+2](\boldsymbol{\epsilon}' \times \boldsymbol{\epsilon}) \cdot \hat{\mathbf{m}}_{xy} & -i[C_f(C_f-2)+10](\boldsymbol{\epsilon}' \times \boldsymbol{\epsilon}) \cdot \hat{\mathbf{m}}_z \end{aligned} \tag{3.7}$$

Thus we arrive at the important result that whenever the pseudospin (or magnetic moment) has components in both $\hat{\mathbf{m}}_{xy}$ and $\hat{\mathbf{m}}_z$, the spherical approximation becomes inaccurate (we emphasise that $\hat{\mathbf{m}}$ is defined in the local trigonal or tetragonal reference frame). In this case, great care should be taken when determining magnetic structures with XRMS. This result is in agreement with a more general symmetry analysis by Haverkort *et al.* [150]. Our microscopic calculation however has the advantage of providing a single tuning parameter, C_f, to calculate the XRMS cross-section.

It is interesting to consider the limit of $\Delta = 0$ and $C_f = 1$. In this case, amplitudes for both trigonal and tetragonal fields become:

$$\mathcal{A}_m = -i(\boldsymbol{\epsilon}' \times \boldsymbol{\epsilon}) \cdot \hat{\mathbf{m}}_{xy} + i(\boldsymbol{\epsilon}' \times \boldsymbol{\epsilon}) \cdot \hat{\mathbf{m}}_z$$

Thus, even in the cubic limit, the XRMS amplitude differs from the spherical approximation. Here the negative sign for the $\hat{\mathbf{m}}_z$ component can be understood from the g-factor of $g = -2$ of the $J_{\text{eff}} = 1/2$ state, which is opposite to a real spin $g = 2$, due to the orbital contribution [14, 129].

An overview of iridates studied with XRMS and the amount of non-cubic distortions is provided in Table 3.1. For example, the perovskite iridates Sr_2IrO_4 and $Sr_3Ir_2O_7$ have small tetragonal distortions and moments in the xy plane and along the z axis of the octahedra [4, 91, 92], respectively, and thus the spherical approximation should provide an accurate description of the XRMS cross-sections. Indeed, this was confirmed by neutron scattering [83, 149]. Similar observations can be made for the pyrochlore iridates $R_2Ir_2O_7$, where the magnetic moments lie parallel to the trigonal z axis [72]. However, for $CaIrO_3$ [135] and the honeycomb iridates $(Na,Li)_2IrO_3$ [26, 27, 29, 30], the magnetic moments are reported to have components in $\hat{\mathbf{m}}_{xy}$ and $\hat{\mathbf{m}}_z$, as well as $C_f \neq 1$. In these cases, it may be worth revisiting the published data using Eqn. 3.7.

Iridate	Type of distortion	Δ (meV)
Sr_2IrO_4	Tetragonal	130 [137]
$Sr_3Ir_2O_7$	Tetragonal	$0 - 200$ [92]
$CaIrO_3$	Tetragonal	700 [121]
Sr_3NiIrO_6	Trigonal	300 [71]
$R_2Ir_2O_7$	Trigonal	450 [136]
Na_2IrO_3	Trigonal	110 [134]
Li_2IrO_3	Trigonal	unknown

Table 3.1: Strength of non-cubic crystal field Δ in magnetically ordered Ir^{4+} iridates.

For completeness, at the Ir L_2 edge we find XRMS amplitudes

$$\begin{aligned}
\mathcal{A}_m^{\text{tet}} &= i[C_f - 1]^2(\boldsymbol{\epsilon}' \times \boldsymbol{\epsilon}) \cdot \hat{\mathbf{m}}_z \\
\mathcal{A}_m^{\text{tri}} &= i[C_f - 1]^2(\boldsymbol{\epsilon}' \times \boldsymbol{\epsilon}) \cdot \hat{\mathbf{m}}_{xy} + \frac{i}{2}[C_f - 1]^2(\boldsymbol{\epsilon}' \times \boldsymbol{\epsilon}) \cdot \hat{\mathbf{m}}_z
\end{aligned}$$

If $C_f \sim 1$, the factor of $(C_f - 1)^2$ will strongly suppress magnetic scattering, and XRMS at the Ir L_2 edge is not expected to be practicable. Nevertheless, the L_2 edge XRMS cross-section illustrates some interesting points. For tetragonal distortions, XRMS will be only be sensitive to the $\hat{\mathbf{m}}_z$ component. For trigonal distortions, any magnetic moment direction can be detected by XRMS, but the response is not isotropic.

3.3.2 RIXS

Spin-flip cross-section

The RIXS transition to the spin-flip state within the f doublet can create single-magnon excitations. While transitions to the g, h doublets could also result in a final state with a flipped spin, the dd excitations act as a momentum sink, preempting the study of the single-magnon dispersion [119]. Substituting initial and final states $\varphi_i = f, -$ and $\varphi_f = f, +$, in the presence of tetragonal distortions, we obtain atomic scattering tensors for spin-flip (sf) transitions:

$$\mathcal{A}_{\text{sf}}^{L_2,\text{tet}} = \frac{(C_f - 1)^2}{C_f^2 + 2} \begin{pmatrix} 0 & i\sin\theta_s & 0 \\ -i\sin\theta_s & 0 & 0 \\ 0 & 0 & 0 \end{pmatrix} \tag{3.8}$$

and

$$\mathcal{A}_{\text{sf}}^{L_3,\text{tet}} = \\ \frac{1}{C_f^2 + 2} \begin{pmatrix} 0 & i[C_f(C_f - 2) - 2]\sin\theta_s & 3C_f[i\cos\theta_s \sin\phi_s + \cos\phi_s] \\ -i[C_f(C_f - 2) - 2]\sin\theta_s & 0 & -3iC_f[\cos\theta_s\cos\phi_s - \sin\phi_s] \\ -3C_f[i\cos\theta_s\sin\phi_s + \cos\phi_s] & 3iC_f[\cos\theta_s\cos\phi_s - \sin\phi_s] & 0 \end{pmatrix} \tag{3.9}$$

Similar expressions can be derived for the case of trigonal distortions, and are given in Appendix A.3.

At the L_2 edge, we find that in an ideal cubic limit, the amplitude for spin-flip transitions goes to zero. This is indeed the case for any RXS transition within the t_{2g} manifold. The dependence on the angle of the pseudospin is now $\sin\theta_s$, thus spin-flip transitions can only be measured if the moment is within the xy plane. Interestingly, the tensor at the Ir L_2 edge with tetragonal distortions takes the same form as tensor for spin-flip transitions at the Cu L_3 edge of cuprates [119]. Conversely, at the L_3 edge, spin-flip transitions remain allowed for any moment orientation, for arbitrary non-cubic crystal fields. It should generally always be possible to study single-magnon excitations with RIXS at the Ir L_3 edge.

It is instructive to compare our spin-flip scattering tensors to the generic, symmetry-allowed spin-flip RIXS tensor, which can be derived through *effective operators*. This approach was first introduced by Haverkort *et al.* [151], and has since been extended by Savary *et al.* [152]. It has the advantage of not relying on any microscopic model or assumptions regarding the intermediate states. For a $S = 1/2$ system in tetragonal symmetry, the effective RIXS operator, involving only single spin operators, for spin-flip transitions can be written as [151]:

$$\mathcal{R} = \begin{pmatrix} 0 & 2S_z\sigma_{a_{2u}} & -2S_y\sigma_{e_u} \\ -2S_z\sigma_{a_{2u}} & 0 & 2S_x\sigma_{e_u} \\ 2S_y\sigma_{e_u} & -2S_x\sigma_{e_u} & 0 \end{pmatrix}$$

where the coefficients $\sigma_{a_{2u}}$ and σ_{e_u} remain to be determined. Using a $S = 1/2$ doublet as basis states, we evaluate $\langle\uparrow|\,\mathcal{R}\,|\downarrow\rangle$ to obtain the most generic, symmetry-allowed spin-flip scattering tensor in tetragonal symmetry:

$$\mathcal{A}_{\mathrm{sf}} = \begin{pmatrix} 0 & i\sigma_{a_{2u}}\sin\theta_s & \sigma_{e_u}\left(\cos\phi_s + i\cos\theta_s\sin\phi_s\right) \\ -i\sigma_{a_{2u}}\sin\theta_s & 0 & \sigma_{e_u}\left(\sin\phi_s - i\cos\theta_s\cos\phi_s\right) \\ -\sigma_{e_u}\left(\cos\phi_s + i\cos\theta_s\sin\phi_s\right) & \sigma_{e_u}\left(i\cos\theta_s\cos\phi_s - \sin\phi_s\right) & 0 \end{pmatrix}$$

which indeed takes the same form as our single-ion model spin-flip tensor. The coefficients $\sigma_{a_{2u}}$ and σ_{e_u} can then be mapped onto our microscopic calculation. For example, in a cubic limit, $C_f = 1$, we find $\sigma_{a_{2u}} = -1$ and $\sigma_{e_u} = 1$, which again reflects the effective g-factor of the $J_{\mathrm{eff}} = 1/2$ isospin being opposite to a real $S = 1/2$. If $\Delta \neq 0$, the RIXS response for spin-flip transitions differs for components $\hat{\mathbf{m}}_{xy}$ and $\hat{\mathbf{m}}_z$, in analogy with the results from REXS.

The atomic scattering tensors for spin-flip transitions only consist of off-diagonal elements. This implies that single-magnon excitations will only appear in cross-polarised photon polarisation channels. While current instrumentation on hard x-ray RIXS beamlines does not yet allow polarisation analysis of the outgoing beam, future investigations could make use of this polarisation dependence to identify or isolate a single-magnon signal.

Crystal field excitations within the t_{2g} manifold

In a similar manner, atomic scattering tensors to the final states $\varphi_f = g, h$ can be derived (using e.g. $\varphi_i = f, -$). These are sometimes referred to as "spin-orbit excitations", when their excitation energy is mainly set by the SOC. As we here explicitly include non-cubic crystal fields, which can be as strong as the spin-orbit coupling, we refer to these transitions as crystal field or *dd* excitations within the t_{2g} manifold. As the analytical expressions of the tensors are somewhat tedious, we here provide a graphical representation. Figure 3.3 shows the RIXS intensity summed over four transitions to $\varphi_f = g, h$ final states (with and without spin-flip), i.e. $I^{\alpha\beta} = \sum_{j=1}^{4} |\mathcal{A}_j^{\alpha\beta}|^2$. As such, they can be thought of as the polarisation-resolved intensity of a hypothetical single IrO$_6$ octahedron. In a real experiment, different symmetry-equivalent sites will contribute and the polarisation vectors will be more complicated. Both need to be treated on an amplitude, as opposed to intensity, level, and hence interference can occur, such that is not possible to relate the single-ion intensities of Fig. 3.3 in a straightforward manner to experimental RIXS intensities (see also section 3.4).

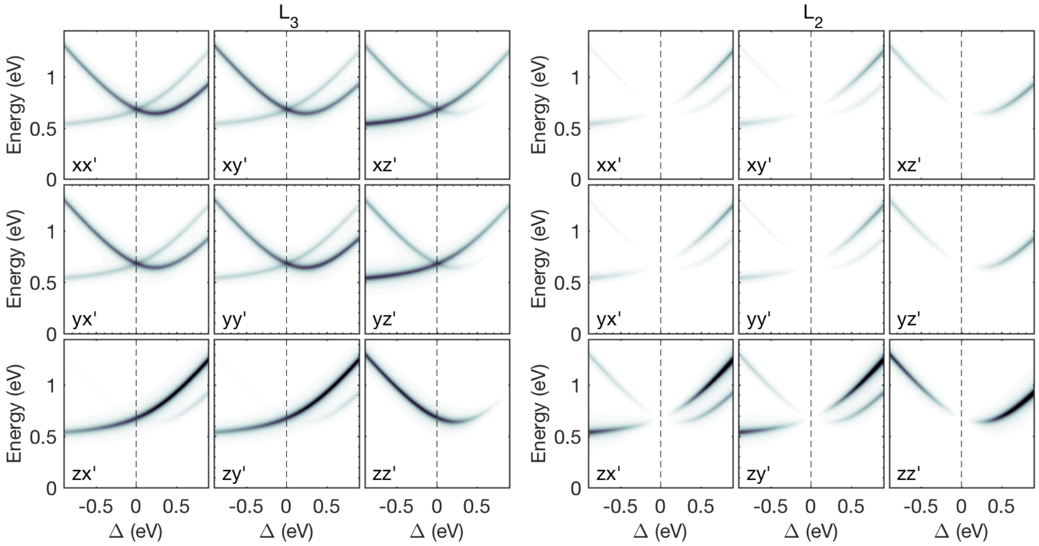

Figure 3.3: Polarisation resolved single-ion RIXS intensity of crystal-field transitions within t_{2g} manifold at the L_3 edge (left) and L_2 edge (right) as a function of trigonal distortion Δ at constant $\zeta = 450$ meV. Each panel corresponds to specific incoming and outgoing polarisations vectors, as indicated in the figure.

Nevertheless, this graphical representation offers some insights. Roughly speaking, the intensities of *dd* excitations hold information on the character of wavefunctions of the involved crystal field levels, whereas the excitation energies determine the energy level spacing. From Figure 3.3, it is clear that the choice of incoming and outgoing polarisation strongly affects the intensity of the respective transitions to g, h final states. Thus, by exploiting polarisation effects, for example through large variations in the scattering geometry, specific crystal field excitations could be selectively enhanced or suppressed. This might be used to determine the sign of the non-cubic crystal field, which can be ambiguous from excitation energies alone [137, 153, 154].

Additionally, the intensity of these dd excitations is strongly tied to the specific absorption edge. While the crystal field excitations are always observable at the L_3 edge, in the limit of a cubic crystal field, the intensity at the L_2 edge becomes zero. Thus the absence of these features at the L_2 edge indicates a close realisation of the $J_{\text{eff}} = 1/2$ state.

3.4 Structure factor for pyrochlore iridates

The atomic scattering tensors $\mathcal{A}$ provide the RXS amplitude of a single Ir ion. In a real experiment, $\mathcal{A}$ is not directly observed. Instead, components of the tensorial structure factor are measured, which includes contributions from different sites, which can be differently orientated within the unit cell. We here consider REXS in pyrochlore iridates as an example on how to obtain the structure factor from atomic scattering tensors. We demonstrate how the absolute size of the ordered magnetic moment can be estimated by REXS, a quantity which hitherto remained elusive to x-ray scattering techniques.

In the pyrochlore unit cell, Ir ions occupy the 16c site. This implies 16 Ir ions within the unit cell. However, it is sufficient to consider four inequivalent sites forming a single tetrahedron. These four sites are all differently orientated, whereas the remaining twelve sites of the pyrochlore lattice can be found through translations. The additional twelve sites will leave the structure factor unchanged, if the face-centred cubic (*fcc*) selection rule is respected ($h, k, l =$ all even or all odd). Figure 3.4 shows the orientations of four Ir sites in the pyrochlore unit cell and their associated local reference frames.

These local bases are convenient, as they coincide with the trigonal reference frames used for the single-ion model of section 3.1, such that the $\mathbf{w}_i$ axes are parallel to the C_3 axes of the IrO$_6$ octahedra. We define rotations R_i that transform between local and crystal reference frames:

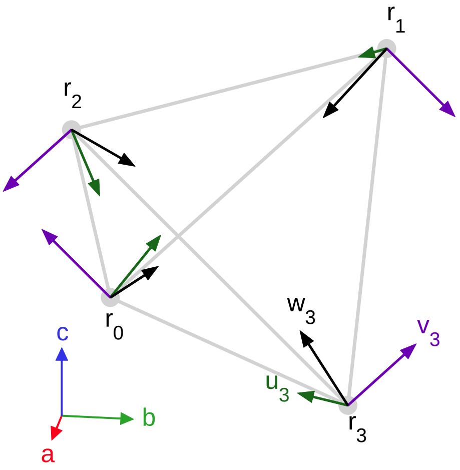

Site i	$\mathbf{r}_i$	$\mathbf{u}_i$	$\mathbf{v}_i$	$\mathbf{w}_i$
0	$(0,0,0)$	$\frac{1}{\sqrt{6}}(\bar{2},1,1)$	$\frac{1}{\sqrt{2}}(0,\bar{1},1)$	$\frac{1}{\sqrt{3}}(1,1,1)$
1	$(0,\frac{1}{4},\frac{1}{4})$	$\frac{1}{\sqrt{6}}(\bar{2},\bar{1},\bar{1})$	$\frac{1}{\sqrt{2}}(0,1,\bar{1})$	$\frac{1}{\sqrt{3}}(1,\bar{1},\bar{1})$
2	$(\frac{1}{4},0,\frac{1}{4})$	$\frac{1}{\sqrt{6}}(2,1,\bar{1})$	$\frac{1}{\sqrt{2}}(0,\bar{1},\bar{1})$	$\frac{1}{\sqrt{3}}(\bar{1},1,\bar{1})$
3	$(\frac{1}{4},\frac{1}{4},0)$	$\frac{1}{\sqrt{6}}(2,\bar{1},1)$	$\frac{1}{\sqrt{2}}(0,1,1)$	$\frac{1}{\sqrt{3}}(\bar{1},\bar{1},1)$

Figure 3.4: The four inequivalent Ir sites in the pyrochlore unit cell. The coordinates of the local bases follow the convention of Ref. [155].

$$R_0 = \begin{pmatrix} \frac{-2}{\sqrt{6}} & 0 & \frac{1}{\sqrt{3}} \\ \frac{1}{\sqrt{6}} & \frac{-1}{\sqrt{2}} & \frac{1}{\sqrt{3}} \\ \frac{1}{\sqrt{6}} & \frac{1}{\sqrt{2}} & \frac{1}{\sqrt{3}} \end{pmatrix} R_1 = \begin{pmatrix} \frac{-2}{\sqrt{6}} & 0 & \frac{1}{\sqrt{3}} \\ \frac{-1}{\sqrt{6}} & \frac{1}{\sqrt{2}} & \frac{-1}{\sqrt{3}} \\ \frac{-1}{\sqrt{6}} & \frac{-1}{\sqrt{2}} & \frac{-1}{\sqrt{3}} \end{pmatrix}$$

$$R_2 = \begin{pmatrix} \frac{2}{\sqrt{6}} & 0 & \frac{-1}{\sqrt{3}} \\ \frac{1}{\sqrt{6}} & \frac{-1}{\sqrt{2}} & \frac{1}{\sqrt{3}} \\ \frac{-1}{\sqrt{6}} & \frac{-1}{\sqrt{2}} & \frac{-1}{\sqrt{3}} \end{pmatrix} R_3 = \begin{pmatrix} \frac{2}{\sqrt{6}} & 0 & \frac{-1}{\sqrt{3}} \\ \frac{-1}{\sqrt{6}} & \frac{1}{\sqrt{2}} & \frac{-1}{\sqrt{3}} \\ \frac{1}{\sqrt{6}} & \frac{1}{\sqrt{2}} & \frac{1}{\sqrt{3}} \end{pmatrix}$$

This is all we need to calculate the structure factor. We recall the atomic scattering tensor for elastic transitions at the Ir L_3 edge in the presence of trigonal fields

$$\mathcal{A}_{\text{el}}^{L_3,\text{tri}} \propto$$
$$\begin{pmatrix} 2(C_f^2+C_f+7) & -i[(C_f-2)C_f+10]\cos\theta_s & -i[2C_f^2+5C_f+2]\sin\theta_s\sin\phi_s \\ i[(C_f-2)C_f+10]\cos\theta_s & 2(C_f^2+C_f+7) & i[2C_f^2+5C_f+2]\cos\phi_s\sin\theta_s \\ i[2C_f^2+5C_f+2]\sin\theta_s\sin\phi_s & -i[2C_f^2+5C_f+2]\cos\phi_s\sin\theta_s & 2(2C_f+1)^2 \end{pmatrix}$$

We identify off-diagonal, imaginary terms proportional to θ_s, ϕ_s arising from resonant magnetic scattering, while diagonal terms originate from resonant charge scattering. For resonant charge scattering, the non-magnetic tensor reads

$$\mathcal{A}_{\mathrm{el}}^{L_3} = \frac{1}{3(C_f^2+2)} \begin{pmatrix} 2[C_f^2+C_f+7] & 0 & 0 \\ 0 & 2[C_f^2+C_f+7] & 0 \\ 0 & 0 & 2[2C_f+1]^2 \end{pmatrix}$$

Resonant x-ray scattering is a coherent process, and hence the contributions of different sites must be treated on an amplitude level [112]. We calculate the tensorial structure factor at wavevector $\mathbf{Q}$ via

$$F(\mathbf{Q}) = \sum_{i=0}^{3} R_i \mathcal{A}_{\mathrm{el}}^{L_3} R_i^T \exp\left(2i\pi \mathbf{Q}\cdot\mathbf{r}_i\right) \tag{3.10}$$

For example, we consider allowed and forbidden $(h00)$ reflections of space group $Fd\bar{3}m$, where $h = 4n$ (allowed) and $h = 4n+2$ (forbidden), respectively. We obtain the structure factors for resonant charge scattering:

$$F^{L_3}(h00) = \begin{cases} \dfrac{8(C_f^2+2C_f+5)}{3(2+C_f^2)} \begin{pmatrix} 1 & 0 & 0 \\ 0 & 1 & 0 \\ 0 & 0 & 1 \end{pmatrix} & \text{if } h = 4n \\ \dfrac{8(C_f^2+C_f-2)}{3(2+C_f^2)} \begin{pmatrix} 0 & 0 & 0 \\ 0 & 0 & 1 \\ 0 & 1 & 0 \end{pmatrix} & \text{if } h = 4n+2 \end{cases}$$

For allowed $(h00)$ reflections, for any value of C_f, there will be a contribution of resonant charge scattering. Furthermore, we find that space group forbidden $(h00)$ reflections can become allowed at the Ir L_3 edge. The factor of $(C_f^2 + C_f - 2)$ implies that there must be a finite amount of trigonal distortion for these reflections to arise (as $C_f = 1$ for $\Delta = 0$). This phenomenon is usually referred to anisotropic tensor susceptibility (ATS) scattering [156].

The contribution of XRMS to the atomic scattering tensor is:

$$\mathcal{A}_m^{L_3} \propto$$

$$\begin{pmatrix} 0 & -i[(C_f-2)C_f+10]\cos\theta_s & -i[2C_f^2+5C_f+2]\sin\theta_s\sin\phi_s \\ i[(C_f-2)C_f+10]\cos\theta_s & 0 & i[2C_f^2+5C_f+2]\cos\phi_s\sin\theta_s \\ i[2C_f^2+5C_f+2]\sin\theta_s\sin\phi_s & -i[2C_f^2+5C_f+2]\cos\phi_s\sin\theta_s & 0 \end{pmatrix}$$

To calculate the structure factor, the direction of the pseudospin, defined through θ_s, ϕ_s, has to specified for each site (we assume that the magnetic structure can be fully described within a single tetrahedron). For the all-in all-out magnetic structure, the effective spins point either all towards or away from the centre of the tetrahedron, such that they lie parallel to the local quantisation axis $\mathbf{w}_i$. We hence set $\theta_s = \phi_s = 0$ for all sites i, and obtain the magnetic tensor

$$\mathcal{A}_m^{L_3} = \frac{1}{3(C_f^2+2)} \begin{pmatrix} 0 & -i[(C_f-2)C_f+10] & 0 \\ i[(C_f-2)C_f+10] & 0 & 0 \\ 0 & 0 & 0 \end{pmatrix}$$

Via eqn. 3.10, we arrive at the resonant magnetic structure factor for $(h00)$ reflections

$$F_m^{L_3}(h00) = \begin{cases} 0 & \text{if } h = 4n \\ \dfrac{4(10+(C_f-2)C_f)}{3\sqrt{3}(2+C_f^2)} \begin{pmatrix} 0 & 0 & 0 \\ 0 & 0 & -i \\ 0 & i & 0 \end{pmatrix} & \text{if } h = 4n+2 \end{cases}$$

We find that only space group forbidden $(h00)$ reflections will be sensitive to a magnetic signal from AIAO magnetic order, regardless of the amount of trigonal distortion. Hence forbidden $(h00)$ reflections with $h = 4n+2$ should contain contributions from both AIAO magnetic order and charge-resonant scattering.

The above tensorial structure factors are defined in the reference frame of the crystal. In order to understand the polarisation dependence in a real experimental situation, it is useful to convert them to a 2 × 2 Jones matrix. In $(h00)$ scattering geometry, the a axis of the crystal lies parallel to the wavevector $\mathbf{Q}$, and the incoming and outgoing beams in the crystal frame are

$$\begin{aligned} \mathbf{k} &= [-\sin\theta, \cos\theta\sin(\phi+\pi/4), \cos\theta\cos(\phi+\pi/4)] \\ \mathbf{k}' &= [+\sin\theta, \cos\theta\sin(\phi+\pi/4), \cos\theta\cos(\phi+\pi/4)] \end{aligned}$$

where θ is the Bragg angle and we have defined the azimuthal angle $\phi = 0°$ when the (011) direction is in the scattering plane. We define polarisation vectors perpendicular ($\boldsymbol{\epsilon}_\sigma$) and parallel ($\boldsymbol{\epsilon}_\pi$) to the scattering plane

$$\begin{aligned} \boldsymbol{\epsilon}_\sigma &= \mathbf{k} \times \mathbf{k}' \\ \boldsymbol{\epsilon}_\pi &= \boldsymbol{\epsilon}_\sigma \times \mathbf{k} \\ \boldsymbol{\epsilon}'_\sigma &= \boldsymbol{\epsilon}_\sigma \\ \boldsymbol{\epsilon}'_\pi &= \boldsymbol{\epsilon}'_\sigma \times \mathbf{k}' \end{aligned}$$

By evaluating $\boldsymbol{\epsilon}' \cdot F(h00) \cdot \boldsymbol{\epsilon}$, we obtain 2 × 2 Jones matrices in the $\sigma\pi$ basis for resonant charge and resonant magnetic scattering from forbidden $(h00)$ reflections:

$$\begin{aligned}
\mathcal{A}_{ats}^{(h00)} &= \frac{8(C_f^2 + C_f - 2)}{3(2 + C_f^2)} \begin{pmatrix} \cos 2\phi & -\sin\theta \sin 2\phi \\ \sin\theta \sin 2\phi & \sin^2\theta \cos 2\phi \end{pmatrix} \\
\mathcal{A}_{m}^{(h00)} &= \frac{4(10 + (C_f - 2)C_f)}{3\sqrt{3}(2 + C_f^2)} \begin{pmatrix} 0 & -i\sin\theta \\ -i\sin\theta & 0 \end{pmatrix}
\end{aligned}$$

A REXS experiment will measure $|\mathcal{A}_{REXS}^{(h00)}|^2 = |\mathcal{A}_{ats}^{(h00)} + \mathcal{A}_{m}^{(h00)}|^2$. The resonant magnetic contribution exists in $\sigma\pi'$ and $\pi\sigma'$ polarisation, increases with the Bragg angle, and is constant in the azimuthal angle ϕ. The resonant charge contribution is present in all polarisation channels, but has a clear azimuthal dependence. Consider the intensity in $\sigma\pi'$ polarisation:

$$\begin{aligned}
I_{REXS}^{\sigma\pi}(h00) = I_{m}^{\sigma\pi}(h00) & \qquad + I_{ats}^{\sigma\pi}(h00) \\
= \frac{16[10 + (C_f - 2)C_f]^2 \sin^2\theta}{27(2 + C_f^2)^2} & \qquad + \frac{64(C_f^2 + C_f - 2)^2 \sin^2\theta \sin^2 2\phi}{9(2 + C_f^2)^2}
\end{aligned}$$

Note that interference terms cancel. For an azimuthal scan (ϕ dependence) of a $(h00)$ reflection, we expect a constant magnetic contribution, as well as an oscillating signal with a period of 2ϕ, if $\Delta \neq 0$. Thus an azimuthal scan can distinguish between the two contributions. The ratio of magnetic to ATS intensities at $\phi = \pi/4$ is

$$\frac{I_m}{I_{ats}} = \frac{[10 + (C_f - 1)C_f]^2}{12(C_f^2 + C_f - 2)^2} \tag{3.11}$$

In the single-ion model, the Ir magnetic moment is given by

$$\langle \mu_z \rangle = \langle L_z \rangle + 2 \langle S_z \rangle = \frac{4 - C_f^2}{2 + C_f^2} \mu_B$$

For pyrochlore iridates, one typically finds $C_f \sim 1/2$ (see section 5.3), giving $I_m/I_{ats} \sim 5$ and a single-ion magnetic moment of $\sim 1.6\ \mu_B$ (the trigonal compression enhances the magnetic moment from $1\ \mu_B$ of the ideal $J_{\text{eff}} = 1/2$ state [51]). The experimental ratio of magnetic to ATS scattering hence provides a measure of the size of the ordered moment. If the measured I_m/I_{ats} ratio is reduced by some factor, we expect that the ordered magnetic moment will be reduced from the single-ion value by the same factor.

This approach of comparing the resonant charge and resonant magnetic contribution can hence be used to determine the size of the ordered magnetic moment. This is an interesting result, as it is generally assumed that the absolute size of the magnetic moment can only be determined by neutron diffraction. Indeed, it should be straightforward to extend the approach described here to other iridates, all that is required is a good estimate of the ratio of spin-orbit coupling to non-cubic crystal fields.

3.5 Conclusion

In this chapter, we derived single-ion RXS cross-section at the Ir $L_{2,3}$ edges of iridates. While similar calculations were previously reported in the literature [25, 130–132], our approach is more comprehensive, as it takes into account tetragonal and trigonal distortions of the cubic field and an arbitrary direction of the magnetic moment. This makes the RXS cross-sections applicable to a wide range of iridates, as well as other d^5 systems with strong spin-orbit coupling.

We formulated atomic scattering tensors for all possible transitions within the t_{2g} manifold, providing an intuitive understanding of the RXS polarisation dependence. By isolating the contribution of resonant magnetic x-ray scattering, we showed how the XRMS cross-section depends on the non-cubic crystal field, which can have important consequences for determining magnetic structures. We also made explicit how spin-flip and crystal-field excitations depend on the moment direction, photon polarisation, non-cubic crystal fields and the specific absorption edge.

Finally, through the example of pyrochlore iridates, we described how the structure factor, which is the quantity measured in RXS experiments, can be constructed out of the atomic scattering tensors. We demonstrated for the first time how REXS can be used to estimate the size of the magnetic moment, by comparing the relative strength of resonant magnetic and resonant charge contributions.

Chapter 4

REXS of R_2Ir$_2$O$_7$ (R = Sm, Nd, Tb)

Contents

4.1 Sm$_2$Ir$_2$O$_7$ 80

4.1.1 Bulk properties 80

4.1.2 XRMS 81

4.1.3 XRMS at high magnetic fields 86

4.2 Nd$_2$Ir$_2$O$_7$ 94

4.2.1 Bulk properties 94

4.2.2 XRMS 95

4.3 Tb$_2$Ir$_2$O$_7$ 97

4.3.1 Bulk properties 97

4.3.2 XRMS 98

4.4 Conclusion 101

In this chapter, we describe resonant elastic x-ray scattering (REXS) experiments at the Ir L_3 edge aimed at determining the magnetic structure of the pyrochlore iridates $R_2Ir_2O_7$ (R = Sm, Nd, Tb). In all samples, long-range $\mathbf{k} = \mathbf{0}$ magnetic order was observed, with transition temperatures of 110 K (Sm), 4 K (Nd) and 70 K (Tb). For Sm and Tb, analysis of the REXS cross-sections reveals that only an all-in all-out (AIAO) or xy antiferromagnetic structure can describe the data. Assuming AIAO order, comparison of the intensities with single-ion REXS cross-sections of section 3.4 indicates a moment size of $\sim 0.3\,\mu_B$ (Sm) and $\sim 0.06\,\mu_B$ (Tb). For $Sm_2Ir_2O_7$, the magnetic structure remained unchanged in magnetic fields up to 12 T.

Parts of this chapter were published in the article "All-in All-Out Magnetic Order and Propagating Spin Waves in $Sm_2Ir_2O_7$" in the journal Physical Review Letters [157].

A detailed discussion of how REXS can be used to investigate $\mathbf{k} = \mathbf{0}$ magnetic order on the pyrochlore lattice, by computing cross-sections for resonant charge and resonant magnetic x-ray scattering for all symmetry-allowed magnetic structures, can be found in Appendix B. We will here only allude to key results of these calculations.

4.1 $Sm_2Ir_2O_7$

A REXS experiment was performed to solve the magnetic structure of the pyrochlore iridate $Sm_2Ir_2O_7$ at beamline P09, Petra III in July 2015. The temperature and polarisation dependence of forbidden ($h00$) reflections suggests $\mathbf{k} = \mathbf{0}$ magnetic order below 110 K. Analysis of the REXS cross-sections reveals that only two irreducible representations are consistent with the data, the all-in all-out (Γ_3) and the xy antiferromagnet (Γ_5). Comparison with single-ion RXS cross-sections indicates an ordered moment of $\sim 0.3\,\mu_B$ at 10 K. REXS experiments under magnetic fields suggest that the magnetic structure is robust up to 12 T.

4.1.1 Bulk properties

Single crystals of $Sm_2Ir_2O_7$ were grown by the self-flux method, as described in Ref. [158]. They were characterised by x-ray diffraction and magnetometry. Figure 4.1 shows the magnetisation of multiple single-crystals of $Sm_2Ir_2O_7$ as

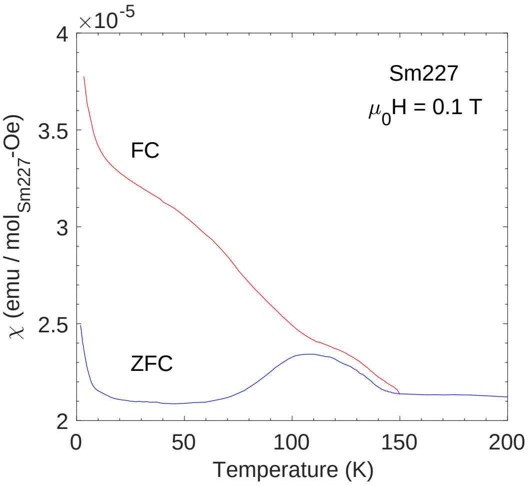

Figure 4.1: Temperature dependence of field-cooled (FC, red line) and zero-field-cooled (ZFC, blue line) magnetisation of multiple $Sm_2Ir_2O_7$ single crystals in a magnetic field of 0.1 T. Data courtesy of D. Prabhakaran.

a function of temperature, measured by D. Prabhakaran at the University of Oxford. At approximately 110 K, field-cooled (FC) and zero-field-cooled (ZFC) magnetisation curves bifurcate, which is usually associated with the onset of antiferromagnetic order on the Ir site [34]. This value is close to a transition temperature of 120 K reported in the literature [34]. A second weakly ferromagnetic transition occurs in our samples at 150 K. This second transition was previously observed in lightly hole-doped pyrochlore iridates and has been proposed to arise from Ir^{5+} impurities [159].

4.1.2 XRMS

Method

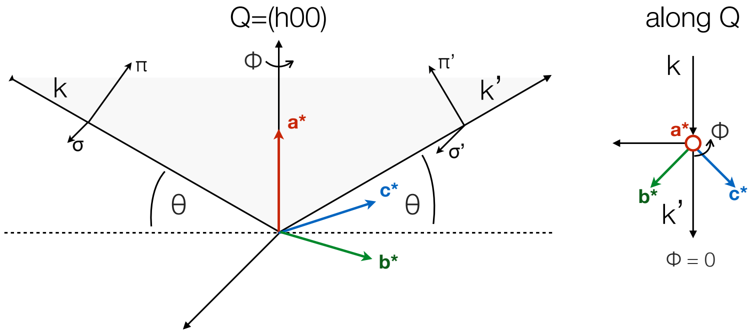

Figure 4.2: Scattering geometry for REXS of $Sm_2Ir_2O_7$.

Figure 4.2 shows the experimental setup on beamline, P09, PETRA III

[122]. A vertical scattering geometry was used, which implies that the incoming linear polarisation was perpendicular to the scattering plane (σ polarisation). Polarisation analysis of the outgoing beam was performed with a Au (333) analyser crystal. The $Sm_2Ir_2O_7$ sample was mounted with GE varnish on the cold finger of a Displex cryostat, such that the (100) and (011) directions were in the scattering plane.

Results

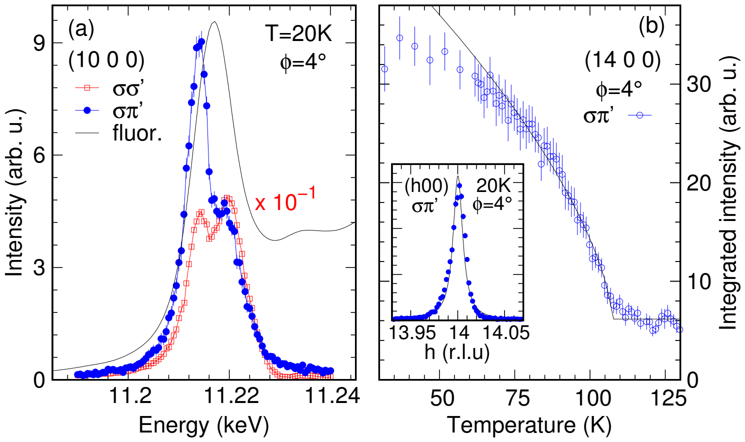

Figure 4.3: REXS data showing $\mathbf{k} = \mathbf{0}$ magnetic order in $Sm_2Ir_2O_7$. (a) Energy dependence of the (10 0 0) reflection in $\sigma\sigma'$ (red squares, ATS resonance) and $\sigma\pi'$ (blue circles, magnetic resonance) polarisation channels, plotted with Ir L_3 absorption spectrum recorded in total fluorescence yield mode (black line). The data were corrected for self-absorption. (b) Temperature dependence of the (14 0 0) magnetic reflection in $\sigma\pi'$ polarisation, revealing $T_N \sim 108$ K.

Figure 4.3 shows REXS data of $Sm_2Ir_2O_7$. At the Ir L_3 edge at 20 K, forbidden (h00) reflections (where $h = 4n+2$) were discovered. This indicates the formation of $\mathbf{k} = \mathbf{0}$ magnetic order. However, in addition to resonant magnetic scattering, resonant charge scattering can also contribute to forbidden (h00) reflections. In the literature, resonant charge scattering is often referred to as anisotropic tensor susceptibility (ATS) scattering[1]. A detailed description of ATS scattering on the pyrochlore lattice is given in Appendix B. The ATS contribution in the magnetically-relevant $\sigma\pi'$ channel can be minimised by bringing the (011) direction into the scattering plane (which here corresponds to an azimuthal angle $\phi = 0°$). In this scattering geometry, we could identify long-range magnetic order, as evidenced by reciprocal lattice scans [see inset 4.3(b)]. Fig. 4.3(a) shows the energy dependence of the (10 0 0) reflection at $\phi = 4°$ (corrected for self-absorption), which resonates 3 eV below the absorption maximum, as expected for resonant magnetic scattering in iridates [4, 92]. Conversely, in $\sigma\sigma'$ polarisation, the scattering is purely of ATS origin. Two features are seen in the ATS resonance, which were previously attributed to transitions to t_{2g} and e_g levels [73, 135, 143]. Fig. 4.3(b) shows the temperature dependence of the (14 0 0) magnetic reflection together with a power law fit. The data were corrected for beam-heating (see below). The remaining intensity above the ordering temperature ($\sim$ 108 K) can be attributed to leakage from the strong ATS resonance in the $\sigma\sigma'$ channel. Leakage occurs as the analyser crystal is not aligned at exactly $2\theta_A = 90°$, and hence the $\sigma\sigma'$ signal in the nominal $\sigma\pi'$ polarisation channel is not fully suppressed.

---

[1] On resonance, when core electrons are promoted to the conduction band, a sensitivity to the local environment of the absorbing atom is achieved. When this local environment is not spherical, the x-ray susceptibility to photon polarisation will also be anisotropic on an atomic level. This is the origin of anisotropic tensor susceptibility (ATS) scattering [156].

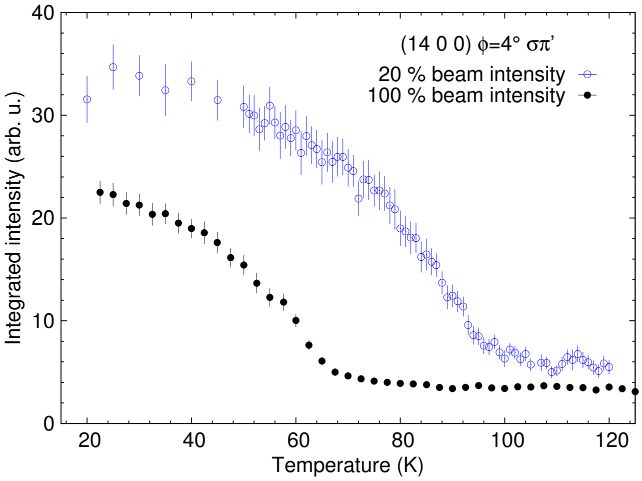

Figure 4.4: Temperature dependence of magnetic (14 0 0) reflection showing substantial beam heating of the sample. The black, filled data points are taken without attenuation, and the blue, open data points are taken with 20% beam intensity.

We observed substantial beam heating of the $Sm_2Ir_2O_7$ sample. Figure 4.4 shows the temperature dependence of the magnetic (14 0 0) reflection, using the full beam intensity and a beam attenuated to 20% transmission. With full beam intensity, heating in excess of 30 K (at nominal 90 K) occurs. In order to quantify any remaining beam heating at 20% beam intensity, we further attenuated the beam to 1% of the full intensity at a nominal temperature of 90 K. With 1% transmission, the integrated intensity of a rocking curve at 90 K increased by a factor of $\sim$ 1.57 compared to 20% beam intensity. As it is not feasible to perform a temperature dependence with 1% beam intensity, we used the fitted power law to estimate beam heating of $\sim$ 11.8 K at 20% beam intensity at nominal 90 K, and corrected the data accordingly. Precise estimates of the transition temperature can therefore not be made with our data.

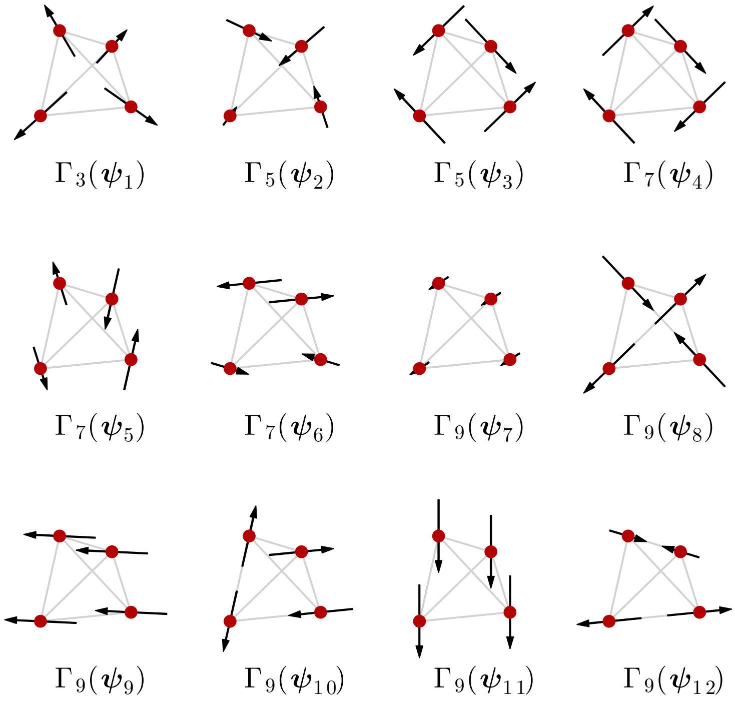

$\Gamma_3(\boldsymbol{\psi}_1)$ $\Gamma_5(\boldsymbol{\psi}_2)$ $\Gamma_5(\boldsymbol{\psi}_3)$ $\Gamma_7(\boldsymbol{\psi}_4)$

$\Gamma_7(\boldsymbol{\psi}_5)$ $\Gamma_7(\boldsymbol{\psi}_6)$ $\Gamma_9(\boldsymbol{\psi}_7)$ $\Gamma_9(\boldsymbol{\psi}_8)$

$\Gamma_9(\boldsymbol{\psi}_9)$ $\Gamma_9(\boldsymbol{\psi}_{10})$ $\Gamma_9(\boldsymbol{\psi}_{11})$ $\Gamma_9(\boldsymbol{\psi}_{12})$

Figure 4.5: Symmetry-allowed $\mathbf{k} = \mathbf{0}$ magnetic structures of Ir site of the pyrochlore lattice, as described in Ref. [160].

Figure 4.5 shows symmetry-allowed $\mathbf{k} = \mathbf{0}$ magnetic structures, which can be classified in four irreducible representations $\Gamma_{3,5,7,9}$ with twelve associated basis vectors $\boldsymbol{\psi}_i$ [160]. All four irreducible representations can give rise to magnetic scattering from forbidden $(h00)$ reflections in the $\sigma\pi'$ channel, although some individual basisvectors do not contribute (see Appendix B). To make further progress, we examine the magnetic structure factor through the REXS cross-sections. Fig. 4.6(a) shows the integrated intensity of the (14 0 0) reflection in $\sigma\pi'$ polarisation (using an incident energy of 11.214 keV) as a function of azimuthal angle ϕ. The sinusoidal variation observed originates from ATS scattering ($\propto \sin^2 2\phi$). Additionally, a temperature dependent intensity offset of similar magnitude to the ATS scattering is present, originat-

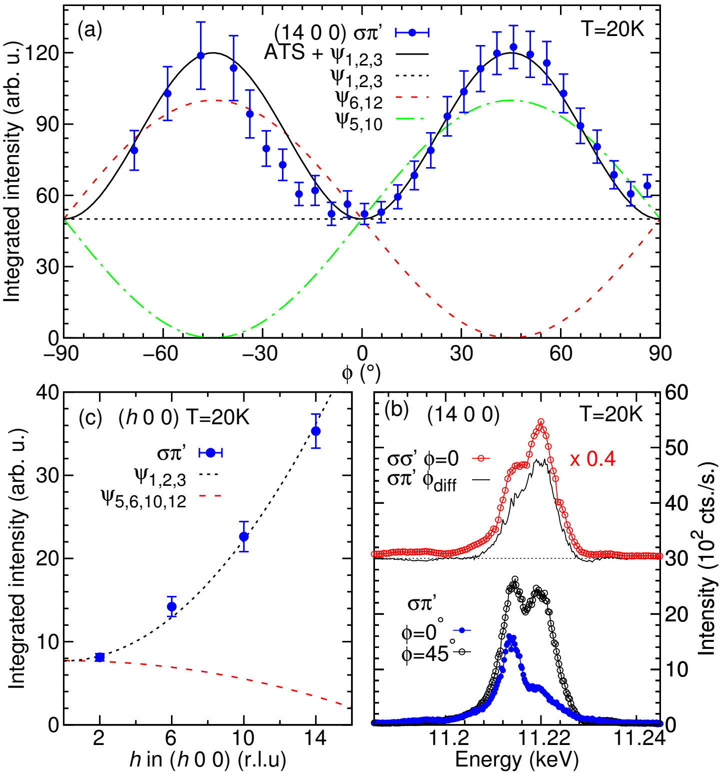

Figure 4.6: Analysis of REXS cross-sections of $Sm_2Ir_2O_7$. (a) Azimuthal dependence of integrated intensity of the (14 0 0) reflection in $\sigma\pi'$ polarisation. The solid line is the calculated ATS and magnetic scattering $\boldsymbol{\psi}_{1,2,3}$, dotted lines are calculated magnetic contributions of basis vectors $\boldsymbol{\psi}_i$. (b) Energy dependence of the (14 0 0) reflection in $\sigma\pi'$ polarisation at azimuthal angles $\phi = 0°$ and $\phi = 45°$ (bottom). The corresponding difference signal is proportional to the resonance at $\phi = 0°$ in the nonmagnetic $\sigma\sigma'$ polarisation channel (top). (c) Integrated intensity of space group forbidden ($h00$) reflections, plotted with calculated intensities of basis vectors $\boldsymbol{\psi}_i$.

ing from magnetic scattering. Fig. 4.6(b) shows that the additional spectral weight at $\phi = 45°$ in $\sigma\pi'$ (ATS + magnetic resonance) shares the same energy dependence as the pure ATS resonance in $\sigma\sigma'$, confirming that the magnetic contribution to the resonance remains constant as a function of azimuth.

The absence of intensity variation with ϕ suggests that the magnetic structure factor lies parallel to the scattering vector. This is also reflected in the intensities of magnetic ($h00$) reflections, which increase with $\sim \sin^2\theta \propto h^2$ [Fig. 4.6(c)]. It is only for basis vectors belonging to irreducible representations Γ_3 ($\boldsymbol{\psi}_1$) and Γ_5 ($\boldsymbol{\psi}_2, \boldsymbol{\psi}_3$) that the magnetic structure factor lies parallel to $\mathbf{Q}$=($h00$) (see Appendix B). We therefore conclude that the magnetic structure must be either AIAO (Γ_3, moments along local z axis) or an xy antiferromagnet (Γ_5, moments within local xy planes). Studying other forbidden reflections cannot yield further information to distinguish between these two cases.

In section 3.4, we have demonstrated that the intensity of ATS and magnetic contributions to forbidden ($h00$) reflections allows to estimate the size of the ordered moment in pyrochlore iridates. For pyrochlore iridates, the compressive trigonal field and spin-orbit coupling are roughly of equal magnitude (yielding $C_f \sim 1/2$, see section 5.3). This corresponds to a single-ion magnetic moment of $\sim 1.6\,\mu_B$ for which the ratio of resonant magnetic to resonant charge contributions becomes $I_m/I_{ats}(h00) \sim 5$. For the (14 0 0) reflection of $Sm_2Ir_2O_7$, the azimuthal scan shows a ratio of $I_m/I_{ats} \sim 1$. We therefore estimate that in $Sm_2Ir_2O_7$ the ordered Ir magnetic moment is reduced from its single-ion value to $\sim 0.3\,\mu_B$ at 10 K. This value compares well to a neutron scattering study on $Nd_2Ir_2O_7$ where a magnetic moment of $0.34(1)\,\mu_B$ was found [72]. This suggests that the relative strength of resonant charge and resonant magnetic intensities can be indeed be used to estimate the absolute magnetic moment size with REXS. There are however a few assumptions necessary to arrive at this number. First, we assume that our single-ion model allows an accurate description of the electronic ground state. It is conceivable that a more sophisticated treatment of the low-energy electronic structure could alter the estimated size of the magnetic moment, the extent of which is difficult to quantify. Additionally, in modelling the ATS resonance, we assume transitions only to $5d(t_{2g})$ states, whereas the data show two resonances, to $5d(t_{2g})$ and $5d(e_g)$ states. While we have set the energy to the maximum of the t_{2g} resonance, it is possible that some contribution from e_g states exists, which would not be accounted for in our model. The value we obtain here should thus be considered a rough estimate.

4.1.3 XRMS at high magnetic fields

In the neighbouring pyrochlore iridate $Nd_2Ir_2O_7$, a metal-insulator transition was discovered under an applied magnetic field of 10 T [161, 162]. This MIT occurred only when the magnetic field was along the [001] direction, and is surprising given a charge gap of 45 meV (note that 10 T $\sim$ 1 meV). It was proposed that a field along [001] polarises the Nd moments from an all-in all-out to a 2-in 2-out configuration, whereas any other field direction leads to a 3-in 1-out state. Tian *et al.* [162] then suggested a Kondo interaction between Nd and Ir spins that contributes to the charge gap. When the Nd moments adopt a 2-in 2-out configuration, the condensation energy from the Kondo term is lost, and the Ir spins are no longer ordered. Conversely, Ueda *et al.* [161] proposed that Ir spins will also be polarised to a 2-in 2-out state. There is thus a need to establish the magnetic structure of $Nd_2Ir_2O_7$ at high magnetic fields. Here, we examine the feasibility of such an experiment by studying the magnetic structure of $Sm_2Ir_2O_7$ with REXS at the Ir L_3 edge under magnetic fields up to 12 T. The experiment was performed at beamline P09, PETRA III, in April 2016.

Experimental method

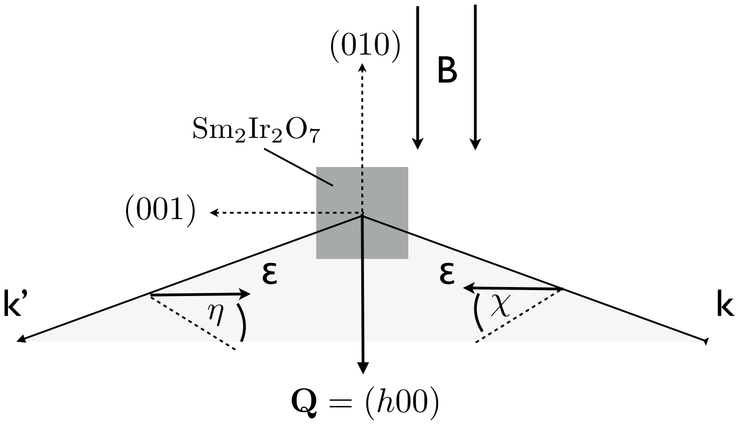

Figure 4.7: Schematic of experimental setup for high-field REXS of $Sm_2Ir_2O_7$. **B** shows the direction of the magnetic field, χ is the rotation of the phase-plate ensemble and η the rotation of the linear polarimeter. Rotating χ corresponds to changing the angle of incoming linear polarisation; rotating η selects the component of outgoing linear polarisation that will reach the detector.

REXS experiments at high magnetic fields were performed on beamline P09 at PETRA III [122]. Compared to a regular REXS experiment, the high-field setup imposes strict constraints on the scattering geometry. In particular, the available diffractometer rotations are restricted to θ and 2θ circles, such that the azimuthal rotation, around the scattering vector $\mathbf{Q}$, is fixed.

Figure 4.7 shows the experimental geometry. By scattering from $(h00)$ reflections, the magnetic field can be projected along an arbitrary direction within the (100) plane of $Sm_2Ir_2O_7$. Changing the magnetic field direction implies a sample rotation, which changes the azimuthal angle. This coupling of magnetic field direction to azimuthal angle limits the amount of information obtainable. This can be somewhat alleviated by varying the polarisation state of the incident x-ray beam. Here, we will rotate the angle of incoming linear polarisation to obtain additional information on the REXS cross-sections. Additionally, a linear polarimeter will be used on the outgoing beam, providing full linear polarisation analysis (FLPA).

Beamline P09 uses a double phase-plate retarder setup to generate linearly polarised x-rays at an arbitrary angle [163]. At the Ir L_3 edge, two 400 μm type IIa Diamond phase plates are operated in quarter-wave plate condition. This is equivalent to a single wave-plate in half-wave plate condition, but has the advantage of a higher degree of linear polarisation. The phase-plates were aligned such that the rotation angle χ of the phase plate ensemble should be equivalent to the angle of the linear polarisation, with $2\chi = 0^\circ$, 90° corresponding to linear polarisation parallel (π) and perpendicular (σ) to the scattering plane. For the scattered beam, a Au (333) polarisation analyser was used, which only diffracts the linear polarisation component parallel to its rotation angle η onto the detector.

Full linear polarisation analysis

It is convenient to use Poincaré-Stokes parameters to describe the polarisation state of arbitrarily polarised light [164]. These consist of four parameters $\{I, P_1, P_2, P_3\}$, where I is the intensity, P_1, P_2 encapsulate the linear polarisation state and P_3 the degree of circular polarisation. The polarisation state of the x-ray beam can then be described by the coherency matrix

$$\rho = \mathbf{1} + \boldsymbol{\sigma} \cdot \mathbf{P} = \begin{pmatrix} 1 + P_1 & P_2 - iP_3 \\ P_2 + iP_3 & 1 - P_1 \end{pmatrix}$$

where $\boldsymbol{\sigma}$ are the Pauli matrices. The Poincaré-Stokes parameters can be obtained through $I = \mathrm{tr}(\rho)$ and $P_i = \frac{1}{I}\mathrm{tr}(\sigma_i \cdot \rho)$. Any optical element, such as diffraction from a magnetic Bragg peak, can be described by a 2×2 Jones matrix M in the $\sigma\pi$ basis. The polarisation state of the beam after the sample is given by $\rho' = M\rho M^\dagger$. A linear polarimeter can be then used to determine P_1' and P_2' of the scattered beam. We first rotate into the reference frame of the analyser via R and then scatter of the Bragg reflection of the analyser through M_A, where

$$R = \begin{pmatrix} \cos\eta & -\sin\eta \\ \sin\eta & \cos\eta \end{pmatrix}, \; M_A = \begin{pmatrix} 1 & 0 \\ 0 & \cos 2\theta_A \end{pmatrix}$$

where $2\theta_A$ is the Bragg angle of the analyser. The polarisation state of the beam at the detector is $\rho'' = M_A(R\rho' R^\dagger)M_A^\dagger$, and we find the intensity

$$I = \mathrm{tr}(\rho'') \propto (S + P_1' \cos 2\eta + P_2' \sin 2\eta) \tag{4.1}$$

where $S = (1+\cos^2 2\theta_A)/\sin^2 2\theta_A$. Thus, by rotating the polarisation analyser in η, the Poincaré-Stokes parameters P_1' and P_2' can be determined. This will be referred to as a "Stokes" scan.

Characterisation of direct beam

We first characterised the polarisation of the incident beam. Ideally, phase plate angles of $2\chi = 0(90)^\circ$ should correspond to linear polarisation parallel (perpendicular) to the horizontal scattering plane, and we expect the Poincaré-Stokes parameters:

$$\begin{aligned} P_1 &= \cos 2\chi \\ P_2 &= \sin 2\chi \\ P_3 &= 0 \end{aligned} \tag{4.2}$$

To determine the experimentally achieved Poincaré-Stokes parameters, we performed Stokes scans of the direct beam as a function of χ: For each χ value, the polarisation analyser was rotated in 15° steps in η, and for each η value a rocking curve of the analyser was taken to obtain the integrated intensity (to minimise artifacts from the instrumental resolution). This provides the direct beam intensity as a function of η, which can be used to determine P_1 and P_2 via Eqn. 4.1.

Figure 4.8 shows the direct beam Poincaré-Stokes parameters P_1 and P_2 as a function of phase-plate angle χ, compared with the ideal case of Eqn. 4.2. We find that the polarisation of the direct beam follows the expected behaviour, and maintains a degree of linear polarisation, $P_{\mathrm{lin}} = \sqrt{P_1^2 + P_2^2}$, of at least 85%.

It is interesting to consider the "remaining" degree of polarisation. Since the beam is not fully linearly polarised at all values of χ, two possibilities exist: Either the beam acquires some circular polarisation, or it is only partially polarised. Within our experimental setup, we cannot distinguish between the two cases. The first case could arise from a misalignment of the phase plates. If we assume that the beam remains fully polarised, the degree of circular

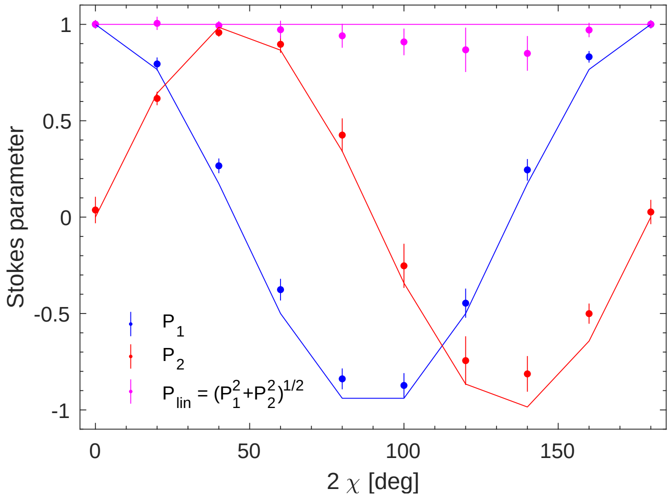

Figure 4.8: Measured Poincaré-Stokes parameters P_1 (blue circles) and P_2 (red circles) of the direct beam at the Ir L_3 edge (11.215 keV), as a function of phase plate rotation χ. P'_{lin} (magenta) is the deduced degree of linear polarisation. The solid lines are calculated Poincaré-Stokes parameters of an ideal setup.

polarisation, P_3, can be found via $P_1^2 + P_2^2 + P_3^2 = 1$. However, the sign of P_3 remains elusive. This leaves the unsatisfactory approach of choosing the sign of P_3 to best fit the data. The second case, of a beam becoming partially polarised, is common when operating phase-plates at high x-ray energies, where the phase-plates become too thin to provide a fully polarised beam [165].

In reality, it is likely that both cases apply to some extent. While introducing circular polarisation in the beam ($P_3 \neq 0$ with $P_1^2+P_2^2+P_3^2 = 1$) could improve the fit to the data, the assumption of a fully-polarised beam seems unlikely[2]. We hence only consider the case of a partially polarised beam with no circular polarisation ($P_3 = 0$ with $P_1^2 + P_2^2 + P_3^2 \neq 1$), using the measured P_1 and P_2 parameters of the direct beam.

FLPA without magnetic field

For all-in all-out magnetic order and ATS scattering from charge-forbidden ($h00$) reflections ($h = 4n+2$), we find the REXS amplitude (see Appendix B):

$$\mathcal{A}(h00) = \begin{pmatrix} F_{ats}\cos 2\phi & \sin\theta[iF_m - F_{ats}\sin 2\phi] \\ \sin\theta[iF_m + F_{ats}\sin 2\phi] & F_{ats}\sin^2\theta\cos 2\phi \end{pmatrix}$$

---

[2] An alternative would be to chose both the magnitude and sign of P_3 as a function of χ to best fit the full set of data, under the constraint of $P_1^2 + P_2^2 + P_3^2 \leq 1$.

where F_m and F_{ats} quantify the strength of magnetic and ATS contributions, respectively, θ the Bragg angle, and ϕ the azimuthal angle (defined as $\phi = 0°$ when the (011) direction is in the scattering plane). In our experiment, we aligned the magnetic field parallel to the crystallographic [001] direction, which dictates an azimuthal angle of $\phi = 45°$. By computing $\mathcal{A}\rho\mathcal{A}^\dagger$, we find the outgoing Poincaré-Stokes parameters:

$$\begin{aligned} P_1' &= -P_1 \\ P_2' &= \frac{-2P_3F_{ats}F_m - P_2F_{ats}^2 + P_2F_m^2}{F_{ats}^2 + F_m^2} \\ P_3' &= \frac{-2P_2F_{ats}F_m + P_3F_{ats}^2 - P_3F_m^2}{F_{ats}^2 + F_m^2} \end{aligned} \tag{4.3}$$

Of particular interest here are interference effects of ATS and magnetic scattering, terms proportional to $F_{ats}F_m$. We find that the presence of ATS and magnetic scattering can induce circular polarisation ($P_3' \neq 0$) in a purely linearly polarised beam ($P_3 = 0$) and vice versa. Indeed, this interference effect was used to obtain sensitivity to time-reversal magnetic domains in $Cd_2Os_2O_7$ [166] (as the interference terms are proportional to F_m as opposed to F_m^2).

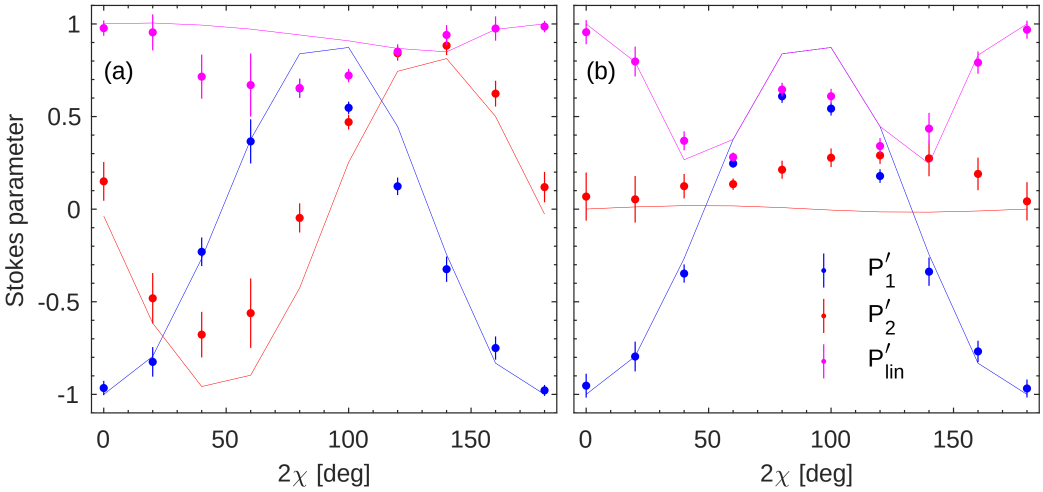

Figure 4.9: Measured (circles) and calculated (solid lines) Poincaré-Stokes parameters P_1' (blue) and P_2' (red) after scattering from the (10 0 0) reflection of $Sm_2Ir_2O_7$ at (a) T = 150 K and (b) T = 5 K, as a function of phase plate rotation χ. P_{lin}' (magenta) is the deduced degree of linear polarisation.

We first discuss the FLPA of REXS without magnetic fields. Figure 4.9 shows the measured Poincaré-Stokes parameters P_1' and P_2' after scattering from the (10 0 0) reflection of $Sm_2Ir_2O_7$ at 150 K and 5 K. At 150 K, we only expect an ATS contribution to the reflection. Using the measured Poincaré-Stokes parameters P_1 and P_2 of the direct beam, we computed the expected polarisation state after scattering from an ATS reflection. The calculations qualitatively reproduce the data.

At 5 K, the presence of magnetic order alters the polarisation state of the outgoing beam. Most strikingly, P_{lin} displays minima at $2\chi \approx 45°$ and $135°$. This originates from the interference of ATS and magnetic scattering. At these χ values, the incident polarisation parameter P_2 reaches a maximum (Fig. 4.8), such that interference terms become significant (Eqn. 4.3) and the scattered beam acquires circular polarisation. Furthermore, we find that $P_2' \approx 0$ at all values of χ. Appealing to Eqn. 4.3, this implies that $F_{ats} \sim F_m$, which is indeed as was found in the previous REXS experiment.

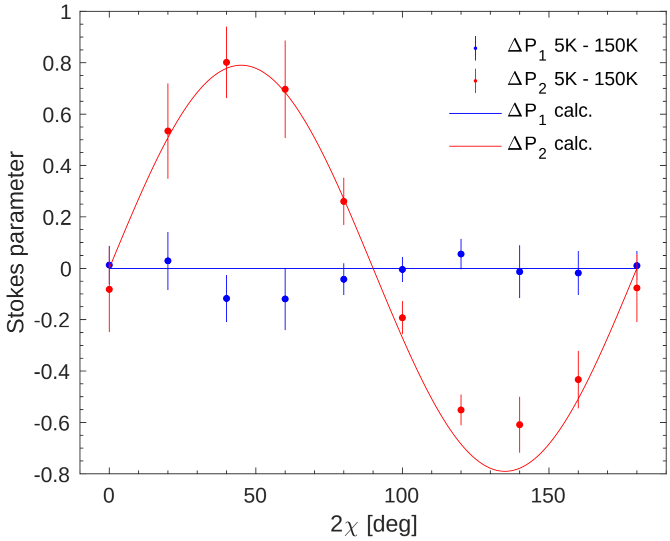

Figure 4.10: Measured (circles) and calculated (solid lines) temperature difference in Poincaré-Stokes parameters, $\Delta P_1'$ (blue) and $\Delta P_2'$ (red), of the (10 0 0) reflection of $Sm_2Ir_2O_7$ at B = 0 T as a function of phase-plate angle χ. This signal is a direct signature of the magnetic structure, and can be well described by AIAO order.

At both temperatures, there are clear discrepancies between measured and calculated Poincaré-Stokes parameters. This is particularly evident at $\chi \sim 90°$, where the σ polarisation of the undulator should be completely converted to π polarisation. This indicates that the phase-plate ensemble introduces systematic errors, such as circular incident polarisation. However, the characterisation of the direct beam suggests that any amount of circular polarisation should be fairly small, and is hence unlikely to fully account for the observed differences.

As the discrepancies between measured and calculated polarisation states appear at both temperatures, this indicates a systematic error, unrelated to the magnetic contribution at low temperature. To eliminate systematic errors in the measurement, we subtracted high-temperature from low-temperature Poincaré-Stokes parameters. The relative change, $\Delta P_1'$ and $\Delta P_2'$, should then be a direct signature of the magnetic contribution. Fig. 4.10 shows the measured and calculated difference signal. We find that the data can be well reproduced by an AIAO magnetic structure using $F_{ats} \sim F_m$.[3]

FLPA at high magnetic fields

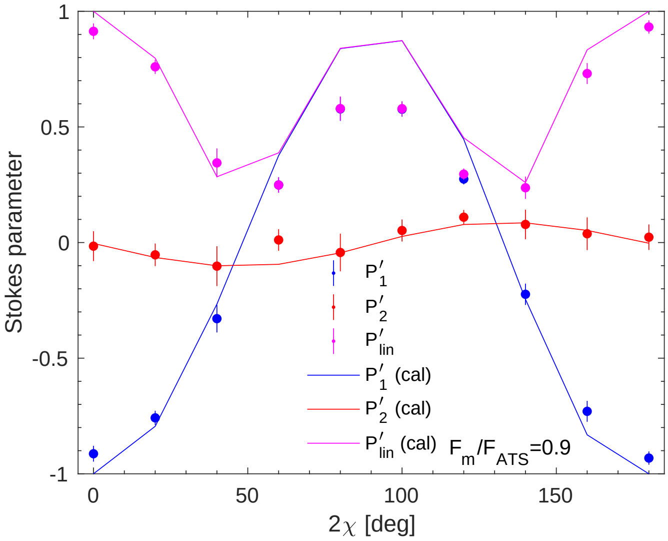

Figure 4.11: Measured (circles) and calculated (solid lines) Poincaré-Stokes parameters P_1' (blue) and P_2' (red) of the (10 0 0) reflection of $Sm_2Ir_2O_7$ at T = 5 K and B = 12 T as a function of phase plate angle χ. P_{lin}' (magenta) is the deduced degree of linear polarisation.

Having established that the polarisation dependence of the (10 0 0) reflection can be roughly described by ATS and AIAO magnetic contributions, we now discuss the data obtained at magnetic fields parallel to the [001] crystal direction. At T = 5 K, we incremented the magnetic field in 1 T steps. The intensity of the (10 0 0) reflection showed no change up to an applied of field of 12 T.

---

[3] The information obtained here is that the magnetic structure factor lies parallel to **Q**, which is the same result as for the previous REXS experiment. As such, the data could again be equally well described by AIAO and xy antiferromagnetic structures.

Figure 4.11 shows the Poincaré-Stokes parameters P_1' and P_2' obtained from Stokes scans of the (10 0 0) reflection at 12 T. Again, the data can be adequately described by ATS and AIAO magnetic contributions. Given that the magnetic field (12 T $\sim$ 0.7 meV) is small compared to the Ir exchange ($J \sim 27$ meV, $D \sim 5$ meV, see section 5.2.1), this is perhaps not surprising. The magnitude of the magnetic contribution appears reduced ($F_m/F_{ats} \sim 0.9$), which may indicate a small canting of the Ir moments, but this cannot be confirmed within the quality of the data.

4.2 $Nd_2Ir_2O_7$

A REXS experiment was performed at the Ir L_3 edge of $Nd_2Ir_2O_7$, at beamline ID20, ESRF in February 2017. We found the onset of long-range, $\mathbf{k} = \mathbf{0}$ magnetic order below 4 K.

4.2.1 Bulk properties

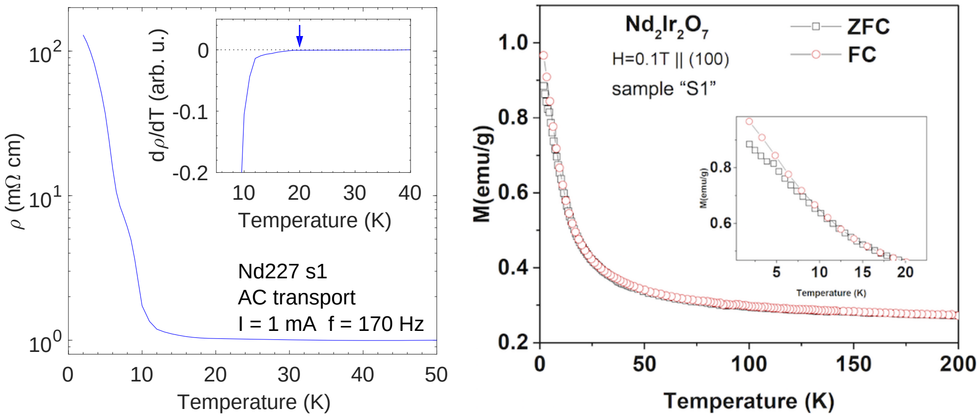

Figure 4.12: Temperature dependence of resistivity (left) and magnetisation (right) of $Nd_2Ir_2O_7$ single-crystal. Data courtesy of M. Rahn and D. Prabhakaran.

The magnetic and electronic properties of $Nd_2Ir_2O_7$ are highly sensitive to growth conditions and resulting stoichiometry [69]. For powder samples at nominal stoichiometry, the literature suggests that a concomitant MIT and antiferromagnetic transition at 35 K [34]. Neutron powder diffraction has confirmed that both Nd and Ir sites order in an AIAO magnetic structure, with moment sizes of 1.27(1) μ_B and 0.34(1) μ_B at 1.8 K, respectively [72]. If there are excess rare-earth ions populating Ir sites, even small deviations of

1-2% in the Ir/Nd ratio suppress the MIT temperature by 10-20 K [78]. Larger deviations result in samples that are conducting at all temperatures, with no signatures of long-range magnetic order [69, 74].

The $Nd_2Ir_2O_7$ samples described here were grown by the self-flux method [158] by D. Prabhakaran at the University of Oxford. Bulk characterisation was performed by M. Rahn and D. Prabhakaran. Figure 4.12 shows the resistivity and magnetisation as a function of temperature, from which we estimate magnetic and metal-insulator transitions occuring at approximately 10 K. In Ref. [78], the MIT temperature was deduced from the first derivative of the resistivity, $d\rho/dT$, which corresponded to the opening of a spectral gap measured by ARPES. This measure would place the MIT of our sample at approximately 20 K (see inset Fig. 4.12). By comparison with the samples studied in Ref. [78], we estimate a small deviation of 1% in the Ir/Nd ratio or our sample.

4.2.2 XRMS

Method

XRMS was performed at beamline ID20, ESRF [106]. As this beamline is primarily designed for RIXS experiments, it does not permit polarisation analysis of the outgoing beam or an azimuthal rotation of the sample. A horizontal scattering geometry was used, such that the incident linear polarisation was parallel to the scattering plane (π polarisation). The $Nd_2Ir_2O_7$ sample was mounted with GE varnish on the coldfinger of a Dynaflow He exchange gas cryostat, the (100) and (011) directions were in the horizontal scattering plane.

Results

At the Ir L_3 edge, initially no magnetic scattering was found at 4 K. In order to observe the onset of magnetic order, it was necessary to strongly attenuate the incident beam. By tracking the intensity of the antiferromagnetic peak as a function of beam attenuation, we found that an attenuation factor of ~ 28 (700 μm Al foil) removes the majority of the heat load. Fig. 4.13 shows the intensity of the forbidden (14 0 0) reflection with this setup. We find a clear increase in intensity below 5 K, a power law fit to the data suggests a magnetic transition at ~ 4.7 K.

As beamline ID20 is designed for RIXS experiments, it was not possible to analyse the polarisation of the outgoing beam or perform azimuthal scans.

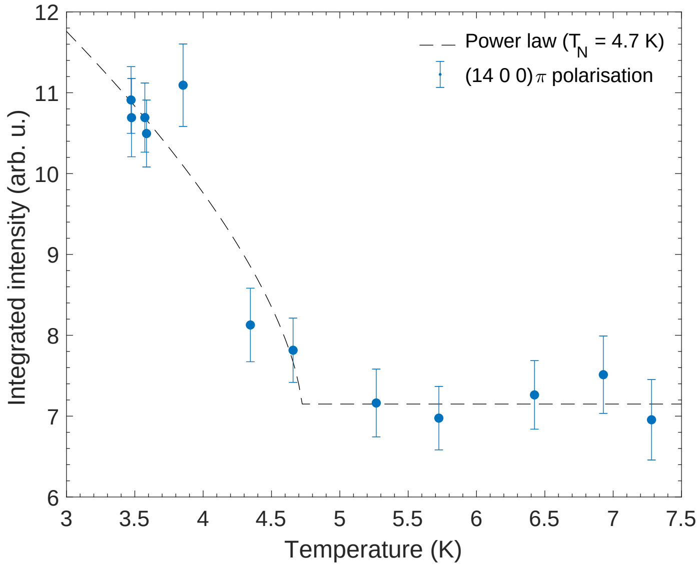

Figure 4.13: Temperature dependence of integrated intensity of (14 0 0) reflection of $Nd_2Ir_2O_7$ at the Ir L_3 edge with incident π polarisation. The incident beam was attenuated by a factor of ~ 28 using 700 μm of Al foil.

Thus our data by itself only confirms $\mathbf{k} = \mathbf{0}$ magnetic order, which could be compatible with various magnetic structures. However, as neutron scattering has previously shown that the Ir moments order in an AIAO fashion in $Nd_2Ir_2O_7$ [72], it is likely that our sample adopts the same magnetic structure.

Our data indicate that magnetic and metal-insulator transitions do not occur concomitantly in $Nd_2Ir_2O_7$. However, we cannot discard the possibility of some beam heating remaining even at high attenuations. It should be noted that on the RIXS beamline ID20 the secondary monochromator already drastically reduces the incident photon flux compared to a REXS beamline with only a primary monochromator. As such, with an attenuated beam, heating in excess of 5 K seems unlikely. Indeed, the magnetisation data indicate a transition between 5-10 K, which should be considered consistent within the uncertainty of our REXS data.

It is interesting to compare these results with ARPES data of $Nd_2Ir_2O_7$ by Nakayama *et al.* [78]. In this study, the MIT temperature was estimated from the first derivative of the resistivity, which corresponded to the opening of a spectral gap measured by ARPES. The authors then suggested two regimes for the MIT: At temperatures close to the MIT, a Slater picture is applicable, where the opening of a gap is driven by magnetic oder. Upon lowering the temperature, the insulating behaviour evolves into a Mott regime, where electronic correlations are primarily responsible for the electronic gap, potentially assisted by the Nd site ordering.

Our data are somewhat at odds with this scenario. By using the first derivate of the resistivity, we would estimate a MIT temperature of ~ 20 K in our sample (see inset Fig. 4.12). The magnetic order on the Ir site only appears between 5-10 K. This suggests that the MIT belongs in a Mott regime at all temperatures, where magnetic order arises only as a secondary effect. However, our data are insufficient to confirm this hypothesis. Future experiments that provide a more detailed temperature dependence of the magnetic order, for example by using a REXS setup dedicated to low-temperature measurements [122], could be of interest in this context.

4.3 $Tb_2Ir_2O_7$

A REXS experiment was performed to examine the magnetic structure of the pyrochlore iridate $Tb_2Ir_2O_7$ at beamline I16, Diamond in July 2016. We found the onset of long-range $\mathbf{k} = \mathbf{0}$ magnetic order below 70 K. Analysis of the REXS cross-section suggests all-in all-out or xy antiferromagnetic order. The ratio of resonant charge and resonant magnetic scattering intensities indicates an ordered magnetic moment of $\sim 0.06\,\mu_B$ at 5 K.

4.3.1 Bulk properties

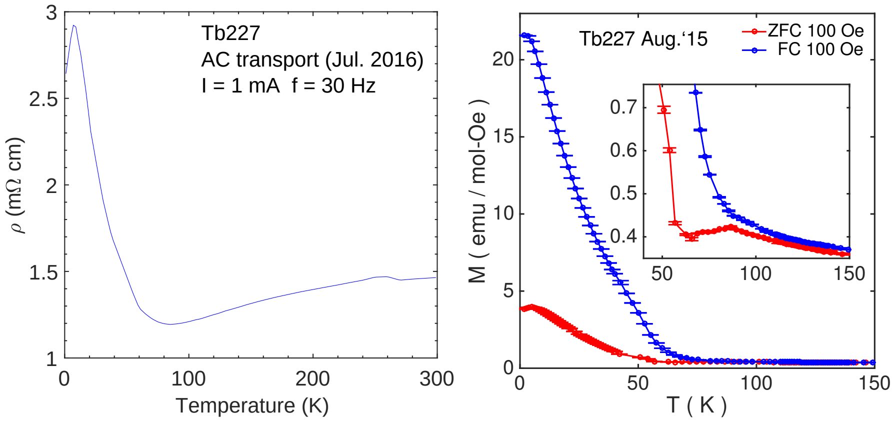

Figure 4.14: (Left) Resistivity of $Tb_2Ir_2O_7$ single-crystal as a function of temperature. (Right) Temperature dependence of magnetisation of multiple $Tb_2Ir_2O_7$ single-crystals. Data courtesy of M. Rahn and D. Prabhakaran.

For $Tb_2Ir_2O_7$, literature magnetisation data suggest that the Ir site orders at 130 K [34, 71]. Literature resistivity data show insulating behaviour at all temperatures, with a small anomaly at the magnetic transition [34]. The magnetic structure of $Tb_2Ir_2O_7$ was studied by neutron powder diffraction [71]. It was found that the Tb moments order in an AIAO structure below 40 K, reaching a moment size of $4.9\,\mu_B$ at 10 K. The temperature dependence suggests that the Tb magnetic moment is induced by the Ir site ordering at 130 K. The weaker Ir moment could not be directly detected, giving an upper boundary on the moment size of $0.2\,\mu_B$ at 10 K.

Single crystals of $Tb_2Ir_2O_7$ were grown by D. Prabhakaran at the University of Oxford, using the self-flux method, as described in Ref. [158]. Bulk characterisation was performed by M. Rahn and D. Prabhakaran. Figure 4.14 shows the magnetisation and resistivity of $Tb_2Ir_2O_7$ as a function of temperature. The bifurcation of FC-ZFC cooled magnetisations occurs at approximately 75 K, strongly reduced from the literature value of 130 K. Furthermore, the resistivity appears significantly more metallic, with absolute values 2-3 orders of magnitude lower than the ones reported in literature powder samples [34]. The discrepancies between our samples and literature $Tb_2Ir_2O_7$ are suspected to arise from excess rare-earth ions populating Ir sites, resulting in an stoichiometry of $Tb_{2+x}Ir_{2-x}O_{7-y}$[4]. This would be supported by a somewhat enlarged lattice parameter at 300 K, in our sample $a = 10.25$ Å, compared to a literature value of $a = 10.23$ Å [71]. Additionally, annealing the $Tb_2Ir_2O_7$ sample in an oxygen atmosphere did not alter the bulk properties.

4.3.2 XRMS

Method

The setup and scattering geometry for REXS of $Tb_2Ir_2O_7$ on beamline I16, Diamond was largely identical to the setup for the REXS experiment on $Sm_2Ir_2O_7$. The incident polarisation was linear, perpendicular to the vertical scattering plane (σ polarisation). The polarisation of the scattered beam was analysed with a Au (333) crystal. The $Tb_2Ir_2O_7$ was mounted with GE varnish on the coldfinger of a Displex cryostat, such that (100) and (011) directions were in the scattering plane.

---

[4] Attempts were made by M. Rahn to quantify the Tb/Ir ratio using single-crystal x-ray diffraction. Within the uncertainty of the measurement, no deviation from a Tb/Ir ratio of 1 could be determined.

Results

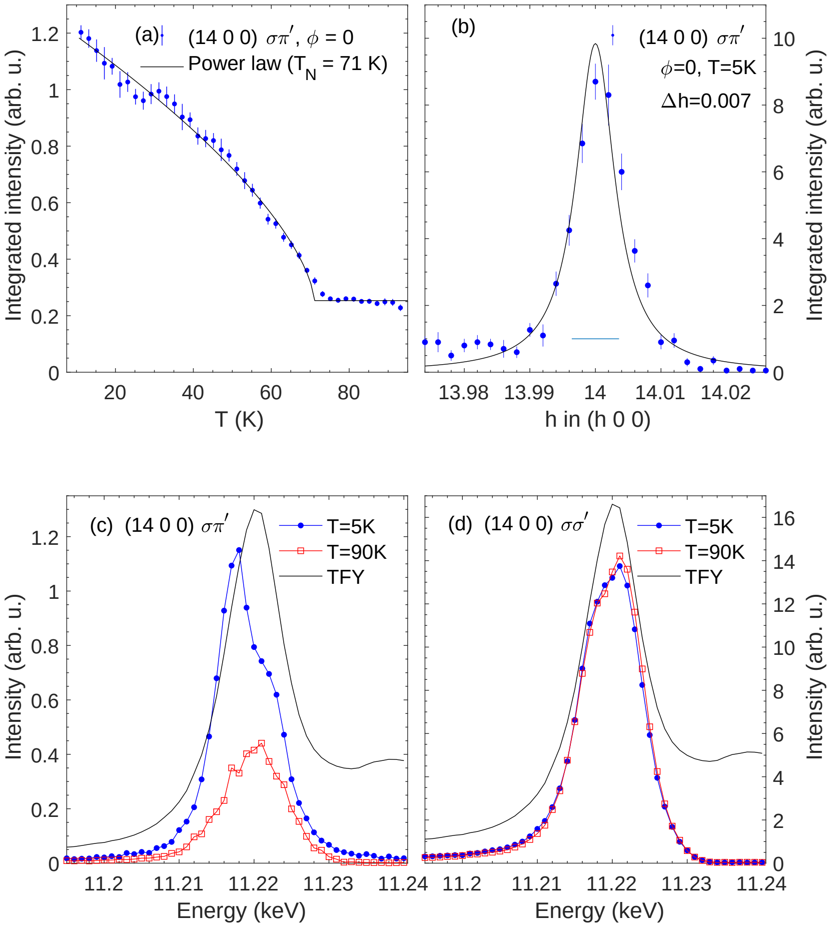

Figure 4.15: REXS data of $Tb_2Ir_2O_7$. (a) Temperature dependence of (14 0 0) reflection in the $\sigma\pi'$ polarisation (blue circles), at an incident energy of 11.215 keV. The solid black line is a power law fit to the data, yielding $T_N = 71$ K. (b) Reciprocal lattice scan along the h direction of (14 0 0) reflection (blue circles) and Lorentzian fit to the data (black solid line). (c, d) Energy dependence of (14 0 0) reflection in $\sigma\pi'$, $\sigma\sigma'$ polarisation at 5 K (blue circles) and 90 K (red squares). The data were corrected for self-absorption. The black solid line is the total fluorescence yield (TFY).

Figure 4.15 shows temperature, reciprocal space and energy dependences of the forbidden (14 0 0) reflection at the Ir L_3 edge. As previously, the ATS contribution in the magnetically-relevant $\sigma\pi'$ polarisation channel was suppressed by bringing the (011) direction into the vertical scattering plane. In this configuration, the temperature dependence of the (14 0 0) reflection follows a power law behaviour, suggesting a magnetic origin of the scattering, with a Néel temperature of 71 K (the data were corrected for beamheating of ~ 7

K[5]). The remaining intensity above the ordering temperature mainly originates from leakage of the strong ATS resonance in the $\sigma\sigma'$ channel. Reciprocal lattice scans confirm long-range magnetic order, with a correlation length of at least a few hundred Å [Fig. 4.15(b)]. The magnetic origin of the signal is further supported by the energy dependence of the resonant signal. In the $\sigma\sigma'$ channel, we find a two peak structure, usually attributed to excitations to t_{2g} and e_g levels, which remains temperature independent [Fig. 4.15(d)]. Conversely, the energy profile in the $\sigma\pi'$ channel shows a strong, temperature dependent enhancement at the incident energy corresponding to transition to t_{2g} states (about 3 eV below the absorption maximum) [Fig. 4.15(c)]. At high temperature, the energy profile resembles pure ATS scattering seen in $\sigma\sigma'$ polarisation, suggesting that it originates from leakage of the strong ATS signal in the $\sigma\sigma'$ polarisation. We conclude that below 71 K, long-range $\mathbf{k} = \mathbf{0}$ magnetic order appears in $Tb_2Ir_2O_7$.

As described above, detecting a magnetic signal on forbidden $(h00)$ reflections establishes a $\mathbf{k} = \mathbf{0}$ propagation vector, which is compatible with different magnetic structures. To further distinguish candidate magnetic structures, we determined the orientation of the magnetic structure factor with an azimuthal scan. Figure 4.16 shows the integrated intensities of rocking curves of the (14 0 0) reflection in $\sigma\pi'$ polarisation as a function of azimuthal angle ϕ at 5 K and 100 K. The strongest contribution to the scattered intensity at both temperatures originates from the sinusoidal ATS scattering ($\propto \sin^2 2\phi$). Additionally, there is temperature dependent scattering, constant in ϕ. The latter is the magnetic contribution, which shows that the magnetic structure factor lies parallel to the scattering vector $\mathbf{Q}$, and is only compatible with AIAO (Γ_3) or xy antiferromagnetic order (Γ_5).

As for $Sm_2Ir_2O_7$, the relative intensities of ATS and magnetic contributions allow to estimate the absolute moment size in $Tb_2Ir_2O_7$. As the strength of the trigonal field is fairly constant for all pyrochlore iridates, the single-ion calculation would again predict $I_m/I_{ats} \sim 5$ and a moment size of $\sim 1.6\,\mu_B$. Here, the azimuthal scan of the (14 0 0) reflection shows a ratio of $I_m/I_{ats} \sim 1/5$ at 5 K. Thus for our $Tb_2Ir_2O_7$ sample, we estimate an ordered moment of only $\sim 0.06\,\mu_B$. This is consistent with an upper boundary of $0.2\,\mu_B$ reported by neutron diffraction on a (more stoichiometric) $Tb_2Ir_2O_7$ powder sample with $T_N \sim 130$ K [71].

---

[5] On beamline I16, the larger beamspot on the sample compared to beamline P09 ($\sim$ 200 x 50 μm^2 vs $\sim$ 50 x 20 μm^2) appears to reduce the heat load.

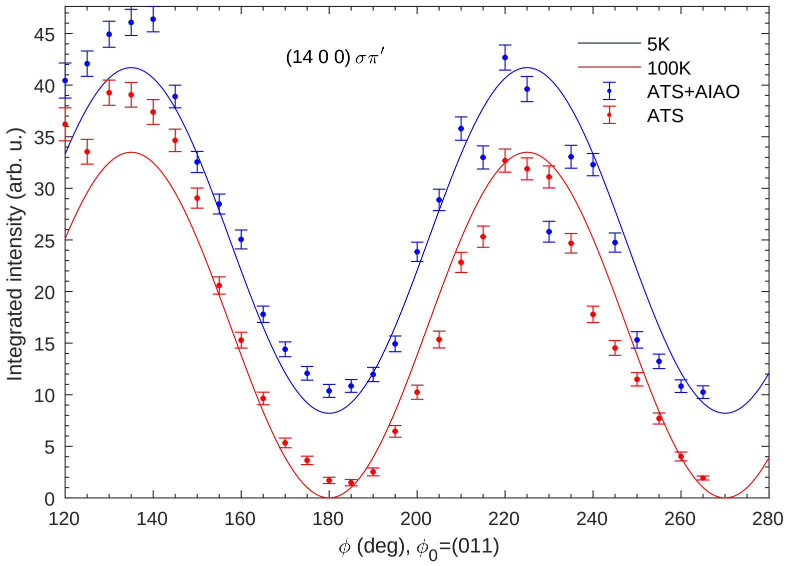

Figure 4.16: Azimuthal scan of (14 0 0) reflection of $Tb_2Ir_{2-x}O_7$ in $\sigma\pi'$ polarisation at 5 K (blue circles) and 100 K (red squares), at an incident energy of 11.215 keV. The solid lines are calculated intensities for ATS scattering and magnetic scattering from AIAO order (blue), and ATS scattering only (red).

As discussed previously, the largest error source for the calculated moment size is probably the assumption that the ATS intensity can be solely described by a $5d(t_{2g})$ resonance, whereas the data clearly show a contribution from a $5d(e_g)$ resonance. We have estimated this error by fitting Lorentzian functions to t_{2g} and e_g resonances. Using this model, the ATS intensity from the t_{2g} resonance would reduce by about 25%, in which case the size of the Ir magnetic moment increases to $\sim 0.08\,\mu_B$. While this is fairly imprecise, it gives an indication of the error associated with the estimated magnetic moment size.

It is interesting to compare these data to the results from $Sm_2Ir_2O_7$. First, the Néel temperature is substantially lower in $Tb_2Ir_2O_7$ (71 K vs 110 K). Second, the ordered moment size is significantly weaker ($0.06\,\mu_B$ vs $0.3\,\mu_B$). While the magnetic properties of $Sm_2Ir_2O_7$ agree with the literature data, in $Tb_2Ir_2O_7$ it is suspected that an excess of rare-earth ions exists, which suppress both the transition temperature and size of the ordered moment.

4.4 Conclusion

In this chapter, we examined the magnetic structure of the pyrochlore iridates $Sm_2Ir_2O_7$, $Nd_2Ir_2O_7$ and $Tb_2Ir_2O_7$ with REXS. All samples show long-range,

$\mathbf{k} = \mathbf{0}$ magnetic order, with ordering temperatures of 110 K (Sm), 4 K (Nd) and 71 K (Tb). For $Sm_2Ir_2O_7$ and $Tb_2Ir_2O_7$, analysis of the XRMS cross-sections reveals that the magnetic structure is either an AIAO (Γ_3) or an xy (Γ_5) antiferromagnet. While the data by itself cannot distinguish between these two possibilities, literature neutron diffraction studies strongly suggests that the magnetic structure is AIAO. Assuming that this is the case in our samples, by comparing resonant magnetic and resonant charge contributions, we find that the magnetic moment is strongly reduced from its single-ion value to $\sim 0.3\,\mu_B$ in $Sm_2Ir_2O_7$ and $\sim 0.06\,\mu_B$ in $Tb_2Ir_2O_7$.

While the magnetic and electronic properties of $Sm_2Ir_2O_7$ and $Nd_2Ir_2O_7$ agree with the literature, the $Tb_2Ir_2O_7$ sample studied here markedly differs, as is evidenced by the low resistance, the suppressed transition temperature and the weakened magnetic moment. This is suspected to arise from an excess of Tb ions that populate Ir sites, which results in a more weakly correlated state. This could be of interest in the context of the magnetic Weyl semimetal (WSM) phase in pyrochlore iridates. Indeed, a recent cluster dynamical mean-field theory study proposed that a transition to a WSM could occur when the ordered moment drops below $0.2\,\mu_B$ [167].

Additionally, we demonstrated how REXS with full linear polarisation analysis can be used to study the evolution of the Ir magnetic structure of pyrochlore iridates under magnetic fields. In $Sm_2Ir_2O_7$, the AIAO order of the Ir site was robust to magnetic fields of 12 T. It would be of interest to perform a similar experiment on $Nd_2Ir_2O_7$, where a field-driven insulator-metal transition occurs at 10 T [161, 162].

Chapter 5

RIXS of R_2Ir$_2$O$_7$ (R = Sm, Nd, Tb)

Contents

5.1 **Preliminaries** **104**

5.2 **Magnetic excitations of R_2Ir$_2$O$_7$ (R = Sm, Nd, Tb)** **106**

  5.2.1 Sm$_2$Ir$_2$O$_7$ 106

  5.2.2 Nd$_2$Ir$_2$O$_7$ 111

  5.2.3 Tb$_2$Ir$_2$O$_7$ 115

5.3 ***dd* excitations of R_2Ir$_2$O$_7$ (R = Sm, Nd, Tb)** . . . **118**

5.4 **Conclusion** **121**

In this chapter, resonant inelastic x-ray scattering (RIXS) experiments at the Ir L_3 edge of the pyrochlore iridates R_2Ir$_2$O$_7$ (R = Sm, Nd, Tb) are presented. We found low-energy, dispersive, temperature dependent features in Sm$_2$Ir$_2$O$_7$ and Nd$_2$Ir$_2$O$_7$, which we attribute to single-magnon excitations from all-in all-out (AIAO) magnetic order. The magnon dispersion can be modelled within linear spin-wave theory. For both Sm and Nd pyrochlores, a minimal nearest-neighbour Hamiltonian of Heisenberg exchange ($J \sim 27$ meV) and Dzyaloshinskii-Moriya interaction ($D \sim 5$ meV) provides an adequate description of the data. The low-energy excitations of Tb$_2$Ir$_2$O$_7$ are less clear. Although features on a similar energy scale are observed, they only exhibit temperature dependence close to the antiferromagnetic zone centre. This indicates that a strong-coupling, linear spin-wave approach becomes inadequate to describe the magnetic excitations of the weakened AIAO state of Tb$_2$Ir$_2$O$_7$. In all samples, crystal-field excitations within the t_{2g} manifold reveal that trigonal distortions are of similar magnitude to the atomic spin-orbit coupling.

Parts of this chapter were published in the article “All-in All-Out Magnetic Order and Propagating Spin Waves in Sm$_2$Ir$_2$O$_7$” in the journal Physical Review Letters [157].

5.1 Preliminaries

Before discussing the high-resolution RIXS measurements aimed at magnetic excitations, it is instructive to map out the RIXS features as a function of incident energy close to the Ir L_3 edge. Figure 5.1 shows the incident energy dependence of RIXS energy loss features of Sm$_2$Ir$_2$O$_7$, collected with a low energy resolution setup ($\sim$ 300 meV) on beamline ID20, ESRF.

We find that the energy loss features show two resonances, at incident energies of 11.213 and 11.216 keV. At an incident energy of 11.213 keV, the core electrons are mainly promoted to $5d(t_{2g})$ levels, whereas at 11.216 keV the core electrons are predominantly promoted to $5d(e_g)$ levels. We observe three inelastic features up to 12 eV energy loss, which remain at fixed energy loss as a function of incident energy, suggesting Raman features as opposed to x-ray fluorescence. We identify these three energy loss features as excitations within the t_{2g} levels, excitations from t_{2g} to e_g levels, and charge transfer excitations. The RIXS scattering process for these features, from initial to intermediate to final state, can be written as:

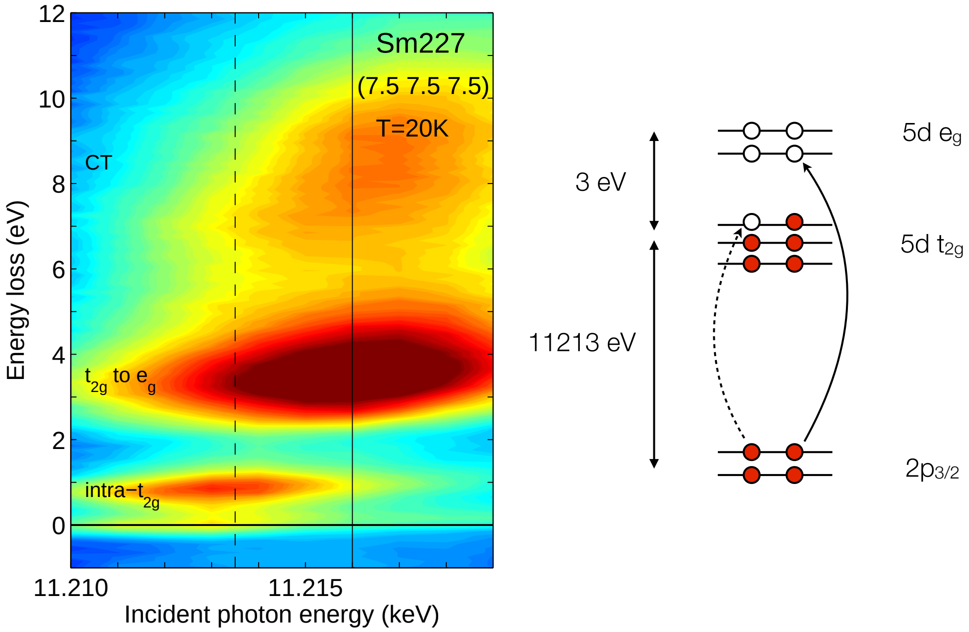

Figure 5.1: Incident energy dependence of RIXS energy loss features of $Sm_2Ir_2O_7$ at $\mathbf{Q} = (7.5\ 7.5\ 7.5)$ at 20 K. The dotted and solid lines indicate incident energies where transitions predominantly to $5d(t_{2g})$ and $5d(e_g)$ levels occur, respectively. The observed energy loss features correspond to excitations within the t_{2g} manifold (intra t_{2g}), crystal field excitation to the e_g manifold (t_{2g} to e_g) and charge transfer (CT) excitations.

$$5d(t_{2g}^5) \rightarrow \begin{cases} 2p_{3/2}^5\,5d(t_{2g}^6) & \rightarrow \left\{ 5d(t_{2g}^{5*}) \quad \text{intra-}t_{2g} \right. \\ 2p_{3/2}^5\,5d(e_g^1) & \rightarrow \begin{cases} 5d(t_{2g}^4)\,5d(e_g^1) & t_{2g} \text{ to } e_g \\ 5d(e_g^1)\,\underline{L} & \text{charge transfer} \end{cases} \end{cases}$$

where the * denotes an excited configuration and $\underline{L}$ a ligand hole. As we are interested in creating excitations within the t_{2g} manifold, such as magnons and t_{2g} crystal-field excitations, we have set the incident energy to 11.213 keV for the high-resolution RIXS measurements described in the following sections.

5.2 Magnetic excitations of R_2Ir$_2$O$_7$ (R = Sm, Nd, Tb)

5.2.1 Sm$_2$Ir$_2$O$_7$

Ir L_3 edge RIXS was performed to study the magnetic excitations of the pyrochlore iridate Sm$_2$Ir$_2$O$_7$ at beamline ID20, ESRF in April 2015. At 20 K, magnetic excitations were observed, dispersing from 25 meV at the zone centre to 45 meV at the zone boundaries. The absence of Goldstone-like modes suggests an AIAO, as opposed to xy, magnetic structure. Under this assumption, the magnon dispersion and intensity can be described within linear spin-wave theory, using a minimal Hamiltonian that includes Heisenberg exchange [$J = 27.5(6)$ meV] and Dzyaloshinskii-Moriya interactions [$D = 5.0(3)$ meV].

Method

At beamline ID20, ESRF, an energy resolution of 25 meV was achieved at the Ir L_3 edge. The incident polarisation was linear, parallel to the horizontal scattering plane (π polarisation). The diced analyser crystal was masked to an active area of a circle of 40 mm diameter, which, at $2\theta = 90°$, corresponds to an acceptance of $\Delta Q_\parallel \sim 0.13$ Å^{-1} in the scattering plane (however, please note that the momentum resolution is not a 1d function, but rather forms a 3d ellipsoid in reciprocal space, see Appendix C.1 for a detailed discussion). The Sm$_2$Ir$_2$O$_7$ sample was mounted with the (111) direction in the scattering plane. The dispersion of magnetic excitations was studied within the (777) Brillouin zone, close to $2\theta = 90°$. This ensures that the elastic component is minimised [as non-resonant (quasi) elastic contributions, such as (diffuse) Thomson scattering and phonons, scale with $|\boldsymbol{\epsilon}' \cdot \boldsymbol{\epsilon}|^2$, or $\cos^2 2\theta$, for π polarisation].

Results

Figure 5.2(a-c) shows constant wave vector energy scans of Sm$_2$Ir$_2$O$_7$ along high symmetry directions of the (777) Brillouin zone at 20 K. A dispersive feature is observed that reaches a maximum energy of 45 meV at the zone boundaries. Towards the Γ point [(777), charge and magnetic Bragg peak], the intensity of this excitation increases, while the energy decreases to 25 meV. This dispersive feature is temperature dependent, its Lorentzian spec-

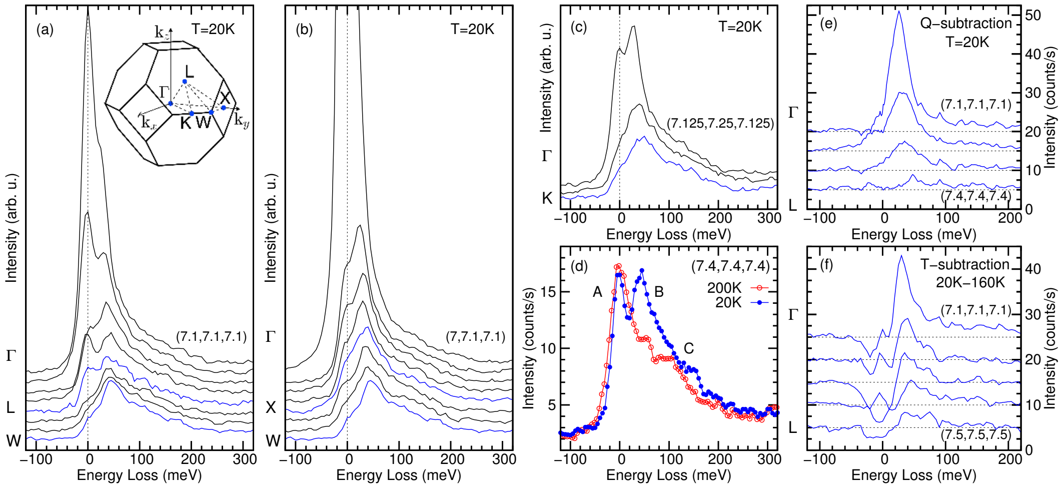

Figure 5.2: (a-c) Constant wave vector RIXS energy scans along high-symmetry directions of $Sm_2Ir_2O_7$ at 20 K. (d) Temperature dependence of magnetic excitations at $\mathbf{Q} = (7.4\ 7.4\ 7.4)$. (e) Momentum subtraction of RIXS energy scans, the energy scan at the zone boundary L was subtracted from energy scans towards the Γ point (elastic line subtracted). (f) Temperature subtraction of RIXS energy scans, the energy scans at 160 K were subtracted from energy scans at 20 K along the $\Gamma - L$ line (elastic line not subtracted).

tral weight disappears above 90 K at the zone boundaries [Fig. 5.2(d)]. An additional broad, asymmetric feature persists to at least 200 K, extending from a quasi-elastic response to approximately 300 meV. This broad feature appears to be independent of momentum transfer and temperature: Subtracting the energy scan at the zone boundary (L) from energy scans towards the zone centre ($\Gamma \rightarrow L$) at 20 K reveals that only the inelastic Lorentzian feature disperses [Fig. 5.2(e)]. Similarly, subtracting energy scans at 160 K from energy scans at 20 K shows that the additional spectral weight at low temperature consists predominantly of a low-energy Lorentzian component [Fig. 5.2(f)]. This suggests that the low-energy RIXS response of $Sm_2Ir_2O_7$ comprises of three features: An elastic signal (at 0 meV, feature A), a gapped, dispersive, temperature-dependent Lorentzian feature (at 25-45 meV, feature B) and a non-dispersive, temperature-independent continuum of excitations (at 0-300 meV, feature C).

The temperature dependence of feature B suggests a magnetic origin. The magnetic excitations of AIAO order in pyrochlore iridates were predicted to be gapped (∼100 meV) with a dispersion bandwidth of 15 meV [168]. While the spin gap we observe is smaller (∼25 meV), the dispersion bandwidth is roughly consistent (∼20 meV). The origin of feature C is unclear. A similar feature has been observed in the magnetically disordered $Pr_2Ir_2O_7$ and was proposed to originate from paramagnetic fluctuations [74]. An alternative interpretation of feature C are lattice vibrations. Raman scattering of $Sm_2Ir_2O_7$ [169] has revealed multiple single-phonon modes that, when including higher harmonics, could appear as a broad continuum of excitations within the RIXS energy resolution, a similar scenario was proposed in Na_2IrO_3 [120]. Based on these considerations, the low-energy RIXS features of $Sm_2Ir_2O_7$ were fitted with a delta function at zero energy loss for elastic scattering (feature A), a Lorentzian function for the single magnon excitation (feature B) and an antisymmetrized Lorentzian for feature C. The functional form of feature C is:

$$L(E) = \frac{\Gamma}{(E - E_0)^2 + \Gamma^2} - \frac{\Gamma}{(E + E_0)^2 + \Gamma^2}$$

where E_0 and Γ are the centre and width, respectively. All features were convoluted with the instrumental energy resolution, which can be approximated by a Pearson VII function with FWHM = 23.4(2) meV and shape parameter $\mu = 2.0(1)$ (where $\mu = 1$ corresponds to a Lorentzian and $\mu = \infty$ to a Gaussian line shape). The functional form of feature C was chosen purely on phenomenological grounds. Its width and centre were determined by a global refinement using the objective function $\sum_i \chi_i^2$, where χ_i is the least-squares goodness of fit of individual **Q**-points i. This minimises the number of fitted parameters for individual **Q**-points and ensures that the dispersive spectral weight is described by feature B. The global optimisation was performed with the conjugate gradient method, using Brent's method for the linesearch, while energy scans for individual **Q**-points were refined with the Levenberg-Marquadt algorithm [170].

We employ a minimal, nearest-neighbour, effective spin-1/2 Hamiltonian to describe the magnetic excitations:

$$H = \sum_{ij} (J\mathbf{S}_i \cdot \mathbf{S}_j + \mathbf{D}_{ij} \cdot \mathbf{S}_i \times \mathbf{S}_j)$$

Here, we have included Heisenberg exchange and the Dzyaloshinskii-Moriya interaction (DMI). The choice of this Hamiltonian is motivated from a strong-coupling limit, previous literature has also included a symmetric anisotropic exchange term [6, 9, 168]. As this term is expected to be comparatively small, we exclude it to reduce the number of free fitting parameters. The sign of the

DMI determines which magnetic ground state is realised [64]: A *direct* (positive) DMI will favor the AIAO ground state, whereas the *indirect* (negative) DMI stabilises an xy ground state. We used SpinW [171] to calculate the spin-wave spectrum in the Holstein-Primakoff approximation.

Figure 5.3 shows the fitted dispersion of magnetic excitations. For an xy ordering and $D < 0$, pseudo-Goldstone modes are expected [172–174]. This can be understood from the continuous, classical degeneracy of ground states, characterised by the arbitrary angle of the moments within the local xy planes. In our data, the magnetic excitations are however gapped throughout the Brillouin zone. While we are limited by the experimental resolution, close to the Γ point a gapped mode that carries the majority of spectral weight is observed [Fig. 5.3(a)], which indicates that Goldstone-like modes are absent. An xy antiferromagnetic ordering therefore appears incompatible with the excitations we observe.

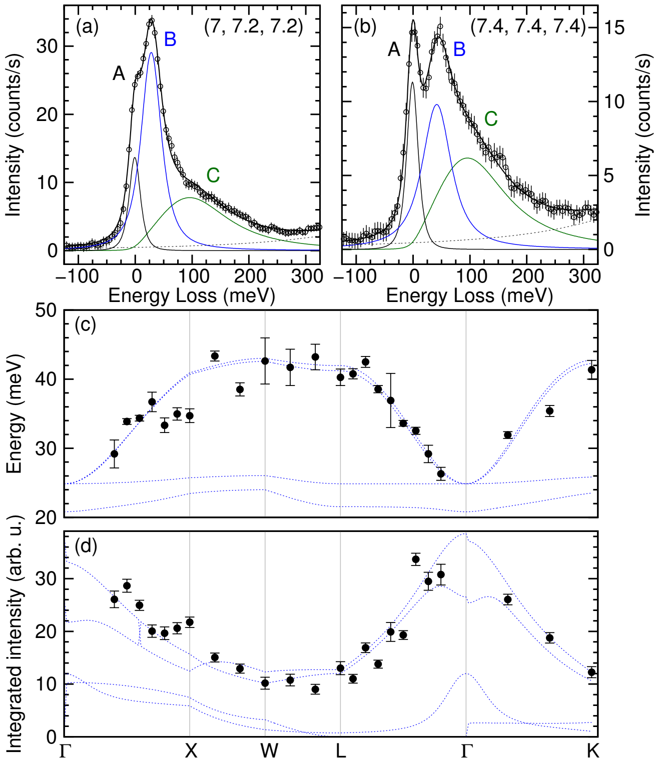

Figure 5.3: (a-b) Representative fitted RIXS energy scans of Sm$_2$Ir$_2$O$_7$. (c) Fitted energy dispersion of feature B as a function of momentum transfer (black dots) plotted with calculated magnon dispersion of AIAO order (blue dotted lines). (d) Fitted intensity dispersion of feature B (black dots) plotted with calculated total dynamical structure factor $\sum_{a=x,y,z} S^{aa}(\mathbf{q},\omega)$ of AIAO order (blue dotted lines).

Conversely, for AIAO order and $D > 0$, all four magnetic modes are gapped [168]. In our data, only one dispersive feature can be distinguished. This feature was fitted with $J = 27.3(6)$ meV and $D = |D_{ij}| = 4.9(3)$ meV. For these parameters, two quasi-degenerate magnon branches disperse from 25 meV to 45 meV, carrying the majority of the spectral weight. While two additional branches are predicted in the calculation, their absence in the data could be explained by their small spectral weight and low energy (20-25 meV) that will make them indistinguishable from an elastic signal.

We emphasise that the errors in these parameters refer to how well the calculated dispersion can approximate the fitted dispersion of feature B. As such, the errors of the exchange parameters are coupled to our choice of phenomenological model for the low-energy RIXS response. It is conceivable that choosing a different set of functions to model the data could yield somewhat different values for the exchange constants and their uncertainties. However, as the "true" functional form of the low-energy RIXS response is unknown, it is unfortunately necessary to choose a phenomenological model for the data. Any physical parameters extracted will only correspond to the true uncertainties inherent to the data insofar as the model provides a good approximation to the true RIXS response.

Linear spin-wave theory implicitly assumes a strong-coupling limit. In Ref. [168], the magnetic excitations have been calculated as a function of the Hubbard interaction U. This allows direct comparison with our data: We observe well-defined spin-waves across the entire Brillouin zone that disperse only towards the Γ point, which is only compatible with large Hubbard U calculations. However, the fit to the data reveals an intrinsic Lorentzian FWHM of 22(2) meV near the Γ point, which is of similar magnitude to the excitation energy and the dispersion bandwidth. Indeed, Ref. [168] predicts that the magnetic excitations become strongly damped as U is decreased. This indicates intermediate-to-strong correlations in Sm$_2$Ir$_2$O$_7$.

It is also interesting to consider the fitted exchange constants. In a cubic limit of ideal $J_{\text{eff}} = 1/2$ moments, larger values for the DMI were predicted ($D/J \approx 0.63$ in a strong coupling limit of Ref. [6], whereas we find $D/J \approx 0.18$). Crystal-field excitations show that trigonal distortions are as strong as the spin-orbit coupling in pyrochlore iridates (see section 5.3 and Refs. [136, 175]). This places the ground state halfway between a $J_{\text{eff}} = 1/2$ and a real spin-1/2 doublet and may explain the smaller exchange anisotropy.

5.2.2 Nd$_2$Ir$_2$O$_7$

We describe a RIXS experiment on Nd$_2$Ir$_2$O$_7$, performed at beamline ID20, ESRF in February 2017. In order to reach the magnetically ordered state, the incident beam had to be strongly attenuated, which severely limited the number and data quality of the **Q** points sampled. Nevertheless, dispersive magnetic excitations were observed, which, within the quality of over data, can be described by the same microscopic Hamiltonian as for Sm$_2$Ir$_2$O$_7$.

Method

Similar to the RIXS experiment on Sm$_2$Ir$_2$O$_7$, an energy resolution of 25 meV was achieved at beamline ID20 with π polarisation. The Nd$_2$Ir$_2$O$_7$ sample was mounted with (100) and (011) directions in the scattering plane. As discussed in section 4.2, the incident beam was attenuated by a factor of ~ 28 (by means of 700 μm Al foil), in order to observed the onset of magnetic order. Using a high He flux for the Dynaflow He exchange gas cryostat, it was possible to maintain a (nominal) base temperature of 2.5 K. With this configuration, we collected high-resolution RIXS energy scans along the (h00) direction from the magnetic zone boundary at (13 0 0) to the zone centre at (14 0 0). Note that for the previous RIXS experiment on Sm$_2$Ir$_2$O$_7$ collection times of one hour were sufficient for each **Q** point. To obtain the same data quality for Nd$_2$Ir$_2$O$_7$ would have required 28 hours counting for each **Q** point, which was unfeasible. We increased the active analyser area to a circle of 60 mm diameter to alleviate the loss in incident beam intensity. This corresponds to an acceptance of $\Delta Q_{\parallel} \sim 0.24$ Å^{-1} within the scattering plane (a detailed discussion on the effects of momentum resolution is given in Appendix C.1). Nevertheless, the lower intensity severely reduced the quality of the data, such that the data analysis is largely guided by previous observations in Sm$_2$Ir$_2$O$_7$.

Results

Figure 5.4 shows a summary of the collected RIXS data of Nd$_2$Ir$_2$O$_7$. Below the magnetic ordering temperature, a sharp feature appears, which disperses from ~ 25 to ~ 45 meV. By performing momentum and temperature subtractions of the data, we establish that this feature accounts for the majority of the dispersive and temperature dependent spectral weight of the RIXS energy scans. An increase in the elastic line is observed at (13.9 0 0) at 2.5 K, which arises

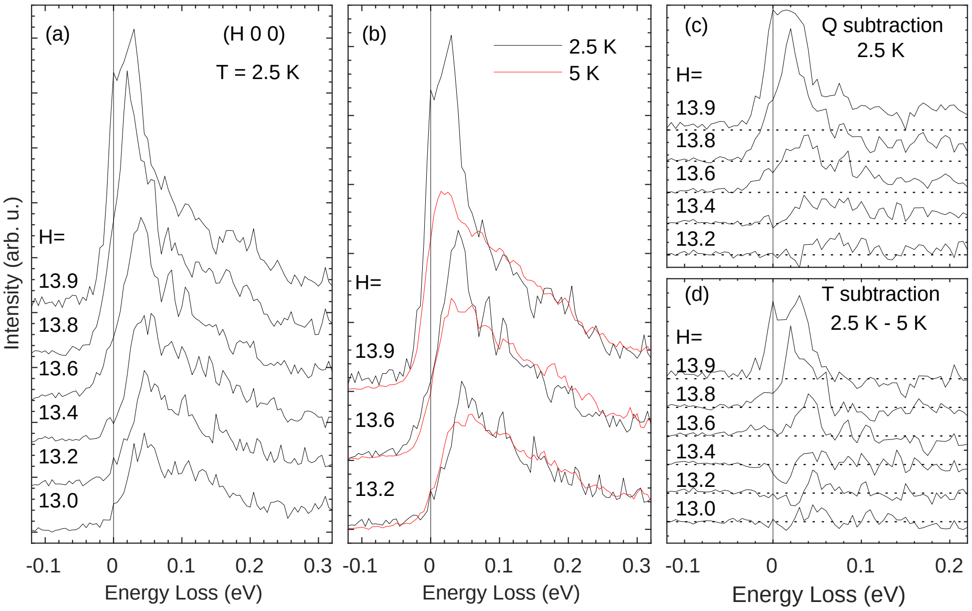

Figure 5.4: Constant wavevector RIXS energy scans of Nd$_2$Ir$_2$O$_7$. (a) Dispersion of low-lying excitations in the magnetically ordered state along (h00) reciprocal lattice direction. (b) Temperature dependence of selected **Q** points, below (black lines) and above (red lines) the ordering temperature. (c) Momentum subtraction of RIXS energy scans at 2.5 K, the zone boundary scan (13 0 0) was subtracted from all other scans. (d) Temperature subtraction of RIXS energy, the data at 5 K were subtracted from the data at 2.5 K.

from the nearby magnetic Bragg peak appearing at (14 0 0). Furthermore, as for Sm$_2$Ir$_2$O$_7$, a broad, temperature-independent feature extends from 0 to 300 meV. This feature is weakly intensity-dispersive and remained unchanged up to 50 K.

In order to provide consistent data analysis, we used to same phenomenological model as for Sm$_2$Ir$_2$O$_7$ to fit the energy scans. This model assumes that the RIXS response comprises of three features at low energy, an elastic peak (feature A), a sharp, temperature dependent feature between 20-50 meV energy loss (feature B), and a broad continuum of excitations extending up to 300 meV energy loss (feature C). A delta function, a Lorentzian, and an antisymmetrized Lorentzian were used to describe the three features. All functions were convoluted by the instrumental energy resolution. Figure 5.5 shows representative fitted energy scans of Nd$_2$Ir$_2$O$_7$.

The energy scale, momentum and temperature dependence of feature B suggests a magnetic origin. As feature B disappears at the transition temperature, and other low-lying excitations show little temperature dependence, we

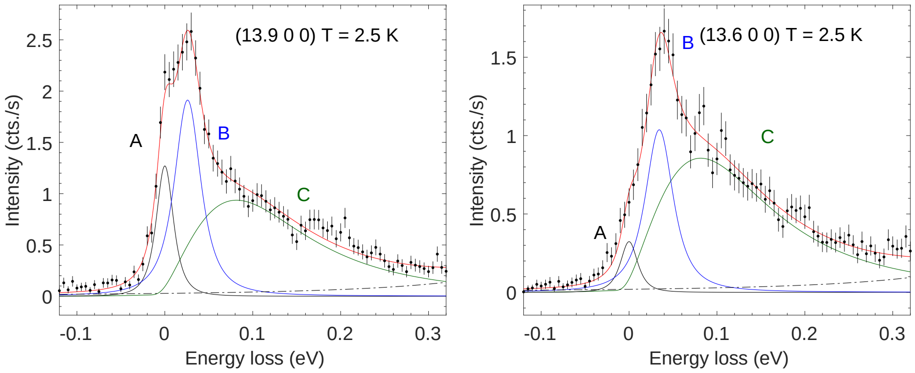

Figure 5.5: Representative fitted energy scans of $Nd_2Ir_2O_7$ at 2.5 K.

ascribe it to single-magnon excitations from long-range AIAO magnetic order. We employ linear spin-wave theory to fit the dispersion of feature B, using the same Hamiltonian as for $Sm_2Ir_2O_7$ [171]. Figure 5.6 shows the fitted dispersion relation, which yielded a Heisenberg exchange of $J = 28(2)$ meV and DM interaction of $D = 4.8(5)$ meV.

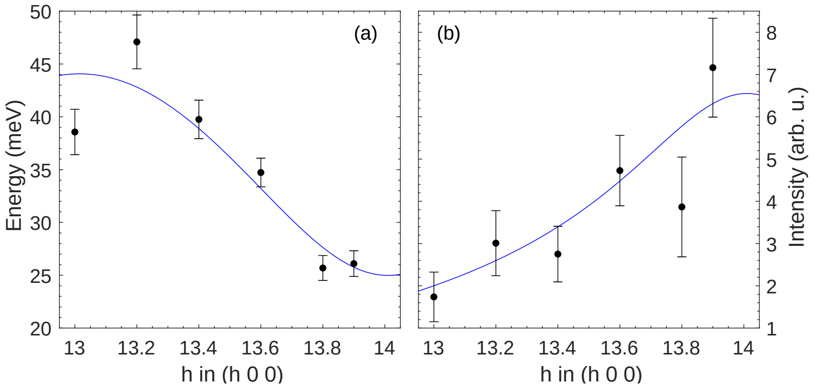

Figure 5.6: Fitted energy (a) and intensity dispersion (b) of feature B, plotted over calculated single-magnon dynamical structure factor $[S^{yy}(\mathbf{q},\omega)+S^{zz}(\mathbf{q},\omega)]$ of AIAO magnetic order within linear spin-wave theory, using J = 28(2) meV and D = 4.8(5) meV.

It is somewhat surprising that despite ordering temperatures differing by 100 K, the microscopic Hamiltonian appears unchanged between $Sm_2Ir_2O_7$ and $Nd_2Ir_2O_7$. We emphasise that the slightly worse momentum resolution used for the RIXS experiment in $Nd_2Ir_2O_7$ has negligible effect on the estimated exchange parameters compared to uncertainties arising from the fitting procedure (see Appendix C.1). Within our Hamiltonian, T_N should scale with $\sim D$, such that $D \sim 5\,\text{meV} \sim 60$ K. This may show the limits of this minimal Hamiltonian, a better approach might be to consider the most generic, symmetry-allowed, nearest neighbour couplings to fit the data. However, this would introduce four exchange parameters [155], which are unlikely to be reliably fitted by our RIXS data.

Looking at the raw data, it appears that the spin-gap is relatively unchanged from $Nd_2Ir_2O_7$ to $Sm_2Ir_2O_7$, but the spin-wave velocity is somewhat higher, which may suggest a larger Heisenberg exchange. As the spin-gap marginally changes from $Sm_2Ir_2O_7$ to $Nd_2Ir_2O_7$, this indicates a Mott description of the thermal MIT, where the opening of the gap is driven by electronic correlations, as opposed to magnetic order. In the latter, the lower transition temperature should be reflected in a change of magnetic anisotropy and a smaller spin-gap. However, if the former is the case, the electronic correlations must weaken in $Nd_2Ir_2O_7$. In a first approximation of a Hubbard model, one would qualitatively expect $J \sim t^2/U$, where t is a hopping term and U the Coulomb repulsions, and hence J should increase from $Sm_2Ir_2O_7$ to $Nd_2Ir_2O_7$. However, within the quality of our data and the fitting model, the effective magnetic Hamiltonian should be considered unchanged from $Sm_2Ir_2O_7$ to $Nd_2Ir_2O_7$.

Excitations above ordering temperature

As for $Sm_2Ir_2O_7$, the RIXS data of $Nd_2Ir_2O_7$ shows a temperature independent continuum of excitations (feature C), from 0-300 meV energy loss. Indeed, feature C has been measured in all pyrochlore iridates so far studied with RIXS [74], regardless of whether long-range magnetic order exists.

The energy scale of feature C is too low to be related to *dd* excitations, which should reside above the spin-orbit coupling energy of $\sim$ 450 meV. This suggests that feature C arises either from resonant phonons or short-range magnetic correlations. In order to observe phonons with RIXS, substantial electron-phonon (e-p) coupling is required [176]. Not only single-phonon excitations, but harmonics should be observed, their relative strength dependent on the e-p coupling. These could extend to higher energies and result in an asymmetric continuum of excitations, as was argued to occur in a Cu L edge RIXS experiment on $Ca_{2+5x}Y_{2-5x}Cu_5O_{10}$ [177]. Although long-range magnetic order disappears above 4 K in $Nd_2Ir_2O_7$, a nearest neighbour Heisenberg exchange $J \sim 28$ meV ~ 300 K, indicates that short-range correlations might persist to this temperature. However, it is unclear whether magnetic excitations can account for an energy scale of up to 300 meV, even when multi-magnon processes are included.

It will be difficult to distinguish between these two possibilities with current instrumentation, although detailed temperature and momentum dependences could shed light on the origin of feature C. Additionally, it has recently become possible to perform RIXS at the Ir L_2 edge on beamline ID20, albeit with lower energy resolution, which might show a qualitatively different low-energy RIXS response. In the near future, the improved energy resolution of $\sim$ 10 meV [178] could provide a more definite answer to the origin of this feature.

5.2.3 $Tb_2Ir_2O_7$

We studied the low-energy excitations of $Tb_2Ir_2O_7$ with RIXS at the Ir L_3 edge at beamline ID27, APS, in April 2017. As opposed to RIXS experiments on $Sm_2Ir_2O_7$ and $Nd_2Ir_2O_7$, here magnetic excitations could not be clearly identified. This is partly due to the lower energy resolution ($\sim$ 30 meV) on beamline ID27, which made it difficult to separate inelastic features from the elastic line. Nevertheless, the absence of clear temperature dependent dispersive features suggests that the magnetic excitations in the weakened AIAO state of $Tb_2Ir_2O_7$ ($\sim 0.06\,\mu_B$) depart from the sharp single-magnon features predicted by linear spin-wave theory.

Method

On beamline ID27, an energy resolution of approximately 30 meV was achieved at the Ir L_3 edge. The polarisation was linear, parallel to the horizontal scattering plane. The analyser was masked to an active area of a circle of two inches ($\sim$ 50 mm) diameter. This corresponds to an acceptance of $\Delta Q_\parallel \sim 0.2$ Å^{-1} within the scattering plane. The $Tb_2Ir_2O_7$ sample was mounted with the (111) direction in the scattering plane. We initially attempted to study excitations within the (777) Brillouin zone. However, we observed a very strong elastic contribution and hence decided to measure excitations within the (886) Brillouin zone, which is closer to $2\theta = 90°$, and results in a stronger suppression of the elastic line.

Results

Figure 5.7 shows a summary of RIXS data collected in the (886) Brillouin zone. At 5 K, energy scans along the (88L) direction do not show any clear dispersive

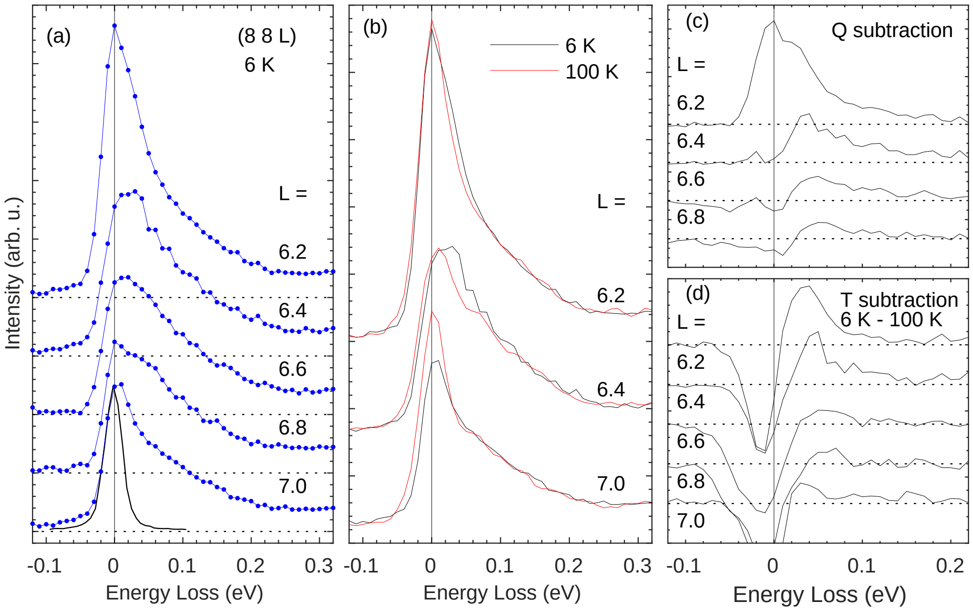

Figure 5.7: RIXS constant wavevector energy scans of $Tb_2Ir_2O_7$. (a) Low-energy excitations along (88L) direction towards the antiferromagnetic zone centre at (886). The black solid line is the measured energy resolution. (b) Temperature dependence of excitations above (red solid line) and below (black solid line) the magnetic ordering temperature. (c) Momentum subtraction, the zone boundary data at (887) were subtracted from (88L) scans. (d) Temperature subtraction, data points at 100 K were subtracted from data at 6 K.

features, which contrasts with data on $Sm_2Ir_2O_7$ and $Nd_2Ir_2O_7$. This is at least partially due to the lower energy resolution at beamline ID27. In energy scans close to the antiferromagnetic zone centre (886), the elastic line is broader than the energy resolution [black solid line in Fig. 5.7(a)], suggesting an unresolved inelastic feature in the energy range $\sim 25 - 50$ meV. At 100 K, well above the ordering temperature of 70 K, inelastic features only show temperature dependence close to the antiferromagnetic zone centre at (886). At the zone boundary, (887), the elastic line intensity increases with temperature, which indicates a phonon contribution that would follow a Bose-Einstein distribution.

However, for this sample, the strength of the elastic line was highly dependent on the beam position on the sample. To ensure optimal alignment for measuring magnetic excitations, the sample position was optimised to maximise the intensity of the magnetic (886) peak at low temperature. When heating to 100 K, thermal expansion of the sample holder requires realignment, which could by itself have introduced an additional elastic component.

The absence of temperature dependence makes it unclear whether the low-

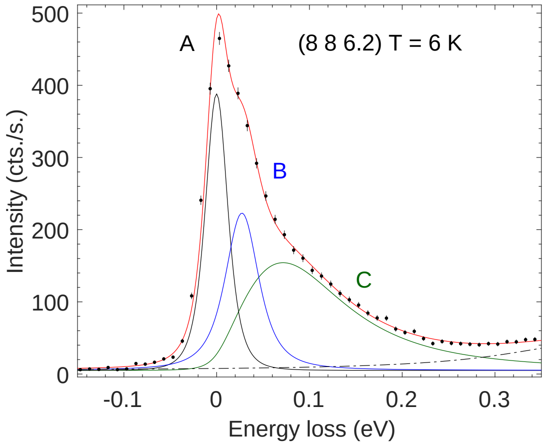

Figure 5.8: Fitted RIXS energy scan of Tb$_2$Ir$_2$O$_7$ at $\mathbf{Q}$ = (8 8 6.2) at 6 K.

energy features can be associated with long-range AIAO magnetic order. Close to the magnetic Bragg peak at (886), some temperature-dependent broadening can be discerned in the elastic line at (8 8 6.2) [Fig. 5.7(b)]. Assuming a magnetic origin, the low temperature energy scan can be fitted with the same model as for Nd$_2$Ir$_2$O$_7$ and Sm$_2$Ir$_2$O$_7$, yielding a spin-gap of $\sim$ 30 meV [see Fig. 5.8]. Using this value as a starting point, the dispersive feature seen in momentum subtracted data [Fig. 5.7(c)] can be approximately fitted. Within same microscopic Hamiltonian of Heisenberg exchange and DM interaction, we very roughly estimate exchange parameters of $J \sim 40$ meV and $D \sim 3$ meV.

It remains unclear whether this estimation of exchange parameters is sound. A linear spin-wave description of magnetic excitations assumes a strong coupling, large U, limit. However, the small ordered moment seen in REXS suggests that a weak-to-intermediate correlations regime may be more appropriate for Tb$_2$Ir$_2$O$_7$. In Ref. [168] the magnetic excitation spectrum was studied within the random-phase approximation (RPA) as a function of Hubbard U. For small values of U, Landau-damping of magnetic excitations occurs in large parts of the Brillouin zone, and only at certain momenta sharp magnetic peaks persist. In particular, their prediction of magnetic excitations in a metallic AIAO state at low U shares some similarities with our data, where magnetic features only appear close to the Γ point. A better description of the data may therefore be achieved by computing the dynamical structure within RPA, and the data analysis should be considered ongoing.

5.3 *dd* excitations of R_2Ir$_2$O$_7$ (R = Sm, Nd, Tb)

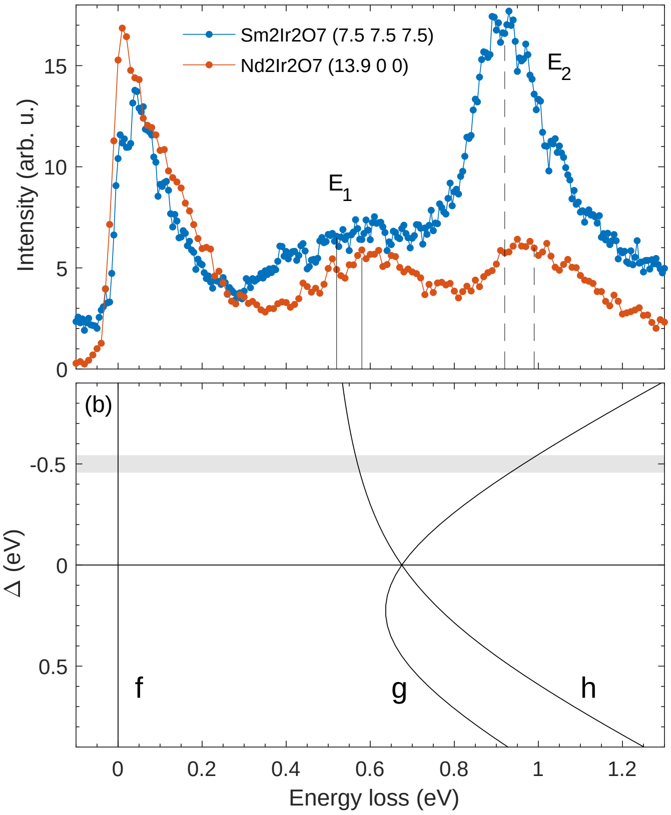

Figure 5.9: (a) RIXS data of Sm$_2$Ir$_2$O$_7$ and Nd$_2$Ir$_2$O$_7$ showing *dd* excitations within t_{2g} manifold. The vertical lines indicate the position of the maxima, as determined by fitting Lorentzian functions to the data. (b) Calculated excitation energies $f \to g, h$ doublets, Δ is the strength of trigonal distortions, the spin-orbit coupling ζ was set to 450 meV. The grey area shows a typical value of Δ for pyrochlore iridates.

At higher energy loss, RIXS energy scans of pyrochlore iridates show crystal-field (or *dd*) excitations within the t_{2g} manifold that largely remain temperature independent. As discussed in chapter 3, when the t_{2g} levels are split by both spin-orbit coupling ζ and non-cubic crystal fields Δ, three Kramers doublets emerge, which we labelled as f, g, h, where the hole resides in the f doublet. Thus, from RIXS excitations to the states g, h, values for ζ, Δ can be estimated. Figure 5.9 shows RIXS data of Sm$_2$Ir$_2$O$_7$ and Nd$_2$Ir$_2$O$_7$, compared with excitation energies E_1, E_2 to the g, h doublets, as a function of trigonal distortion Δ. We find a unique solution of $\Delta \sim -0.5$ eV and $\zeta \sim 0.42$ eV. Similar parameters can be obtained for Nd and Tb, see Table 5.3. These values can be compared with literature RIXS data on Eu and Pr pyrochlore iridates

[74], which reveals a trend towards stronger non-cubic crystal fields for larger rare-earth ions.

$R_2Ir_2O_7$	E_1 (eV)	E_2 (eV)	Δ (eV)	ζ (eV)
Tb	0.57(1)	0.94(1)	-0.47	0.45
Eu [74]	0.59(1)	0.95(1)	-0.46	0.46
Sm	0.52(1)	0.92(1)	-0.50	0.42
Nd	0.58(1)	0.99(1)	-0.52	0.45
Pr [74]	0.52(1)	0.98(1)	-0.56	0.42

Table 5.1: Summary of t_{2g} crystal-field excitations of pyrochlore iridates. The values for E_1 and E_2 and their respective errorbars were determined by fitting Lorentzian functions to the data. Energy scales of spin-orbit coupling ζ and trigonal distortion Δ were estimated within the single-ion model.

The excited features E_1, E_2 show substantial intrinsic widths, much larger than the instrumental energy resolution. This indicates that the excited final states, where the hole resides in the g, h bands, show metallic behaviour, possibly due to the larger spatial extent of g, h orbitals, such that width of E_1, E_2 features correspond to a momentum averaged or density of states measurement [130]. There is no detectable energy dispersion as a function of momentum transfer. This is similar to the crystal field excitations in $(Na/Li)_2IrO_3$ [134] and Sr_3CuIrO_6 [133], but contrasts with RIXS data of Sr_2IrO_4 [17], $Sr_3Ir_2O_7$ [94] and $CaIrO_3$ [121]. What distinguishes the former from the latter is a much weaker magnetic coupling, which indicates that the dispersion of these excitations scales with the superexchange coupling, as was suggested in the literature [137] (although there is some debate on the origin of the dispersion in these features [179]).

The intensity of the crystal-field excitations is determined by the RIXS cross-sections. We can use the single-ion RXS cross-sections of chapter 3 to calculate the intensity of these excitations. We use the example of $Nd_2Ir_2O_7$. We recall the tensorial structure factor at wavevector $\mathbf{Q}$

$$F_c(\mathbf{Q}) = \sum_{i=0}^{3} R_i \mathcal{A}^{L_3} R_i^T \exp\left(2i\pi \mathbf{Q}\cdot\mathbf{r}_i\right)$$

where we substitute the four atomic scattering tensors for transitions $|f,-\rangle \rightarrow |g,\uparrow(\downarrow)\rangle$, $|h,\uparrow(\downarrow)\rangle$ doublets, with and without spin-flip, for $\mathcal{A}^{L_3}$.

As the structure factor is computed within the crystal reference frame, we rotate to a more convenient laboratory frame x, y, z (see Fig. 5.10). For the scattering setup of this experiment, (100) and (011) directions were in the

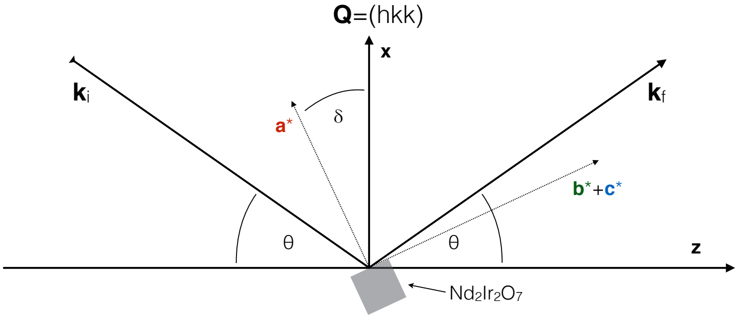

Figure 5.10: RIXS experimental geometry for Nd$_2$Ir$_2$O$_7$.

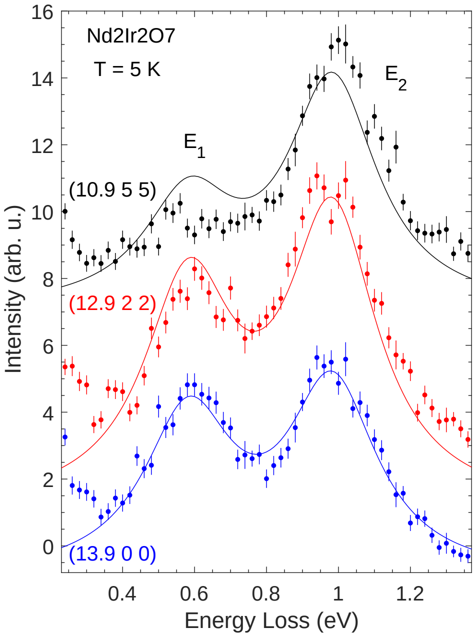

Figure 5.11: RIXS constant wavevector energy scans of Nd$_2$Ir$_2$O$_7$ along (hkk), showing t_{2g} crystal-field excitations E_1, E_2 (circles) plotted with calculated RXS intensities (solid lines). For the latter, a phenomenological Lorentzian broadening was introduced.

scattering plane, allowing access to (hkk) reflections. Starting from a condition where $\mathbf{a} \parallel \mathbf{Q} = (h00)$, we can scatter of ($hkk$) planes by rotating around the y axis. Thus the structure factor becomes

$$F_d(hkk) = R_y^T(\delta) F_c(hkk) R_y(\delta)$$

where $\cos\delta = \frac{h^2}{h^2+2k^2}$. It is straightforward to describe $\mathbf{k}_i$ and $\mathbf{k}_f$ in this x, y, z laboratory frame to compute the Jones matrix (see section 3.4). The RIXS intensity is then given by the sum of $\pi\sigma'$ and $\pi\pi'$ polarisation channels. We note that the four possible final states consist of doubly degenerate Kramers doublets, over which we sum. Figure 5.11 shows a comparison between experimental and calculated RIXS intensities of $Nd_2Ir_2O_7$, where a phenomenological broadening was introduced in the latter. The calculated intensities appear to roughly reproduce the data, and follow the trends in the spectral weight of specific transitions.

While the success of this model is scientifically not very interesting, it perhaps shows that a fairly simple single-ion calculation can give accurate RIXS intensities of crystal-field excitations in iridates. This could be useful when the excitation energies by themselves do not allow an unambiguous determination of the crystal-field energy scales. Furthermore, it would be of interest to extend this approach to Os and Re based $5d$ transition metal oxides, where recent RIXS measurements have revealed more complicated dd excitations [180, 181].

5.4 Conclusion

In this chapter, we presented Ir L_3 edge RIXS experiments on the pyrochlore iridates $R_2Ir_2O_7$ (R = Sm, Nd, Tb) to study magnetic and t_{2g} crystal-field excitations. For Sm and Nd, sharp low-energy features appeared in the magnetically ordered state, dispersing from 25 meV to 45 meV. We interpret these features as single-magnon excitations. For both Sm and Nd, an effective Hamiltonian of Heisenberg exchange ($J \sim 27$ meV) and Dzyaloshinskii-Moriya interaction ($D \sim 5$ meV) can provide a good description of the energy and intensity dispersion. This set of exchange parameters leads to a consistent description of the magnetic order and excitations, and establishes the low-energy effective Hamiltonian of pyrochlore iridates.

For $Tb_2Ir_2O_7$, no clear magnetic excitations could be discerned. This is at least partly due to a lower energy resolution used in the experiment. Only close to the antiferromagnetic zone centre, temperature dependent features were observed. The spin-gap appears at somewhat higher energy (~ 30 meV) than in Sm and Nd, indicating a larger exchange coupling, possible to due reduced Coulomb interactions. This qualitatively agrees with the weakened magnetic moment seen in REXS experiments, and suggests that a linear spin-wave description of the data becomes inadequate.

Additionally, a broad continuum of excitations from 0-300 meV was observed in all compounds. The origin of this feature remains unknown, it shows negligible temperature dependence up to 200 K, but exhibits weak intensity dispersion. Possible origins are resonant phonons or short-range magnetic excitations. It is likely that future advances in instrumentation, such as higher energy-resolution or polarisation analysis, are required to understand its origin.

For all pyrochlore iridates, crystal-field excitations within the t_{2g} manifold show strong compressive trigonal distortions, of similar magnitude to the atomic spin-orbit coupling. A trend towards stronger trigonal fields for larger rare-earth ions was found. The intensities of these excitations could be reproduced by the single-ion RXS cross-sections of chapter 3.

Chapter 6

Structural and electronic properties of $Sr_3Ir_2O_7$ at high pressure

Contents

6.1 Introduction 126
6.2 High-pressure x-ray diffraction 128
  6.2.1 Experimental method 128
  6.2.2 Results and discussion 128
6.3 High-pressure x-ray absorption spectroscopy . . . 132
  6.3.1 Experimental method 133
  6.3.2 Results and discussion 133
6.4 Conclusion 141

In this chapter, the structural and electronic properties of $Sr_3Ir_2O_7$ at high pressure are investigated by powder x-ray diffraction (XRD) and x-ray absorption spectroscopy (XAS). XRD shows a first-order structural transition at 54 GPa at room temperature, in close vicinity to the high-pressure insulator-metal transition (IMT). Rietveld refinement indicates a novel modification of the Ruddlesden-Popper structure in the high-pressure phase, where the stacking sequence of perovskite bilayers is altered. Up to the structural transition, XAS measurements show that the cubic crystal-field gradually suppresses the spin-orbit induced hybridisation of $J_{\text{eff}} = 3/2$ and e_g levels. In the high-pressure structure, the electronic state of $Sr_3Ir_2O_7$ can no longer be described by a single-ion $J_{\text{eff}} = 1/2$ model, which may arise from crystal-field distortions and increased bandwidths that hybridise $J_{\text{eff}} = 1/2$ and $J_{\text{eff}} = 3/2$ states.

Parts of this chapter were published in the article "Pressure dependence of the structure and electronic properties of $Sr_3Ir_2O_7$" in the journal Physical Review B [182].

6.1 Introduction

Members of the Ruddlesden-Popper (RP) series of iridates $Sr_{n+1}Ir_nO_{3n+1}$, where n is the number of decoupled $SrIrO_3$ perovskite layers, have been at the focus of many investigations since the discovery of a spin-orbit induced Mott insulating state in single-layer Sr_2IrO_4 ($n = 1$) [3, 4]. In these Ir^{4+} ($5d^5$) iridates, the cubic crystal field (CF) $10Dq$ dominates over Hund's coupling J_H ($10Dq > 3J_H$), resulting in a t_{2g}^5 configuration. Subsequently, the spin-orbit coupling (SOC) splits the t_{2g} manifold into a $J_{\text{eff}} = 1/2$ doublet and a $J_{\text{eff}} = 3/2$ quartet (where $J_{\text{eff}} = |-\mathbf{L} + \mathbf{S}|$). Coulomb interactions can then open an energy gap in the half-filled $J_{\text{eff}} = 1/2$ band, giving rise to a $J_{\text{eff}} = 1/2$ Mott insulator. As the dimensionality increases with the number of perovskite layers n, the insulating gap closes in the RP iridates, eventually reaching a metallic state in $SrIrO_3$ ($n = \infty$) [80, 93]. The insulating bilayer $Sr_3Ir_2O_7$ ($n = 2$) is in close proximity to this insulator-metal boundary, such that it may be metallised by the application of high-pressure [100].

At ambient pressure, the crystal structure of $Sr_3Ir_2O_7$ can be approximated by a tetragonal model (space group $I4/mmm$), where the in-plane IrO_6 rotations ($\sim 12°$) are treated as disordered [183]. Other studies have claimed that the octahedral rotations are correlated, resulting in an orthorhombic, twinned structure (*Bbcb*) [184, 185], as well as finding an out-of-plane octahedral tilt ($\sim 0.2°$), which lowers the symmetry to monoclinic ($C2/c$) [186]. The electronic gap of $Sr_3Ir_2O_7$ was estimated to be $\sim$ 100 meV by scanning tunnelling microscopy (STM) [86], angle-resolved photoemission spectroscopy (ARPES) [87–89] and optical conductivity [90].

At high pressure, Zhao *et al.* reported a second-order structural transition in $Sr_3Ir_2O_7$ at 14 GPa [187]. This transition was accompanied by a drastic reduction in resistivity, although up to a 35 GPa no fully metallic state was observed [188]. High-pressure transport measurements by Zocco *et al.* [102] have seen no evidence for this transition at 14 GPa, and instead report a gradual reduction of the electronic gap up to 104 GPa. Again, no metallic state was observed up to 104 GPa. Most recent high-pressure resistance measurements by Ding *et al.* [100] reported a transition to a "confined metal" at 59.5 GPa, where conductance was found in the *ab* plane, but an insulating behaviour persists along the *c* axis. Given the relatively modest charge-gap at ambient conditions, the persistence of an insulating state up to very high pressures was proposed to arise from an increased octahedral rotation, which alleviates the pressure-induced bandwidth broadening. Additionally, Ding *et al.* report high-pressure RIXS measurements, which show that the spin-orbit coupling remains robust up to 64.8 GPa [100].

Here, we investigate the structural and electronic properties of $Sr_3Ir_2O_7$ at high-pressure using powder XRD and XAS. XRD reveals anisotropic compressibility at low pressures, indicative of increased octahedral rotation. We observe a first-order structural transition to a monoclinic symmetry at 54 GPa at room temperature. Rietveld refinement indicates that the stacking sequence of the perovskite bilayers is altered in the high-pressure phase, resulting in a novel modification of the Ruddlesden-Popper structure. The transition occurs in close proximity to the transition the IMT reported by Ding *et al.* [100], which suggests that structural and electronic transitions are coupled. In contrast to the study by Zhao *et al.* [187], no evidence for a second-order structural transition around 14 GPa was found either at room temperature or at 20 K. We examined the electronic ground-state at high-pressure via XAS. In agreement with RIXS measurements, we find that the pressure-driven increase in the cubic crystal-field dominates the evolution of the electronic ground state up to the structural transition. While the spin-orbit coupling remains strong in the high-pressure phase, our data indicate that its influence on the electronic ground state is diminished, as a singe-ion $J_{\text{eff}} = 1/2$ model can no longer describe the electronic ground state. This may originate from crystal-field distortions or bandwidth-driven hybridisation of $J_{\text{eff}} = 1/2$ and $J_{\text{eff}} = 3/2$ states, and suggests that the electronic ground state significantly deviates from the $J_{\text{eff}} = 1/2$ limit.

6.2 High-pressure x-ray diffraction

We studied the pressure evolution of the structure of $Sr_3Ir_2O_7$ with powder XRD. At 54 GPa at room temperature, we observe a first-order structural phase transition, associated with a change from tetragonal to monoclinic symmetry, and accompanied by a 4% volume collapse. Rietveld refinement of the data suggests that the stacking sequence of perovskite bilayers is altered in the high-pressure structure.

6.2.1 Experimental method

We conducted high-pressure x-ray diffraction experiments at beamlines ID09a, ESRF and I15, Diamond Light Source. Single crystals of $Sr_3Ir_2O_7$ were flux grown as described in Ref. [92] and characterised by SQUID magnetometry. Symmetrical diamond-anvil cells were used, fitted with Boehler-Almax diamonds with culet diameters of 250 μm. The gasket material was rhenium, indented to 30 μm thickness, into which a 100-μm-diameter hole was laser-drilled. The $Sr_3Ir_2O_7$ single crystals were ground into powders and loaded with Helium as the pressure transmitting medium. Pressure was measured in situ using the SrB_4O_7:Sm^{2+} fluorescence pressure scale [189]. The diffraction patterns were recorded on MAR345 and MAR555 detectors and integrated with the Fit2D software [190]. Full profile Rietveld refinements were performed using the FullProf software [191].

6.2.2 Results and discussion

Figure 6.1 shows diffraction patterns of $Sr_3Ir_2O_7$ at high pressure. At ambient temperature in a helium pressure-transmitting medium, $Sr_3Ir_2O_7$ remained in its tetragonal phase (space group $I4/mmm$) up to pressures of 53 GPa. It has been argued that the rotations of the oxygen octahedra are correlated, resulting in a 90° twinned structure of pseudo-orthorhombic space groups *Bbcb* and *Acaa* [185]. As our measurements were performed on powder samples, the

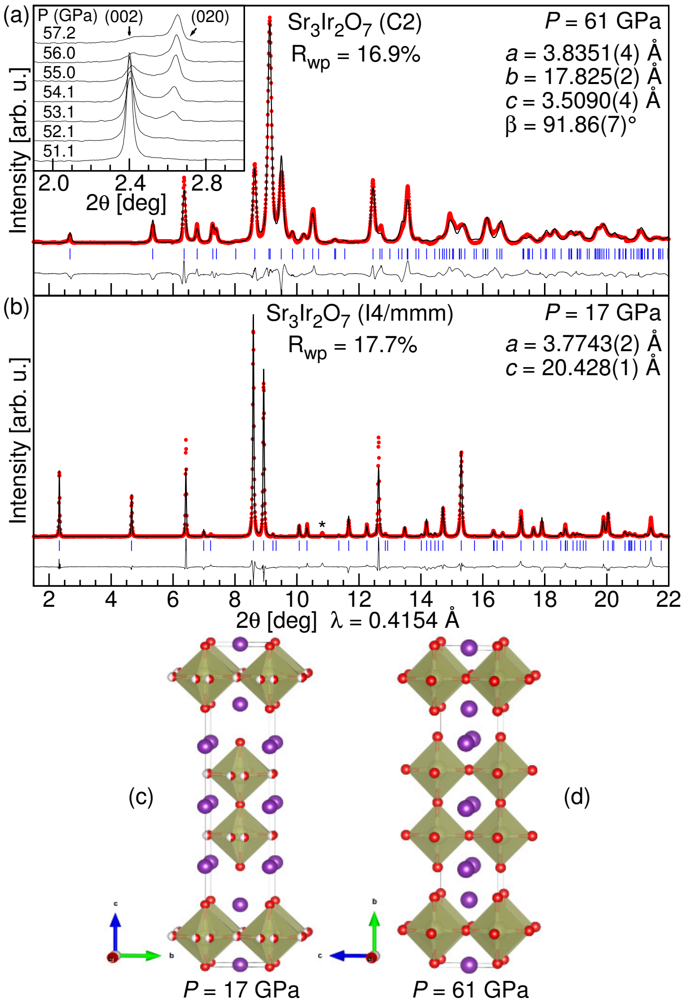

Figure 6.1: Integrated XRD spectra of $Sr_3Ir_2O_7$ at high pressure at ambient temperature. (a) $Sr_3Ir_2O_7$ in its monoclinic phase (space group $C2$) at 61 GPa; (d) the corresponding structure. (b) Tetragonal phase of $Sr_3Ir_2O_7$ (space group $I4/mmm$) at 17 GPa; (c) the corresponding structure. In (a) and (b) the red circles are background-subtracted data points, the black solid line presents the Rietveld refinement, blue tick marks are the calculated Bragg reflections, and the residuals of the refinement are shown by the black line beneath. Reflections from $SrB_4O_7{:}Sm^{2+}$ are marked by an asterisk. The inset in (a) shows the pressure evolution of small-angle reflections. In (c) and (d) the iridium atoms are shown in bronze, the oxygen atoms in red and the strontium atoms in purple. The structures in (c) and (d) were visualised via VESTA [33].

tetragonal $I4/mmm$ structural model effectively averages over the two space groups. Rietveld refinements of our data confirm the $I4/mmm$ structural model to be adequate. Crucially, no second-order structural transition was observed near 14 GPa. We used helium as the pressure-transmitting medium (at room temperature and 20 K), and not neon as in Ref. [187] (at 25 K).

The discrepancy between our studies may therefore arise from non-hydrostatic pressure conditions in the previous study. In our experiments, the pressure was determined by SrB_4O_7:Sm^{2+} fluorescence. No significant broadening of the SrB_4O_7:Sm^{2+} fluorescence line shapes was observed, indicating that hydrostatic pressure conditions were maintained. At pressures above 54 GPa, new reflections started to emerge. Further increase in pressure resulted in the complete disappearance of the $I4/mmm$ reflections. The new reflections could be indexed in a C-centered monoclinic system, space group $C2/m$, $C2$, or Cm. Indexing the reflections in a higher symmetry proved not to be possible. This high-pressure phase remained stable up to 61 GPa, the maximum pressure reached in this study. Upon decompression, the monoclinic signature disappeared below 49 GPa, corresponding to a 5 GPa hysteresis, and $Sr_3Ir_2O_7$ reverted to its tetragonal phase.

The high-pressure phase of $Sr_3Ir_2O_7$ departs strongly from the Ruddlesden-Popper structure. Most notably, the reflection with the largest d spacing, (002) at $2\theta = 2.4°$, disappears [see inset Fig. 6.1(a)]. All new reflections possess smaller d spacings, indicating that the long c axis of tetragonal $Sr_3Ir_2O_7$ is not retained. Figure 6.2 shows the refined lattice parameters as a function of pressure. In the tetragonal phase, the compression of $Sr_3Ir_2O_7$ is anisotropic; the c axis exhibits a lower compressibility than the a=b axes. The c/a ratio thus increases with pressure by 3% to a critical value, where the system undergoes a structural phase transition. This anisotropic compression is indicative of an increased in-plane rotation of the oxygen octahedra, although a refinement of oxygen position was not possible with our data. We indexed the new phase in a monoclinic symmetry, space group $C2/m$, $C2$, or Cm, with lattice parameters $a = 3.8351(4)$ Å, $b = 17.825(2)$ Å, $c = 3.5090(4)$ Å, and $\beta = 91.86(7)°$ at 61 GPa. This corresponds to a volume collapse of 4% at the phase transition. A discontinuity of 2 Å in the long c axis of the unit cell (labeled the b axis in the high-pressure phase) occurs at the structural transition. The lower compressibility along the c axis in the tetragonal phase appears to be alleviated by the phase transition to monoclinic symmetry. A Vinet equation of state was fitted to the pressure-volume data of the tetragonal phase, yielding a bulk modulus of $B_0 = 157(4)$ GPa [$B_0' = 4.3(3)$], in agreement with the literature [187].

To understand the transition at an atomic level, we attempted structural refinement of the high-pressure phase through Rietveld analysis. In general, the calculated intensities adequately reproduced the experimental intensities

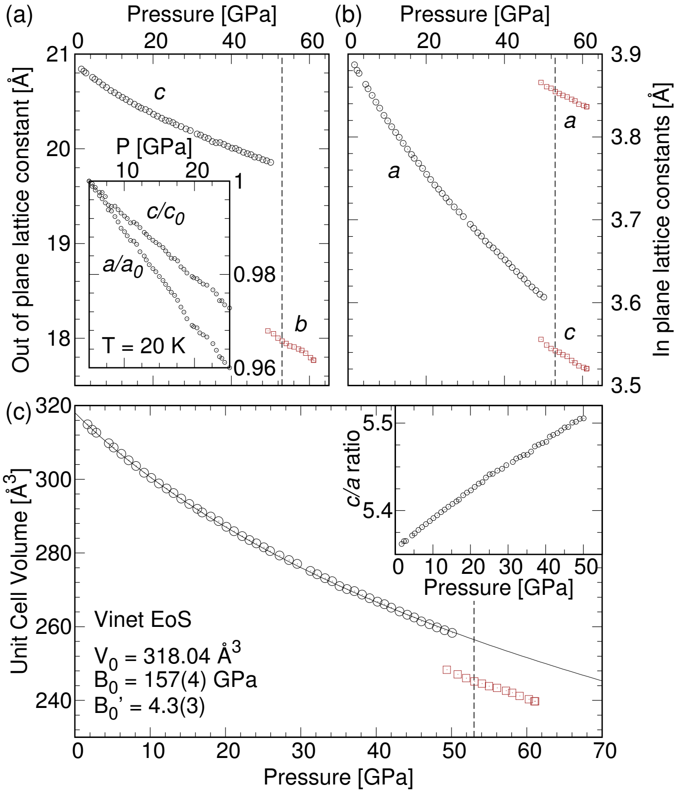

Figure 6.2: Equation of state of $Sr_3Ir_2O_7$. (a) and (b) Lattice parameters as a function of pressure at room temperature. The inset in (a) shows the normalised lattice constants as a function of pressure at 20 K. (c) Equation of state of $Sr_3Ir_2O_7$ at room temperature. The solid line is a Vinet-type fit to the observed equation of state of $Sr_3Ir_2O_7$. The inset in (c) shows the c/a ratio as a function of pressure at room temperature. In all panels, the black circles and red squares correspond to low and high pressure phases of $Sr_3Ir_2O_7$, respectively, and the dotted line indicates the transition pressure of 53 GPa. Data points of the high-pressure phase falling below the dotted line were taken during decompression.

when one of the perovskite bilayers of $Sr_3Ir_2O_7$ is translated by half a unit cell in the basal plane [see Fig. 6.1(d)]. This may explain the discontinuity in the lattice parameter of the long axis of the unit cell: While in its tetragonal phase the compressibility along the c axis appears to be limited, this is alleviated in the monoclinic phase by an alteration in the stacking sequence of the perovskite bilayers. Furthermore, in the high-pressure phase, the Sr^{2+} atoms are arranged within a single plane, parallel to the a axis in the unit cell. To accommodate this configuration, the lattice parameter a increases, such that the in-plane lattice constants (a, c) of the monoclinic structure differ by 10%, and the angle spanned between a and c is 91.8°.

This high-pressure structure could be described in the space group $C2/m$. The presence of a mirror plane perpendicular to the b axis minimises the number of free parameters to two y coordinates for Ir and Sr (the second Sr atom is fixed at $y = 0.5$). However, the fit of the calculated diffraction pattern was deemed unsatisfactory. We therefore decided to remove the mirror plane and adopt $C2$ symmetry. This allowed to move atoms independently along the y axis, through two adjustable y coordinates for both Ir and Sr atoms (here, the third Sr atom remained at $y = 0.5$). This provided the best fit to the data. The weighted profile Rietveld R factor R_{wp} of the monoclinic structure at 61 GPa then became comparable to the one obtained from the Rietveld refinement of the tetragonal phase at 17 GPa. Thus our proposed structural model for the high-pressure phase provides as good a description of the data as the $I4/mmm$ structure at lower pressures. We note that the visually worse fit of the calculated intensities at 61 GPa at least partly originates from the difficulty of accurately describing the background at very high pressures.

As the oxygen atoms scatter only weakly compared to the electron-heavy Ir and Sr atoms, a precise refinement of the oxygen positions was not possible for the high-pressure phase. Small deviations from the proposed positions shown in Fig. 6.1(d), for example through rotations or tilts of the octahedral complex, cannot be excluded or confirmed within the quality of our data.

6.3 High-pressure x-ray absorption spectroscopy

High-pressure x-ray absorption spectroscopy was performed at the Ir L_3 and L_2 absorption edges of $Sr_3Ir_2O_7$. The branching ratio of white line intensities continuously decreases with pressure, reflecting a reduction in the expectation value of the spin-orbit coupling operator, $\langle \mathbf{L} \cdot \mathbf{S} \rangle$. Up to the high-pressure structural transition at 53 GPa, this behavior can be explained within a single-ion model, where pressure increases the strength of the cubic crystal field, which suppresses the spin-orbit induced hybridization of $J_{\text{eff}} = 3/2$ and e_g levels. We observe a further reduction of the branching ratio above the structural transition, which cannot be explained within a single-ion model of spin-orbit coupling and cubic crystal fields. This change in $\langle \mathbf{L} \cdot \mathbf{S} \rangle$ in the high-pressure, metallic phase of $Sr_3Ir_2O_7$ could arise from non-cubic crystal fields or a bandwidth-driven hybridization of $J_{\text{eff}} = 1/2$, $3/2$ states, and suggests that the electronic ground state significantly deviates from the $J_{\text{eff}} = 1/2$ limit.

6.3.1 Experimental method

High-pressure energy-dispersive XAS experiments were performed in transmission mode at beamline ID24, ESRF [128]. We conducted independent experiments at the Ir L_3 and L_2 absorption edges. Single crystals of $Sr_3Ir_2O_7$ were flux-grown as described in Ref. [92]. Symmetrical diamond anvil cells (DACs) fitted with polycrystalline diamond anvils were used. Single crystals of $Sr_3Ir_2O_7$ were ground into a powder, pressed into a pellet and then loaded into DACs. Pressure was measured in situ using Ruby fluorescence. Neon was used as the pressure transmitting medium. All data were taken at room temperature.

6.3.2 Results and discussion

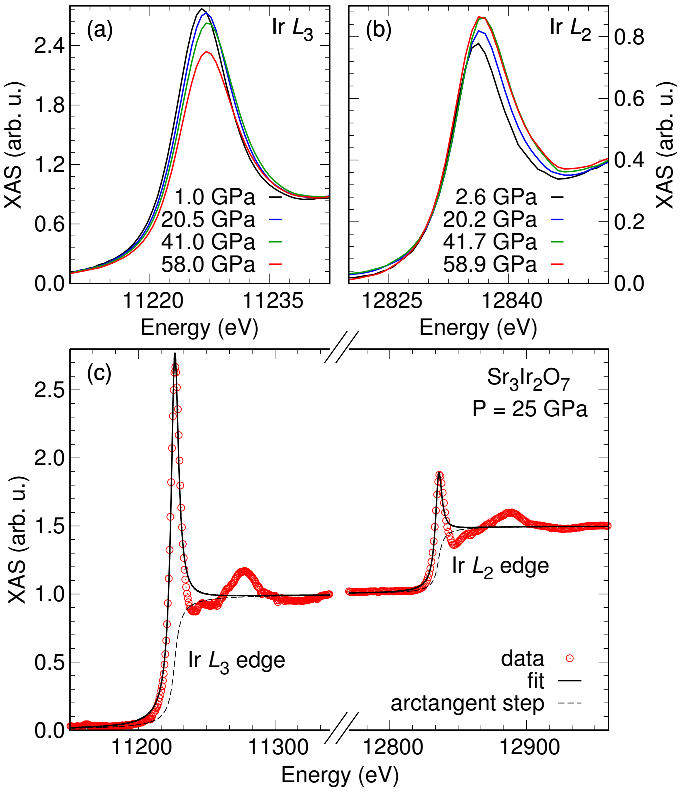

Figure 6.3: High-pressure XAS data of $Sr_3Ir_2O_7$. (a, b) Pressure evolution of XAS at the Ir L_3, L_2 absorption edges. (c) Representative fitted XAS at 25 GPa at the Ir L_3 and L_2 absorption edges of $Sr_3Ir_2O_7$. The red circles are the normalised data points, the black solid line is a fit of arctangent and a Lorentzian functions, as described in the text.

Figure 6.3 shows representative high-pressure x-ray absorption spectra at the Ir L_3 and L_2 edges of $Sr_3Ir_2O_7$. The data were normalised to absorption steps of 1 and 1/2 for L_3 and L_2 edges, respectively.

The branching ratio of integrated white line intensities, $\mathrm{BR} = I_{L_3}/I_{L_2}$, can be directly related to the angular part of the ground state expectation value of the spin-orbit coupling, via $\mathrm{BR} = (2+r)/(1-r)$, where $r = \langle \mathbf{L}\cdot\mathbf{S}\rangle / n_h$ and n_h is the number of holes in the $5d$ manifold [192, 193]. Without performing any data analysis, it is clear that the observed BR exceeds the statistical value of 2 [obtained by setting $\langle \mathbf{L}\cdot\mathbf{S}\rangle = 0$ (we define $\hbar = 1$ throughout the manuscript)], which shows that the spin-orbit coupling plays a significant role in the electronic ground state. Near ambient pressure, we estimate a BR of ~ 5.5, which, by using $n_h = 5$ for Ir^{4+} ($5d^5$), yields $\langle \mathbf{L}\cdot\mathbf{S}\rangle \sim 2.7$. This SOC expectation value is characteristic for Ir^{4+} in a cubic crystal field [101, 138, 194, 195].

However, as Laguna-Marco *et al.* [138] pointed out, the SOC expectation value exceeds that expected from a $J_{\mathrm{eff}} = 1/2$ state: If we consider the ground-state as one hole in the $J_{\mathrm{eff}} = 1/2$ doublet and four holes in the e_g levels, only the $J_{\mathrm{eff}} = 1/2$ state would contribute to the SOC expectation value, as $\langle \mathbf{L}\cdot\mathbf{S}\rangle_{e_g} = 0$, and we obtain a total $\langle \mathbf{L}\cdot\mathbf{S}\rangle = 1$. Thus a model that considers SOC acting on the isolated t_{2g} submanifold cannot accurately describe XAS data of iridates. Generally, this approximation is valid when the spin-orbit coupling ζ can be treated as a weak perturbation on the cubic CF $10Dq$, i.e. when $\zeta \ll 10Dq$. However, in Ir^{4+} iridates, typically $\zeta \sim \frac{1}{6}10Dq$, which makes this assumption questionable. Indeed, using configuration interaction calculations, Laguna-Marco *et al.* have shown that SOC hybridizes $J_{\mathrm{eff}} = 3/2$ and e_g levels [138]. The hybridized e_g levels then acquire non-zero $\langle \mathbf{L}\cdot\mathbf{S}\rangle_{e_g}$, and SOC expectation values comparable to the ones derived from the BR could be obtained.

In order to accurately extract the BR from our data, we used a simple model that captures the salient features of the XAS spectra. Following Ref. [194], we fitted the absorption step and white line with an arctangent and a Lorentzian function:

$$\mu(E) = C_0 + C_1 E + C_2 \arctan\left(\frac{E - E_0}{\Gamma/2}\right) + \frac{C_3}{1 + \left(\frac{E-E_0}{\Gamma/2}\right)^2}$$

where C_0 and C_1 describe a first-order polynomial background, C_2 the absorption step height, C_3 the white line intensity; E_0 and Γ are the centre and width of both arctan and Lorentzian functions.

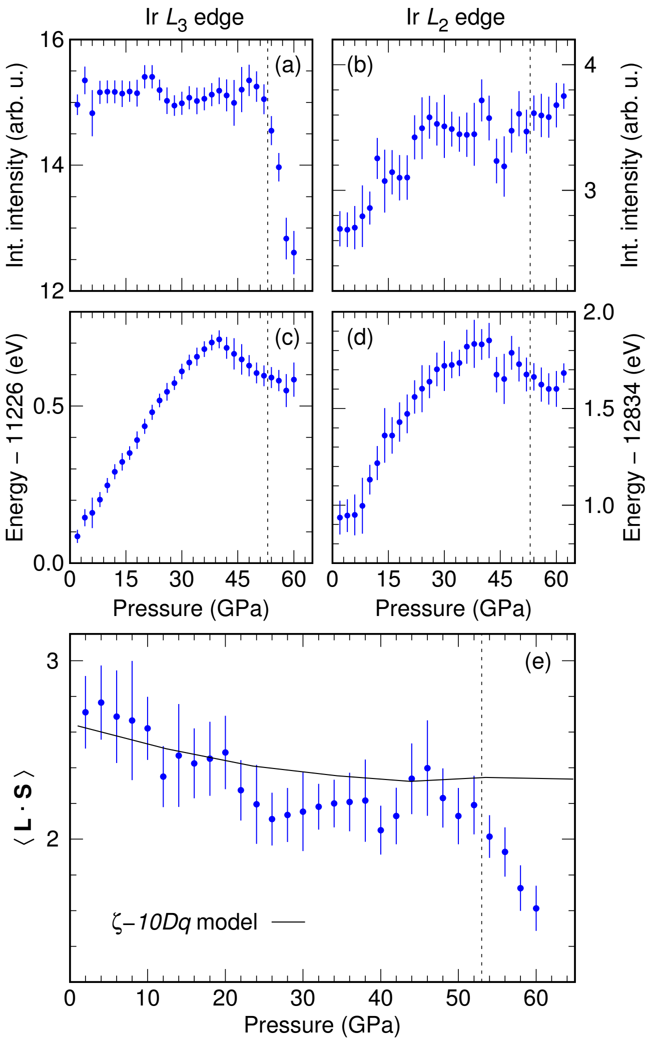

Figure 6.4: Fitted high-pressure XAS data of $Sr_3Ir_2O_7$. (a, b) White line integrated intensities at the Ir L_3, L_2 edge. (c, d) White line energy position (absorption maximum) of the Ir L_3, L_2 edge. (e) Ground state SOC expectation value $\langle \mathbf{L} \cdot \mathbf{S} \rangle$, deduced from the branching ratio of integrated intensities of white lines, I_{L_3}/I_{L_2}. The solid line is the calculated $\langle \mathbf{L} \cdot \mathbf{S} \rangle$ of the $\zeta - 10Dq$ model, using $\zeta = 0.45$ eV and $10Dq$ values from Ref. [100]. In all panels, the vertical dotted line denotes the structural phase transition at 53 GPa.

Figure 6.3 shows representative fitted XAS spectra. Here, the polynomial background was subtracted and the data and fitted parameters normalised to the respective absorption step. While the fit fails to reproduce details, such as oscillations above the absorption edge, it allows to accurately track the evolution of the white line in a robust manner. This was confirmed by numerical integration of the white line after subtracting the arctangent step, which, within error bars, yielded identical BRs (data not shown). Due to the large number of collected pressure points ($\sim$ 100 spectra per absorption edge), we binned the data in 2 GPa intervals.

Figure 6.4 shows the results of the fitting procedure. Panels (a-b) show that up to the structural transition, the integrated intensity of the L_3 edge white line stays approximately constant, whereas an increase in intensity occurs at the L_2 edge. Across the structural transition ($\sim$ 53 GPa), the L_3 edge white line intensity shows a rapid decrease, while the L_2 edge intensity is largely unaffected. The resulting BR, converted to $\langle \mathbf{L}\cdot\mathbf{S}\rangle$ as described above, is plotted in panel (e). Panels (c, d) show the evolution of the energy position of the white line (defined as the absorption maximum) at $L_{3,2}$ edges. At both edges, the white line energy increases approximately linearly with pressure, followed by an anomaly incipient at $\sim$ 40 GPa.

Branching ratio in the low-pressure phase

We first discuss the pressure evolution of the BR up to the structural transition. From ambient pressure to 50 GPa, the BR gradually decreases from $\sim$ 5.5 to $\sim$ 4. Rewriting $\langle \mathbf{L}\cdot\mathbf{S}\rangle = n_h(\mathrm{BR}-2)/(\mathrm{BR}+1)$, this corresponds to $\langle \mathbf{L}\cdot\mathbf{S}\rangle$ reducing from $\sim$ 2.7 to $\sim$ 2.3.

Following the argument by Laguna-Marco *et al.* [138], we here consider $t_{2g} - e_g$ hybridisation within a single-ion model of SOC ζ and cubic CF splitting $10Dq$. While a single-ion approach fails to account for band effects, such as covalence and electron-electron interactions, it has the advantage of focussing on the two dominant energy scales and therefore requires only a single adjustable parameter, $\zeta/10Dq$. The Hamiltonian of spin-orbit coupling ζ and cubic CF $10Dq$, in a basis of e_g and t_{2g} orbitals, can be written as:

$$\begin{aligned}\mathcal{H} &= \mathcal{H}_{\mathrm{SOC}} + \mathcal{H}_{\text{Cubic-CF}}\\ &= \zeta\mathbf{L}\cdot\mathbf{S} + Dq\left(6d^{\dagger}_{e_g,\sigma}d_{e_g,\sigma} - 4d^{\dagger}_{t_{2g},\sigma}d_{t_{2g},\sigma}\right)\end{aligned}$$

We will not show the explicit eigenfunctions for lack of space. Their energies are:

$$\begin{aligned}E_{e_g} &= \tfrac{1}{20}(2\Delta - 5\zeta + 5c)\\ E_{J_{\mathrm{eff}}=1/2} &= \tfrac{1}{5}\left(5\zeta - 2\Delta\right)\\ E_{J_{\mathrm{eff}}=3/2} &= \tfrac{1}{20}\left(2\Delta - 5\zeta - 5c\right)\end{aligned}$$

where $c = \sqrt{4\Delta^2 + 4\Delta\zeta + 25\zeta^2}$ and we have defined $\Delta = 10Dq$ for ease of notation. For simplicity, we have kept the labels $\{|e_g\rangle, |J_{\text{eff}} = 1/2\rangle, |J_{\text{eff}} = 3/2\rangle\}$, which strictly only apply in the absence of $t_{2g} - e_g$ hybridisation. The resulting intra-t_{2g} excitation energies are:

$$\begin{aligned} e_1 &= \tfrac{1}{4}\left(2\Delta - 5\zeta + c\right) && \text{for } |J_{\text{eff}} = 1/2\rangle \rightarrow |e_g\rangle \\ e_2 &= \tfrac{1}{4}\left(-2\Delta + 5\zeta + c\right) && \text{for } |J_{\text{eff}} = 1/2\rangle \rightarrow |J_{\text{eff}} = 3/2\rangle \end{aligned}$$

The expectation values of the spin-orbit coupling are:

$$\begin{aligned} \langle \mathbf{L} \cdot \mathbf{S} \rangle_{e_g} &= \tfrac{1}{4c}\left(2\Delta + 25\zeta - c\right) \\ \langle \mathbf{L} \cdot \mathbf{S} \rangle_{J_{\text{eff}}=1/2} &= 1 \\ \langle \mathbf{L} \cdot \mathbf{S} \rangle_{J_{\text{eff}}=3/2} &= \tfrac{-1}{4c}\left(2\Delta + 25\zeta + c\right) \end{aligned}$$

In the limit of $10Dq \gg \zeta$, we can recover the $\langle \mathbf{L} \cdot \mathbf{S} \rangle$ values derived by configuration interaction calculations of Ref. [138].

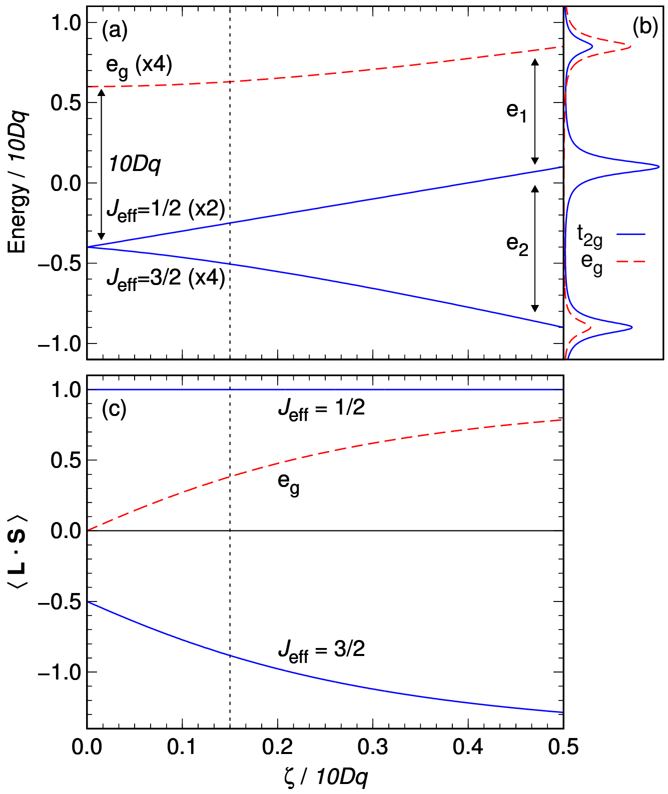

Figure 6.5: Spin-orbit induced hybridisation of t_{2g} and e_g levels within $\zeta - 10Dq$ model. (a) $5d$ energy levels as a function of $\zeta/10Dq$. The energy differences e_1 and e_2 are defined in the text. (b) Projection of $5d$ wavefunctions onto t_{2g} (blue, solid line) and e_g (red, dashed line) basis states at $\zeta/10Dq = 0.5$. (c) $\langle \mathbf{L} \cdot \mathbf{S} \rangle$ contributions of individual $5d$ levels as a function of $\zeta/10Dq$. In panels (a) and (c) the vertical dotted line denotes a characteristic value of $\zeta/10Dq = 0.15$ for Ir^{4+} iridates at ambient pressure.

The resulting CF levels and corresponding $\langle \mathbf{L} \cdot \mathbf{S} \rangle$ values are plotted in Fig. 6.5, as a function of $\zeta/10Dq$. Effectively, this $\zeta - 10Dq$ model allows to continuously tune the electronic state from a $J_{\text{eff}} = 1/2$, $3/2$ and e_g splitting ($\zeta \ll 10Dq$) to a $J = 3/2$, $5/2$ splitting of the d manifold ($\zeta \gg 10Dq$). As $\zeta/10Dq$ increases, $J_{\text{eff}} = 3/2$ and e_g levels start to hybridise, which has a pronounced effect on their $\langle \mathbf{L} \cdot \mathbf{S} \rangle$ values. It is interesting to note that the orbital character of the $J_{\text{eff}} = 1/2$ doublet is unaffected. Hence models relying on a single hole in a $J_{\text{eff}} = 1/2$ state remain accurate even in the presence of SOC-induced $t_{2g} - e_g$ mixing. However, when other states are involved, as is the case in a XAS experiment, $t_{2g} - e_g$ hybridisation should be taken into account.

Near ambient pressure, analysis of our XAS data of $Sr_3Ir_2O_7$ yields $\langle \mathbf{L} \cdot \mathbf{S} \rangle \sim 2.7$. For iridates, typical empirical values of ζ and $10Dq$ are 0.45 eV [17, 121, 133, 134] and 3 eV [100, 134, 196], respectively, thus $\zeta/10Dq = 0.15$. The ground state SOC expectation value can then be computed as $\langle \mathbf{L} \cdot \mathbf{S} \rangle = 4 \langle \mathbf{L} \cdot \mathbf{S} \rangle_{e_g} + \langle \mathbf{L} \cdot \mathbf{S} \rangle_{J_{\text{eff}}=1/2} \approx 2.5$. This is indeed close to the experimental estimate, and suggests that the $\zeta - 10Dq$ model can accurately describe the observed BR. However, it must be emphasised that some variation exists in the value of the BR and the strength of the cubic CF reported in the literature [100, 101, 194, 196]. Without clear consensus in the experimental data, precise energy scales cannot be extracted. Nevertheless, the evolution of the BR within a consistent experimental setup offers valuable insights into the character of the electronic ground state.

As pressure is applied, the strength of the cubic CF increases, reducing $\zeta/10Dq$ and hence quenching $\langle \mathbf{L} \cdot \mathbf{S} \rangle_{e_g}$. Empirical values of $10Dq$ in $Sr_3Ir_2O_7$ as a function of pressure were determined by RIXS [100]. Using these $10Dq$ values and a constant SOC of $\zeta = 0.45$ eV [17, 121, 133, 134] (we assume that the ζ is mainly determined by the nuclear charge and therefore pressure independent), we computed $\langle \mathbf{L} \cdot \mathbf{S} \rangle$ within the $\zeta - 10Dq$ model. Fig. 6.4(e) shows that despite its simplicity, the model offers a good description of the XAS data, up to 53 GPa. The observed reduction in the BR up to the structural transition can thus be understood from an increase in $10Dq$ with pressure, which suppresses the SOC-induced $t_{2g} - e_g$ hybridisation.

We also note that the sum of white line intensities at L_2 and L_3 edges increases by $\sim 5\%$ up to phase transition. Appealing to the absorption sum rule, this indicates that the number of holes in the Ir $5d$ states increases with pressure [197]. This is supported by density functional theory (DFT) calculations, which suggest that the strong Ir-O hybridization at high-pressure increases the number of holes on the Ir site [182]. However, at all pressures, taking into account a pressure dependent number of holes has negligible effect on the obtained $\langle \mathbf{L} \cdot \mathbf{S} \rangle$ values.

Pressure dependence of white line energy

We now discuss the pressure dependence of the white line energy, defined as the absorption maximum. We observe a linear increase of 17.4(2) meV/ GPa and 26(1) meV/ GPa at L_3 and L_2 edges, respectively (note that the absorption threshold, defined as the inflection point of the XAS, shows the same pressure dependence). The leading order term of a cubic CF is a spherically symmetric potential, inversely proportional to the Ir-O distance, which raises the energy of all d-levels. Assuming the $2p$ core levels are sufficiently screened from the CF, as a function of pressure, this term should approximately linearly increase the energy required to promote an electron from $2p$ to $5d$ levels [182].

The white line energy increases more rapidly with pressure at the L_2 edge. Selection rules imply that only XAS transitions to empty e_g levels are allowed at the L_2 edge, not to the half-occupied $J_{\text{eff}} = 1/2$ doublet. The energy position of the L_2 edge white line will hence be determined by the energy of e_g states. At the L_3 edge, transitions to both $J_{\text{eff}} = 1/2$ and e_g states are allowed, and the white line will be a sum of t_{2g} and e_g final states. This is reflected in the width of the L_3 edge white line, which is about 1 eV broader than the L_2 edge white line (individual t_{2g} and e_g features cannot be discerned). As $10Dq$ increases with pressure, the energy of t_{2g} levels is lowered relative to e_g states, and hence the overall L_3 edge energy will be raised less. In this case, we would also expect that the width of the white line at the L_3 edge increases more rapidly with pressure. However, within the experimental uncertainty, the increase in width is identical for both edges (about 9 meV/ GPa), indicating that it is dominated by bandwidth and core-hole lifetime broadening.

Above 40 GPa, the white line energy of both edges shifts to lower energies. This behaviour could be related to the IMT: In a metallic state, additional transitions to the Fermi level become allowed, which could move the white line to lower energies. However, the observed energy shift is substantially larger than the insulating gap ($\sim$ 100 meV). Furthermore, as at the L_2 edge only transitions to e_g states are allowed, one should be insensitive to the appearance of a $J_{\text{eff}} = 1/2$ Fermi surface. We hence deem an IMT unlikely as the cause of this anomaly.

An alternative interpretation is that the strength of the cubic CF decreases above 40 GPa. This would explain the energy shift at both absorption edges, as well as the larger effect observed at the L_2 edge. Indeed, RIXS measurements indicate that $10Dq$ reaches a maximum at 40 GPa and then decreases at higher pressures [100]. The microscopic origin of this effect is however unclear.

Branching ratio in the high-pressure phase

Finally, we discuss the XAS data across the high-pressure structural transition of $Sr_3Ir_2O_7$. Above 50 GPa, we observe a further decrease in the BR, which originates from the L_3 edge white line intensity. At 60 GPa, the BR reaches $\sim$ 3, which corresponds to $\langle \mathbf{L} \cdot \mathbf{S} \rangle \sim 1.6$. Within the $\zeta - 10Dq$ model, the ratio of SOC to cubic CF would have to reach $\zeta/10Dq \sim 0.05$ in order to yield this $\langle \mathbf{L} \cdot \mathbf{S} \rangle$ value. This would require either $10Dq \sim 10$ eV at constant $\zeta = 0.45$ eV, or alternatively $\zeta \sim 0.18$ eV at $10Dq = 3.5$ eV. Both options appear unphysical and incompatible with high-pressure RIXS data [100], and we conclude that a single-ion model of SOC and cubic crystal fields cannot provide an adequate description of the electronic state of $Sr_3Ir_2O_7$ at high-pressure.

While uncertainties remain regarding the details of the high-pressure structure of $Sr_3Ir_2O_7$, the first-order nature of the transition and resulting monoclinic unit cell could result in significant changes to the local environment of the Ir ion [182]. For example, if the transition results in strong non-cubic crystal fields, the $J_{\text{eff}} = 1/2$ state will not be fully realised, resulting in a suppression of $\langle \mathbf{L} \cdot \mathbf{S} \rangle$. Another interpretation of a reduced BR at high-pressure was provided in a XAS study on Sr_2IrO_4, where it was argued that a continuous, bandwidth-driven mixing of $J_{\text{eff}} = 1/2$, $3/2$ levels occurs with pressure [101]. Most recently, a decrease in the BR was observed at only 2 GPa in β-Li_2IrO_3, which the authors attributed to a reduction in the effective electronic correlations [198].

It is insightful to compare our observations to high-pressure RIXS data of $Sr_3Ir_2O_7$, where the $|J_{\text{eff}} = 1/2\rangle \rightarrow |J_{\text{eff}} = 3/2\rangle$ crystal field excitation was measured [100]. This feature is sensitive to the amount of CF distortions and bandwidth of J_{eff} states [130]. Above the structural transition, the excitation energy of this feature increased by 15% compared to its ambient pressure value [100]. This increase in excitation energy could suggest a splitting of $J_{\text{eff}} = 3/2$ states through non-cubic CFs, which may not be resolvable due to large t_{2g}

bandwidths.

While our data show that a reconstruction of the $5d$ states occurs at the high-pressure transition of $Sr_3Ir_2O_7$, the resulting electronic state remains uncertain. Nevertheless, we can make the following conclusions. First, while the BR at 60 GPa is substantially reduced from its ambient pressure value, the resulting $\langle \mathbf{L} \cdot \mathbf{S} \rangle$ value is not yet fully quenched, which implies that the spin-orbit coupling still affects the electronic ground state. Whether the remaining $\langle \mathbf{L} \cdot \mathbf{S} \rangle$ originates solely from holes in the e_g levels, or still has a considerable contribution from the hole in the $J_{\text{eff}} = 1/2$ level, cannot be ascertained from our data. Second, we note that all of the above scenarios leading to a reduced BR will affect the orbital character of the hole in the ground state doublet. In particular, this suggests that in the high-pressure phase of $Sr_3Ir_2O_7$ a significant departure from the ideal $J_{\text{eff}} = 1/2$ limit occurs.

6.4 Conclusion

We have studied the evolution of structural and electronic aspects of $Sr_3Ir_2O_7$ with XRD and XAS to unprecedented pressures. We discovered a first-order structural transition at 54 GPa, preceded by a strongly anisotropic compression, characterised by an increasing c/a ratio with pressure. The high-pressure phase could be indexed in a monoclinic symmetry (space group $C2/m$, $C2$, or Cm). Rietveld refinement of the diffraction data suggests that the stacking sequence of the perovskite bilayers is altered in the high-pressure structure. A precise refinement of the oxygen positions was not possible due to the comparatively weak x-ray scattering signal compared to Ir and Sr atoms. This high-pressure structural transition is in close vicinity to the transition to a confined metal at 59 GPa reported by Ding *et al.* [100].

The branching ratio of the XAS white lines at the Ir $L_{2,3}$ absorption edges of $Sr_3Ir_2O_7$ allowed to characterise the electronic ground state at high-pressure. Up to the structural transition at 53 GPa, the BR gradually reduces from ~ 5.5 to ~ 4 (corresponding to $\langle \mathbf{L} \cdot \mathbf{S} \rangle \sim 2.7$ and ~ 2.3, respectively). This could be understood within a single-ion model that takes into account the spin-orbit induced hybridization of t_{2g} and e_g levels. As the cubic CF increases with pressure, SOC-induced mixing of $J_{\text{eff}} = 3/2$ and e_g states is suppressed, reducing the $\langle \mathbf{L} \cdot \mathbf{S} \rangle$ contribution of e_g levels. Above the structural transition, the BR decreases further, eventually yielding $\langle \mathbf{L} \cdot \mathbf{S} \rangle \sim 1.6$ (BR ~ 3) at 60

GPa. This could be driven by non-cubic crystal fields or bandwidth-driven mixing of $J_{\text{eff}} = 1/2$, $3/2$ levels, and indicates that the high-pressure electronic state of $Sr_3Ir_2O_7$ significantly deviates from the $J_{\text{eff}} = 1/2$ state known at ambient conditions.

Thus our study of $Sr_3Ir_2O_7$ at high-pressure suggests that the emergence of the unconventional metallic state is coupled to a structural transition. The high-pressure metallic state only shows conductance in the basal plane [100], which may be related to the altered stacking sequence of perovskite bilayers. In this context, our result that the electronic ground state of the high-pressure phase departs from the $J_{\text{eff}} = 1/2$ model may also be of importance to understand the unusual transport properties.

Chapter 7

Conclusion

In this thesis, we used x-ray techniques to first detect the symmetry breaking at magnetic and structural transitions in iridates, and then to characterise the resulting state. Additionally, a comprehensive calculation of resonant x-ray scattering (RXS) cross-sections for iridates was provided. We here conclude with a short summary of the key results, concerning the RXS cross-sections, the magnetic transition in pyrochlore iridates, and the structural transition in $Sr_3Ir_2O_7$. Possible future directions of this research are discussed.

7.1 RXS of pyrochlore iridates

In order to obtain a better understanding of resonant x-ray scattering in iridates, we derived RXS cross-sections within a single-ion model of Ir^{4+} at the Ir $L_{2,3}$ edges. Although similar calculations were reported previously, here a more comprehensive account was provided, by computing atomic scattering tensors of all transitions within the t_{2g} manifold, in the presence of tetragonal or trigonal distortions, for an arbitrary magnetic moment direction. This makes the cross-sections applicable to a large variety of iridates. One key result is the formulation of the x-ray resonant magnetic scattering (XRMS) amplitude at the Ir L_3 edge, which, in the presence of non-cubic crystal fields, deviates from the spherical approximation commonly used in the literature. In particular, when the magnetic moment has components in the xy plane and along the z axis of the local trigonal or tetragonal basis, the spherical approximation becomes inaccurate. Furthermore, through the example of pyrochlore iridates, we demonstrated for the first time how comparing resonant charge and resonant magnetic intensities can reveal the absolute size of the magnetic moment, a quantity that was hitherto believed to be elusive to resonant x-ray scattering.

Resonant elastic x-ray scattering (REXS) experiments at the Ir L_3 of the pyrochlore iridates $R_2\mathrm{Ir}_2\mathrm{O}_7$, where R = Sm, Nd, Tb, has shown that all samples adopt a $\mathbf{k} = 0$ magnetic propagation vector, with ordering temperatures of 110 K (Sm), 4 K (Nd) and 70 K (Tb). Analysis of the cross-sections revealed that only two magnetic structures can describe the data, the all-in all-out (AIAO, Γ_3) or xy (Γ_5) antiferromagnetic structure. Given the literature published during and after this research was conducted, it is probable that all three pyrochlores order in AIAO fashion. Assuming that this is the case, we estimated an ordered moment size of $\sim 0.3\,\mu_B$ (Sm) and $\sim 0.06\,\mu_B$ (Tb). The suppressed ordering temperature and reduced magnetic moment size for $\mathrm{Tb}_2\mathrm{Ir}_2\mathrm{O}_7$ indicates off-stoichiometry, possibly due to excess Tb ions occupying Ir sites.

The magnetic dynamics of these pyrochlore iridates were studied by resonant inelastic x-ray scattering (RIXS). For Sm and Nd, below the magnetic ordering temperature, sharp, dispersive, low-energy features appeared. These could be well described by single-magnon excitations from an AIAO ground state, using a minimal nearest-neighbour Hamiltonian of Heisenberg exchange (27 meV) and Dzyaloshinskii-Moriya interaction (5 meV) within linear spin-wave theory. For Tb, temperature-dependent excitations could only be observed close to the antiferromagnetic wave-vector. This, along with the weakened magnetic state observed in REXS measurements, suggests that the electronic correlations are reduced, and a strong-coupling, linear spin-wave theory description of the magnetic excitations may become inadequate. In all samples, crystal-field excitations within the t_{2g} manifold show that the Ir ion experiences strong compressive trigonal distortions, of similar magnitude to the atomic spin-orbit coupling. A minor trend towards stronger trigonal fields with larger rare-earth ion radius was found. The intensities of these excitations could be accurately computed using the single-ion RXS cross-sections.

Thus our combined elastic and inelastic measurements strongly suggests an AIAO magnetic ground state for pyrochlore iridates, which enables a Weyl semimetal state to be realised. Furthermore, the determination of the ordered moment size and the establishment of the low-energy effective spin Hamiltonian should be of great interest to determine the applicability of various theoretical models that have been put forth to describe the microscopic physics at play in this family of materials.

7.2 $Sr_3Ir_2O_7$ at high pressure

The pressure-evolution of structural and electronic properties of $Sr_3Ir_2O_7$ was studied with x-ray diffraction and x-ray absorption spectroscopy. Up to 54 GPa, the compression of the unit cell is strongly anisotropic, the c axis compresses slower than the a, b axes. At 54 GPa, a first-order structural transition from tetragonal to monoclinic symmetry was found, close to the insulator-metal transition at 59 GPa [100]. The structure was solved by Rietveld refinement, which revealed that the stacking arrangement of perovskite layers is altered in the high-pressure phase. Additionally, the electronic ground state was investigated through the branching ratio of x-ray absorption spectroscopy intensities at the Ir $L_{2,3}$ edges. Up to the phase transition, we found that the evolution of the electronic state is driven by an increase in the cubic crystal field, which reduces the spin-orbit induced hybridisation of crystal-field levels. In the high-pressure phase, the effect of spin-orbit coupling appears reduced, possibly due to a bandwidth or non-cubic crystal field induced hybridisation of orbitals, and the electronic ground state deviates from the $J_{\text{eff}} = 1/2$ picture.

Our results thus indicate that high-pressure structural and insulator-metal transitions are coupled in $Sr_3Ir_2O_7$. The altered stacking arrangement of perovskite layers in the high-pressure phase could be related to the emergence of the confined metallic behaviour, where conductance only occurs in the basal planes. The precise electronic state in this phase remains to be determined, but our data suggest that it significantly differs from the $J_{\text{eff}} = 1/2$ state at ambient conditions. The high-pressure metallisation of $Sr_3Ir_2O_7$ hence appears most singular, and shows that much remains to be understood on the nature of the insulator-metal transition in the strong spin-orbit coupling limit.

7.3 Future perspectives

The Ir^{4+} single-ion RXS cross-sections could be successfully applied to REXS experiments, perhaps the most interesting result here is the determination of the absolute size of the magnetic moment. This approach could be readily extended to infer the absolute moment size in other iridates, all that is required is a good understanding of the electronic ground state and accurate intensities of resonant charge and resonant magnetic contributions. Furthermore, the formulation of the XRMS cross-section at the Ir L_3 edge in the presence of non-cubic crystal fields might prompt re-examination of published literature

[26, 27, 29, 30], or inform future experiments on the limitations of the spherical approximation for determining magnetic structures of iridates with XRMS.

It would be of interest to use the derived RXS cross-sections more extensively to interpret RIXS experiments. While the intensities of crystal-field excitations could be accurately computed, the magnetic excitations were treated by standard linear-spin wave theory without incorporating RIXS cross-sections. Momentum dispersive excitations imply going beyond a single-ion formalism, which should remain tractable in a strong coupling limit. This would allow insight into the contribution of multi-magnon processes, as well as the relative strengths of magnetic and crystal-field excitations, which might lead to a better understanding of the low-energy RIXS response of pyrochlore iridates. However, it is conceivable that more sophisticated techniques will be required to fully reproduce the experimental data, such as exact diagonalisation of phenomenological Hubbard models.

Experimentally, a few possible future investigations present themselves. A REXS experiment of $Nd_2Ir_2O_7$ under high magnetic fields would be of great interest to understand the role of Ir magnetism in the field-induced insulator-metal transition [161, 162]. We have demonstrated how such an experiment could be conducted through the example of $Sm_2Ir_2O_7$. In this study, we have also shown how circular polarisation can induce interference between XRMS and resonant charge scattering contributions. This, along with the RXS cross-sections, could be used to map the magnetic domains [166] and the absolute moment size in real space. There are many other pyrochlore iridates that might be synthesised as single crystals, and their magnetic structures could be examined using the approach detailed in this thesis. However, the question of the type of Ir magnetic structure in pyrochlore iridates can be largely considered to be solved, in some small part due to the experiments presented in this thesis, which may dampen the interest to perform such investigations.

The all-in all-out magnetic structure suggest that a Weyl semimetal state could be realised in pyrochlore iridates. Unfortunately, many experiments and theory now indicate that pyrochlore iridates are strongly-correlated [37, 51, 52], which makes the prediction of Weyl semimetal state uncertain. In this context, the $Tb_2Ir_2O_7$ sample described in this thesis might be of interest, as the suppressed magnetic order indicates a more weakly correlated state. Indeed, it was recently suggested that when the ordered moment falls below $0.2\,\mu_B$ a transition to Weyl semimetal state could occur [167]. The "smoking-gun" signature of the WSM could be found via angle-resolved photoemission spectroscopy, but this technique is very challenging in pyrochlore iridates. Other measurements, such as magneto-transport, optical conductivity and the Hall effect should all show signatures of a Weyl semimetal phase, but may be more difficult to interpret.

Concerning RIXS experiments on pyrochlore iridates, the presence of a broad continuum of excitations between 0 and 300 meV energy loss remains to be addressed. As this feature was observed regardless of whether long-range magnetic order exists, we conjectured that it could arise from resonant phonons or short-range magnetic excitations. More detailed temperature and momentum dependences could be of interest, as well as a RIXS study at the Ir L_2 edge. A non-resonant inelastic x-ray scattering (IXS) study might also be enlightening, as it could reveal phonon modes and their energy scale. Furthermore, if there is significant magnon-phonon coupling, for which there has been some evidence in iridates [199, 200], the magnetic dynamics are also accessible with IXS, as was recently demonstrated in Ref. [201]. As IXS offers a superior energy resolution of only a few meV, one might obtain a much clearer picture of the magnetic excitations. In the intermediate term, advances in RIXS instrumentation will offer a 10 meV energy resolution at the Ir L_3 edge [178], which could disentangle the low-energy RIXS response of pyrochlore iridates.

The study of perovskite iridates under pressure has shown some features of interest. The structural transition we discovered in the bilayer $Sr_3Ir_2O_7$ may be coupled to the emergence of the unconventional metallic state [100]. Unfortunately, the very high pressure of 53 GPa severely restricts the experimental techniques available to further characterise this phase. Our XAS data indicate that the electronic state in this phase departs from the one at ambient conditions, which could be confirmed by a RIXS experiment at the Ir L_2 edge, where the strength of inelastic features could be used as a proxy for how well the $J_{\text{eff}} = 1/2$ state is realised. Preliminary high-pressure REXS experiments were already performed on $Sr_3Ir_2O_7$, which showed that long-range magnetic order persists to at least 14 GPa. While it is feasible to extend such investigations up to 60 GPa, it poses a formidable experimental challenge.

Furthermore, preliminary x-ray diffraction experiments have shown that a similar structural transition occurs in the single-layer Sr_2IrO_4 at around 50 GPa. It could be of interest to further characterise this high-pressure phase of Sr_2IrO_4 using resistivity and resonant x-ray scattering techniques. The close similarity of Sr_2IrO_4 to parent compounds of cuprate superconductors may provide an incentive for these challenging experiments.

Bibliography

[1] W. Witczak-Krempa, G. Chen, Y. B. Kim, and L. Balents, Annu. Rev. of Condens. Matter Phys. **5**, 57 (2014).

[2] J. G. Rau, E. K.-H. Lee, and H.-Y. Kee, Annu. Rev. of Condens. Matter Phys. **7**, 195 (2016).

[3] B. J. Kim, H. Jin, S. J. Moon, J.-Y. Kim, B.-G. Park, C. S. Leem, J. Yu, T. W. Noh, C. Kim, S.-J. Oh, J.-H. Park, V. Durairaj, G. Cao, and E. Rotenberg, Phys. Rev. Lett. **101**, 076402 (2008).

[4] B. J. Kim, H. Ohsumi, T. Komesu, S. Sakai, T. Morita, H. Takagi, and T. Arima, Science **323**, 1329 (2009).

[5] G. Jackeli and G. Khaliullin, Phys. Rev. Lett. **102**, 017205 (2009).

[6] D. Pesin and L. Balents, Nat. Phys. **6**, 376 (2010).

[7] B.-J. Yang and Y. B. Kim, Phys. Rev. B **82**, 085111 (2010).

[8] X. Wan, A. M. Turner, A. Vishwanath, and S. Y. Savrasov, Phys. Rev. B **83**, 205101 (2011).

[9] W. Witczak-Krempa and Y. B. Kim, Phys. Rev. B **85**, 045124 (2012).

[10] R. Schaffer, E. K.-H. Lee, B.-J. Yang, and Y. B. Kim, Rep. Prog. Phys. **79**, 094504 (2016).

[11] S. Blundell, *Magnetism in Condensed Matter* (Oxford University Press, 2003).

[12] L. D. Landau and E. M. Lifshitz, *Quantum mechanics: non-relativistic theory* (Pergamon, 1958).

[13] D. Khomskii, *Transition metal compounds* (Cambridge University Press, 2014).

[14] A. Abragam and B. Bleaney, *Electron paramagnetic resonance of transition ions*, International series of monographs on physics (Clarendon P., 1970).

[15] F. Wang and T. Senthil, Phys. Rev. Lett. **106**, 136402 (2011).

[16] A. Kitaev, Ann. Phys. **321**, 2 (2006).

[17] J. Kim, D. Casa, M. H. Upton, T. Gog, Y.-J. Kim, J. F. Mitchell, M. van Veenendaal, M. Daghofer, J. van den Brink, G. Khaliullin, and B. J. Kim, Phys. Rev. Lett. **108**, 177003 (2012).

[18] Y. K. Kim, O. Krupin, J. D. Denlinger, A. Bostwick, E. Rotenberg, Q. Zhao, J. F. Mitchell, J. W. Allen, and B. J. Kim, Science **345**, 187 (2014).

[19] Y. J. Yan, M. Q. Ren, H. C. Xu, B. P. Xie, R. Tao, H. Y. Choi, N. Lee, Y. J. Choi, T. Zhang, and D. L. Feng, Phys. Rev. X **5**, 041018 (2015).

[20] A. de la Torre, S. McKeown Walker, F. Y. Bruno, S. Riccó, Z. Wang, I. Gutierrez Lezama, G. Scheerer, G. Giriat, D. Jaccard, C. Berthod, T. K. Kim, M. Hoesch, E. C. Hunter, R. S. Perry, A. Tamai, and F. Baumberger, Phys. Rev. Lett. **115**, 176402 (2015).

[21] X. Chen, T. Hogan, D. Walkup, W. Zhou, M. Pokharel, M. Yao, W. Tian, T. Z. Ward, Y. Zhao, D. Parshall, C. Opeil, J. W. Lynn, V. Madhavan, and S. D. Wilson, Phys. Rev. B **92**, 075125 (2015).

[22] H. Watanabe, T. Shirakawa, and S. Yunoki, Phys. Rev. Lett. **110**, 027002 (2013).

[23] Y. Yang, W.-S. Wang, J.-G. Liu, H. Chen, J.-H. Dai, and Q.-H. Wang, Phys. Rev. B **89**, 094518 (2014).

[24] Z. Y. Meng, Y. B. Kim, and H.-Y. Kee, Phys. Rev. Lett. **113**, 177003 (2014).

[25] S. Di Matteo and M. R. Norman, Phys. Rev. B **94**, 075148 (2016).

[26] A. Biffin, R. D. Johnson, I. Kimchi, R. Morris, A. Bombardi, J. G. Analytis, A. Vishwanath, and R. Coldea, Phys. Rev. Lett. **113**, 197201 (2014).

[27] A. Biffin, R. D. Johnson, S. Choi, F. Freund, S. Manni, A. Bombardi, P. Manuel, P. Gegenwart, and R. Coldea, Phys. Rev. B **90**, 205116 (2014).

[28] J. A. Sears, M. Songvilay, K. W. Plumb, J. P. Clancy, Y. Qiu, Y. Zhao, D. Parshall, and Y.-J. Kim, Phys. Rev. B **91**, 144420 (2015).

[29] S. Hwan Chun, J.-W. Kim, J. Kim, H. Zheng, C. C. Stoumpos, C. D. Malliakas, J. F. Mitchell, K. Mehlawat, Y. Singh, Y. Choi, T. Gog, A. Al-Zein, M. M. Sala, M. Krisch, J. Chaloupka, G. Jackeli, G. Khaliullin, and B. J. Kim, Nat. Phys. **11**, 462 (2015).

[30] S. C. Williams, R. D. Johnson, F. Freund, S. Choi, A. Jesche, I. Kimchi, S. Manni, A. Bombardi, P. Manuel, P. Gegenwart, and R. Coldea, Phys. Rev. B **93**, 195158 (2016).

[31] A. Banerjee, J. Yan, J. Knolle, C. A. Bridges, M. B. Stone, M. D. Lumsden, D. G. Mandrus, D. A. Tennant, R. Moessner, and S. E. Nagler, Science **356**, 1055 (2017).

[32] M. Z. Hasan and C. L. Kane, Rev. Mod. Phys. **82**, 3045 (2010).

[33] K. Momma and F. Izumi, J. Appl. Crystallogr. **41**, 653 (2008).

[34] K. Matsuhira, M. Wakeshima, Y. Hinatsu, and S. Takagi, J. Phys. Soc. Jpn. **80**, 094701 (2011).

[35] D. Yanagishima and Y. Maeno, J. Phys. Soc. Jpn. **70**, 2880 (2001).

[36] K. Matsuhira, M. Wakeshima, R. Nakanishi, T. Yamada, A. Nakamura, W. Kawano, S. Takagi, and Y. Hinatsu, J. Phys. Soc. Jpn. **76**, 043706 (2007).

[37] K. Ueda, J. Fujioka, and Y. Tokura, Phys. Rev. B **93**, 245120 (2016).

[38] A. M. Turner and A. Vishwanath, ArXiv e-prints (2013), arXiv:1301.0330 [cond-mat.str-el] .

[39] O. Vafek and A. Vishwanath, Annu. Rev. Condens. Matter Phys. **5**, 83 (2014).

[40] N. P. Armitage, E. J. Mele, and A. Vishwanath, ArXiv e-prints (2017), arXiv:1705.01111 [cond-mat.str-el] .

[41] H. Weyl, Z. Phys. **56**, 330 (1929).

[42] H. Nielsen and M. Ninomiya, Phys. Lett. B **130**, 389 (1983).

[43] C. Herring, Phys. Rev. **52**, 365 (1937).

[44] B. Q. Lv, H. M. Weng, B. B. Fu, X. P. Wang, H. Miao, J. Ma, P. Richard, X. C. Huang, L. X. Zhao, G. F. Chen, Z. Fang, X. Dai, T. Qian, and H. Ding, Phys. Rev. X **5**, 031013 (2015).

[45] B. Q. Lv, N. Xu, H. M. Weng, J. Z. Ma, P. Richard, X. C. Huang, L. X. Zhao, G. F. Chen, C. E. Matt, F. Bisti, V. N. Strocov, J. Mesot, Z. Fang, X. Dai, T. Qian, M. Shi, and H. Ding, Nat. Phys. **11**, 724 (2015).

[46] S.-Y. Xu, I. Belopolski, N. Alidoust, M. Neupane, G. Bian, C. Zhang, R. Sankar, G. Chang, Z. Yuan, C.-C. Lee, S.-M. Huang, H. Zheng, J. Ma, D. S. Sanchez, B. Wang, A. Bansil, F. Chou, P. P. Shibayev, H. Lin, S. Jia, and M. Z. Hasan, Science **349**, 613 (2015).

[47] S.-Y. Xu, N. Alidoust, I. Belopolski, Z. Yuan, G. Bian, T.-R. Chang, H. Zheng, V. N. Strocov, D. S. Sanchez, G. Chang, C. Zhang, D. Mou, Y. Wu, L. Huang, C.-C. Lee, S.-M. Huang, B. Wang, A. Bansil, H.-T. Jeng, T. Neupert, A. Kaminski, H. Lin, S. Jia, and M. Zahid Hasan, Nat. Phys. **11**, 748 (2015).

[48] L. X. Yang, Z. K. Liu, Y. Sun, H. Peng, H. F. Yang, T. Zhang, B. Zhou, Y. Zhang, Y. F. Guo, M. Rahn, D. Prabhakaran, Z. Hussain, S. K. Mo, C. Felser, B. Yan, and Y. L. Chen, Nat. Phys. **11**, 728 (2015).

[49] A. Go, W. Witczak-Krempa, G. S. Jeon, K. Park, and Y. B. Kim, Phys. Rev. Lett. **109**, 066401 (2012).

[50] W. Witczak-Krempa, A. Go, and Y. B. Kim, Phys. Rev. B **87**, 155101 (2013).

[51] H. Shinaoka, S. Hoshino, M. Troyer, and P. Werner, Phys. Rev. Lett. **115**, 156401 (2015).

[52] H. Zhang, K. Haule, and D. Vanderbilt, Phys. Rev. Lett. **118**, 026404 (2017).

[53] S. T. Bramwell and M. J. P. Gingras, Science **294**, 1495 (2001).

[54] M. J. P. Gingras, C. V. Stager, N. P. Raju, B. D. Gaulin, and J. E. Greedan, Phys. Rev. Lett. **78**, 947 (1997).

[55] B. Canals and C. Lacroix, Phys. Rev. Lett. **80**, 2933 (1998).

[56] M. Hermele, M. P. A. Fisher, and L. Balents, Phys. Rev. B **69**, 064404 (2004).

[57] S. Petit, E. Lhotel, B. Canals, M. Ciomaga Hatnean, J. Ollivier, H. Mutka, E. Ressouche, A. R. Wildes, M. R. Lees, and G. Balakrishnan, Nat. Phys. **12**, 746 (2016).

[58] O. Benton, Phys. Rev. B **94**, 104430 (2016).

[59] Y. Onose, T. Ideue, H. Katsura, Y. Shiomi, N. Nagaosa, and Y. Tokura, Science **329**, 297 (2010).

[60] A. Mook, J. Henk, and I. Mertig, Phys. Rev. Lett. **117**, 157204 (2016).

[61] J. N. Reimers, A. J. Berlinsky, and A.-C. Shi, Phys. Rev. B **43**, 865 (1991).

[62] P. W. Anderson, Phys. Rev. **115**, 2 (1959).

[63] T. Moriya, Phys. Rev. **120**, 91 (1960).

[64] M. Elhajal, B. Canals, R. Sunyer, and C. Lacroix, Phys. Rev. B **71**, 094420 (2005).

[65] B.-J. Yang and N. Nagaosa, Phys. Rev. Lett. **112**, 246402 (2014).

[66] S. Zhao, J. M. Mackie, D. E. MacLaughlin, O. O. Bernal, J. J. Ishikawa, Y. Ohta, and S. Nakatsuji, Phys. Rev. B **83**, 180402 (2011).

[67] S. M. Disseler, C. Dhital, T. C. Hogan, A. Amato, S. R. Giblin, C. de la Cruz, A. Daoud-Aladine, S. D. Wilson, and M. J. Graf, Phys. Rev. B **85**, 174441 (2012).

[68] S. M. Disseler, C. Dhital, A. Amato, S. R. Giblin, C. de la Cruz, S. D. Wilson, and M. J. Graf, Phys. Rev. B **86**, 014428 (2012).

[69] M. J. Graf, S. M. Disseler, C. Dhital, T. Hogan, M. Bojko, A. Amato, H. Luetkens, C. Baines, D. Margineda, S. R. Giblin, M. Jura, and S. D. Wilson, J. Phys. Conf. Ser. **551**, 012020 (2014).

[70] K. Tomiyasu, K. Matsuhira, K. Iwasa, M. Watahiki, S. Takagi, M. Wakeshima, Y. Hinatsu, M. Yokoyama, K. Ohoyama, and K. Yamada, J. Phys. Soc. Jpn. **81**, 034709 (2012).

[71] E. Lefrançois, V. Simonet, R. Ballou, E. Lhotel, A. Hadj-Azzem, S. Kodjikian, P. Lejay, P. Manuel, D. Khalyavin, and L. C. Chapon, Phys. Rev. Lett. **114**, 247202 (2015).

[72] H. Guo, C. Ritter, and A. C. Komarek, Phys. Rev. B **94**, 161102 (2016).

[73] H. Sagayama, D. Uematsu, T. Arima, K. Sugimoto, J. J. Ishikawa, E. O'Farrell, and S. Nakatsuji, Phys. Rev. B **87**, 100403 (2013).

[74] J. P. Clancy, H. Gretarsson, E. K. H. Lee, D. Tian, J. Kim, M. H. Upton, D. Casa, T. Gog, Z. Islam, B.-G. Jeon, K. H. Kim, S. Desgreniers, Y. B. Kim, S. J. Julian, and Y.-J. Kim, Phys. Rev. B **94**, 024408 (2016).

[75] E. Lefrançois, V. Cathelin, E. Lhotel, J. Robert, P. Lejay, C. V. Colin, B. Canals, F. Damay, J. Ollivier, B. Fåk, L. C. Chapon, R. Ballou, and V. Simonet, Nat. Commun. **8**, 209 (2017).

[76] D. Kumar, S. Y. Chen, M. K. Lee, C. M. N. Kumar, R. Aldus, and L. J. Chang, J. Phys. Confer. Ser. **828**, 012008 (2017).

[77] M. C. Shapiro, S. C. Riggs, M. B. Stone, C. R. de la Cruz, S. Chi, A. A. Podlesnyak, and I. R. Fisher, Phys. Rev. B **85**, 214434 (2012).

[78] M. Nakayama, T. Kondo, Z. Tian, J. J. Ishikawa, M. Halim, C. Bareille, W. Malaeb, K. Kuroda, T. Tomita, S. Ideta, K. Tanaka, M. Matsunami, S. Kimura, N. Inami, K. Ono, H. Kumigashira, L. Balents, S. Nakatsuji, and S. Shin, Phys. Rev. Lett. **117**, 056403 (2016).

[79] G. Cao and P. Schlottmann, ArXiv e-prints (2017), arXiv:1704.06007 [cond-mat.str-el] .

[80] S. J. Moon, H. Jin, K. W. Kim, W. S. Choi, Y. S. Lee, J. Yu, G. Cao, A. Sumi, H. Funakubo, C. Bernhard, and T. W. Noh, Phys. Rev. Lett. **101**, 226402 (2008).

[81] S. Boseggia, R. Springell, H. C. Walker, H. M. Rønnow, C. Rüegg, H. Okabe, M. Isobe, R. S. Perry, S. P. Collins, and D. F. McMorrow, Phys. Rev. Lett. **110**, 117207 (2013).

[82] S. Boseggia, H. C. Walker, J. Vale, R. Springell, Z. Feng, R. S. Perry, M. M. Sala, H. M. Rønnow, S. P. Collins, and D. F. McMorrow, J. Phys. Condens. Matter **25**, 422202 (2013).

[83] C. Dhital, T. Hogan, Z. Yamani, C. de la Cruz, X. Chen, S. Khadka, Z. Ren, and S. D. Wilson, Phys. Rev. B **87**, 144405 (2013).

[84] M. K. Crawford, M. A. Subramanian, R. L. Harlow, J. A. Fernandez-Baca, Z. R. Wang, and D. C. Johnston, Phys. Rev. B **49**, 9198 (1994).

[85] R. Coldea, S. M. Hayden, G. Aeppli, T. G. Perring, C. D. Frost, T. E. Mason, S.-W. Cheong, and Z. Fisk, Phys. Rev. Lett. **86**, 5377 (2001).

[86] Y. Okada, D. Walkup, H. Lin, C. Dhital, T.-R. Chang, S. Khadka, W. Zhou, H.-T. Jeng, M. Paranjape, A. Bansil, Z. Wang, S. D. Wilson, and V. Madhavan, Nat. Mater. **12**, 707 (2013).

[87] B. M. Wojek, M. H. Berntsen, S. Boseggia, A. T. Boothroyd, D. Prabhakaran, D. F. McMorrow, H. M. Rønnow, J. Chang, and O. Tjernberg, J. Phys. Condens. Matter **24**, 415602 (2012).

[88] Q. Wang, Y. Cao, J. A. Waugh, S. R. Park, T. F. Qi, O. B. Korneta, G. Cao, and D. S. Dessau, Phys. Rev. B **87**, 245109 (2013).

[89] P. D. C. King, T. Takayama, A. Tamai, E. Rozbicki, S. M. Walker, M. Shi, L. Patthey, R. G. Moore, D. Lu, K. M. Shen, H. Takagi, and F. Baumberger, Phys. Rev. B **87**, 241106 (2013).

[90] H. J. Park, C. H. Sohn, D. W. Jeong, G. Cao, K. W. Kim, S. J. Moon, H. Jin, D.-Y. Cho, and T. W. Noh, Phys. Rev. B **89**, 155115 (2014).

[91] J. W. Kim, Y. Choi, J. Kim, J. F. Mitchell, G. Jackeli, M. Daghofer, J. van den Brink, G. Khaliullin, and B. J. Kim, Phys. Rev. Lett. **109**, 037204 (2012).

[92] S. Boseggia, R. Springell, H. C. Walker, A. T. Boothroyd, D. Prabhakaran, D. Wermeille, L. Bouchenoire, S. P. Collins, and D. F. McMorrow, Phys. Rev. B **85**, 184432 (2012).

[93] H. Zhang, K. Haule, and D. Vanderbilt, Phys. Rev. Lett. **111**, 246402 (2013).

[94] J. Kim, A. H. Said, D. Casa, M. H. Upton, T. Gog, M. Daghofer, G. Jackeli, J. van den Brink, G. Khaliullin, and B. J. Kim, Phys. Rev. Lett. **109**, 157402 (2012).

[95] M. Moretti Sala, V. Schnells, S. Boseggia, L. Simonelli, A. Al-Zein, J. G. Vale, L. Paolasini, E. C. Hunter, R. S. Perry, D. Prabhakaran, A. T. Boothroyd, M. Krisch, G. Monaco, H. M. Rønnow, D. F. McMorrow, and F. Mila, Phys. Rev. B **92**, 024405 (2015).

[96] G. Cao, V. Durairaj, S. Chikara, L. E. DeLong, S. Parkin, and P. Schlottmann, Phys. Rev. B **76**, 100402 (2007).

[97] R. Arita, J. Kuneš, A. V. Kozhevnikov, A. G. Eguiluz, and M. Imada, Phys. Rev. Lett. **108**, 086403 (2012).

[98] D. Hsieh, F. Mahmood, D. H. Torchinsky, G. Cao, and N. Gedik, Phys. Rev. B **86**, 035128 (2012).

[99] H. Watanabe, T. Shirakawa, and S. Yunoki, Phys. Rev. B **89**, 165115 (2014).

[100] Y. Ding, L. Yang, C.-C. Chen, H.-S. Kim, M. J. Han, W. Luo, Z. Feng, M. Upton, D. Casa, J. Kim, T. Gog, Z. Zeng, G. Cao, H.-k. Mao, and M. van Veenendaal, Phys. Rev. Lett. **116**, 216402 (2016).

[101] D. Haskel, G. Fabbris, M. Zhernenkov, P. P. Kong, C. Q. Jin, G. Cao, and M. van Veenendaal, Phys. Rev. Lett. **109**, 027204 (2012).

[102] D. A. Zocco, J. J. Hamlin, B. D. White, B. J. Kim, J. R. Jeffries, S. T. Weir, Y. K. Vohra, J. W. Allen, and M. B. Maple, J. Phys. Condens. Matter **26**, 255603 (2014).

[103] I. V. Solovyev, V. V. Mazurenko, and A. A. Katanin, Phys. Rev. B **92**, 235109 (2015).

[104] K. Ishii, I. Jarrige, M. Yoshida, K. Ikeuchi, J. Mizuki, K. Ohashi, T. Takayama, J. Matsuno, and H. Takagi, Phys. Rev. B **83**, 115121 (2011).

[105] S. Boseggia, R. Springell, H. C. Walker, A. T. Boothroyd, D. Prabhakaran, S. P. Collins, and D. F. McMorrow, J. Phys. Condens. Matter **24**, 312202 (2012).

[106] M. M. Sala, C. Henriquet, L. Simonelli, R. Verbeni, and G. Monaco, J. Electron Spectrosc. Relat. Phenom. **188**, 150 (2013).

[107] S. K. Choi, R. Coldea, A. N. Kolmogorov, T. Lancaster, I. I. Mazin, S. J. Blundell, P. G. Radaelli, Y. Singh, P. Gegenwart, K. R. Choi, S.-W. Cheong, P. J. Baker, C. Stock, and J. Taylor, Phys. Rev. Lett. **108**, 127204 (2012).

[108] http://dx.doi.org/10.14324/000.ds.10042850 .

[109] J. S. Schwinger, *On radiation by electrons in a betatron*, Tech. Rep. (SCAN-9611207, 1996).

[110] J. Baruchel, J.-L. Hodeau, M. S. Lehmann, J.-R. Regnard, and C. Schlenker, *Neutron and synchrotron radiation for condensed matter studies* (Springer, 1993).

[111] M. Altarelli, in *Magnetism: A Synchrotron Radiation Approach* (Springer, 2006) pp. 201–242.

[112] L. J. P. Ament, M. van Veenendaal, T. P. Devereaux, J. P. Hill, and J. van den Brink, Rev. Mod. Phys. **83**, 705 (2011).

[113] Y. Joly, S. D. Matteo, and O. Bunău, Eur. Phys. J. Spec. Top. **208**, 21 (2012).

[114] D. F. McMorrow, K. A. McEwen, U. Steigenberger, H. M. Rønnow, and F. Yakhou, Phys. Rev. Lett. **87**, 057201 (2001).

[115] Y. Murakami, J. P. Hill, D. Gibbs, M. Blume, I. Koyama, M. Tanaka, H. Kawata, T. Arima, Y. Tokura, K. Hirota, and Y. Endoh, Phys. Rev. Lett. **81**, 582 (1998).

[116] F. M. F. de Groot, P. Kuiper, and G. A. Sawatzky, Phys. Rev. B **57**, 14584 (1998).

[117] B. H. Kim and J. van den Brink, Phys. Rev. B **92**, 081105 (2015).

[118] J. van den Brink, Europhys. Lett. **80**, 47003 (2007).

[119] L. J. P. Ament, G. Ghiringhelli, M. M. Sala, L. Braicovich, and J. van den Brink, Phys. Rev. Lett. **103**, 117003 (2009).

[120] H. Gretarsson, J. P. Clancy, Y. Singh, P. Gegenwart, J. P. Hill, J. Kim, M. H. Upton, A. H. Said, D. Casa, T. Gog, and Y.-J. Kim, Phys. Rev. B **87**, 220407 (2013).

[121] M. Moretti Sala, K. Ohgushi, A. Al-Zein, Y. Hirata, G. Monaco, and M. Krisch, Phys. Rev. Lett. **112**, 176402 (2014).

[122] J. Strempfer, S. Francoual, D. Reuther, D. K. Shukla, A. Skaugen, H. Schulte-Schrepping, T. Kracht, and H. Franz, J. Synchrotron Radiat. **20**, 541 (2013).

[123] R. Verbeni, M. Kocsis, S. Huotari, M. Krisch, G. Monaco, F. Sette, and G. Vanko, J. Phys. Chem. Solids **66**, 2299 (2005), 5th International Conference on Inelastic X-ray Scattering (IXS 2004).

[124] C. Ponchut, J. M. Rigal, J. Clément, E. Papillon, A. Homs, and S. Petitdemange, J. Instrum. **6**, C01069 (2011).

[125] H. H. Johann, Z. Phys. **69**, 185 (1931).

[126] W. A. Bassett, High Press. Res. **29**, 163 (2009).

[127] K. Syassen, High Press. Res. **28**, 75 (2008).

[128] S. Pascarelli, O. Mathon, T. Mairs, I. Kantor, G. Agostini, C. Strohm, S. Pasternak, F. Perrin, G. Berruyer, P. Chappelet, C. Clavel, and M. C. Dominguez, J. Synchrotron Radiat. **23**, 353 (2016).

[129] L. J. P. Ament, *Resonant inelastic x-ray scattering studies of elementary excitations*, Ph.D. thesis, Leiden University (2010).

[130] L. J. P. Ament, G. Khaliullin, and J. van den Brink, Phys. Rev. B **84**, 020403 (2011).

[131] M. Moretti Sala, S. Boseggia, D. F. McMorrow, and G. Monaco, Phys. Rev. Lett. **112**, 026403 (2014).

[132] S. Boseggia, *Magnetic order and excitations in perovskite iridates studied with resonant X-ray scattering techniques*, Ph.D. thesis, University College London (2014).

[133] X. Liu, V. M. Katukuri, L. Hozoi, W.-G. Yin, M. P. M. Dean, M. H. Upton, J. Kim, D. Casa, A. Said, T. Gog, T. F. Qi, G. Cao, A. M. Tsvelik, J. van den Brink, and J. P. Hill, Phys. Rev. Lett. **109**, 157401 (2012).

[134] H. Gretarsson, J. P. Clancy, X. Liu, J. P. Hill, E. Bozin, Y. Singh, S. Manni, P. Gegenwart, J. Kim, A. H. Said, D. Casa, T. Gog, M. H. Upton, H.-S. Kim, J. Yu, V. M. Katukuri, L. Hozoi, J. van den Brink, and Y.-J. Kim, Phys. Rev. Lett. **110**, 076402 (2013).

[135] K. Ohgushi, J.-i. Yamaura, H. Ohsumi, K. Sugimoto, S. Takeshita, A. Tokuda, H. Takagi, M. Takata, and T.-h. Arima, Phys. Rev. Lett. **110**, 217212 (2013).

[136] L. Hozoi, H. Gretarsson, J. P. Clancy, B.-G. Jeon, B. Lee, K. H. Kim, V. Yushankhai, P. Fulde, D. Casa, T. Gog, J. Kim, A. H. Said, M. H. Upton, Y.-J. Kim, and J. van den Brink, Phys. Rev. B **89**, 115111 (2014).

[137] J. Kim, M. Daghofer, A. H. Said, T. Gog, J. van den Brink, G. Khaliullin, and B. J. Kim, Nat. Commun. **5**, 4453 (2014).

[138] M. A. Laguna-Marco, D. Haskel, N. Souza-Neto, J. C. Lang, V. V. Krishnamurthy, S. Chikara, G. Cao, and M. van Veenendaal, Phys. Rev. Lett. **105**, 216407 (2010).

[139] L. E. C. Savary, *Exotic Phenomena in Quantum Pyrochlore Materials*, Ph.D. thesis, University of California Santa Barbara (2014).

[140] J. c. v. Chaloupka and G. Khaliullin, Phys. Rev. B **94**, 064435 (2016).

[141] H. A. Kramers and W. Heisenberg, Z. Phys. **31**, 681 (1925).

[142] L. C. Chapon and S. W. Lovesey, J. Phys. Condens. Matter **23**, 252201 (2011).

[143] Y. Hirata, K. Ohgushi, J.-i. Yamaura, H. Ohsumi, S. Takeshita, M. Takata, and T.-h. Arima, Phys. Rev. B **87**, 161111 (2013).

[144] X. Liu, T. Berlijn, W.-G. Yin, W. Ku, A. Tsvelik, Y.-J. Kim, H. Gretarsson, Y. Singh, P. Gegenwart, and J. P. Hill, Phys. Rev. B **83**, 220403 (2011).

[145] S. Calder, G.-X. Cao, M. D. Lumsden, J. W. Kim, Z. Gai, B. C. Sales, D. Mandrus, and A. D. Christianson, Phys. Rev. B **86**, 220403 (2012).

[146] S. Calder, G.-X. Cao, S. Okamoto, J. W. Kim, V. R. Cooper, Z. Gai, B. C. Sales, M. D. Lumsden, D. Mandrus, and A. D. Christianson, Phys. Rev. B **89**, 081104 (2014).

[147] S. Calder, J. W. Kim, G.-X. Cao, C. Cantoni, A. F. May, H. B. Cao, A. A. Aczel, M. Matsuda, Y. Choi, D. Haskel, B. C. Sales, D. Mandrus, M. D. Lumsden, and A. D. Christianson, Phys. Rev. B **92**, 165128 (2015).

[148] J. P. Hannon, G. T. Trammell, M. Blume, and D. Gibbs, Phys. Rev. Lett. **61**, 1245 (1988).

[149] C. Dhital, S. Khadka, Z. Yamani, C. de la Cruz, T. C. Hogan, S. M. Disseler, M. Pokharel, K. C. Lukas, W. Tian, C. P. Opeil, Z. Wang, and S. D. Wilson, Phys. Rev. B **86**, 100401 (2012).

[150] M. W. Haverkort, N. Hollmann, I. P. Krug, and A. Tanaka, Phys. Rev. B **82**, 094403 (2010).

[151] M. W. Haverkort, Phys. Rev. Lett. **105**, 167404 (2010).

[152] L. Savary and T. Senthil, ArXiv e-prints (2015), arXiv:1506.04752 [cond-mat.str-el] .

[153] E. Lefrançois, A.-M. Pradipto, M. Moretti Sala, L. C. Chapon, V. Simonet, S. Picozzi, P. Lejay, S. Petit, and R. Ballou, Phys. Rev. B **93**, 224401 (2016).

[154] M. Rossi, M. Retegan, C. Giacobbe, R. Fumagalli, A. Efimenko, T. Kulka, K. Wohlfeld, A. I. Gubanov, and M. Moretti Sala, Phys. Rev. B **95**, 235161 (2017).

[155] K. A. Ross, L. Savary, B. D. Gaulin, and L. Balents, Phys. Rev. X **1**, 021002 (2011).

[156] V. E. Dmitrienko, K. Ishida, A. Kirfel, and E. N. Ovchinnikova, Acta Crystallogr. Sect. A **61**, 481 (2005).

[157] C. Donnerer, M. C. Rahn, M. M. Sala, J. G. Vale, D. Pincini, J. Strempfer, M. Krisch, D. Prabhakaran, A. T. Boothroyd, and D. F. McMorrow, Phys. Rev. Lett. **117**, 037201 (2016).

[158] J. N. Millican, R. T. Macaluso, S. Nakatsuji, Y. Machida, Y. Maeno, and J. Y. Chan, Mater. Res. Bull. **42**, 928 (2007).

[159] W. K. Zhu, M. Wang, B. Seradjeh, F. Yang, and S. X. Zhang, Phys. Rev. B **90**, 054419 (2014).

[160] A. S. Wills, M. E. Zhitomirsky, B. Canals, J. Sanchez, P. Bonville, P. D. de Rotier, and A. Yaouanc, J. Phys. Condens. Matter **18**, L37 (2006).

[161] K. Ueda, J. Fujioka, B.-J. Yang, J. Shiogai, A. Tsukazaki, S. Nakamura, S. Awaji, N. Nagaosa, and Y. Tokura, Phys. Rev. Lett. **115**, 056402 (2015).

[162] Z. Tian, Y. Kohama, T. Tomita, H. Ishizuka, T. H. Hsieh, J. J. Ishikawa, K. Kindo, L. Balents, and S. Nakatsuji, Nat. Phys. **12**, 134 (2016).

[163] S. Francoual, J. Strempfer, D. Reuther, D. K. Shukla, and A. Skaugen, J. Phys. Conf. Ser. **425**, 132010 (2013).

[164] C. Detlefs, M. Sanchez del Rio, and C. Mazzoli, Eur. Phys. J. Spec. Top. **208**, 359 (2012).

[165] S. P. Collins, I. Dolbnya, B. A. Palmer, G. R. Edwards-Gau, A. Morte-Rdenas, B. M. Kariuki, G. K. Lim, K. D. M. Harris, and Y. Joly, J. Phys. Conf. Ser. **425**, 132015 (2013).

[166] S. Tardif, S. Takeshita, H. Ohsumi, J.-i. Yamaura, D. Okuyama, Z. Hiroi, M. Takata, and T.-h. Arima, Phys. Rev. Lett. **114**, 147205 (2015).

[167] R. Wang, A. Go, and A. Millis, ArXiv e-prints (2017), arXiv:1707.04676 [cond-mat.str-el] .

[168] E. K.-H. Lee, S. Bhattacharjee, and Y. B. Kim, Phys. Rev. B **87**, 214416 (2013).

[169] T. Hasegawa, N. Ogita, K. Matsuhira, S. Takagi, M. Wakeshima, Y. Hinatsu, and M. Udagawa, J. Phys. Conf. Ser. **200**, 012054 (2010).

[170] W. H. Press, *Numerical recipes 3rd edition: The art of scientific computing* (Cambridge university press, 2007).

[171] S. Toth and B. Lake, J. Phys. Condens. Matter **27**, 166002 (2015).

[172] J. P. C. Ruff, J. P. Clancy, A. Bourque, M. A. White, M. Ramazanoglu, J. S. Gardner, Y. Qiu, J. R. D. Copley, M. B. Johnson, H. A. Dabkowska, and B. D. Gaulin, Phys. Rev. Lett. **101**, 147205 (2008).

[173] L. Savary, K. A. Ross, B. D. Gaulin, J. P. C. Ruff, and L. Balents, Phys. Rev. Lett. **109**, 167201 (2012).

[174] M. E. Zhitomirsky, M. V. Gvozdikova, P. C. W. Holdsworth, and R. Moessner, Phys. Rev. Lett. **109**, 077204 (2012).

[175] D. Uematsu, H. Sagayama, T.-h. Arima, J. J. Ishikawa, S. Nakatsuji, H. Takagi, M. Yoshida, J. Mizuki, and K. Ishii, Phys. Rev. B **92**, 094405 (2015).

[176] L. J. P. Ament, M. van Veenendaal, and J. van den Brink, Europhys. Lett. **95**, 27008 (2011).

[177] W. S. Lee, S. Johnston, B. Moritz, J. Lee, M. Yi, K. J. Zhou, T. Schmitt, L. Patthey, V. Strocov, K. Kudo, Y. Koike, J. van den Brink, T. P. Devereaux, and Z. X. Shen, Phys. Rev. Lett. **110**, 265502 (2013).

[178] J. Kim, D. Casa, A. Said, B. J. Kim, E. Kasman, X. Huang, and T. Gog, unpublished .

[179] E. M. Plotnikova, M. Daghofer, J. van den Brink, and K. Wohlfeld, Phys. Rev. Lett. **116**, 106401 (2016).

[180] A. E. Taylor, S. Calder, R. Morrow, H. L. Feng, M. H. Upton, M. D. Lumsden, K. Yamaura, P. M. Woodward, and A. D. Christianson, Phys. Rev. Lett. **118**, 207202 (2017).

[181] B. Yuan, J. P. Clancy, A. M. Cook, C. M. Thompson, J. Greedan, G. Cao, B. C. Jeon, T. W. Noh, M. H. Upton, D. Casa, T. Gog, A. Paramekanti, and Y.-J. Kim, Phys. Rev. B **95**, 235114 (2017).

[182] C. Donnerer, Z. Feng, J. G. Vale, S. N. Andreev, I. V. Solovyev, E. C. Hunter, M. Hanfland, R. S. Perry, H. M. Rønnow, M. I. McMahon, V. V. Mazurenko, and D. F. McMorrow, Phys. Rev. B **93**, 174118 (2016).

[183] M. Subramanian, M. Crawford, and R. Harlow, Mater. Res. Bull. **29**, 645 (1994).

[184] G. Cao, Y. Xin, C. S. Alexander, J. E. Crow, P. Schlottmann, M. K. Crawford, R. L. Harlow, and W. Marshall, Phys. Rev. B **66**, 214412 (2002).

[185] H. Matsuhata, I. Nagai, Y. Yoshida, S. Hara, S. ichi Ikeda, and N. Shirakawa, J. Solid State Chem. **177**, 3776 (2004).

[186] T. Hogan, L. Bjaalie, L. Zhao, C. Belvin, X. Wang, C. G. Van de Walle, D. Hsieh, and S. D. Wilson, Phys. Rev. B **93**, 134110 (2016).

[187] Z. Zhao, S. Wang, T. F. Qi, Q. Zeng, S. Hirai, P. P. Kong, L. Li, C. Park, S. J. Yuan, C. Q. Jin, G. Cao, and W. L. Mao, J. Phys. Condens. Matter **26**, 215402 (2014).

[188] L. Li, P. P. Kong, T. F. Qi, C. Q. Jin, S. J. Yuan, L. E. DeLong, P. Schlottmann, and G. Cao, Phys. Rev. B **87**, 235127 (2013).

[189] F. Datchi, R. LeToullec, and P. Loubeyre, J. Appl. Phys. **81**, 3333 (1997).

[190] A. P. Hammersley, S. O. Svensson, M. Hanfland, A. N. Fitch, and D. Hausermann, High Press. Res. **14**, 235 (1996).

[191] J. Rodriguez-Carvajal, Physica B **192**, 55 (1993).

[192] B. T. Thole and G. van der Laan, Phys. Rev. A **38**, 1943 (1988).

[193] G. van der Laan and B. T. Thole, Phys. Rev. Lett. **60**, 1977 (1988).

[194] J. P. Clancy, N. Chen, C. Y. Kim, W. F. Chen, K. W. Plumb, B. C. Jeon, T. W. Noh, and Y.-J. Kim, Phys. Rev. B **86**, 195131 (2012).

[195] M. A. Laguna-Marco, P. Kayser, J. A. Alonso, M. J. Martínez-Lope, M. van Veenendaal, Y. Choi, and D. Haskel, Phys. Rev. B **91**, 214433 (2015).

[196] M. Moretti Sala, M. Rossi, A. Al-Zein, S. Boseggia, E. C. Hunter, R. S. Perry, D. Prabhakaran, A. T. Boothroyd, N. B. Brookes, D. F. McMorrow, G. Monaco, and M. Krisch, Phys. Rev. B **90**, 085126 (2014).

[197] J. Stöhr and H. C. Siegmann, *Magnetism: From Fundamentals to Nanoscale Dynamics* (Springer, Berlin, 2006).

[198] L. S. I. Veiga, M. Etter, K. Glazyrin, F. Sun, C. A. Escanhoela, G. Fabbris, J. R. L. Mardegan, P. S. Malavi, Y. Deng, P. P. Stavropoulos, H.-Y. Kee, W. G. Yang, M. van Veenendaal, J. S. Schilling, T. Takayama, H. Takagi, and D. Haskel, Phys. Rev. B **96**, 140402 (2017).

[199] S. Calder, J. H. Lee, M. B. Stone, M. D. Lumsden, J. C. Lang, M. Feygenson, Z. Zhao, J. Q. Yan, Y. G. Shi, Y. S. Sun, Y. Tsujimoto, K. Yamaura, and A. D. Christianson, Nat. Commun. **6**, 8916 (2015).

[200] H. Gretarsson, N. H. Sung, M. Höppner, B. J. Kim, B. Keimer, and M. Le Tacon, Phys. Rev. Lett. **116**, 136401 (2016).

[201] S. Tóth, B. Wehinger, K. Rolfs, T. Birol, U. Stuhr, H. Takatsu, K. Kimura, T. Kimura, H. M. Rønnow, and C. Rüegg, Nat. Commun. **7**, 13547 (2016).

[202] J. S. Gardner, M. J. P. Gingras, and J. E. Greedan, Rev. Mod. Phys. **82**, 53 (2010).

[203] J. Yamaura, K. Ohgushi, H. Ohsumi, T. Hasegawa, I. Yamauchi, K. Sugimoto, S. Takeshita, A. Tokuda, M. Takata, M. Udagawa, M. Takigawa, H. Harima, T. Arima, and Z. Hiroi, Phys. Rev. Lett. **108**, 247205 (2012).

[204] J. P. Hill and D. F. McMorrow, Acta Crystallogr. Sect. A **52**, 236 (1996).

[205] A. Kirfel and W. Morgenroth, Acta Crystallogr. Sect. A **49**, 35 (1993).

[206] S. P. Collins, D. Laundy, and A. Stunault, J. Phys. Condens. Matter **13**, 1891 (2001).

Appendix A

Details on Ir RXS cross-section computations

A.1 Trigonal and tetragonal frames

	Tetragonal	Trigonal
$\vert 0\rangle$	$\sqrt{\frac{1}{2}}(Y_{22} - Y_{2\bar{2}})$	$-Y_{20}$
$\vert 1\rangle$	Y_{21}	$\sqrt{\frac{2}{3}}Y_{22} - \sqrt{\frac{1}{3}}Y_{2\bar{1}}$
$\vert \bar{1}\rangle$	$Y_{2\bar{1}}$	$\sqrt{\frac{2}{3}}Y_{2\bar{2}} + \sqrt{\frac{1}{3}}Y_{21}$

Table A.1: Definitions of t_{2g} orbitals in tetragonal and trigonal basis functions.

One can rotate from tetragonal to trigonal reference frames via:

$$R_{\text{tri}} = R_x\left(\arccos\sqrt{1/3}\right)R_z(\pi/4) = \begin{pmatrix} \sqrt{\frac{1}{2}} & -\sqrt{\frac{1}{2}} & 0 \\ \sqrt{\frac{1}{6}} & \sqrt{\frac{1}{6}} & -\sqrt{\frac{2}{3}} \\ \sqrt{\frac{1}{3}} & \sqrt{\frac{1}{3}} & \sqrt{\frac{1}{3}} \end{pmatrix}$$

A.2 $p - d$ matrix elements

The dipole operators for linear polarisation, $\mathcal{D}_{x,y,z}$, where x, y, z defines the direction of the electric field, can be written as

$\mathbf{E} \parallel x$	$\mathcal{D}_x = \frac{r}{\sqrt{2}}(C^1_{-1} - C^1_1)$
$\mathbf{E} \parallel y$	$\mathcal{D}_y = i\frac{r}{\sqrt{2}}(C^1_{-1} + C^1_1)$
$\mathbf{E} \parallel z$	$\mathcal{D}_z = rC^1_0$

where $C^l_m = \sqrt{\frac{4\pi}{2l+1}} Y_{l,m}(\theta,\phi)$. At the iridium L edges we are interested in $2p$ to $5d$ transitions, i.e. $Y_{1,m}$ to $Y_{2,m}$. The non-vanishing angular matrix elements are [197]:

$$\begin{aligned}
\langle l+1,m|\, C^1_0 \,|l,m\rangle &= \sqrt{\tfrac{(l+1)^2-m^2}{(2l+3)(2l+1)}} \\
\langle l-1,m|\, C^1_0 \,|l,m\rangle &= \sqrt{\tfrac{l^2-m^2}{(2l-1)(2l+1)}} \\
\langle l+1,m+1|\, C^1_1 \,|l,m\rangle &= \sqrt{\tfrac{(l+m+2)(l+m+1)}{2(2l+3)(2l+1)}} \\
\langle l-1,m-1|\, C^1_1 \,|l,m\rangle &= -\sqrt{\tfrac{(l-m)(l-m-1)}{2(2l-1)(2l+1)}} \\
\langle l+1,m-1|\, C^1_{-1} \,|l,m\rangle &= \sqrt{\tfrac{(l-m+2)(l-m+1)}{2(2l+3)(2l+1)}} \\
\langle l-1,m-1|\, C^1_{-1} \,|l,m\rangle &= -\sqrt{\tfrac{(l+m)(l+m-1)}{2(2l-1)(2l+1)}}
\end{aligned}$$

Everything else is zero. Thus we can evaluate all possible transitions (neglecting a constant radial integral):

$\mathcal{D}_x$	$\lvert Y_{22}\rangle$	$\lvert Y_{21}\rangle$	$\lvert Y_{20}\rangle$	$\lvert Y_{2\bar{1}}\rangle$	$\lvert Y_{2\bar{2}}\rangle$
$\langle Y_{11}\rvert$	$-\sqrt{\frac{1}{5}}$	0	$\sqrt{\frac{1}{30}}$	0	0
$\langle Y_{10}\rvert$	0	$-\sqrt{\frac{1}{10}}$	0	$\sqrt{\frac{1}{10}}$	0
$\langle Y_{1\bar{1}}\rvert$	0	0	$-\sqrt{\frac{1}{30}}$	0	$\sqrt{\frac{1}{5}}$

$\mathcal{D}_y$	$\lvert Y_{22}\rangle$	$\lvert Y_{21}\rangle$	$\lvert Y_{20}\rangle$	$\lvert Y_{2\bar{1}}\rangle$	$\lvert Y_{2\bar{2}}\rangle$
$\langle Y_{11}\rvert$	$-i\sqrt{\frac{1}{5}}$	0	$-i\sqrt{\frac{1}{30}}$	0	0
$\langle Y_{10}\rvert$	0	$-i\sqrt{\frac{1}{10}}$	0	$-i\sqrt{\frac{1}{10}}$	0
$\langle Y_{1\bar{1}}\rvert$	0	0	$-i\sqrt{\frac{1}{30}}$	0	$-i\sqrt{\frac{1}{5}}$

$\mathcal{D}_z$	$\lvert Y_{22}\rangle$	$\lvert Y_{21}\rangle$	$\lvert Y_{20}\rangle$	$\lvert Y_{2\bar{1}}\rangle$	$\lvert Y_{2\bar{2}}\rangle$
$\langle Y_{11}\rvert$	0	$\sqrt{\frac{1}{5}}$	0	0	0
$\langle Y_{10}\rvert$	0	0	$\sqrt{\frac{4}{15}}$	0	0
$\langle Y_{1\bar{1}}\rvert$	0	0	0	$\sqrt{\frac{1}{5}}$	0

Any L edge RXS transition can be calculated by some combination of these entries. For completeness, we define the (spin-orbit split) $2p$ core levels. At the L_2 edge, the $2p_{1/2}$ intermediate states are:

$$\begin{aligned}
|p_{\frac{1}{2},\frac{1}{2}}\rangle &= \sqrt{\frac{2}{3}}\,|Y_{11},\downarrow\rangle - \sqrt{\frac{1}{3}}\,|Y_{10},\uparrow\rangle \\
|p_{\frac{1}{2},-\frac{1}{2}}\rangle &= \sqrt{\frac{1}{3}}\,|Y_{10},\downarrow\rangle - \sqrt{\frac{2}{3}}\,|Y_{1\bar{1}},\uparrow\rangle
\end{aligned}$$

At the L_3 edge, the $2p_{3/2}$ intermediate states are:

$$\begin{aligned}
|p_{\frac{3}{2},\frac{3}{2}}\rangle &= |Y_{11},\uparrow\rangle \\
|p_{\frac{3}{2},\frac{1}{2}}\rangle &= \sqrt{\frac{2}{3}}\,|Y_{10},\uparrow\rangle + \sqrt{\frac{1}{3}}\,|Y_{11},\downarrow\rangle \\
|p_{\frac{3}{2},-\frac{1}{2}}\rangle &= \sqrt{\frac{1}{3}}\,|Y_{1\bar{1}},\uparrow\rangle + \sqrt{\frac{2}{3}}\,|Y_{10},\downarrow\rangle \\
|p_{\frac{3}{2},-\frac{3}{2}}\rangle &= |Y_{1\bar{1}},\downarrow\rangle
\end{aligned}$$

A.3 Atomic scattering tensors

A.3.1 Tetragonal reference frame

L_2 **edge**

Transition	Atomic scattering tensor
$\vert f,-\rangle \rightarrow \vert f,-\rangle$	$\frac{(C_f-1)^2}{(2+C_f^2)}\begin{pmatrix} 1 & -i\cos\theta_s & 0 \\ i\cos\theta_s & 1 & 0 \\ 0 & 0 & 0 \end{pmatrix}$
$\vert f,-\rangle \rightarrow \vert f,+\rangle$	$\frac{(C_f-1)^2}{(2+C_f^2)}\begin{pmatrix} 0 & -i\sin\theta_s & 0 \\ i\sin\theta_s & 0 & 0 \\ 0 & 0 & 0 \end{pmatrix}$
$\vert f,-\rangle \rightarrow \vert g,\downarrow\rangle$	$\frac{(C_f-1)(C_g+1)}{\sqrt{(2+C_f^2)(2+C_g^2)}}\begin{pmatrix} -1 & i\cos\theta_s & 0 \\ -i\cos\theta_s & -1 & 0 \\ 0 & 0 & 0 \end{pmatrix}$
$\vert f,-\rangle \rightarrow \vert g,\uparrow\rangle$	$\frac{(C_f-1)(C_g+1)}{\sqrt{(2+C_f^2)(2+C_g^2)}}\begin{pmatrix} 0 & i\sin\theta_s & 0 \\ -i\sin\theta_s & 0 & 0 \\ 0 & 0 & 0 \end{pmatrix}$
$\vert f,-\rangle \rightarrow \vert h,\downarrow\rangle$	$\frac{(C_f-1)}{\sqrt{2(2+C_f^2)}}\begin{pmatrix} -1 & -i\cos\theta_s & 2i\sin\theta_s\sin\phi_s \\ -i\cos\theta_s & 1 & 2i\cos\phi_s\sin\theta_s \\ 0 & 0 & 0 \end{pmatrix}$
$\vert f,-\rangle \rightarrow \vert h,\uparrow\rangle$	$\frac{(C_f-1)}{\sqrt{2(2+C_f^2)}}\begin{pmatrix} 0 & -i\sin\theta_s & -2\left(\cos\phi_s+i\cos\theta_s\sin\phi_s\right) \\ -i\sin\theta_s & 0 & 2\left(\sin\phi_s-i\cos\theta_s\cos\phi_s\right) \\ 0 & 0 & 0 \end{pmatrix}$

L_3 edge

Transition	Atomic scattering tensor
$\lvert f,-\rangle \rightarrow \lvert f,-\rangle$	$\frac{1}{(2+C_f^2)}\begin{pmatrix} 2\left(C_f^2+C_f+1\right) & i\cos\theta_s\left(\left(C_f-2\right)C_f-2\right) & -3i\sin\theta_s\sin\phi_s C_f \\ -i\cos\theta_s\left(\left(C_f-2\right)C_f-2\right) & 2\left(C_f^2+C_f+1\right) & 3i\cos\phi_s\sin\theta_s C_f \\ 3i\sin\theta_s\sin\phi_s C_f & -3i\cos\phi_s\sin\theta_s C_f & 6 \end{pmatrix}$
$\lvert f,-\rangle \rightarrow \lvert f,+\rangle$	$\frac{1}{(2+C_f^2)}\begin{pmatrix} 0 & i\sin\theta_s\left(\left(C_f-2\right)C_f-2\right) & 3\left(\cos\phi_s+i\cos\theta_s\sin\phi_s\right)C_f \\ -i\sin\theta_s\left(\left(C_f-2\right)C_f-2\right) & 0 & 3\left(\sin\phi_s-i\cos\theta_s\cos\phi_s\right)C_f \\ -3\left(\cos\phi_s+i\cos\theta_s\sin\phi_s\right)C_f & 3i\cos\theta_s\cos\phi_s C_f-3\sin\phi_s C_f & 0 \end{pmatrix}$
$\lvert f,-\rangle \rightarrow \lvert g,\downarrow\rangle$	$\frac{1}{\sqrt{(2+C_f^2)(2+C_g^2)}}\begin{pmatrix} -2C_gC_f+C_f-C_g+2 & -i\cos\theta_s\left(C_f+\left(C_f-1\right)C_g+2\right) & -3i\sin\theta_s\sin\phi_s C_f \\ i\cos\theta_s\left(C_f+\left(C_f-1\right)C_g+2\right) & -2C_gC_f+C_f-C_g+2 & 3i\cos\phi_s\sin\theta_s C_f \\ -3i\sin\theta_s\sin\phi_s C_g & 3i\cos\phi_s\sin\theta_s C_g & 6 \end{pmatrix}$
$\lvert f,-\rangle \rightarrow \lvert g,\uparrow\rangle$	$\frac{1}{\sqrt{(2+C_f^2)(2+C_g^2)}}\begin{pmatrix} 0 & -i\sin\theta_s\left(C_f+\left(C_f-1\right)C_g+2\right) & 3\left(\cos\phi_s+i\cos\theta_s\sin\phi_s\right)C_f \\ i\sin\theta_s\left(C_f+\left(C_f-1\right)C_g+2\right) & 0 & 3\left(\sin\phi_s-i\cos\theta_s\cos\phi_s\right)C_f \\ 3\left(\cos\phi_s+i\cos\theta_s\sin\phi_s\right)C_g & 3\left(\sin\phi_s-i\cos\theta_s\cos\phi_s\right)C_g & 0 \end{pmatrix}$
$\lvert f,-\rangle \rightarrow \lvert h,\downarrow\rangle$	$\frac{1}{\sqrt{2(2+C_f^2)}}\begin{pmatrix} C_f+2 & i\cos\theta_s\left(C_f+2\right) & i\sin\theta_s\sin\phi_s\left(C_f+2\right) \\ i\cos\theta_s\left(C_f+2\right) & -C_f-2 & i\cos\phi_s\sin\theta_s\left(C_f+2\right) \\ 0 & 0 & 0 \end{pmatrix}$
$\lvert f,-\rangle \rightarrow \lvert h,\uparrow\rangle$	$\frac{1}{\sqrt{2(2+C_f^2)}}\begin{pmatrix} 0 & i\sin\theta_s\left(C_f+2\right) & -\left(\cos\phi_s+i\cos\theta_s\sin\phi_s\right)\left(C_f+2\right) \\ i\sin\theta_s\left(C_f+2\right) & 0 & \left(\sin\phi_s-i\cos\theta_s\cos\phi_s\right)\left(C_f+2\right) \\ 0 & 0 & 0 \end{pmatrix}$

A.3.2 Trigonal reference frame

L_2 edge

Transition	Atomic scattering tensor
$\lvert f,-\rangle \to \lvert f,-\rangle$	$\frac{(C_f-1)^2}{3(2+C_f^2)}\begin{pmatrix} 1 & i\cos\theta_s & 2i\sin\theta_s\sin\phi_s \\ -i\cos\theta_s & 1 & -2i\cos\phi_s\sin\theta_s \\ -2i\sin\theta_s\sin\phi_s & 2i\cos\phi_s\sin\theta_s & 4 \end{pmatrix}$
$\lvert f,-\rangle \to \lvert f,+\rangle$	$\frac{(C_f-1)^2}{3(2+C_f^2)}\begin{pmatrix} 0 & i\sin\theta_s & -2\left(\cos\phi_s+i\cos\theta_s\sin\phi_s\right) \\ -i\sin\theta_s & 0 & 2i\cos\theta_s\cos\phi_s-2\sin\phi_s \\ 2\left(\cos\phi_s+i\cos\theta_s\sin\phi_s\right) & 2\left(\sin\phi_s-i\cos\theta_s\cos\phi_s\right) & 0 \end{pmatrix}$
$\lvert f,-\rangle \to \lvert g,\downarrow\rangle$	$\frac{(C_f-1)(C_g+1)}{3\sqrt{(2+C_f^2)(2+C_g^2)}}\begin{pmatrix} -1 & -i\cos\theta_s & -2i\sin\theta_s\sin\phi_s \\ i\cos\theta_s & -1 & 2i\cos\phi_s\sin\theta_s \\ 2i\sin\theta_s\sin\phi_s & -2i\cos\phi_s\sin\theta_s & -4 \end{pmatrix}$
$\lvert f,-\rangle \to \lvert g,\uparrow\rangle$	$\frac{(C_f-1)(C_g+1)}{3\sqrt{(2+C_f^2)(2+C_g^2)}}\begin{pmatrix} 0 & -i\sin\theta_s & 2\left(\cos\phi_s+i\cos\theta_s\sin\phi_s\right) \\ i\sin\theta_s & 0 & 2\left(\sin\phi_s-i\cos\theta_s\cos\phi_s\right) \\ -2\left(\cos\phi_s+i\cos\theta_s\sin\phi_s\right) & 2i\cos\theta_s\cos\phi_s-2\sin\phi_s & 0 \end{pmatrix}$
$\lvert f,-\rangle \to \lvert h,\downarrow\rangle$	$\frac{(C_f-1)}{3\sqrt{(2+C_f^2)}}\begin{pmatrix} 1-2i\sqrt{2}\sin\theta_s\sin\phi_s & -i\left(\cos\theta_s-2\sqrt{2}\cos\phi_s\sin\theta_s\right) & 0 \\ -i\left(\cos\theta_s-2\sqrt{2}\cos\phi_s\sin\theta_s\right) & 2i\sqrt{2}\sin\left(\theta_S\right)\sin\phi_s-1 & 0 \\ -2i\sin\theta_s\sin\phi_s-4\sqrt{2} & -2i\left(2\sqrt{2}\cos\theta_s+\cos\left(\phi_S\right)\sin\theta_s\right) & 0 \end{pmatrix}$
$\lvert f,-\rangle \to \lvert h,\uparrow\rangle$	$\frac{(C_f-1)}{3\sqrt{2(2+C_f^2)}}\begin{pmatrix} 2\sqrt{2}\left(\cos\phi_s+i\cos\theta_s\sin\phi_s\right) & -2i\sqrt{2}\cos\left(\theta_S\right)\cos\phi_s-i\sin\theta_s+2\sqrt{2}\sin\phi_s & 0 \\ -2i\sqrt{2}\cos\theta_s\cos\phi_s-i\sin\theta_s+2\sqrt{2}\sin\phi_s & -2\sqrt{2}\left(\cos\phi_s+i\cos\theta_s\sin\phi_s\right) & 0 \\ 2\left(\cos\phi_s+i\cos\theta_s\sin\phi_s\right) & 2i\left(\cos\theta_s\cos\phi_s-2\sqrt{2}\sin\theta_s+i\sin\phi_s\right) & 0 \end{pmatrix}$

L_3 edge

Transition	Atomic scattering tensor
$\lvert f,-\rangle \rightarrow \lvert f,-\rangle$	$\frac{1}{3(2+C_f^2)}\begin{pmatrix} 2\left(C_f^2+C_f+7\right) & -i\cos\theta_s\left(\left(C_f-2\right)C_f+10\right) & -i\sin\theta_s\sin\phi_s\left(C_f+2\right)\left(2C_f+1\right) \\ i\cos\theta_s\left(\left(C_f-2\right)C_f+10\right) & 2\left(C_f^2+C_f+7\right) & i\cos\phi_s\sin\theta_s\left(C_f+2\right)\left(2C_f+1\right) \\ i\sin\theta_s\sin\phi_s\left(C_f+2\right)\left(2C_f+1\right) & -i\cos\phi_s\sin\left(\theta_S\right)\left(C_f+2\right)\left(2C_f+1\right) & 2\left(2C_f+1\right)^2 \end{pmatrix}$
$\lvert f,-\rangle \rightarrow \lvert f,+\rangle$	$\frac{1}{3(2+C_f^2)}\begin{pmatrix} 0 & -i\sin\theta_s\left(\left(C_f-2\right)C_f+10\right) & \left(\cos\phi_s+i\cos\theta_s\sin\phi_s\right)\left(C_f+2\right)\left(2C_f+1\right) \\ i\sin\theta_s\left(\left(C_f-2\right)C_f+10\right) & 0 & \left(\sin\phi_s-i\cos\theta_s\cos\phi_s\right)\left(C_f+2\right)\left(2C_f+1\right) \\ -\left(\cos\phi_s+i\cos\theta_s\sin\phi_s\right)\left(C_f+2\right)\left(2C_f+1\right) & -\left(\sin\phi_s-i\cos\theta_s\cos\phi_s\right)\left(C_f+2\right)\left(2C_f+1\right) & 0 \end{pmatrix}$
$\lvert f,-\rangle \rightarrow \lvert g,\downarrow\rangle$	$\frac{1}{3\sqrt{(2+C_f^2)(2+C_g^2)}}\begin{pmatrix} -2C_gC_f+C_f-C_g+3i\sqrt{2}\sin\theta_s\sin\phi_s\left(C_f+C_g\right)+14 & i\left(3\sqrt{2}\cos\phi_s\sin\theta_s\left(C_f+C_g\right)+\cos\theta_s\left(C_f+\left(C_f-1\right)C_g-10\right)\right) & i\sin\theta_s\sin\phi_s\left(C_f+2\right)\left(2C_g-1\right) \\ 3i\sqrt{2}\cos\phi_s\sin\theta_s\left(C_f+C_g\right)-i\cos\theta_s\left(C_f+\left(C_f-1\right)C_g-10\right) & -2C_gC_f+C_f-C_g-3i\sqrt{2}\sin\theta_s\sin\phi_s\left(C_f+C_g\right)+14 & -i\cos\phi_s\sin\theta_s\left(C_f+2\right)\left(2C_g-1\right) \\ -i\sin\theta_s\sin\phi_s\left(2C_f+1\right)\left(C_g-2\right) & i\cos\phi_s\sin\theta_s\left(2C_f+1\right)\left(C_g-2\right) & -2\left(2C_f+1\right)\left(2C_g-1\right) \end{pmatrix}$
$\lvert f,-\rangle \rightarrow \lvert g,\uparrow\rangle$	$\frac{1}{3\sqrt{(2+C_f^2)(2+C_g^2)}}\begin{pmatrix} -3\sqrt{2}\left(\cos\phi_s+i\cos\theta_s\sin\phi_s\right)\left(C_f+C_g\right) & -3i\sqrt{2}\cos\theta_s\cos\left(\phi_S\right)\left(C_f+C_g\right)+3\sqrt{2}\sin\phi_s\left(C_f+C_g\right)+i\sin\theta_s\left(C_f+\left(C_f-1\right)C_g-10\right) & -\left(\cos\left(\phi_S\right)+i\cos\theta_s\sin\phi_s\right)\left(C_f+2\right)\left(2C_g-1\right) \\ -ie^{-i\phi_S}\left(\frac{3\left(-1+e^{2i\phi_S}\right)\left(C_f+C_g\right)}{\sqrt{2}}+e^{i\phi_S}\left(3\sqrt{2}\cos\theta_s\cos\phi_s\left(C_f+C_g\right)+\sin\theta_s\left(C_f+\left(C_f-1\right)C_g-10\right)\right)\right) & 3\sqrt{2}\left(\cos\phi_s+i\cos\theta_s\sin\phi_s\right)\left(C_f+C_g\right) & i\left(\cos\theta_s\cos\phi_s+i\sin\phi_s\right)\left(C_f+2\right)\left(2C_g-1\right) \\ \left(\cos\phi_s+i\cos\theta_s\sin\phi_s\right)\left(2C_f+1\right)\left(C_g-2\right) & \left(\sin\phi_s-i\cos\left(\theta_S\right)\cos\phi_s\right)\left(2C_f+1\right)\left(C_g-2\right) & 0 \end{pmatrix}$
$\lvert f,-\rangle \rightarrow \lvert h,\downarrow\rangle$	$\frac{1}{3\sqrt{2(2+C_f^2)}}\begin{pmatrix} -i\left(\sqrt{2}\sin\theta_s\sin\phi_s-i\right)\left(C_f+2\right) & i\left(\cos\left(\theta_S\right)+\sqrt{2}\cos\phi_s\sin\theta_s\right)\left(C_f+2\right) & 3i\sin\theta_s\sin\phi_sC_f+6\sqrt{2} \\ i\left(\cos\theta_s+\sqrt{2}\cos\phi_s\sin\theta_s\right)\left(C_f+2\right) & \left(i\sqrt{2}\sin\theta_s\sin\phi_s+1\right)\left(C_f+2\right) & 3i\left(2\sqrt{2}\cos\theta_s+\cos\phi_s\sin\theta_sC_f\right) \\ 2\left(\sqrt{2}-i\sin\theta_s\sin\phi_s\right)\left(2C_f+1\right) & 2i\left(\sqrt{2}\cos\left(\theta_S\right)-\cos\phi_s\sin\theta_s\right)\left(2C_f+1\right) & 0 \end{pmatrix}$
$\lvert f,-\rangle \rightarrow \lvert h,\uparrow\rangle$	$\frac{1}{3\sqrt{2(2+C_f^2)}}\begin{pmatrix} \sqrt{2}\left(\cos\phi_s+i\cos\theta_s\sin\phi_s\right)\left(C_f+2\right) & \left(-i\sqrt{2}\cos\theta_s\cos\phi_s+i\sin\theta_s+\sqrt{2}\sin\phi_s\right)\left(C_f+2\right) & -3\left(\cos\phi_s+i\cos\theta_s\sin\phi_s\right)C_f \\ \left(-i\sqrt{2}\cos\theta_s\cos\phi_s+i\sin\theta_s+\sqrt{2}\sin\phi_s\right)\left(C_f+2\right) & -\sqrt{2}\left(\cos\phi_s+i\cos\theta_s\sin\phi_s\right)\left(C_f+2\right) & 6i\sqrt{2}\sin\theta_s-3i\cos\theta_s\cos\phi_sC_f+3\sin\left(\phi_S\right)C_f \\ 2\left(\cos\phi_s+i\cos\theta_s\sin\phi_s\right)\left(2C_f+1\right) & 2i\left(\cos\theta_s\cos\phi_s+\sqrt{2}\sin\theta_s+i\sin\phi_s\right)\left(2C_f+1\right) & 0 \end{pmatrix}$

Appendix B

REXS on the pyrochlore lattice

The geometric frustration inherent to the pyrochlore lattice has attracted considerable interest in its magnetic properties [202]. Most literature studies investigating the magnetic order and excitations have been performed with neutron scattering, and only recently resonant x-ray scattering is becoming used to study the magnetic properties of these materials [73, 166, 203]. This is mainly due to a lack of large single crystal samples of $5d$ pyrochlores, with the additional complication of highly neutron absorbing elements, such as Ir and Cd, and small moment sizes. Compared to neutron scattering, the reciprocal space where XRMS can achieve sensitivity to magnetic scattering is highly restricted. Nevertheless, there are advantages to using x-rays, such as nano-focussed beams and easily manipulable polarisation states, which enable fairly unique experiments, such as mapping magnetic domains on a nanometer scale [166]. This chapter describes how XRMS can be used to determine the magnetic order on the pyrochlore lattice.

B.1 XRMS of $\mathbf{k} = \mathbf{0}$ magnetic order

We will confine the discussion to magnetic structures with a $\mathbf{k} = \mathbf{0}$ propagation vector, which appears to be most common case for pyrochlore oxides [202] and is of particular relevance to the pyrochlore iridates. The magnetic structure can then be fully described within a single tetrahedron comprising of four inequivalent Ir sites. Figure B.1 shows all symmetry-allowed $\mathbf{k} = \mathbf{0}$ magnetic structures for the Ir $16c$ site on the pyrochlore lattice, which can be classified in four irreducible representations $\Gamma_{3,5,7,9}$ with twelve associated basis vectors ψ_i [160].

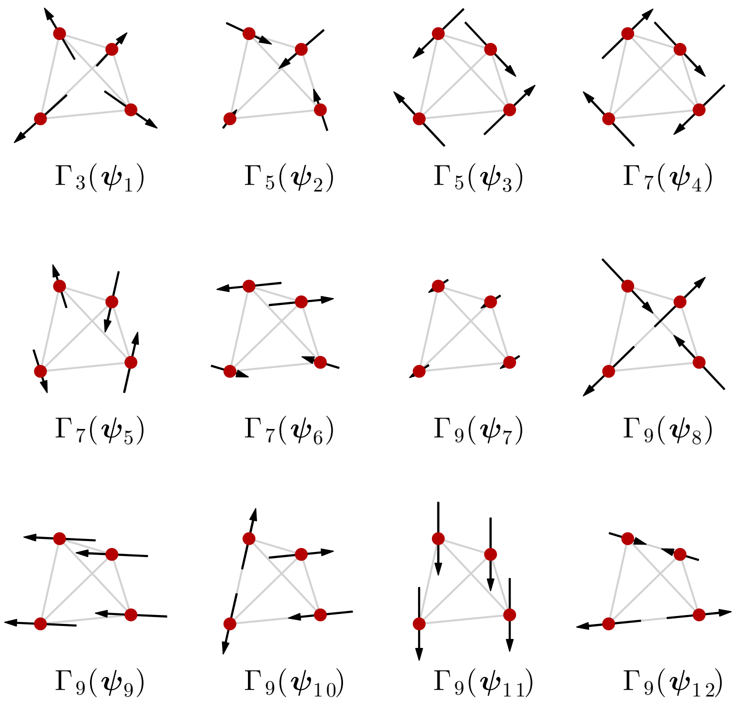
$\Gamma_3(\boldsymbol{\psi}_1)$ $\Gamma_5(\boldsymbol{\psi}_2)$ $\Gamma_5(\boldsymbol{\psi}_3)$ $\Gamma_7(\boldsymbol{\psi}_4)$

$\Gamma_7(\boldsymbol{\psi}_5)$ $\Gamma_7(\boldsymbol{\psi}_6)$ $\Gamma_9(\boldsymbol{\psi}_7)$ $\Gamma_9(\boldsymbol{\psi}_8)$

$\Gamma_9(\boldsymbol{\psi}_9)$ $\Gamma_9(\boldsymbol{\psi}_{10})$ $\Gamma_9(\boldsymbol{\psi}_{11})$ $\Gamma_9(\boldsymbol{\psi}_{12})$

Figure B.1: Symmetry-allowed $\mathbf{k} = \mathbf{0}$ magnetic structures of 16*c* or 16*d* site of the pyrochlore lattice, as described in Ref. [160].

In this classification, the irreducible representation Γ_3, consisting of basisvectors $\boldsymbol{\psi}_1$, is the all-in all-out (AIAO) magnetic structure, where the magnetic moments all lie along the local z axis, pointing either towards or away from the centre of the tetrahedron. This permits two time-reversal magnetic domains, sometimes referred to as all-in all-out and all-out all-in. In contrast, for the irreducible representations Γ_5 and Γ_7, the magnetic moments lie within the local xy planes. Γ_5 is described by basisvectors $\boldsymbol{\psi}_{2,3}$, linear combinations of which allow a continuous rotation of the moments within the local xy planes. Conversely, the basisvectors $\boldsymbol{\psi}_{4,5,6}$ of Γ_7 form a discrete set. Finally, the irreducible representation Γ_9 describes ferromagnetic structures. These include collinear ferromagnets $\boldsymbol{\psi}_{7,9,11}$, as well as more complex arrangements, such as the manifold of spin-ice states.

$\mathbf{k} = \mathbf{0}$ magnetic order implies that magnetic Bragg peaks fall on integer reciprocal lattice points, where usually Thomson scattering occurs. At transition metal L edges, it is typically not feasible to obtain sensitivity to an XRMS signal that is 4-5 orders of magnitude weaker than Thomson scattering. However, while magnetic and chemical unit cells are identical, their symmetries need not be. In particular, the symmetry of the chemical unit cell, $Fd\bar{3}m$, implies that the *fcc* selection rule ($h, k, l =$ all even or all odd) is modified, and certain reflections become forbidden. The following families of space group forbidden reflections are available for pyrochlores:

$$\begin{array}{ll} (h00) & \text{if } h = 4n+2 \\ (hk0) & \text{if } h = 4n+2 \text{ and } k = 4n \\ (hkk) & \text{if } h+k = 4n+2 \text{ and } h, k = 2n \end{array}$$

The cubic symmetry implies that any permutation of $\{h, k, l\}$ indices must yield identical selection rules. The magnetic structure factor for $\mathbf{k} = \mathbf{0}$ order at wavevector $\mathbf{Q}$ can be written as:

$$\mathbf{M}(\mathbf{Q}) = \sum_{j=1}^{4} \mathbf{m}_j e^{2i\pi\mathbf{Q}\cdot\mathbf{r}_j}$$

where the sum j runs over four inequivalent Ir sites and $\mathbf{m}_j$ are the magnetic Fourier components. In our case, the $\mathbf{m}_j$ vectors are real and therefore directly correspond to the magnetic moments. Note that the additional twelve Ir atoms in the unit cell leave the magnetic structure factor unchanged, as the translations (0, 0.5, 0.5), (0.5, 0, 0.5), (0.5, 0.5, 0) only introduce a 2π phase shift, if the *fcc* selection rule is respected. For the above forbidden reflections, the magnetic structure factor simplifies to:

$$\mathbf{M}(h00) = \mathbf{M}(hk0) = \mathbf{M}(hkk) = \mathbf{m}_1 + \mathbf{m}_2 - \mathbf{m}_3 - \mathbf{m}_4$$

Thus we establish that the magnetic structure factor is identical for all forbidden reflections; they all hold the same information on the magnetic structure. We therefore only discuss forbidden $(h00)$ reflections, where $h = 4n+2$. Substituting the basis vectors defined in Ref. [160], we obtain the magnetic structure factors:

IR	domain	BV	$\mathbf{M}(h00)$
Γ_3	1	$\boldsymbol{\psi}_1$	$(\frac{4}{\sqrt{3}}, 0, 0)$
Γ_5	1	$\boldsymbol{\psi}_2$	$(\frac{8}{\sqrt{6}}, 0, 0)$
		$\boldsymbol{\psi}_3$	$(0, 0, 0)$
	2	$\boldsymbol{\psi}_2$	$(\frac{-4}{\sqrt{6}}, 0, 0)$
		$\boldsymbol{\psi}_3$	$(\frac{-4}{\sqrt{2}}, 0, 0)$
	3	$\boldsymbol{\psi}_2$	$(\frac{-4}{\sqrt{6}}, 0, 0)$
		$\boldsymbol{\psi}_3$	$(\frac{4}{\sqrt{2}}, 0, 0)$
Γ_7	1	$\boldsymbol{\psi}_4$	$(0, 0, 0)$
		$\boldsymbol{\psi}_5$	$(0, 0, \frac{4}{\sqrt{2}})$
		$\boldsymbol{\psi}_6$	$(0, \frac{-4}{\sqrt{2}}, 0)$
Γ_9	1	$\boldsymbol{\psi}_7$	$(0, 0, 0)$
		$\boldsymbol{\psi}_8$	$(0, 0, 0)$
		$\boldsymbol{\psi}_9$	$(0, 0, 0)$
		$\boldsymbol{\psi}_{10}$	$(0, 0, \frac{4}{\sqrt{2}})$
		$\boldsymbol{\psi}_{11}$	$(0, 0, 0)$
		$\boldsymbol{\psi}_{12}$	$(0, \frac{4}{\sqrt{2}}, 0)$

where we have included the three S-domains for Γ_5 that arise from the degeneracy of the crystallographic axes.

We find that all irreducible representations can yield a non-zero magnetic structure factor, although not all individual basisvectors will contribute. To make further progress, we calculate how the magnetic structure factors translate to experimental intensities, by computing the XRMS cross-sections. For the antiferromagnetic structures $\Gamma_{3,5,7}$, the moments either lie along the local z axis or within the xy plane. Appealing to the RXS calculations of chapter 3, it is in this case permissible to use the spherical approximation of the XRMS cross-section. The amplitude for XRMS at the Ir L_3 edge becomes [148]:

$$\mathcal{A}_m = -iF_m(\boldsymbol{\epsilon}' \times \boldsymbol{\epsilon}) \cdot \mathbf{M}(\mathbf{Q})$$

where $\boldsymbol{\epsilon}^{(\prime)}$ are the incoming (outgoing) polarisation and F_m quantifies the strength of the magnetic resonance. Alternatively, this can be cast into a 2×2 Jones matrix of $\sigma\pi$ polarisation states [204]:

$$\mathcal{A}_m = -iF_m \begin{pmatrix} 0 & M_1' \cos\theta + M_3' \sin\theta \\ M_3' \sin\theta - M_1' \cos\theta & -M_2' \sin 2\theta \end{pmatrix}$$

where M_i' are the components of $\mathbf{M}(\mathbf{Q})$ in the laboratory reference frame, as defined in Ref. [204], and θ the Bragg angle. In ($h00$) scattering condition, the crystallographic axes map onto this laboratory frame as:

$$\mathbf{M} = \frac{1}{\sqrt{2}} \begin{pmatrix} 0 & 0 & -\sqrt{2} \\ \sin\phi + \cos\phi & \cos\phi - \sin\phi & 0 \\ \cos\phi - \sin\phi & -\sin\phi - \cos\phi & 0 \end{pmatrix} \mathbf{M}'$$

where ϕ is the azimuthal angle ($\phi = 0$ when the (011) direction is parallel to the scattering plane). The amplitude for XRMS in $\sigma\pi'$ polarisation becomes:

IR	domain	BV	$\mathcal{A}_m^{\sigma\pi'}(h00)$
Γ_3	1	$\boldsymbol{\psi}_1$	$-iF_m \sin\theta$
Γ_5	1	$\boldsymbol{\psi}_2$	$-iF_m \sin\theta$
		$\boldsymbol{\psi}_3$	0
	2	$\boldsymbol{\psi}_2$	$iF_m \sin\theta$
		$\boldsymbol{\psi}_3$	$iF_m \sin\theta$
	3	$\boldsymbol{\psi}_2$	$iF_m \sin\theta$
		$\boldsymbol{\psi}_3$	$-iF_m \sin\theta$
Γ_7	1	$\boldsymbol{\psi}_4$	0
		$\boldsymbol{\psi}_5$	$iF_m(\cos\phi - \sin\phi)\cos\theta$
		$\boldsymbol{\psi}_6$	$-iF_m(\cos\phi + \sin\phi)\cos\theta$
Γ_9	1	$\boldsymbol{\psi}_7$	0
		$\boldsymbol{\psi}_8$	0
		$\boldsymbol{\psi}_9$	0
		$\boldsymbol{\psi}_{10}$	$iF_m(\cos\phi - \sin\phi)\cos\theta$
		$\boldsymbol{\psi}_{11}$	0
		$\boldsymbol{\psi}_{12}$	$iF_m(\cos\phi + \sin\phi)\cos\theta$

B.2 Anisotropic tensor susceptibility (ATS)

When the x-ray energy is tuned to an absorption edge, XRMS is not the only process that can give rise to forbidden reflections. In general, when core electrons are promoted to the conduction band, a sensitivity to the local environment of the absorbing atom is achieved. When this local environment is not spherical, the x-ray susceptibility to photon polarisation will also be anisotropic on an atomic level. This is the origin of anisotropic tensor susceptibility (ATS) scattering [156]. To construct the structure factor for diffraction, all sites must be coherently summed over. As for each individual site the anisotropic tensors can be differently orientated within the unit cell, space group forbidden reflections can become allowed on resonance. While the microscopic model of chapter 3 allows to calculate the ATS reflections for the specific $2p \to 5d(t_{2g})$ transition of Ir^{4+}, we here derive the generic symmetry-allowed ATS structure factor, following Kirfel and Morgenroth [205] and Collins *et al.* [206]. For dipolar transitions, the most generic, non-magnetic atomic scattering tensor is the symmetric rank-2 tensor [113]:

$$T = \begin{pmatrix} a & b & c \\ b & d & e \\ c & e & f \end{pmatrix}$$

where the elements $a, \ldots, f$ can be complex and depend on the incident energy in a non-trivial manner. Requiring that the tensor must be invariant to the 12 point group symmetry operations of the Ir site at $\mathbf{r} = \mathbf{0}$ of $Fd\bar{3}m$, we find

$$T = \begin{pmatrix} a & b & b \\ b & a & b \\ b & b & a \end{pmatrix}$$

We set $a = 0$, as we are only interested in the anisotropic part. The ATS structure factor at wavevector $\mathbf{Q}$ can then be calculated via

$$F_c(\mathbf{Q}) = \sum_{p=1}^{192} R_p T R_p^T \exp\left[2i\pi \mathbf{Q} \cdot (\mathbf{t_p} + R_p \mathbf{r})\right]$$

where R_p, t_p are the rotational and translational parts of the symmetry operator p of $Fd\bar{3}m$. Table B.1 shows the ATS structure factors for space group forbidden reflections.

As for XRMS, the structure factors are equivalent for all forbidden reflections, and permuting $\{h, k, l\}$ indices corresponds to permutations of $\{x, y, z\}$ elements. We hence establish that forbidden reflections will always contain an ATS contribution. However, the scattering geometry and x-ray polarisation can be used to suppress ATS scattering. As the above ATS structure factors are defined in the crystal reference frame, we convert to a Jones matrix, as described in section 3.4. For $(h00)$ ATS reflections we find

$$\mathcal{A}_{ats}^{(h00)} = F_{ats} \begin{pmatrix} \cos 2\phi & -\sin\theta \sin 2\phi \\ \sin\theta \sin 2\phi & \sin^2\theta \cos 2\phi \end{pmatrix} \tag{B.1}$$

where F_{ats} quantifies the strength of ATS scattering, θ is the Bragg angle and ϕ the azimuth, such that $\phi = 0$ when (011) is in the scattering plane.

Structure factor	Reflection conditions	
$\begin{pmatrix} 0 & 0 & 0 \\ 0 & 0 & 1 \\ 0 & 1 & 0 \end{pmatrix}$	$(h00)$	if $h = 4n + 2$
	(hkk)	if $h + k = 4n + 2$ and $h, k = 2n$
	$(hk0)$	if $h = 4n + 2$ and $k = 4n$
	$(h0l)$	if $h = 4n + 2$ and $l = 4n$
$\begin{pmatrix} 0 & 0 & 1 \\ 0 & 0 & 0 \\ 1 & 0 & 0 \end{pmatrix}$	$(0k0)$	if $k = 4n + 2$
	(hkh)	if $h + k = 4n + 2$ and $h, k = 2n$
	$(hk0)$	if $h = 4n$ and $k = 4n + 2$
	$(0kl)$	if $h = 4n + 2$ and $k = 4n$
$\begin{pmatrix} 0 & 1 & 0 \\ 1 & 0 & 0 \\ 0 & 0 & 0 \end{pmatrix}$	$(00l)$	if $l = 4n + 2$
	(hhl)	if $h + l = 4n + 2$ and $h, l = 2n$
	$(h0l)$	if $h = 4n$ and $l = 4n + 2$
	$(0kl)$	if $h = 4n$ and $k = 4n + 2$

Table B.1: ATS-allowed, forbidden reflections for dipolar transitions involving the $16d$ or $16c$ site of $Fd\bar{3}m$. The structure factors are defined in the crystallographic reference frame.

B.3 REXS cross sections

Using the example of all-in all-out magnetic order, we can construct the REXS amplitude for forbidden $(h00)$ reflections, which involves magnetic and ATS contributions:

$$\mathcal{A}_{REXS}^{(h00)} = \mathcal{A}_{m}^{(h00)} + \mathcal{A}_{ats}^{(h00)} = \begin{pmatrix} F_{ats}\cos 2\phi & -\sin\theta[iF_m + F_{ats}\sin 2\phi] \\ \sin\theta[F_{ats}\sin 2\phi - iF_m] & F_{ats}\sin^2\theta\cos 2\phi \end{pmatrix} \tag{B.2}$$

Sensitivity to magnetic scattering is thus found in either $\pi\sigma'$ or $\sigma\pi'$ polarisation. The intensity for $\sigma\pi'$ polarisation is:

$$I_{\sigma\pi}^{h00}(\phi) = \sin^2\theta\left(F_m^2 + F_{ats}^2\sin^2\phi\right)$$

In this case, ATS scattering should hence be suppressed at $\phi = 0$, where the intensity becomes $F_m^2\sin^2\theta$, or proportional to h^2 at constant wavelength.

Appendix C

RIXS momentum resolution effects

C.1 RIXS momentum resolution

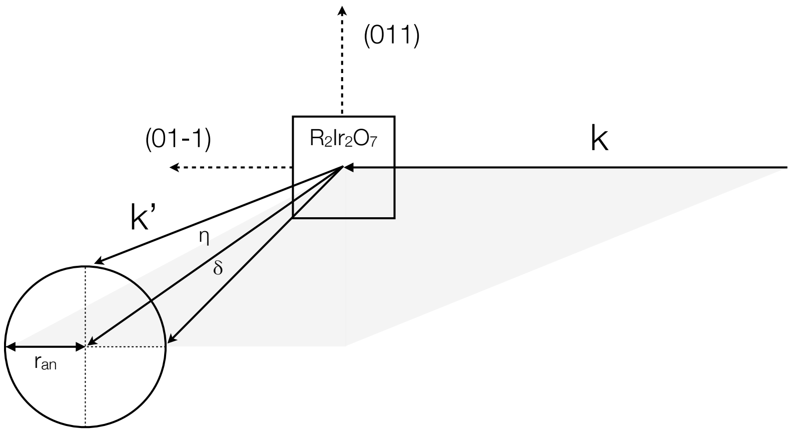

Figure C.1: RIXS momentum resolution due to finite analyser crystal area.

An accurate estimation of exchange constants should take into account the momentum resolution of the instrument. For a hard x-ray RIXS spectrometer, in an energy scan one samples over a solid angle of scattered x-rays covered by the analyser crystal (see Fig. C.1). This corresponds to a 3d slice of reciprocal space, centred on the nominal **Q** vector. Experimentally, we have control over the size (and shape) of this slice by using masks that shadow parts of the analyser. For the experiments described in chapter 5, the crystal analyser was masked to an "active" area of a circle of 60 mm diameter (r_{an} = 30 mm) or smaller. On a 2 m Rowland circle (R = 2 m), this corresponds to an angular acceptance of ±0.86°, both parallel (η) and perpendicular (δ) to the horizontal scattering plane. We can thus construct an equally-spaced grid of the solid angle, under the constraint $\tan^2\eta + \tan^2\delta \leq (r_{an}/R)^2$ and then convert to reciprocal space. This requires knowledge of the orientation of the sample. For example, the $Nd_2Ir_2O_7$ sample was aligned such that [100] and [011] directions were in the horizontal scattering plane. Data were taken along the ($h00$) direction. Hence for $\mathbf{Q} = (h00)$, introducing an angular offset in η (or δ) will result in a small component of ($0kl$):

$$\begin{aligned} h &= \left[\frac{2a\sin(\alpha/2)}{\lambda}\right]\frac{1}{\sqrt{1+\Delta_1^2+\Delta_2^2}} \\ k &= \Delta_1 h \\ l &= \Delta_2 h \end{aligned}$$

where

$$\begin{aligned} \Delta_1 &= \frac{\sin\eta+\sin\delta}{\cos\eta+\cos\delta} \\ \Delta_2 &= \frac{\sin\eta-\sin\delta}{\cos\eta+\cos\delta} \\ \cos\alpha &= \frac{\cos 2\theta}{\sqrt{1+\tan^2\delta}} \end{aligned}$$

where α is defined as the scattering angle between incident and outgoing beams, in order to keep the definition of 2θ as the scattering angle in the horizontal scattering plane.

Figure C.2 shows the conversion from real-space angular grid to reciprocal lattice grid [using $r_{an} = 30$ mm, $R = 2$ m, $\mathbf{Q} = (14\ 0\ 0)$]. It should be noted that the momentum resolution is not constant as a function of the nominal $\mathbf{Q}$ vector, even if the momentum transfer remains in the same reciprocal lattice direction. Alternatively, the 3d reciprocal space slice can be integrated along two directions to obtain one-dimensional resolution functions, shown in Fig. C.3. While this gives some intuitive measure of the RIXS momentum resolution, in practice the 3d reciprocal space grid should be used.

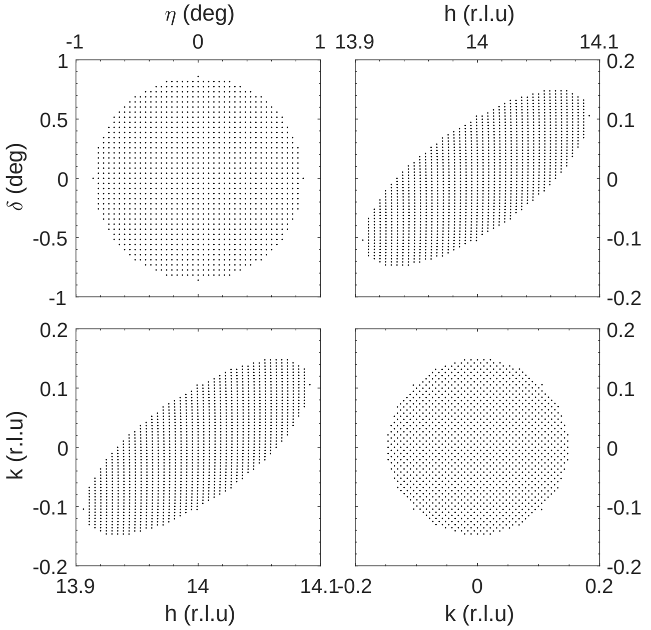

Figure C.2: RIXS momentum resolution in real and reciprocal space for $Nd_2Ir_2O_7$ at $\mathbf{Q} = (14\ 0\ 0)$, using a circular analyser mask of $r_{an} = 30$ mm.

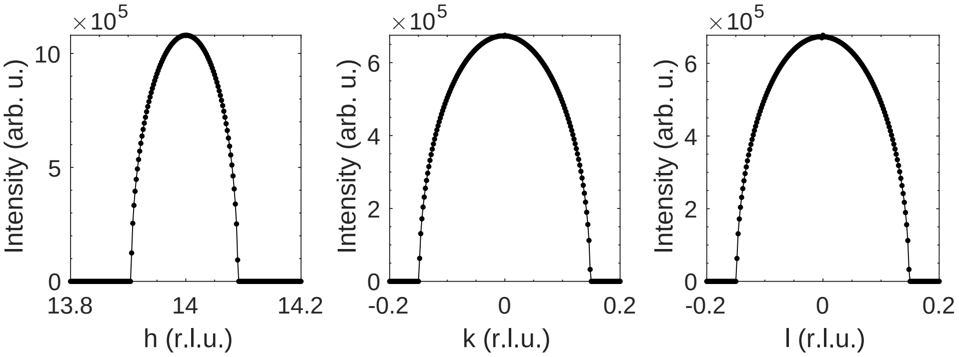

Figure C.3: Integrated momentum resolution along specific reciprocal space directions at $\mathbf{Q} = (14\ 0\ 0)$.

C.2 Effect of momentum resolution on magnetic excitations

For fitting the spin-wave Hamiltonian, the nominal $\mathbf{Q}$ value was used to compute the spin-wave spectrum. This must be considered an approximation; ideally the data should be fitted against slices of reciprocal space, centred on the nominal $\mathbf{Q}$ value[1]. To quantify how this would affect the collected data, we computed the effect of the momentum resolution as a r_{an}.

---

[1] This assumes that the intensity of the magnetic excitation measured by RIXS for $Nd_2Ir_2O_7$ can be well described by $S^{yy} + S^{zz}$. While our data indicates that this is roughly the case, it should be considered an approximation.

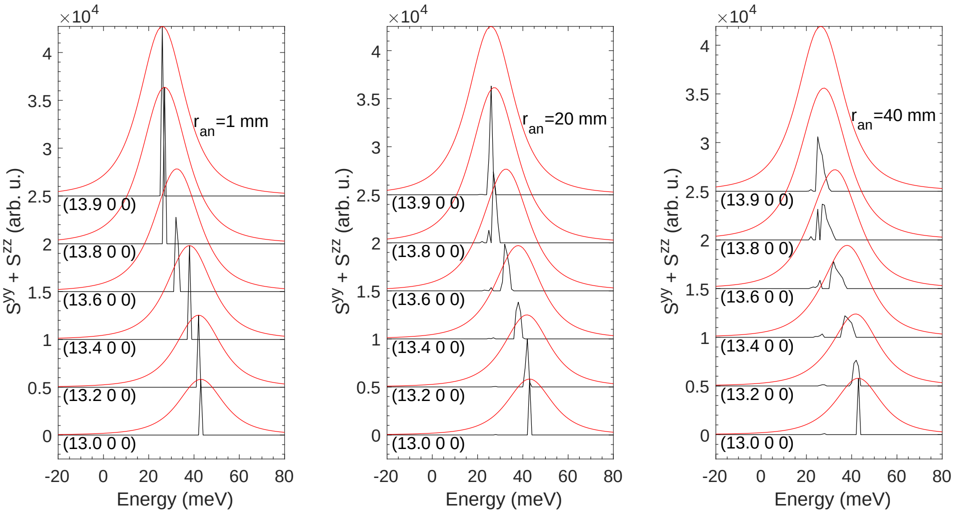

Figure C.4: Effect of momentum resolution on the magnetic excitations in $Nd_2Ir_2O_7$. The black solid lines are the expected dispersion of magnetic excitations using a reciprocal space grid of $\sim$ 1e3 points centred on the nominal $\mathbf{Q}$ value. The red line is a convolution of the momentum sampled data with the energy resolution, and corresponds to what would be measured in a RIXS experiment.

Figure C.4 shows the effect of finite momentum resolution on the dispersion of magnetic excitations. For small r_{an}, the reciprocal space area sampled for each $\mathbf{Q}$ is small and and the magnetic excitations show a sharp peak at the nominal excitation energy (black solid line). The data can be convoluted with the energy resolution to show the expected RIXS energy scan (red solid line). As the active analyser area is increased, the corresponding area in reciprocal space increases, and the magnetic excitations become more distributed in energy. However, even for the lowest momentum resolutions, one should be able to discern a dispersive feature. Nevertheless, with increasing r_{an}, the peak shape becomes asymmetric and acquires an intrinsic width of more than 10 meV, which can affect the fitted energy dispersion.

Figure C.5 shows how the momentum resolution affects the dispersion of the single-magnon excitation, where we have assumed that the maximum of the dispersive feature can be reliably extracted. The effect is small compared to typical uncertainties in the fitted RIXS data. Thus we conclude that the effect of finite momentum resolution on the fitted exchange parameter is negligible, but note that the asymmetric shape and finite line-width could however affect

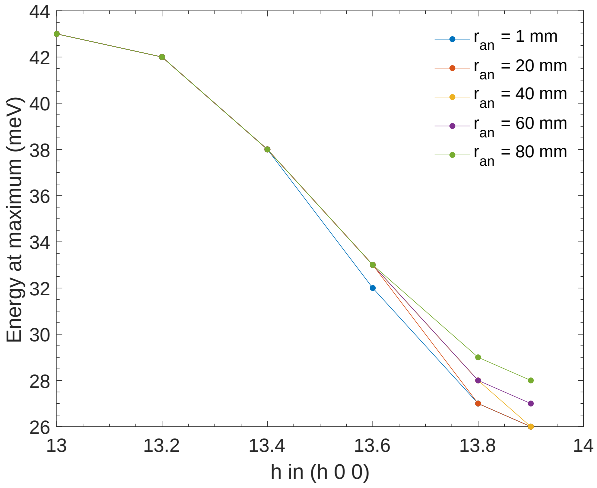

Figure C.5: Effect of momentum resolution on the single-magnon dispersion of AIAO order, using J=27 meV, D = 5 meV. The data points indicate the maxima of the single-magnon excitation, after taking into account momentum and energy resolution.

how well the data can be fitted, in particular if a strong elastic line is present.[2]

---

[2] A related effect is that nearby Bragg peaks can start to “bleed” into energy scans if the momentum resolution is low. In this case, it can be feasible to use a custom mask that only blocks the offending Bragg peak, in order to obtain clean energy scans.